THE MODELING OF ARSENIC REMOVAL FROM CONTAMINATED WATER USING COAGULATION AND SORPTION

A Dissertation

by

JIN-WOOK KIM

Submitted to the Office of Graduate Studies of
Texas A&M University
in partial fulfillment of the requirements for the degree of

DOCTOR OF PHILOSOPHY

August 2005

Major Subject: Civil Engineering

THE MODELING OF ARSENIC REMOVAL FROM CONTAMINATED WATER USING COAGULATION AND SORPTION

A Dissertation

by

JIN-WOOK KIM

Submitted to the Office of Graduate Studies of
Texas A&M University
in partial fulfillment of the requirements for the degree of

DOCTOR OF PHILOSOPHY

Approved by:

Chair of Committee,	Timothy A. Kramer
Committee Members,	Bill Batchelor
	James S. Bonner
	Richard H. Loeppert
Head of Department,	David V. Rosowsky

August 2005

Major Subject: Civil Engineering

ABSTRACT

The Modeling of Arsenic Removal from Contaminated Water
Using Coagulation and Sorption. (August 2005)
Jin-Wook Kim, B.S., Yonsei University, South Korea:
M.S., Yonsei University, South Korea
Chair of Advisory Committee: Dr. Timothy A. Kramer

To achieve predictive capability for complex environmental systems with coagulation and arsenic sorption, a unified improved coagulation model coupled with arsenic sorption was developed. A unified coagulation model coupled with arsenic sorption was achieved by the following steps: (1) an improved discretized population balance equation (PBE) was developed to obtain the exact solution of conventional coagulation, (2) the improved PBE was extended to an adjustable geometric size interval having higher numerical stability, accuracy, and computational efficiency than existing models for fractal aggregate coagulation that includes agglomeration and fragmentation, (3) a surface complexation equilibrium model and a sorption kinetic model was introduced to predict arsenic sorption behavior onto hydrous metal oxide surfaces, and (4) an improved discretized PBE was coupled with arsenic sorption kinetics and equilibrium models by aid of collision efficiency $\alpha(\mathrm{r}_i, \mathrm{r}_j)$ depending on surface charge (potential) on the hydrous metal oxide particles, colliding particle size ratio, and fluid strain-rate in applied flow system. The collision efficiency $\alpha(\mathrm{r}_i, \mathrm{r}_j)$ into the improved

discretized coagulation model for fractal aggregate yielded a unified improved coagulation model coupled with arsenic sorption kinetics and the equilibrium model. Thus, an improved unified coagulation model could provide high statistical accuracy, numerical stability, and computational efficiency to enhance predictive capability for behavior of arsenic sorption and fractal colloid particle aggregation and break-up, simultaneously.

From the investigation, it is anticipated that the unified coagulation model coupled with arsenic sorption kinetics and equilibrium will provide a more complete understanding of the arsenic removal mechanism and its application to water/wastewater treatment. Further, this coupled model can be applied to other water and wastewater treatment systems combined with sorption and filtration processes. These combined processes can be optimized by the coupled model that was developed in this study. By simulating the arsenic sorption and particle size distribution as a pretreatment before filtration (sand filtration or membrane filtration), the overall arsenic removal efficiency and operation cost can be estimated.

DEDICATION

This thesis is dedicated to my parents, daughters, sisters, and companion
who have stood by patiently all of these years;
especially to my wife, Eunjung Choi,
with all my love.

ACKNOWLEDGEMENTS

I wish to extend my faithful thanks and appreciation to the following individuals. I thank and appreciate Dr. Timothy Kramer, my committee chair, for the advice, inspiration, suggestions, criticism and support throughout the whole course of this investigation. I also would like to extend my sincere thanks to Dr. Bill Batchelor, Dr. James Bonner, and Dr. Richard Loeppert for their patience, time commitments, and helpful comments as my committee members.

Further, I thank all my colleagues and fellow research group members for their friendship, support, generosity, and time sharing. My special thanks to Namryong Her and Chunwoo Lee who was always with me during five years of life in College Station.

Finally, a very special thanks goes to my mother who always watches and encourages me from heaven and to my two little tiny lovely daughters, Yumin and Ariana, with priceless smiles.

TABLE OF CONTENTS

Page

CHAPTER

CHAPTER Page

LIST OF TABLES

LIST OF FIGURES

FIGURE Page

FIGURE Page

FIGURE Page

FIGURE Page

FIGURE Page

FIGURE Page

NOMENCLATURE

$|\dot{\gamma}'_{\max}|$ = the maximum absolute principal component of the local flow strain-rate

$\overline{|\dot{\gamma}'_{\max}|}$ = the average absolute maximum principle strain-rate

$\dot{\gamma}$ = flow strain-rate

$\dot{\gamma}_{\mathrm{L}}$ = flow local strain-rate

$\dot{\gamma}'_{mm}$ = the principal strain-rates that act in the principal directions

$\dot{\boldsymbol{\gamma}}$ = the strain-rate tensor

$\alpha(\mathrm{r}_i, \mathrm{r}_j)$ = collision efficiency between colliding particles

$\mathrm{W}(\mathrm{r}_i, \mathrm{r}_j)$ = colloid stability ratio

$\beta(\mathrm{r}_i, \mathrm{r}_j)$ = collision frequency between colliding particles

$\mathrm{b}_{k,j}$ = break-up distribution function

$\mathrm{s}_{k,j}$ = break-up rate coefficient,

b = break-up strain-rate exponent

s = break-up aggregate size exponent

η = break-up concentration exponent

$\phi(i)$ = a random distribution function for the daughter fragments of size class k

r_k = radius of size class k aggregate

d_k = dameter of size class k aggregate

υ_k = volume of size class k aggregate

$\overline{\upsilon}_k$ = average volume of size class k aggregate

n_k = number concentration of size class k aggregate

D_f = fractal dimension

D_{PF} = perimeter-based fractal dimension

K_{B} = break-up rate constant

q = geometric size interval

$\mathrm{C}_{i,j,k}$ = probability distribution function

$\mathrm{D}_{i,j,k}$ = probability distribution function

μ = fluid dynamic viscosity

ν = fluid kinematic viscosity

ρ = particle density

A = the Hamaker constant

k_B = Boltzmann's constant

g = gavitational constant

T = temperature

u_x = velocity in the x-direction

v_k = terminal settling velocity of size class *k* aggregate

τ = dimensionless time

κ = dimensionless break-up

N_k = dimensionless concentration of size class *k* aggregate

ψ_i = surface potential in the i^{th} surface plane

σ_P = total net surface charge density

σ_H = adsorbed proton charge density

σ_{is} = Inner-sphere complex charge density

F = Faraday constant

R = the molar gas constant

ε = the relative dielectric constant of water

ε_o = the permittivity of free space

c_{eq} = the adsorbate equilibrium concentration

k_f = mass transfer coefficient

D_p = pore diffusion coefficient

D_s = surface diffusion coefficient

κ = the Debye parameter (inverse of Debye-Huckel distance)

δ = thickness of (Stern) double layer

z = charge number (valence)

e = elementary charge

λ = colliding particles size ratio

λ_L = London wave length

H_o = the shortest separation distance between two spherical particles

$G(S,\lambda)$ = hydrodynamic function

k_{agg} = the aggregation rate constant

$\partial u_X/\partial y$ = non-rotational velocity gradient

ε = the turbulent eddy energy dissipation rate

V_T = the total interactive energy

V_A = van der Waals attraction energy

V_R = the electrical repulsion energy

Φ_L = the energy dissipation function in fluid system

$\overline{G}$ = the root-mean square velocity-gradient

Φ = the dissipation of energy per unit volume brought about by fluid viscosity

G' = normal strain-rate

G'' = shear strain-rate

c = mean clearance

e = eccentricity (center to center distance between outer and inner cylinders)

u' = characteristic velocity fluctuation

CHAPTER I

INTRODUCTION

1.1 Statement of Purpose

In 2001, USEPA adopted a new arsenic standard (< 10 ppb) and public water systems must obey the 10 ppb new arsenic standard beginning January 23, 2006 and the agency declared that the final arsenic standard of 10 ppb in drinking water would become effective on January 1, 2006 (USEPA 2001a). However, the National Arsenic Occurrence Survey (NAOS) reported that 20.7 % of all water systems would be out of compliance if the standard was set at 2 ppb, 9.3 % would be out of compliance if the standard was set at 5 ppb, 3.6 % if the arsenic standard was set at 10 ppb, and if the standard was set at 20 ppb, 1.7 % of all water systems would not be in compliance (USEPA 2000). As is well known, the exposure to arsenic can lead to many health-related concerns both cancerous and non-cancerous. Further, arsenic is classified by the International Agency of Research on Cancer and the EPA as a human carcinogen.

The current lowering of the maximum contaminant level (MCL) established by the USEPA for arsenic in drinking water is 10 ppb. Thus, the need for adequate methods for removal of arsenic has become urgent. The sorption of the toxic metals on a hydrous metal oxide (HMO), i.e. $Al(OH)_3(s)$ (HAO) or $Fe(OH)_3(s)$ (HFO), is the most practical method for removing the toxic compounds from contaminated water. Ferric iron (Fe^{3+}) can act as a coagulant for suspended particle removal as well as an adsorbent, which is

---

The style and format of this thesis follows that of *Journal of Environmental Engineering*.

often called amorphous ferric oxy-hydroxide (am-$Fe(OH)_{3(s)}$) or 2-line ferrihydrite ($Fe_pO_r(OH)_s{\cdot}nH_2O$) for toxic metals such as arsenic, chromium, and lead. However, the hydrous metal oxide particle behaviors such as aggregation and break-up in the applied fluid flow are not easily predicted especially when these toxic metals coexist within the fluid system applied due to particle surface charge/potential evolution with time resulting from metal sorption onto the particle surface. To achieve predictive capability for the complex environmental system with coagulation and metal sorption, a unified coagulation model coupled with arsenic sorption should be developed.

First, an improved discretized population balance equation (PBE) will be developed in this study to obtain the exact solution of conventional coagulation model (Smoluchowski 1917) coupled with chemical reactions (i.e., arsenic sorption) and fluid dynamics. Furthermore, relatively little attention has been paid to fractal aggregate modeling including agglomeration and fragmentation. Spherical particle coalescence applies only to ideal bubbles and droplets and most particle aggregates are found to be fractal, especially in solid colloidal particle coagulation. Thus, fractal aggregate coagulation via the higher numerical stability and accuracy is needed for realistic simulation. Second, a surface complexation equilibrium model using a thermodynamic equilibrium database and a sorption kinetic model using diffusion mass transport will be introduced to predict arsenic sorption behavior onto hydrous metal oxide surfaces and arsenic sorption effects on the hydrous metal oxide particle surface charge/potential and particle collision resulting in charged colloid particle coagulation phenomenon. Third, an improved coagulation model coupled with arsenic sorption kinetics and equilibrium models will be developed. The collision efficiency $\alpha(r_i, r_j)$ between colliding hydrous metal oxide particles will be calculated by aid of the surface charge/potentials on the hydrous metal oxide particles. Finally, introducing the collision efficiency $\alpha(r_i, r_j)$ into the improved coagulation model for fractal aggregate will yield a unified improved coagulation model coupled with arsenic sorption kinetics and equilibrium model.

Thus, an improved unified coagulation model, consisting of a simplified non-uniform discretized population balance equations for fractal aggregate and arsenic sorption reactions, will provide high statistical accuracy, numerical stability, and computational efficiency to enhance predictive capability for behavior of arsenic sorption and fractal colloid particle aggregation and break-up, simultaneously.

1.2 Background

1.2.1 Arsenic in Drinking Water

In the nineteenth century, arsenic, the twentieth most abundant element on the planet, was recognized as being toxic to humans and other living organisms (Pontius et al. 1994). Further, arsenic is one of the most common inorganic environmental contaminants and it is on the National Priority List as the second most common contaminant of concern. Over the years, extensive research has been performed to determine ways that arsenic may enter water sources, risks associated with arsenic exposure, and appropriate methods for arsenic removal. To adhere to the inevitably of stricter arsenic standards in the future, it is imperative that better methods for arsenic removal from drinking water are developed.

1.2.2 Aquatic Chemistry of Arsenic

According to the periodic table, arsenic is considered a nonmetal with an atomic number of 33 and an atomic mass of 74.922 grams per mole. The chemistry of arsenic is extremely complicated due to its stability in four different oxidation states, +5, +3, 0, and –3, which are dependent upon redox conditions (Gupta and Chen 1978). However, in most natural waters, the primary oxidation states are +5 and +3. Arsenic species with a +5 oxidation state are known as arsenate or arsenic acid, whereas species with a +3 oxidation state are referred to as arsenite or arsenous acid (Masscheleyn et al. 1992). The common and most stable forms of arsenic occurring in oxidized surface waters are the arsenate species, H_3AsO_4, $H_2AsO_4^-$, $HAsO_4^{-2}$, and AsO_4^{-3}. The arsenite species, $H_4AsO_3^+$, H_3AsO_3, $H_2AsO_3^-$, $HAsO_3^{-2}$, and AsO_3^{-3} which are three to twenty times more toxic than the arsenate species (Frank and Clifford 1986), become predominate in moderately reducing conditions (Gupta and Chen 1978).

According to the above arsenic pC-pH diagrams (Figures 1 and 2), it is apparent that arsenate species are present in the form of an anion at the normal pH range (6~9) of natural waters, and that the predominant form of As (V) present is dependent upon the pH of the water. In contrast, arsenite species have a neutral charge in this pH range. The neutral charge renders the arsenite species more mobile and less adsorbable than the arsenate species (Masscheleyn et al. 1992), which is an important characteristic when considering removal of arsenic by adsorption.

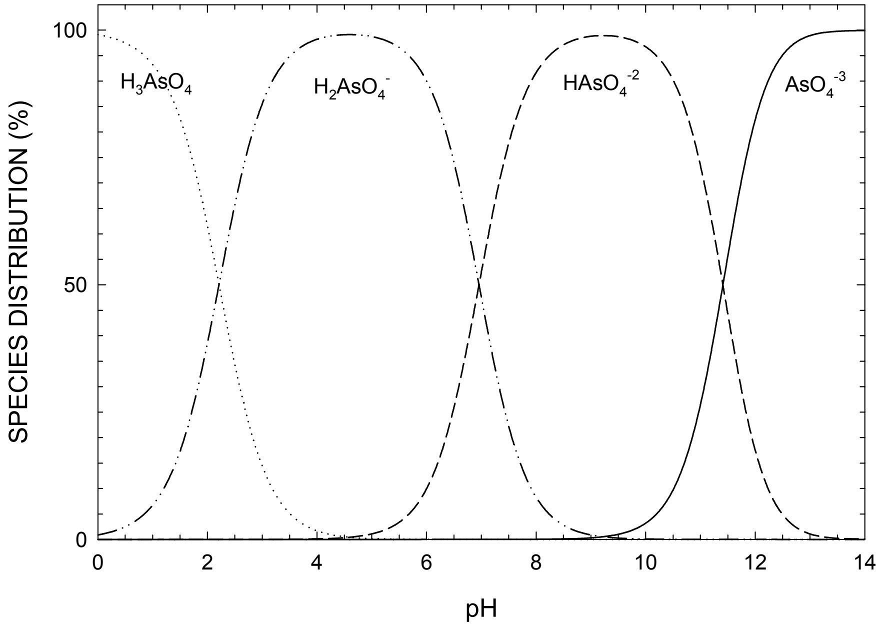

Figure 1.1 pC-pH diagram for arsenate species ($[As]_o$ = 100 ppb, I = 10^{-3} M)

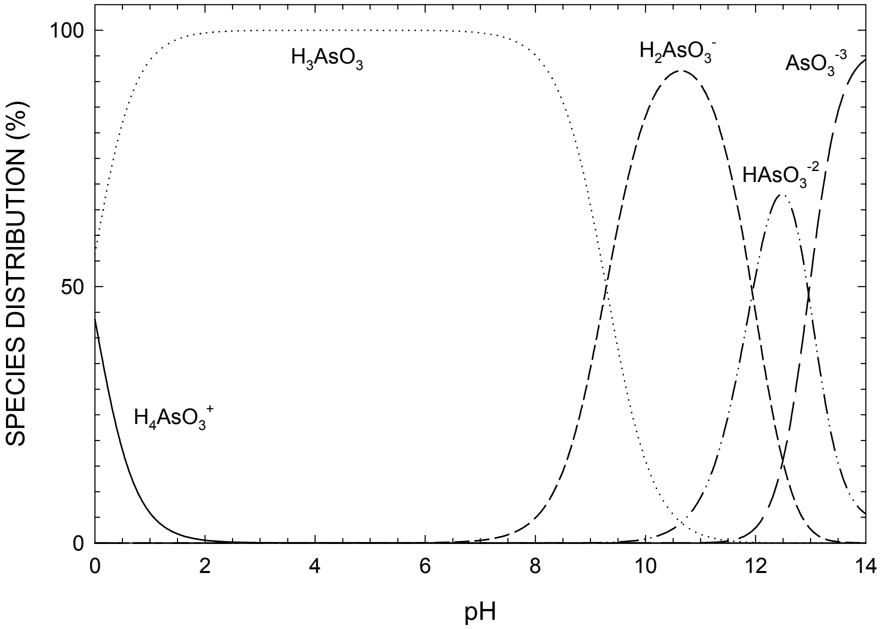

Figure 1.2 pC-pH diagram for arsenite species ($[As]_o$ = 100 ppb, I = 10^{-3} M)

1.2.3 Methods of Arsenic Removal from Drinking Water

A variety of methods are available for arsenic removal from contaminated water (Kartinen and Martin 1995; Papadiamas et al. 1997; Fields et al. 2000; Jiang 2001; USEPA 2001b), including (1) coagulation and filtration with or without sedimentation, (2) coagulation assisted micro-filtration membrane separation, (3) lime softening, (4) adsorption on granular activated alumina, (5) adsorption on ion exchange resins, and (6) reverse osmosis, and (7) electro-dialysis. However, each of these traditional methods of treatment involves substantial costs and is often difficult to properly control, especially for small water treatment systems. It is noteworthy that sorption of the toxic metals on hydrous metal oxy-hydroxides was found to be the most cost effective and practical toxic metals removal technology. Coagulation using the salts of metals such as Al(III) and Fe(III) has been proven to be an adequate technique by forming hydrous metal oxides for the removal of arsenic(V) from contaminated water. The binding mechanism is mainly the sorption via surface complexation of these compounds onto the hydrous metal oxides, i.e. $Al(OH)_3(s)$ and $Fe(OH)_3(s)$, and subsequent co-precipitation. Although, it is possible to form ferric arsenate ($FeAsO_4 \cdot 2H_2O$) as the results of co-precipitation, this possibility is excluded as ferric arsenate can be formed only at relatively high concentration of Fe(III) and As(V) (over 1.0 mM) and low pH (below 2.0) (Robins 2001). Thus, in this study, at lower concentrations of As(V) and relatively higher Fe(III) concentrations with neutral pH range of 6~8, simply adsorptive binding (surface complexation) of arsenic onto oxy-hydroxides occurs and this method is the most effective for arsenic removal from aqueous solutions.

1.2.4 Coagulation in Water Treatment Process

In water treatment, coagulation refers to the agglomeration of small suspended particulate material and is defined as three separate and sequential steps of coagulant formation, particle destabilization, and interparticle collisions (Letterman et al. 1999). The process of generating interparticle collisions is frequently termed flocculation. Flocculation has been subdivided into three basic collision-inducing mechanisms of perikinetic, orthokinetic, and differential sedimentation. Brownian motion, the random diffusion of the particles, is responsible for perikinetic flocculation. The variables that control perikinetic flocculation are the temperature and the particle size. Differential sedimentation results from larger and/or denser particles settling at a higher velocity than other particles. The mechanism of orthokinetic flocculation is due to the particle collisions that occur from the fluid and particle motion. Since the fluid motion can be manipulated by mechanical agitation, orthokinetic flocculation is of great interest in various science and engineering fields. It must be noted that as flocculation is a subset of coagulation the words coagulation and flocculation will be used interchangeably when referring to the particle collision mechanisms. A proper method of analyzing and predicting orthokinetic flocculation is thus desired for water treatment processes.

In recent years, numerous studies have attempted to solve the particle aggregation problem consisting of the continuous population balance equations (PBE), where the continuous PBE can be expressed as an continuous integro-partial-differential equation (Drake 1972; Ramkrishna 1985) (Eq. (1.1)),

$$\left(\frac{dn(\upsilon,t)}{dt}\right)_{Agg} = \frac{1}{2}\int_0^{\upsilon} \alpha\beta(\upsilon-w,w)n(\upsilon-w,t)n(w,t)dw - \int_0^{\infty} \alpha\beta(\upsilon,w)n(\upsilon,t)n(w,t)dw \quad (1.1)$$

where n is the number concentration of particles, r is the particle or aggregate radius, α is a collision efficiency, υ and *w* are particle volume, *i*, *j*, *k*, and *l* refer to particle size class indices, and t is time. The quantity β is termed the collision frequency kernel and is dependent on particle size, the particle movement mechanism, and collision geometry.

Aggregate breakup mechanisms have been applied to various fields, such as floc disintegration, droplet fragmentation, and comminution of particle solids (Vanni 1999). Population balance equations related to a breakup reaction can be expressed by continuous and discrete approaches (Patil et al. 2001). Few analytical solutions using either method are available under limited conditions (Ziff and McGrady 1985; Peterson 1986). Thus, numerical solutions are required for these breakup models. A pure breakup reaction in the form of a continuous breakup PBE can be expressed by Eq. (1.2) (Prasher 1987; Randolph and Larson 1988),

$$\left(\frac{dn(\upsilon,t)}{dt}\right)_{Break} = \int_0^{\infty} b(\upsilon,w)s(w)n(w,t)dw - s(\upsilon)n(\upsilon,t) \quad (1.2)$$

where $b(\upsilon, w)$ is the breakup distribution function, and $s(\upsilon)$ is the breakup rate coefficient.

In a straightforward manner, a final coagulation population balance model can be obtained from the combination of aggregation and breakup, yielding an overall population balance equation. Thus, an overall continuous population balance equation with aggregation and breakup reactions can be expressed by Eq. (1.3) after summation of Eqs. (1.1) and (1.2) (Ramkrishna 1985; Randolph and Larson 1988).

$$\left(\frac{\mathrm{dn}(\upsilon,\mathrm{t})}{\mathrm{dt}}\right)_{\mathrm{Total}} = \frac{1}{2}\int_0^{\upsilon}\alpha\beta(\upsilon-w,w)\mathrm{n}(\upsilon-w,\mathrm{t})\mathrm{n}(w,\mathrm{t})\mathrm{d}w - \int_0^{\infty}\alpha\beta(\upsilon,w)\mathrm{n}(\upsilon,\mathrm{t})\mathrm{n}(w,\mathrm{t})\mathrm{d}w + \int_0^{\infty}\mathrm{b}(\upsilon,w)\mathrm{s}(w)\mathrm{n}(w,\mathrm{t})\mathrm{d}w - \mathrm{s}(\upsilon)\mathrm{n}(\upsilon,\mathrm{t}) \tag{1.3}$$

Although numerous studies have attempted to solve the classical coagulation equation of Eq. (1.3), it is impossible to find an exact solution. Only limited analytical solutions exist with the assumptions of a monodisperse initial condition and simplified collision and breakup kernels. After converting a continuous particle size distribution into a discretized particle-size domain (like a histogram) where integrals are replaced with summations, an overall discretized coagulation model including aggregation and breakup is produced as Eq. .

$$\left(\frac{\mathrm{dn}_k}{\mathrm{dt}}\right)_{\mathrm{Total}} = \frac{1}{2}\sum_{i+j=k}\alpha\beta(\mathrm{r}_i,\mathrm{r}_j)\mathrm{n}_i\mathrm{n}_j - \mathrm{n}_k\sum_{l=1}^{\infty}\alpha\beta(\mathrm{r}_l,\mathrm{r}_k)\mathrm{n}_l + \sum_{j=k+1}^{\infty}\mathrm{b}_{k,j}\mathrm{s}_j(\mathrm{n}_j)^{\eta} - \mathrm{s}_k(\mathrm{n}_k)^{\eta} \tag{1.4}$$

To obtain exact numerical solutions of the overall continuous coagulation population balance equations of Eq. (1.4), extensive computation time and hardware are required. A realistic maximum size used in coagulation modeling would therefore produce an unmanageable number of simultaneous equations to solve. To overcome this computational non-efficiency of the continuous coagulation model , various non-uniform discrete schemes have been introduced for aggregation (Gelbard and Seinfeld 1978; Gelbard et al. 1980; Batterham et al. 1981; Hounslow et al. 1988; Marchal et al. 1988; Litster et al. 1995; Hill and Ng 1996; Kumar and Ramkrishna 1996; Kramer 2000; Vanni

2000) and breakup (Coulaloglou and Tavlarides 1977; Pandya and Spielman 1982; Lu and Spielman 1985; Chen et al. 1990; Kusters 1991; Ziff 1991; Hill and Ng 1995; Spicer and Pratsinis 1996a; Serra and Casamitjana 1998; Kramer and Clark 1999; Zhang and Li 2003).

Relatively little attention has been paid to fractal particle coagulation modeling. Spherical particle coalescence applies only to ideal bubbles and droplets and most particle aggregates are found to be fractal, especially in solid colloidal particle coagulation. Thus, fractal coagulation modeling is needed for realistic simulation.

1.3 Research Objectives

The goal of this research is to develop a coupled model for arsenic (V) (arsenate) removal by the sequential processes of coagulation and sorption. The model will provide enhanced predictive capability for the exact behavior of arsenic and colloid growth as well as required doses and process operating cost. This goal will be achieved by accomplishing the following objectives:

1.3.1 Development of an Improved Coagulation Model

To obtain the numerical solution of Eq. (1.3) or (1.4) coupled with chemical reactions and fluid dynamics, a simplified coagulation model should be developed, rather than continuous model or uniform discretization model. In this study, an improved coagulation model will be developed and coupled with arsenic sorption kinetics. Thus, the improved coagulation model, consisting of a simplified non-uniform discretization scheme, will provide high statistical accuracy, numerical stability, and computational efficiency. Furthermore, relatively little attention has been paid to fractal aggregate modeling including agglomeration and fragmentation. Spherical particle coalescence applies only to ideal bubbles and droplets and most particle aggregates are found to be fractal, especially in solid colloidal particle coagulation. Thus, fractal aggregate coagulation via the higher numerical stability and accuracy is needed for realistic simulation. Developing an improved coagulation model will consist of several steps as follows:

(1) An improved coagulation model will have aggregation and breakup kernels with the addition of an adjustable geometric size interval (*q*), where *q* is a volume ratio of class *k+1* particle to class *k* particle ($q = \upsilon_{k+1} / \upsilon_k$). This improved coagulation model overcomes two limitations; a huge number of variable domain sizes for the uniform discrete model and the rough resolution of larger aggregates for the non-uniform discrete model with a fixed class size interval.

(2) The improved adjustable discretized model will be converted to a dimensionless form to enhance computational efficiency (CPU time) in orthokinetic coagulation modeling.

(3) The model will be verified with the time derivative of the zero and first moment methods and compared with analytical and numerical solutions. Also, the self-preserving distribution test will be conducted by using size-independent and size-dependent kernels.

(4) Two parameters, the collision efficiency and breakup coefficient, will be calculated from experimental data using a parameter estimation scheme (least square error method).

(5) Relatively little attention has been paid to fractal aggregate modeling including agglomeration and fragmentation. Thus, fractal aggregate coagulation modeling will be developed for realistic simulation. This study will examine several techniques of discretization and compare them to uniform discrete modeling. Further, modifications are made to incorporate breakup in the orthokinetic population balances while improved discretization methods are developed and applied to fractal aggregation modeling.

(6) Computational efficiency, statistical accuracy, and numerical stability tests will be conducted and these results will be compared with a uniform discretized coagulation model.

1.3.2 Application of an Arsenic Sorption Model

It is anticipated that hydrous ferric oxide (HFO) surface charge will be changed during arsenic sorption onto the HFO surface and the changed in surface charge affects the particle coagulation process. A number of investigations on coagulation have focused on the collision of particles having neutralized surface charge. That is, coagulation studies, including experimental and theoretical aspects, have been conducted under ideal conditions such as the fixed aqueous pH values to the particle pH_{ZPC} (zero point of charge). Thus, the sorption model should be applied to predict the time evolution of particle surface charge during arsenic sorption onto the particle. The sorption kinetic model will be applied by the aid of equilibrium surface complexation model. The arsenic sorption kinetic model will be coupled with the improved coagulation model that will be developed in next task.

Two sorption models will be applied to describe the arsenic sorption behavior onto hydrous ferric oxide (am-$Fe(OH)_3(s)$ or 2-line ferrihydrite ($Fe_pO_r(OH)_s \cdot nH2O$)) generated from the coagulation process via metal hydrolysis. These two models consist of a chemical equilibrium model (surface complexation model) and a kinetic model (diffusion transport model). For arsenic sorption kinetic modeling, a diffusion transport model will be developed to predict the arsenic sorption rate. Various model parameters (equilibrium coefficients, particle properties, diffusivity, and mass-transport coefficient) will be derived from the literature and calculated if needed. After determining the arsenic sorption rate with sorption kinetic model, this sorption kinetics will be coupled with surface complexation model using local equilibrium assumption. Finally, using two sorption model schemes, the kinetics of surface potential or surface charge density will be calculated and introduced to next step to develop the unified model with As(V) sorption model and coagulation.

1.3.3 Coupling the Coagulation Model with Sorption Model

This phase of research will provide modeling capability for the complicated arsenic removal mechanisms throughout the coagulation and arsenic sorption processes. It is anticipated that the coupled model will provide a more complete understanding of arsenic removal mechanism and its application to drinking water treatment. For this purpose, objectives of arsenate sorption modeling and improved coagulation modeling will be used to develop this coupled model. Further, this coupled model will be applicable to other water and wastewater treatment systems combined with sorption and filtration processes. These combined processes will be optimized by a coupled model that will be developed in this research. By simulating the arsenic sorption and particle size distribution as pretreatment before filtration (sand filtration or membrane filtration), the overall arsenic removal efficiency and operation cost can be anticipated.

Model coupling will be achieved by combining the sorption model with the improved coagulation model. Two arsenic sorption models introduced in previous task will be coupled with an improved coagulation model previously developed. This coupling will be carried out on the basis of kinetic models (time dependent reactions). Relationships between surface charge/potential and particle collision rate (surface charge (σ) vs. collision efficiency (α)) will be developed and applied to an improved coagulation model developed. Finally, using the various collision efficiency, a unified model with arsenic sorption and coagulation will be achieved.

CHAPTER II

IMPROVED MODELS FOR COLLOID AGGLOMERATION: COMPUTATIONALLY EFFICIENT ALGORITHMS

2.1 Overview

A variety of modeling techniques for the population balances resulting from particle coagulation were examined. The simplified models using the non-uniform discretization scheme were compared to uniform discrete models. Further, new algorithms that incorporate a non-uniform discretization were developed. The uniform discrete population balance was used as the basis of comparison as it considers a continuous distribution of size classes of particles. Comparisons included the particle collision mechanisms of perikinetic, orthokinetic, and differential sedimentation with the inclusion of flow induced break-up. Initial particle populations considered were both monodisperse and polydisperse. The analysis focused on the resulting population distribution and a statistical comparison to the uniform discrete model. In the course of the investigation new algorithms were found to be substantial improvements in terms of computational time over the other models and compared favorably to the discrete/continuous model with respect to accuracy.

New probability distribution functions for aggregates produced in non-uniform discrete coagulation modeling were derived and incorporated into the population balance equations. These new algorithms made it possible to simulate fractal aggregate coagulation with high accuracy, perfect mass conservation and exceptional computational efficiency. Parameter sensitivity analysis showed that a break-up kernel does not influence total particle concentration within the limited range of having the break-up coefficient less than collision efficiency, but does influence the particle size distribution and coagulation patterns. An aggregate break-up study with various kernel parameters indicated that break-up rate is more influenced by particle volume and not size class or diameter as previously suspected. The new probability distribution functions are found to be useful in fractal aggregation modeling via the higher numerical stability and accuracy. The new particle population model is shown in the investigation to be superior to all of the other models, having mass conservation factor of over 0.99 and computation time of 3.125×10^{-2} sec, thus the new coagulation model can be used to develop predictive simulations for coagulation in computational fluid dynamics and reaction modeling.

2.2 Introduction

Coagulation is the growth of larger agglomerates by collisions and subsequent bonding of smaller particles contained in a fluid. These particles can be either fluid droplets or solids suspended in a gas or liquid. Inter particle motion induces the particle collisions and has been attributed to three basic mechanisms; fluid motion or orthokinetic coagulation, Brownian diffusion or perikinetic coagulation and differential sedimentation. Fluid motion also creates disruptive stresses that can cause fracture of the agglomerates. Coagulation of droplets or bubbles is often viewed as the coalescence of a continuous distribution, while the agglomeration of solid particles is discrete.

Smoluchowski derived population balance equations for the coagulation of discrete particles in simple shearing flow and Brownian motion, and these equations have been used extensively in modeling agglomeration (Smoluchowski 1917). The population balance equations take the form (Drake 1972),

$$\frac{\mathrm{dn}_k}{\mathrm{dt}} = \frac{1}{2}\sum_{i+j=k} \alpha\beta(\mathrm{r}_i, \mathrm{r}_j)\mathrm{n}_i \mathrm{n}_j - \mathrm{n}_k \sum_{l=1}^{\infty} \alpha\beta(\mathrm{r}_l, \mathrm{r}_k)\mathrm{n}_l \tag{2.1}$$

where, n is the number concentration of particles (number/volume), r is the particle or agglomerate radius, α is a collision efficiency ($0 \le \alpha \le 1.0$), t is time, and *i*, *j*, *k*, and *l* refer to particle size class indices. The quantity $\beta(\mathrm{r}, \mathrm{r})$ is termed the collision frequency kernel and is dependent on particle size, the particle movement mechanism, and collision geometry. Equation (2.1) is strictly realized only for a truly discrete particle size distribution, i.e., where *i*, *j*, *k*, and *l* are the number of primary particles making up the aggregate. For coalescence, a continuous integro-differential equation has been derived for the agglomeration between particles of volume υ and w and is given as,

$$\left(\frac{\mathrm{dn}(\upsilon, \mathrm{t})}{\mathrm{dt}}\right)_{\mathrm{Agg}} = \frac{1}{2}\int_0^{\upsilon} \alpha\beta(\upsilon - w, w)\mathrm{n}(\upsilon - w, \mathrm{t})\mathrm{n}(w, \mathrm{t})\mathrm{d}w - \int_0^{\infty} \alpha\beta(\upsilon, w)\mathrm{n}(\upsilon, \mathrm{t})\mathrm{n}(w, \mathrm{t})\mathrm{d}w \tag{2.2}$$

with the number of particles of volume υ replacing the discrete index *i* and the collision frequency kernel a function of the volume rather than a radius. To solve the population balance equations it is customary to discretize the distribution of Eq. (2.2) into size or volume classes as represented by Eq.(2.1). In Eq. (2.1) the indices *i*, *j*, and *k* refer to size classes; a primary particle will be of size class 1, a doublet of two primary particles a size class 2 etc. Obviously the smaller the primary size, the closer the discrete approximation approaches the continuous model of Eq. (2.2). Unfortunately, reducing primary size class significantly expands computational time for even a limited aggregate size range. For example, if fractal aggregate coagulation is modeled with an initial primary particle diameter of 1.0 μm and 1000 equations are solved, the maximum size is approximately 30 μm in diameter. A realistic maximum size used in coagulation modeling would therefore produce an unmanageable number of simultaneous equations to solve.

In recent years, numerous studies have attempted to solve the coalescence continuous integro-differential equation of Eq. (2.2). One of these approaches is to use a non-uniform discretization technique. Various computational algorithms based on this non-uniform discretization of the size classes have been proposed by previous researchers (Gelbard et al. 1980; Batterham et al. 1981; Hounslow et al. 1988; Marchal et al. 1988; Litster et al. 1995; Hill and Ng 1996; Kumar and Ramkrishna 1996a) and were rigorously studied by Vanni concerning their computational accuracy, error, and efficiency (Vanni 2000).

Although several researches have used these coagulation models for real aggregate systems (Spicer and Pratsinis 1996a; Spicer and Pratsinis 1996b; Biggs and Lant 2002; Diemer and Olson 2002b; Diemer and Olson 2002a), relatively little attention has been paid to fractal aggregate modeling including agglomeration and fragmentation. Spherical particle coalescence applies only to ideal bubbles and droplets and most particle aggregates are found to be fractal, especially in solid colloidal particle coagulation. Thus, fractal aggregate coagulation modeling is needed for realistic simulation. This paper will examine several techniques of discretization and compare them to uniform discrete modeling. Further, modifications are made to incorporate break-up in the orthokinetic population balances while improved discretization methods are developed and applied to fractal aggregation modeling. Finally, model comparisons are made using simulation data of particle size distributions, conservation of mass, sensitivity of parameters, and computational time.

2.3 Background

2.3.1 Coagulation Rate Kernels

Equation (2.1) generates an infinite number of coupled differential equations that, when solved, will produce particle number concentrations for each size class of k = 1 to ∞. It is apparent that any attempt at a real solution would not be able to solve an infinite number of equations and therefore Eq. (2.1) is rewritten

$$\frac{\mathrm{dn}_k}{\mathrm{dt}} = \frac{1}{2}\sum_{i+j=k} \alpha\beta(\mathrm{r}_i, \mathrm{r}_j)\mathrm{n}_i\mathrm{n}_j - \mathrm{n}_k \sum_{l=1}^{\max} \alpha\beta(\mathrm{r}_l, \mathrm{r}_k)\mathrm{n}_l \tag{2.3}$$

where *max* refers to a maximum size class. In essence Eq. (2.3) is a finite number of second order reaction rate equations which are coupled by the inclusion of all other size class concentrations. The rate constants for these equations are the β terms, or kernels and may vary with particle size and collision mechanism. These rate constants can be simple linear operators or obtained from mass balances of the colliding particles.

The population balance equations given by Eq. (2.3) are irreversible. To consider reversibility the potential for aggregate break-up can be included. Typically, break-up occurs in orthokinetic coagulation as the stresses of fluid motion are the likely fracture inducing forces (Thomas 1964; Argaman and Kaufman 1970; Parker et al. 1972; Tambo and Watanabe 1979a; Lu and Spielman 1985; Ray and Hogg 1986; Sonntag and Russel 1987). Kramer and Clark provide a rigorous discussion of contemporary aggregate break-up models and propose several break-up kernels (Kramer and Clark 1999). Using a break-up kernel that has units consistent with Eq. (2.3) produces new population balance equations of,

$$\frac{\mathrm{dn}_k}{\mathrm{dt}} = \frac{1}{2}\sum_{i+j=k} \alpha\beta(\mathrm{r}_i,\mathrm{r}_j)\mathrm{n}_i\mathrm{n}_j - \mathrm{n}_k\sum_{l=1}^{\max} \alpha\beta(\mathrm{r}_l,\mathrm{r}_k)\mathrm{n}_l + \sum_{j=k+1}^{\max} \mathrm{b}_{k,j}\mathrm{s}_j(\mathrm{n}_i)^{\eta} - \mathrm{s}_j(\mathrm{n}_i)^{\eta} \tag{2.4}$$

where $\mathrm{b}_{k,j}$ is a break-up distribution function, s_j is a break-up rate coefficient, and η is a break-up concentration exponent.

In both continuous and discrete modeling the volume and/or radii of the particles are significant parameters in the rate kernels. In droplet coalescence conservation of the volumes will produce a new droplet radius and is easily computed. In terms of a size class, such a radius is given by,

$$\mathrm{r}_k = \sqrt[3]{\frac{3k\upsilon_1}{4\pi}} \tag{2.5}$$

with υ_1 the volume of the primary size class droplet. Aggregates comprised of solid particles can be treated using a fractal dimension. Thus, the radius r_k of a size class k aggregate (comprised of k primary particles of radius r_1) can be expressed as,

$$\mathrm{r}_k = \mathrm{r}_1\left(\mathrm{k}\right)^{1/\mathrm{D_f}} \tag{2.6}$$

where D_f is the fractal dimension. A list of fractal dimensions for floc aggregates produced during coagulation studies is presented in Table 2.1.

Table 2.1 Fractal Dimension Obtained by Coagulation Studies

System	Fractal Dimension	Study
Ferric sulfate floc	2.3 ~ 2.8	Lagavankar and Gemmell 1968
Kaolin with aluminum sulfate	1.95 (low alum) , 1.60 (high alum)	Tambo and Watanabe 1979b
Alum aggregates	1.59 ~ 1.97	
Activated sludge floc	1.4	
Clay-iron or Clay-magnesium flocs	1.91 ~ 1.92	
Minerals with aluminum sulfate in jar test		Gorczyca and Ganczarczyk 1996
(a) Illite	1.71 (D_2) 1.49 (D_3)	
(b) Montmorillonite	1.86 (D_2) 1.79 (D_3)	
(c) Calcite	1.97 (D_2) 1.65 (D_3)	
(d) Silt	1.80 (D_2) 1.37 (D_3)	
(e) Activated slude	1.81 (D_2) 1.76 (D_3)	
Ferric chloride (< 0.75mm)	2.3	Wiesner and Mazounie 1987
Ferric chloride	1.7 ~ 2.0	Tchoubar et al. 1991
Ferric chloride (fresh HFO)	1.48 ~ 2.58	Lo and Waite 2000
Ferric chloride	2.25 → 2.52	Jung et al. 1996
HFO by freezing and thawing (dense HFO)	2.5 ~ 2.8	Hofmann et al. 2004
HFO by freeze-dried (2-line ferrihydrite)	2.7 ~ 2.8	Weidler and Stanjek 1998
Hematite in light scattering apparatus	2.3 (DLCA)	Amal et al. 1990a
Hematite in light scattering apparatus	2.3 (DLCA) ~ 2.8 (RLCA)	Amal et al. 1990b
Hematite in light scattering apparatus		Amal et al. 1994
a) with KCl 0.1 M	2.21 (DLCA)	
b) with KCl 0.1 M + fulvic acid 2.5 mg/L	2.82 (DLCA)	
Hematite particles w/o shear	1.25 ~ 1.50	Gardner et al. 1998
Hematite particles	1.68 ~ 1.87 (DLA) 2.2 (RLA)	Zhang and Buffle 1996
α-FeOOH	1.6 (DLA) 2.0 (RLA)	Hackley and Anderson 1989
γ-Alumina with		Waite et al. 2001
a) $CaCl_2$	2.11 (0.2M) ~ 2.23 (0.6M)	
b) NaCl	2.09 (0.6M) ~ 2.10 (0.7M)	
c) Na_2SO_4	1.85 (0.2M) ~ 1.91 (0.3M)	
Kaolin	1.31 ~ 1.42	Glasgow 1989
Kaolinite in shear flow		Herrington and Midmore 1993
a) 1.0 M KCl, pH 6.5	3.00	
b) 10^{-3} M KCl, pH 3.21	2.92	
c) 10^{-3} M KCl, pH 4.58	1.88	
d) 10^{-3} M KCl, pH 6.45	1.80	
Bentonite in cylindrical Burchard cell, shear flow	1.8 (DLA) @ pH < 4.21 3.0 (DLA) @ pH > 4.21	Axford and Herrington 1994
Silica	2.12 ± 0.5 (DLCA)	Schaefer et al. 1984
Silica particle	2.1 (RLA)	Axford 1997
Inorganic particles (gold, silica, latex)	1.85 ± 0.05 (DLCA) 2.11 ± 0.05 (RLCA)	Lin et al. 1989b; Lin et al. 1990a; Lin et al. 1990b; Lin et al. 1990c
Inorganic particles (gold, silica, latex)	1.85 (DLCA) 2.11 (RLCA)	Lin et al. 1989a
Latex spheres with aluminum sulfate	1.5 ~ 1.9	Clark and Flora 1991
Latex spheres with sodium chloride	1.43 ~ 2.08 (Couette) 1.77 ~ 1.83 (Paddle mixer)	Jiang and Logan 1996
Latex spheres	1.75 ~ 1.80 (DLA) 2.09 ~ 2.20 (RLA)	Burns et al. 1997
Latex spheres	2.48	Sonntag and Russel 1987
Latex spheres with sodium chloride	1.79 ~ 2.25	Johnson et al. 1996

Table 2.1 (Continued)

System	Fractal Dimension	Study
Latex spheres		Logan and Kilps 1995
(a) Rolling cylinder	1.68 (D_2) 1.59 (D_3)	
(b) Paddle mixer	1.89 (D_2) 1.92 (D_3)	
Latex spheres in Couette-Flow	1.98 (D_2) 2.60 (D_3) 1.12 (D_{PF}) 1.06 (D_1)	Serra and Casamitjana 1998b; Spicer et al. 1998
Latex spheres in Rhshton, 4-brade	2.1 (small floc) 2.5 (large floc)	Spicer et al. 1998
Latex spheres in Rhshton, 4-brade	1.2 ~1.3 (D_{PF})	Spicer et al. 1996
Latex spheres in Rhshton, 4-brade	1.1 → 1.3 (D_{PF})	Spicer and Pratsinis 1996b
Latex spheres in Couette-Flow	2.1 → 2.5	Oles 1992
3D off-lattice modeling	1.8 → 2.1 (DLA)	Meakin and Jullien 1988
Latex spheres in baffled mixing tank	1.7 → 2.1 (DLA)	Selomulya et al. 2001
Simplified modeling	1.85 (DLCA) 2.05 (RCLA)	Lattuada et al. 2003
Latex spheres	1.8 (DLCA) 2.0 ~ 2.2 (RCLA)	Sandkuhler et al. 2003
Latex spheres in blood tube rotator	1.79 (D_2) 1.80 (D_3) (DLCA) 1.61 (D_2) 2.00 (D_3) (RLCA)	Tang et al. 2001
Latex spheres in blood tube rotator	1.82 ~ 1.86 (DLCA) 2.06 (RLCA)	Tang 1999
Latex spheres in Couette-Flow		Tang et al. 2000
a) DLCA	1.8 (rpm 700) ~ 2.0 (rpm 2500)	
b) RLCA	2.06	
Particle - Cluster mechanism	2.5 ~ 3.0	Schaefer 1989
Cluster – Cluster mechanism	1.6 ~ 2.2	Witten and Cates 1986
Nickel hydroxycarbonate microspheres	1.7 ~ 1.8 (w/o shear) 2.2 ~ 2.7 (w/ shear)	Sonntag and Russel 1986
Latex spheres in Couette-Flow	2.0	Axford 1996
Latex spheres		Torres et al. 1991
a) Shear coagulation in Couette-Flow	1.80 (DLA)	
b) Brownian coagulation light scattering cell	1.80 (DLA)	
Latex spheres (DLA)	1.6	Hoekstra et al. 1992
Latex sheres in Couette-Flow	2.2 ~ 2.5	
Latex spheres in Y-shaped mixing cell	1.75 / 1.87 (fitting) (DLCA)	Schmitt et al. 2000
Latex spheres in Y-shaped mixing cell	1.75 (DLCA)	Odriozola et al. 1999
Latex spheres in Y-shaped mixing cell	1.75 (DLCA) ~ 2.10 (RLCA)	Odriozola et al. 2001
Latex spheres	1.65 (DLCA) ~ 2.03 (RLCA)	Asnaghi et al. 1992
Latex spheres	1.75 (DLCA) 2.10 (RLCA)	Magazu et al. 1989
Latex lattices	1.75 ± 0.03 (RLCA ~ DLCA)	Bolle et al. 1987
TiO_2 aerosol and Latex spheres	1.75 (DLCA) 2.15 (RLCA)	Wang and Sorensen 1999
Ludox silica spheres	1.75 (DLA) 2.08 (RLA)	Aubert and Cannell 1986
Aqueous gold colloids	1.75 (DLA) 2.05 (RLA)	Weitz et al. 1984; Weitz and Oliveria 1984; Weitz et al. 1985
Sludge, alum, iron, clay, and mixtures	1.4 ~ 2.8	Li and Ganczarczyk 1989
Activated sludge	1.13 ~ 1.22 (D_{PF})	
Marine snow	1.28 ~ 1.86	Kilps et al. 1994
Calcium carbonate in propeller mixer	1.8 & 2.4 (erosion)	Yeung and Pelton 1996
Lake water with alum	2.12 ~ 2.93 (D_3) 1.65 ~ 1.96 (D_2)	Chakraborti et al. 2000
Montmorillonite with alum	2.39 ~ 2.71 (D_3) 1.77 ~ 1.89 (D_2)	

* D_{PF} = perimeter-based fractal dimension
DLCA = Diffusion-Limitted Cluster Aggregation
RLCA = Reaction-Limitted Cluster Aggregation

2.3.2 Discretization of the Population Balance Equations

When solving either Eq. (2.1) or (2.2) numerically, some form of discretization must be conducted. The most straight forward is to use uniform size class increments beginning with a primary size that represents the smallest particle volume or size modeled. All other particles are integer multiples of the primary size class and all aggregates then range in size from size class 1 to a selected maximum as represented by Eq. (2.3). A drawback to this approach is that a very large number of equations must be generated, coefficients stored in memory and the equations solved simultaneously resulting in long computational time. To limit the number of equations, non-uniform size increments can be used. Instead of each size class, a range can be developed establishing an interval or bin which would in theory contain particles of size classes between the upper and lower limits of the bin. However, conserving mass or the number of particles becomes a problem.

In Fig. 2.1, bins are selected using a scheme with the histograms representing the number of particles in each bin. If it is assumed that a continuous range of particle sizes exist in each bin the size of the aggregates formed is uncertain. For example, particles from intervals 1 and 2 could collide and form particles that would fall into either interval 2 or interval 3 ($\upsilon_1 + \upsilon_1 = \upsilon_2$ or $\upsilon_2 + \upsilon_2 = \upsilon_4$). The problem then becomes how to allocate the product particles. Should all aggregates fall into interval 3 or should half be allocated to each interval 2 and 3? Failure to adequately account for the discretization problem leads to an incorrect mass balance in the computation. Several techniques have been proposed to generate a non-uniform discrete algorithm to model coagulation and are the main focus of this paper.

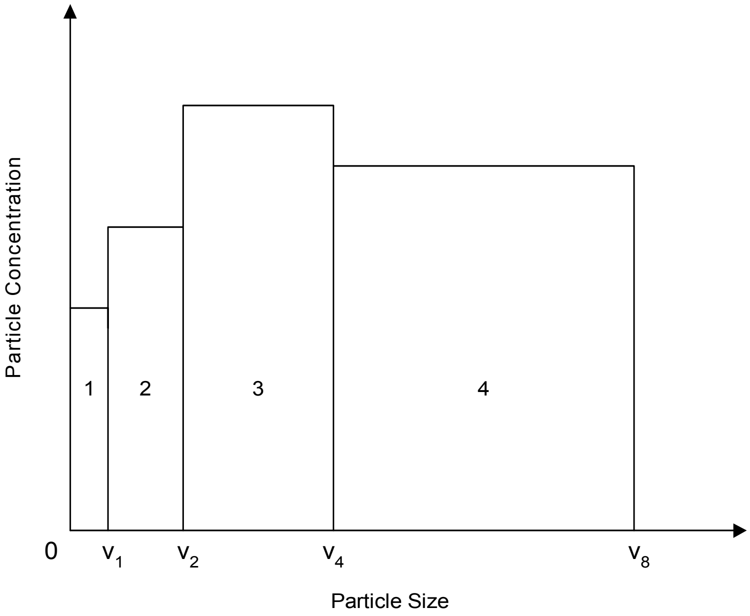

Figure 2.1 Non-uniform discrete particle size distribution

One of the most straight forward methods to obtain a non-uniform discretization of the coagulation population balance equations is to assume that the particles collide bi-kinetically. In the bi-kinetic assumption only equal sized particles collide. Then in Eq. (2.3) size class $i = j$ and the population balance becomes,

$$\frac{dn_k}{dt} = \frac{1}{2}\alpha\beta(r_{k-1}, r_{k-1})(n_{k-1})^2 - \alpha\beta(r_k, r_k)(n_k)^2 + K''_{B,k+1}(r_{k+1})^3(n_{k+1})^2 - K''_{B,k}(r_k)^3(n_k)^2 \quad (2.7)$$

where K''_B is overall break-up rate constant. Equation (2.7) consists of a non-uniform discretization where the size class index $k = 2i$. One advantage to Eq. (2.7) is that it can be solved analytically to obtain the time dependent total particle concentration which can be used to check the accuracy of the computation (Kramer 2000). Unfortunately, Eq. (2.7) can not model differential sedimentation as the rate kernel is always zero due to r_i equaling r_j. Equation (2.7) is very easy to solve numerically and is extremely stable using a variety of solution techniques.

Batterham et *al*. proposed a discretization procedure where volume size class intervals are configured as $\upsilon_{k+1} = 2\upsilon_k$ as in Fig. 2.1 (Batterham et al. 1981). To account for the problem in the contribution of the product aggregates formed from the collisions of particles in adjacent intervals described above, a scheme that has half the number of products formed added to each possible interval. The resulting population size distribution becomes,

$$\begin{aligned}\frac{dn_k}{dt} &= \frac{3}{8}\alpha\beta(r_{k-2}, r_{k-1})n_{k-2}n_{k-1} - \frac{3}{4}\alpha\beta(r_{k-1}, r_k)n_{k-1}n_k + \alpha\beta(r_{k-1}, r_{k-1})n_{k-1}n_{k-1} \\ &+ \sum_{j=1}^{k-2}\alpha\beta(r_k, r_j)(1+2^{j-k})n_k n_j - \sum_{j=1}^{\max}\alpha\beta(r_k, r_j)n_k n_j - \alpha\beta(r_k, r_k)n_k n_k\end{aligned} \qquad (2.8)$$

Hounslow et *al*. cite that while the procedure of Batterham et *al*. correctly conserves particle number and mass, the scheme of arbitrarily dividing agglomerates between size classes incorrectly predicts coagulation rate (Hounslow et al. 1988). The method of Hounslow et *al*. differs from Batterham et *al*. by considering continuous intervals rather than discrete boundaries. They also compute the zero moment (total particle mass) and note a gain in mass that they alleviate by multiplying the first and third mechanism by 2/3. The final product is a population distribution given by,

$$\begin{aligned}\frac{\mathrm{dn}_k}{\mathrm{dt}} &= \frac{1}{2}\alpha\beta(\mathrm{r}_{k-1},\mathrm{r}_{k-1})(\mathrm{n}_{k-1})^2 + \mathrm{n}_{k-1}\sum_{j=1}^{k-1}\alpha(2^{j-k+1})\beta(\mathrm{r}_{k-1},\mathrm{r}_j)\mathrm{n}_j \\ &\quad - \mathrm{n}_k\sum_{j=1}^{k-1}\alpha(2^{j-k})\beta(\mathrm{r}_k,\mathrm{r}_j)\mathrm{n}_j - \mathrm{n}_k\sum_{j=k}^{\max}\alpha\beta(\mathrm{r}_k,\mathrm{r}_j)\mathrm{n}_j\end{aligned} \tag{2.9}$$

Litster et *al*. extended the model of Eq. (2.9) to improve the accuracy for a high aggregation intensity using an adjustable geometric size interval scheme given as $\upsilon_{i+1}/\upsilon_i = 2^{1/q}$ with arbitrary "*q*" values. In the case of a *q* value equal to 1, the advanced model (see equation below) is equivalent to the original equation (Litster et al. 1995). As the *q* value approaches infinity, Eq. (2.10) becomes approximately the uniform discrete model. These adjustable sectional methods with arbitrary class size refinement capacity have been examined by past researchers (Gelbard et al. 1980; Marchal et al. 1988; Kumar and Ramkrishna 1996b; Vanni 2000).

$$\begin{aligned}\frac{\mathrm{dn}_k}{\mathrm{dt}} &= \sum_{j=1}^{k-S(q)-1}\alpha\beta(r_{k-1},r_j)\mathrm{n}_{k-1}\mathrm{n}_j\frac{2^{(j-k+1)/q}}{2^{1/q}-1} + \sum_{i=2}^{q}\sum_{j=k-S(q-i+2)-i+1}^{k-S(q-i+1)-i}\alpha\beta(r_{k-i},r_j)\mathrm{n}_{k-i}\mathrm{n}_j\frac{2^{(j-k+1)/q}-1+2^{-(i-1)/q}}{2^{1/q}-1} \\ &\quad + \frac{1}{2}\alpha\beta(r_{k-q},r_{k-q})(\mathrm{n}_{k-q})^2 + \sum_{i=2}^{q}\sum_{j=k-S(q-i+2)-i+2}^{k-S(q-i+1)-i+1}\alpha\beta(r_{k-i+1},r_j)\mathrm{n}_{k-i+1}\mathrm{n}_j\frac{-2^{(j-k)/q}+2^{1/q}-2^{-(i-1)/q}}{2^{1/q}-1} \\ &\quad + \sum_{j=1}^{k-S(q)}\alpha\beta(r_k,r_j)\mathrm{n}_k\mathrm{n}_j\frac{2^{(j-k)/q}}{2^{1/q}-1} - \sum_{j=k-S(q)+1}^{\infty}\alpha\beta(r_k,r_j)\mathrm{n}_k\mathrm{n}_j\end{aligned} \tag{2.10}$$

Hill and Ng produced what they felt was an improved population balance equation based on probability density functions for the particle population contributions in each interval *k* (Hill and Ng 1996). The analysis of Hill and Ng also included break-up (Hill and Ng 1995). To account for the possibility of products from the collisions of two intervals producing aggregates that may fall into two larger size intervals, probability distributions are assumed. Thus, there is a probability $\mathrm{C}_{i,j,k}$ that collisions between particles from intervals *i* and *j* will fall into interval *k*. There is also the probability $\mathrm{D}_{i,j,k-1}$ that the *i* and *j* interval particles will form a particle of a size in the range of interval $k-1$. Further, there is a 100% probability that particles from intervals *i* and *j* will fall into either *k* or $k-1$, therefore $\mathrm{C}_{i,j,k}+\mathrm{D}_{i,j,k-1}=1$. Hill and Ng concluded that the volume of particles removed from intervals *i* and *j* ($\bar{\upsilon}_i$ and $\bar{\upsilon}_j$) must be equal to the particle volume added to intervals *k* and $k-1$ ($\bar{\upsilon}_k$ and $\bar{\upsilon}_{k-1}$) and found the probability distribution to be,

$$\mathrm{C}_{i,j,k}=\frac{\bar{\upsilon}_i+\bar{\upsilon}_j-\bar{\upsilon}_{k-1}}{\bar{\upsilon}_k-\bar{\upsilon}_{k-1}},\qquad \mathrm{D}_{i,j,k-1}=\frac{\bar{\upsilon}_k-\bar{\upsilon}_i-\bar{\upsilon}_j}{\bar{\upsilon}_k-\bar{\upsilon}_{k-1}} \tag{2.11}$$

The volume over bar ($\bar{\upsilon}_k$) represents the average volume in interval *k* and the agglomeration rate equation obtained by Hill and Ng takes the form,

$$\begin{aligned}\frac{\mathrm{dn}_k}{\mathrm{dt}}&=\sum_{j=1}^{k-2}\alpha\beta(\mathrm{r}_{k-1},\mathrm{r}_j)(\mathrm{C}_{k-1,j,k})\mathrm{n}_{k-1}\mathrm{n}_j+\sum_{j=1}^{k-1}\alpha\beta(\mathrm{r}_k,\mathrm{r}_j)(\mathrm{D}_{k,j,k})\mathrm{n}_k\mathrm{n}_j\\&+\frac{1}{2}\alpha\beta(\mathrm{r}_{k-1},\mathrm{r}_{k-1})(\mathrm{C}_{k-1,k-1,k})\mathrm{n}_{k-1}\mathrm{n}_{k-1}+\frac{1}{2}\alpha\beta(\mathrm{r}_k,\mathrm{r}_k)(\mathrm{D}_{k,k,k})\mathrm{n}_k\mathrm{n}_k-\mathrm{n}_k\sum_{i=1}^{\max}\alpha\beta(\mathrm{r}_i,\mathrm{r}_k)\mathrm{n}_i\end{aligned} \tag{2.12}$$

2.3.3 Improved Schemes for the Probability Distributions

A possible approach to solve the Hill and Ng model of Eq. (2.12) is to equate the probability density functions in terms of the average volume ranges of each interval. Using the particle average volume calculation for each class size results in the population balance of Eq. (2.13). For the interval scheme, $\upsilon_{k+1}=2\upsilon_k$, using an average volume concept ($\bar{\upsilon}_k=0.5(\upsilon_k+\upsilon_{k-1})$) and the definition of $\upsilon_k\propto\mathrm{r}_k^3$, Eq. (2.12) can also be expressed in terms of the particle radii with volume based new probability functions termed “new probability I” and given by Eq. (2.13).

$$\begin{aligned}\frac{\mathrm{dn}_k}{\mathrm{dt}} = \sum_{j=1}^{k-2} \alpha\beta(\mathrm{r}_{k-1},\mathrm{r}_j)\left(\frac{2(\mathrm{r}_j)^3}{(\mathrm{r}_k)^3}\right)\mathrm{n}_{k-1}\mathrm{n}_j + \sum_{j=1}^{k-1} \alpha\beta(\mathrm{r}_k,\mathrm{r}_j)\left(\frac{(\mathrm{r}_k)^3-(\mathrm{r}_j)^3}{(\mathrm{r}_k)^3}\right)\mathrm{n}_k\mathrm{n}_j \\ + \frac{1}{2}\alpha\beta(\mathrm{r}_{k-1},\mathrm{r}_{k-1})\mathrm{n}_{k-1}\mathrm{n}_{k-1} - \mathrm{n}_k \sum_{i=1}^{\max} \alpha\beta(\mathrm{r}_i,\mathrm{r}_k)\mathrm{n}_i\end{aligned} \qquad (2.13)$$

Also, for the interval scheme, $\upsilon_{k+1} = 2\upsilon_k$, a break-up distribution function can be obtained as Eq. (14),

$$\mathrm{b}_{k,j} = \frac{3}{2}\frac{(\mathrm{r}_j)^3 + (\mathrm{r}_j)^3}{(\mathrm{r}_{k-1})^3} \qquad (2.14)$$

Using Eqs. (2.4) and (2.14), the break-up rate equation, for the interval scheme, $\upsilon_{k+1} = 2\upsilon_k$, can be expressed as,

$$\left.\frac{\mathrm{dn}_k}{\mathrm{dt}}\right|_{\mathrm{Breakup}} = \frac{3}{2}\sum_{j=k+1}^{\infty}\left(\frac{(\mathrm{r}_j)^3 + (\mathrm{r}_j)^3}{(\mathrm{r}_{k-1})^3}\right)\mathrm{s}_j\mathrm{n}_j - \frac{1}{2}\mathrm{s}_k\mathrm{n}_k \qquad (2.15)$$

where s_j is a break-up rate coefficient and η is a break-up concentration exponent.

Furthermore, coagulation simulation using Eq. (2.13) can not be applied to fractal aggregates based on the models inability to conserve mass, which will be discussed in a later section. That is, the model of Eq. (2.13) is stable only for spherical particle aggregation, due to using an average volume approach. To obtain solutions for fractal aggregate coagulation it must be assumed that the probability functions are proportional to aggregate size having an exponent of a fractal dimension, not an exponent of 3 (volume). This new probability functions are termed "new probability II" and given by Eq. (2.16).

$$C_{k-1,j,k} = 2\left(\frac{r_j}{r_k}\right)^{D_f}, \qquad D_{k,j,k} = \frac{(r_k)^{D_f} - (r_j)^{D_f}}{(r_k)^{D_f}} \tag{2.16}$$

Thus, Eq. (2.13) can be replaced by Eq. (2.17) using the new probability II for geometric-size intervals of 2.

$$\begin{aligned}\frac{dn_k}{dt} = {} & 2\sum_{j=1}^{k-2} \alpha\beta(r_{k-1}, r_j)\left(\frac{r_j}{r_k}\right)^{D_f} n_{k-1}n_j + \sum_{j=1}^{k-1} \alpha\beta(r_k, r_j)\left(\frac{(r_k)^{D_f} - (r_j)^{D_f}}{(r_k)^{D_f}}\right) n_k n_j \\ & + \frac{1}{2}\alpha\beta(r_{k-1}, r_{k-1})(n_{k-1})^2 - \sum_{i=1}^{\max} \alpha\beta(r_k, r_i) n_k n_i\end{aligned} \tag{2.17}$$

An additional improved scheme for the probability density functions can be derived from a primary particle mass balance approach. Consider two particle aggregation related to the probability functions of $C_{k-1,j,k}$, $D_{k-1,j,k-1}$ and $C_{k,j,k+1}$, $D_{k,j,k}$. The first reaction related to the probability distribution functions of $C_{k-1,j,k}$ and $D_{k-1,j,k-1}$ can be expressed as

$$n_{k-1} + n_j = n_k + n_{k-1} \tag{2.18}$$

From a mass balance on aggregates comprised of primary particles yields

$$(k-1)\Delta n_{k-1} + j\Delta n_j = k\Delta n_k + (k-1)\Delta n_{k-1} \tag{2.19}$$

where Δn is the change in the number of aggregates in the interval. However,

$$\Delta n_k = (\Delta n_{k-1} + \Delta n_j) C_{k-1,j,k} \tag{2.20}$$

and

$$\Delta n_{k-1} = (\Delta n_{k-1} + \Delta n_j) D_{k-1,j,k-1} \tag{2.21}$$

therefore,

$$j\Delta \mathrm{n}_j = k(\Delta \mathrm{n}_{k-1} + \Delta \mathrm{n}_j)\mathrm{C}_{k-1,j,k} \tag{2.22}$$

or since

$$\mathrm{C}_{k-1,j,k} + \mathrm{D}_{k-1,j,k-1} = 1 \tag{2.23}$$

therefore

$$\mathrm{C}_{k-1,j,k} = \frac{j\Delta \mathrm{n}_j}{k(\Delta \mathrm{n}_{k-1} + \Delta \mathrm{n}_j)} \tag{2.24}$$

and

$$\mathrm{D}_{k-1,j,k-1} = \frac{k\Delta \mathrm{n}_{k-1} + (k-j)\Delta \mathrm{n}_j}{k(\Delta \mathrm{n}_{k-1} + \Delta \mathrm{n}_j)} \tag{2.25}$$

Also, the second reaction can be expressed as

$$\mathrm{n}_k + \mathrm{n}_j = \mathrm{n}_{k+1} + \mathrm{n}_k \tag{2.26}$$

Using the same manner for the first reaction on the basis of primary particle mass balance, the “new probability III” can be derived as

$$\mathrm{C}_{k,j,k+1} = \frac{j\Delta \mathrm{n}_j}{(k+1)(\Delta \mathrm{n}_k + \Delta \mathrm{n}_j)} \tag{2.27}$$

and

$$\mathrm{D}_{k,j,k} = \frac{(k+1)\Delta \mathrm{n}_k + (k-j+1)\Delta \mathrm{n}_j}{k(\Delta \mathrm{n}_{k-1} + \Delta \mathrm{n}_j)} \tag{2.28}$$

where Δn is the difference between two solutions resulting from previous and current iteration time steps. Substituting Eqs. (2.24) and (2.28) into Eq. (2.12) yields an improved population balance equations given as,

$$\frac{dn_k}{dt} = \sum_{j=1}^{k-2} \alpha\beta(r_{k-1}, r_j)\left(\frac{j\Delta n_j}{(k+1)(\Delta n_k + \Delta n_j)}\right) n_{k-1} n_j + \sum_{j=1}^{k-1} \alpha\beta(r_k, r_j)\left(\frac{(k+1)\Delta n_k + (k-j+1)\Delta n_j}{k(\Delta n_{k-1} + \Delta n_j)}\right) n_k n_j + \frac{1}{2}\alpha\beta(r_{k-1}, r_{k-1})(n_{k-1})^2 - n_k \sum_{i=1}^{\max} \alpha\beta(r_k, r_i) n_i \tag{2.29}$$

2.4 Modeling Analysis Results

2.4.1 Modeling Conditions

A variety of solutions to the population balance equations were compared on the basis of particle size distribution and mass conservation. These analyses consist of various coagulation kernels, initial colloid population conditions, the addition of a break-up kernel, and aggregate fractal dimension. For each computation a maximum size class of 1024 was used. This maximum size class was selected based on computational considerations in using the uniform discrete model as the basis of comparison and compatibility with the non-uniform discrete population balance equations. Although it would be desirable to have an unlimited size class such that the aggregate growth would be unbounded, computationally this is not possible. Thus, a reasonable maximum size class must be selected. Further, a theoretical coagulation modeling time of 30 minutes was used in all of the analyses. The selection of 30 minutes was based on conventional practice in the water treatment field (Letterman et al. 1999).

Table 2.2 Coagulation Modeling Conditions

Parameters	Monodisperse	Polydisperse
Particle concentration (no./cm^3)	$n_{primary} = 1.819 \times 10^9$ $n_{total} = 1.819 \times 10^9$	$n_{primary} = 8.489 \times 10^9$ $n_{total} = 1.819 \times 10^9$
Primary particle diameter	1.0 μm (10 nm for perikinetic coagulation)	
Particle density	1.0 ~ 1.7 (g cm^{-3})	
Liquid density	1.0 (g cm^{-3})	
Temperature	303 K	
Viscosity	7.97×10^{-3} (g cm^{-1} s^{-1})	
Hamaker constant	1.0×10^{-20} (J)	
Boltzmann's constant	1.38×10^{-16} (g cm^2 s^{-2} K^{-1})	
Gravitational constant	981 (cm s^{-2})	
Fractal dimension	2.00 ~ 3.00	

The population balance equations were computed over time using the initial conditions as presented in Table 2.2. As shown in Table 2.2, two types of colloidal dispersion conditions were used in this study; monodisperse initial conditions where all of the initial particles have the same particle size (either 1 μm or 10 nm in diameter), and polydisperse initial populations where different particle concentrations for each size class were examined. Comparisons of the PBE model results were conducted by computing R^2 and a sum-of-squares of the residuals between the non-uniform models (geometric size interval of 2) and the uniform discrete solution (geometric size interval of 1) in each variable case with respect to particle size of r_k.

2.4.2 Numerical Solutions

In solving the various population balance equations comprising a set of ordinary differential equations (ODEs), the main program calls two subprograms, IVPAG of the IMSL library (1987) and a user-supplied program that generates the coagulation kernels (collision efficiency, collision frequency, break-up, probability functions, and random number generation). Two different solution algorithms in IVPAG, the Adams-Moulton method and Gear's method, can be used. Both methods are effective algorithms for solving stiff ODEs. The IVPAG program determines the optimum step size to be taken based on the rate that a function is changing at a particular point in the computation. The error tolerance selected was 10^{-6} for all numerical solutions for the coagulation models.

Table 2.3 Summary of the Four Kernels Used as Coagulation Modeling

Kernels	Formula
Perikinetic Aggregation	$\beta(r_i, r_j) = \frac{2k_B T}{3\mu}\left(\frac{1}{r_i} + \frac{1}{r_j}\right)(r_i + r_j)$
Orthokinetic Aggregation	$\beta(r_i, r_j) = \frac{4}{3}\frac{\partial u_x}{\partial y}(r_i + r_j)^3$
Differential Sedimentation	$\beta(r_i, r_j) = \pi(r_i + r_j)^2 \lvert v_i - v_j \rvert$
Break-up due to flow strain-rate ($\dot{\gamma}$)	$r_{Breakup} = K_B(\dot{\gamma})^b (r_i)^s (n_i)^\eta$

* $\partial u_x/\partial y$ is the flow rate of strain (non-rotational velocity gradient) in the x-y direction, k is Boltzmann's constant, T is the absolute temperature, μ is the fluid viscosity, v is the terminal settling velocity of each respective particle, and K_B is break-up coefficient.

Discretized population balance models (geometric size interval of 2) used for this study were the bi-kinetic (Eq. (2.7)), Batterham (Eq. (2.8)), Hounslow (Eq. (2.9)), the new models of Eqs. (2.13), (2.17) and (2.29), and the uniform discrete population balance model (geometric size interval of 1) incorporating various coagulation kernels (i.e., perikinetic, orthokinetic, and differential sedimentation) summarized in Table 2.3. Also, two different colloid initial population conditions (monodisperse and polydisperse) were examined and various break-up kernels applied to the orthokinetic coagulation modeling. In addition, the new improved probability functions were investigated to simulate fractal aggregate coagulation in order to improve mass conservation, especially when incorporating break-up.

2.4.3 Perikinetic Coagulation Modeling

Perikinetic coagulation was examined for both monodisperse and polydisperse particle systems. Resulting data is shown in Figs. 2.2 to 2.5. For the perikinetic examination, four discretized models (Eq. (2.7), Eq. (2.8), Eq. (2.9) and the model of Eq. (2.13)) were used and compared to the uniform discretized model. Modeling conditions are presented in Table 2.2 with a primary particle diameter of 10 nm, maximum aggregate size of 63.5 nm and a fractal dimension of 3.0. An aggregate fractal dimension of 3.0 implies spherical coalescence.

The data for monodisperse perikinetic modeling is shown in Figs. 2.2 and 2.3 displays the cumulative particle size distributions for all models. The model of Eq. (2.7) overestimates particle aggregation, however, the other four models (Eq. (2.8), Eq. (2.9), Eq. (2.13), and uniform discrete model) show similar predictions. Deviations between each method and the uniform discrete model were compared using statistical analysis represented by an R^2 and the square root of the sum-of-squares of the residuals (see Fig. 2.3). From Fig. 2.3, all models, except the model of Eq. (2.7), have R^2 greater than 0.9591 and residuals less than 13.7889; however, the model of Eq. (2.7) has the values of 0.8718 and 31.7441, respectively. That is, the model of Eq. (2.7) has less accuracy compared to the uniform discrete model than the other coagulation models for monodisperse perikinetic coagulation.

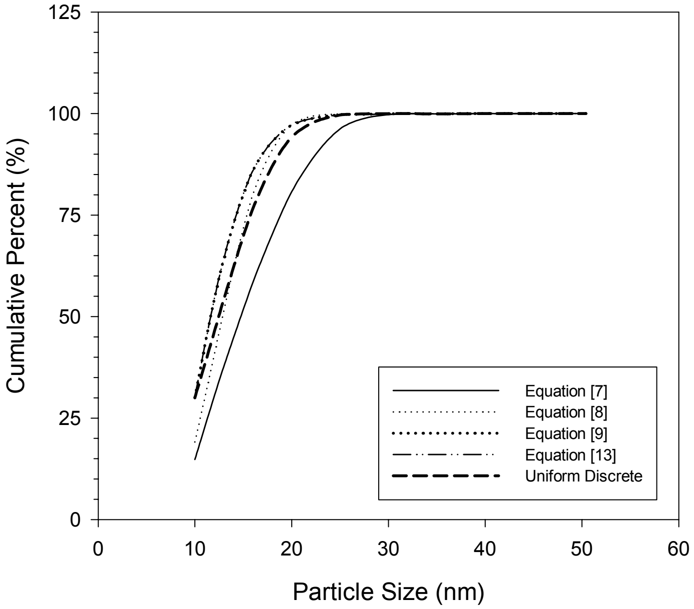

Figure 2.2 Cumulative particle size distribution for monodisperse perikinetic coagulation ($n_{initial} = 1.819 \times 10^9/cm^3$, $\alpha = 0.1$, $D_f = 3.0$, after 30 min.)

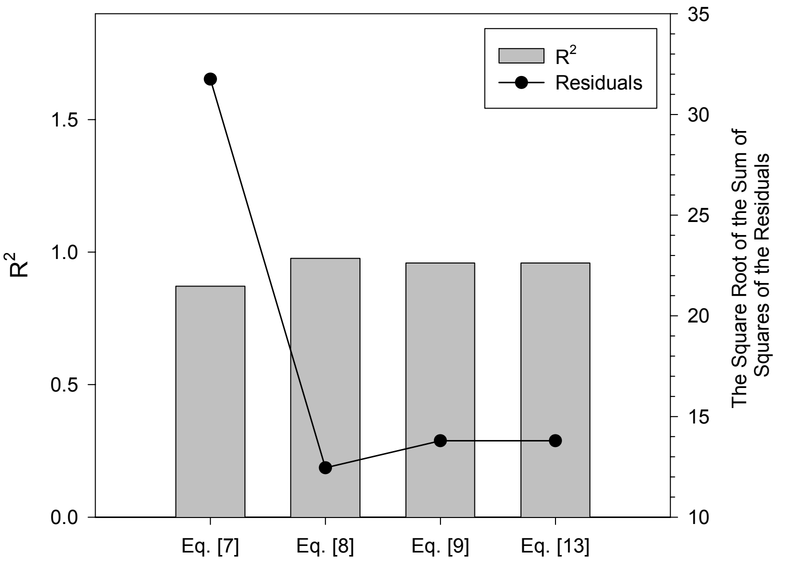

Figure 2.3 Statistical analysis for monodisperse perikinetic coagulation models

The model of Eq. (2.8) has excellent numerical accuracy and the models of Eq. (2.9) and Eq. (2.13) have similar results with respect to accuracy for this monodisperse perikinetic coagulation simulation.

Polydisperse initial population conditions were also examined for the perikinetic case (see Figs. 2.4 and 2.5). The uniform discrete or continuous models have a major disadvantage when applied to polydisperse simulation, especially in large particle size class ranges (e.g., $k \geq 1000$), due to the problem of inputting the initial particle concentrations for each class size. However, a nonlinear regression technique can be used to obtain a population equation (number as a function of size) and makes it possible to input the initial particle concentrations easily. After the nonlinear regression fitting (particle size versus cumulative percent), particle concentrations for each class size were calculated through a matrix representing the relationship between size class and particle size including fractal dimension. Similar to the monodisperse model results, the model of Eq. (2.8) has excellent numerical accuracy while the models of Eq. (2.9) and Eq. (2.13) have similar results in accuracy. The results of cumulative particle size distribution (Fig. 2.4) shows that all models, except for the model of Eq. (2.7), have similar predictions compared to the uniform discrete model, having the statistic data of R^2 and residuals of greater than 0.9936 and less than 9.6043, respectively (see Fig. 2.5). These results show that the simulation accuracy of polydisperse perikinetic coagulation is better than that of monodisperse modeling when compared to the uniform discrete model. This is most likely due to stiffness inaccuracies with the monodisperse system.

As shown in the monodisperse modeling, the model of Eq. (2.7) has less accuracy (R^2 of 0.9675 and residuals of 19.7038) than the other models. However, this accuracy is higher than monodisperse case (0.8718 and 31.7441, respectively).

Model stability tests were examined for both monodisperse and polydisperse particle systems. The stability was measured by the number or mass conservation during coagulation modeling and can be represented by a mass conservation factor that is the ratio of the total number of primary particles for each floc size class to the initial primary particle number concentration. The mass conservation factor concept was used for evaluating the stability and is given as,

$$\text{Mass conservation factor} = \frac{\sum_{i=1}^{\max} i\left(\mathrm{n}_i\right)_t}{\left(\mathrm{n}_1\right)_{t=0}}$$

Here, mass conservation factor merely means the model stability, not aggregation intensity or aggregation kinetics. For both monodisperse and polydisperse perikinetic coagulation modeling, all models generated perfect mass conservation during the coagulation modeling time limit of 30 min.

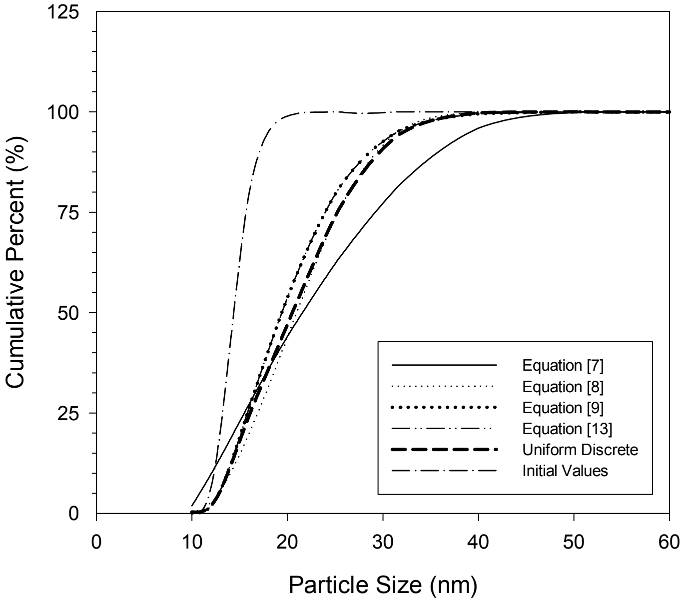

Figure 2.4 Cumulative particle size distribution for polydisperse perikinetic coagulation ($\alpha = 0.1$, $D_f = 3.0$, after 30 min.)

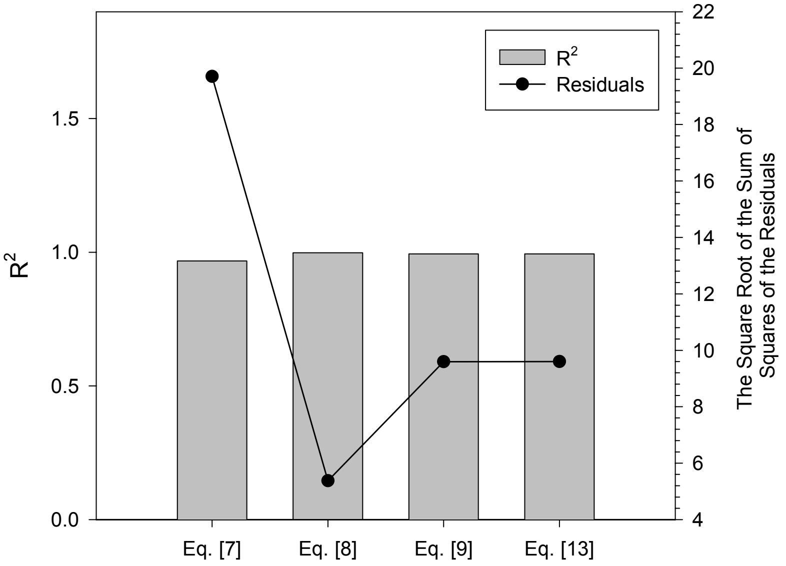

Figure 2.5 Statistical analysis for polydisperse perikinetic coagulation models

2.4.4 Differential Sedimentation

Initially, polydisperse coagulation was examined for the differential sedimentation mechanisms using the models (Eq. (2.8), Eq. (2.9) and Eq. (2.13)) and the results were compared to the uniform discrete model. The model of Eq. (2.7) is excluded in this study due to the assumption in the model that only particle collisions occur between particles having the same size and, thus, would have the same sedimentation velocities. The modeling results are shown in Figs. 2.6 and 2.7, representing particle cumulative percent and statistical analysis, respectively. In this study, only the effect of particle density was examined as density is a major factor in the collision frequency function for differential sedimentation. It was found that all models, except for the model of Eq. (2.8), have similar patterns in cumulative particle size distribution results. With the exception of the model of Eq. (2.8) (Fig. 2.6(a)), all models have the similar results when compared to the uniform discrete model (Fig. 2.6(d)).

Relative comparisons between the uniform discrete model and the other three models using the same statistical analyses used in the perikinetic modeling study were conducted at different particle density (ρ_p) conditions ranging from 1.1 to 1.7 g/cm^3 and displayed in Fig. 2.7. These results show that the models of Eq. (2.9) and Eq. (2.13) have much better accuracy than the model of Eq. (2.8). Furthermore, there are excellent agreements between the models of Eq. (2.9) and Eq. (2.13) compared with cumulative distributions (Fig. 2.6) and the statistical analysis (Fig. 2.7).

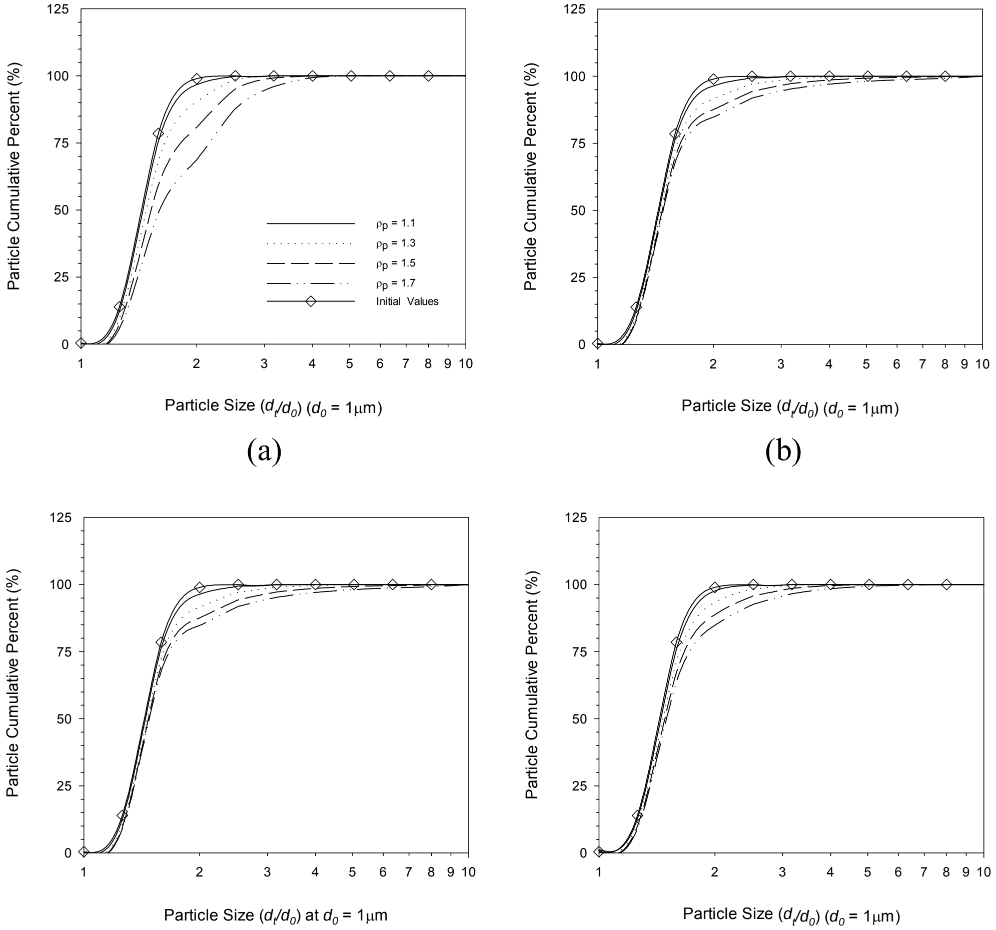

(a) (b)

(c) (d)

Figure 2.6 Particle cumulative percent for differential sedimentation coagulation models after 30 min. (a) Eq. (2.8), (b) Eq. (2.9), (c) Eq. (2.13), and (d) uniform discrete models ($\alpha = 0.1$, $d_0 = 1.0$ μm, particle density = 1.1 ~ 1.7 g/cm^3, liquid density = 1.0 g/cm^3)

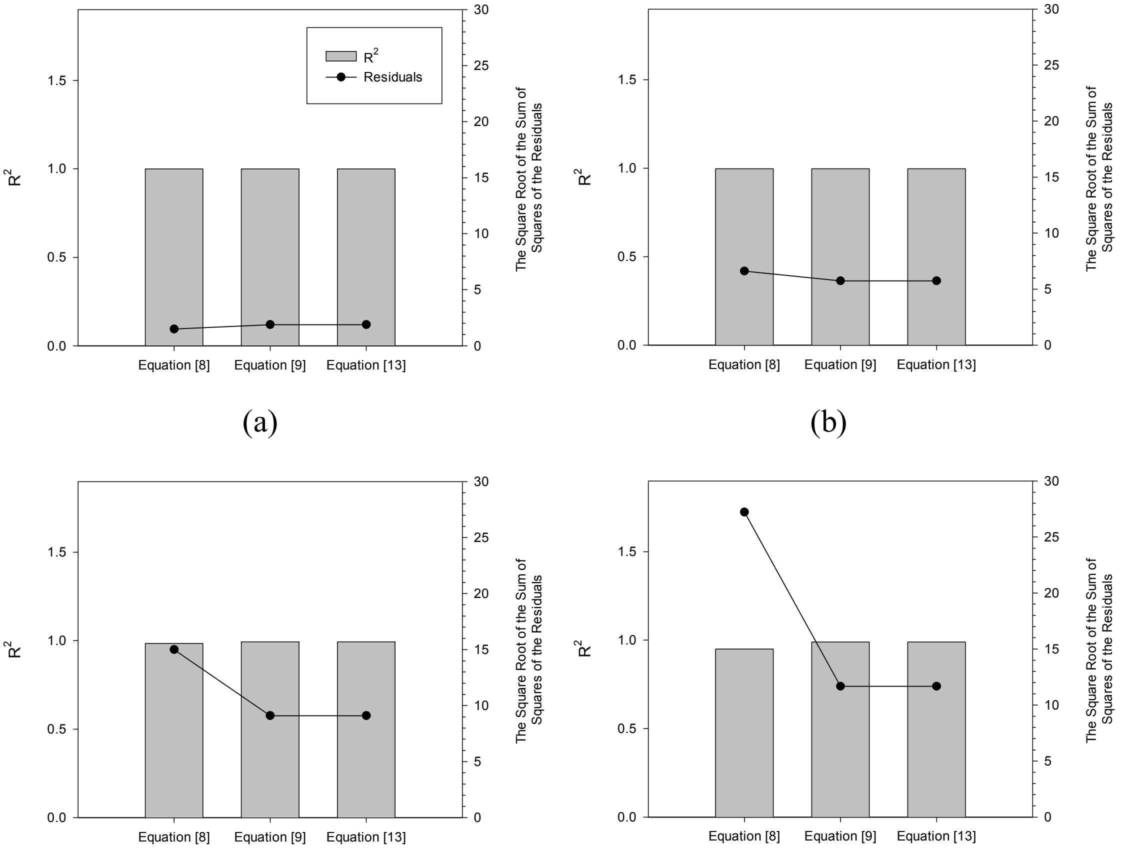

(a) (b)

(c) (d)

Figure 2.7 Statistical analysis for differential sedimentation coagulation models at particle density (ρ_p, g/cm^3). (a) 1.1, (b) 1.3, (c) 1.5, and (d) 1.7

These two models can maintain higher numerical accuracy (higher R^2 and lower residuals) as particle density is increased from 1.1 to 1.7 g/cm^3. However, the model of Eq. (2.8) has high accuracy only at low particle density conditions (1.1 ~ 1.3 g/cm^3). As particle density is increased to exceed 1.5 g/cm^3, the model of Eq. (2.8) has less accuracy than the coagulation model of Eq. (2.13) or the model of Eq. (2.9). When the particle density is increased from 1.1 to 1.7 g/cm^3, the magnitude of the coagulation kernel for the differential sedimentation case is increased in a range from 1.61×10^{-14} ~ 6.63×10^{-11}

cm^3/sec to $1.13\times10^{-13} \sim 4.64\times10^{-10}$ cm^3/sec, depending on particle size. However, at relatively higher coagulation kernel magnitudes, the models of Eq. (2.9) and Eq. (2.13) achieve better accuracy than the model of Eq. (2.8).

Stability tests which represent the mass conservation factor in terms of total primary particle number concentration were examined for each coagulation model. For both initial monodisperse and polydisperse conditions, all models generated perfect mass conservation during the theoretical coagulation time of 30 min.

2.4.5 Orthokinetic Coagulation Modeling

Examining the orthokinetic coagulation model in terms of particle size distribution and mass conservation, both monodisperse and polydisperse initial particle populations were considered and the results are presented in Figs. 2.8 to 2.12. Aggregate fragmentation or breakage was not included in these analyses and will be discussed later. However, the influence of flow strain-rate on particle size distribution and conservation of mass was explored.

For the initial monodisperse case, the modeling parameters of $\alpha = 0.05$, flow strain-rate = 10 1/s, and a fractal dimension of 3.0, were used and are displayed in Fig. 2.8. As shown in Fig. 2.8, four of the coagulation models show similar modeling results. Deviations between each method and the uniform discrete model were compared using the statistical analyses represented by R^2 and the square root of the sum-of-squares of the residuals (see Fig. 2.9).

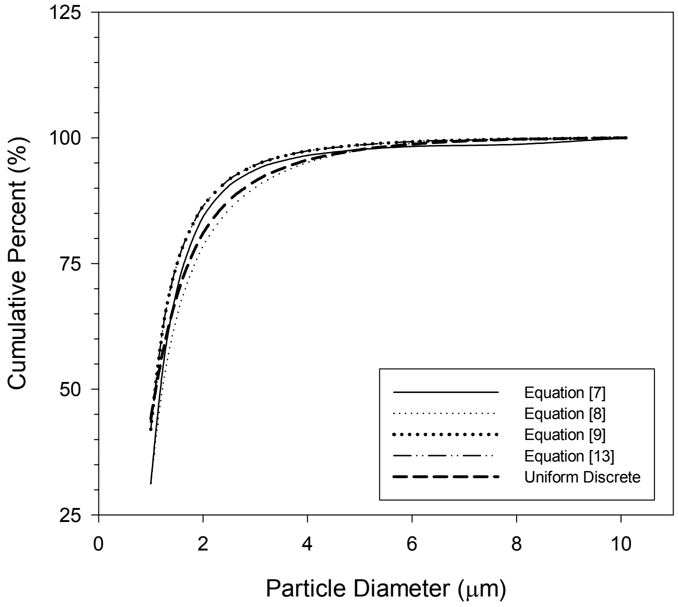

Figure 2.8 Cumulative percent for monodisperse orthokinetic coagulation models after 30 min. ($\alpha = 0.05$, $\gamma = 10$ (1/s), $D_f = 3.0$)

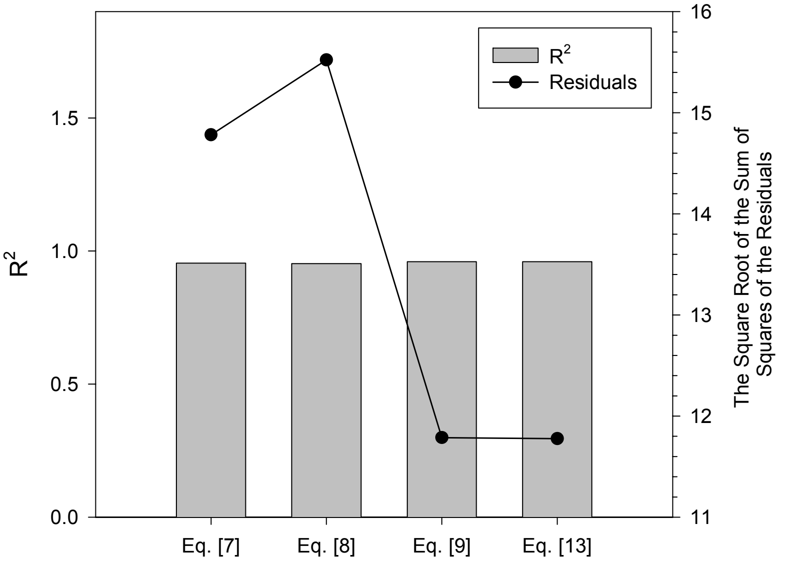

Figure 2.9 Statistical analysis for monodisperse orthokinetic coagulation models

As shown in Fig. 2.9, the models of Eq. (2.9) and Eq. (2.13) obtain relatively higher accuracy than the models of Eq. (2.7) and Eq. (2.8). It is notable that the model of Eq. (2.8) for initially monodisperse orthokinetic coagulation modeling has much less accuracy than other previous coagulation simulations having perikinetic and differential sedimentation kernels. That is, the model of Eq. (2.8) fails to achieve similar numerical accuracy as collision rate (α × β) is increased. In this study, the collision rate is increased from $1.40\times10^{-12} \sim 2.98\times10^{-12}$ cm^3/sec (perikinetic) to $2.09\times10^{-12} \sim 3.56\times10^{-10}$ cm^3/sec (orthokinetic), depending on aggregate size.

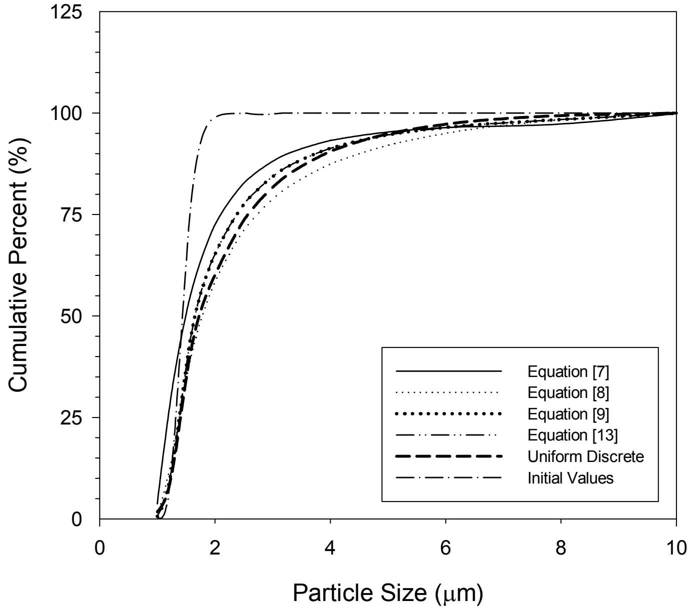

Figure 2.10 Particle size distribution for polydisperse orthokinetic coagulation having no break-up kernel after 30 min. (α = 0.01, γ = 10 (1/s), D_f = 3.0)

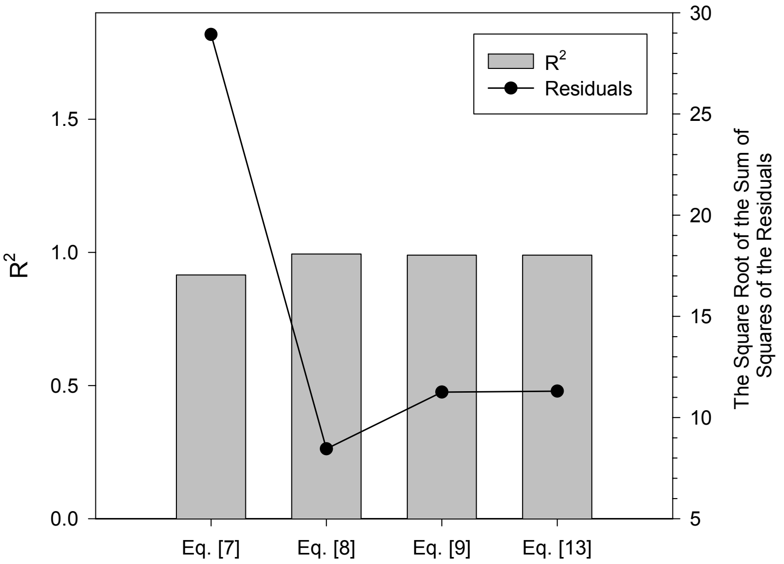

Figure 2.11 Statistical analysis for polydisperse orthokinetic coagulation models

Initially, polydisperse orthokinetic coagulation modeling was also conducted and compared to the uniform discrete model. Figures 2.10 and 2.11 show particle cumulative percent after 30 min of theoretical coagulation. As shown in Figs. 2.10 and 2.11, the model of Eq. (2.7) underestimates population and has low numerical accuracy, having lower R^2 (0.9154) and a large square root of the sum-of-squares of the residuals (28.9227). The models of Eq. (2.9) and Eq. (2.13) fit the simulation results well and have better numerical accuracy than the other models. The model of Eq. (2.8) has excellent numerical accuracy, however, it is notable that the model of Eq. (2.8) has less compatibility with respect to the stiffness problem. Compared with mono- and poly-disperse orthokinetic results shown in Figs. 2.9 and 2.11, the model of Eq. (2.8) has less accuracy when the higher stiffness exists (monodisperse initial condition) than when lower stiffness (polydisperse initial condition) is present. This stiffness sensitivity is seen in the model of Eq. (2.8) by having the square root of the sum-of-squares of the residuals; 15.5224 and 8.4557, respectively. In addition, as previously shown in the stability test, all models generated perfect mass conservation for both monodisperse and polydisperse orthokinetic coagulation modeling.

2.4.6 Aggregate Breakage

Researchers have proposed particle fragmentation (break-up) models based on five basic categories; limiting strength, strain-rate or flow dependence, limiting size, reaction rate, and stochastic dependence (Kramer and Clark 1999). The most common approach to aggregate break-up is the use of flow strain-rate as the primary break-up parameter (Thomas 1964; Argaman and Kaufman 1970; Parker et al. 1972; Kao and Mason 1975; Tambo and Watanabe 1979a; Lu and Spielman 1985; Ray and Hogg 1986; Sonntag and Russel 1987; Spicer and Pratsinis 1996a; Kramer and Clark 1999; Serra and Casamitjana 1999). Break-up kernels that have been proposed could be summarized in the kernel;

$$\mathrm{r_{KB}} = \mathrm{K_B}\left(\dot{\gamma}\right)^{\mathrm{b}}\left(\mathrm{r}_k\right)^{\mathrm{s}}\left(\mathrm{n}_k\right)^{\eta} \tag{2.30}$$

where K_B is the break-up rate constant (the reversible coagulation rate), b is a strain-rate exponent, s is an aggregate size exponent, and η is a break-up concentration exponent. As populations of the aggregates are exposed to increasing levels of fluid strain-rate and stress, thus it is expected that increasing amounts of break-up will be seen. Since the size exponent (s) is arbitrary the aggregate radius (or diameter) would serve just as well as the aggregate area or volume (s = 2 or s = 3).

As shown in Eq. (2.30) and Table 2.4, particle break-up is directly related to flow strain-rate, particle geometric properties (size, area, or volume), and break-up reaction orders. Previous researchers have proposed various model parameters (exponents of Eq. (30)) for the particle fragmentation given by Eq. (30). In this study, the various break-up parameters were compared with respect to the conservation of mass and cumulative particle percent using a random discretized break-up model and a bi-kinetic break-up model (binary breakage) for both monodisperse and polydisperse initial particle populations.

Table 2.4 The Summary of Various Break-Up Kernels

Cases		*b*	*s*	η	Break-up Kernels
Case I		0	0	1	$r_{KB} = K_B(n_k)$
Case II		1	0	1	$r_{KB} = K_B(\dot{\gamma})(n_k)$
Case III	A	1	1	1	$r_{KB} = K_B(\dot{\gamma})(r_k)^1(n_k)$
	B	1	2	1	$r_{KB} = K_B(\dot{\gamma})(r_k)^2(n_k)$
	C	1	3	1	$r_{KB} = K_B(\dot{\gamma})(r_k)^3(n_k)$
Case IV		1	3	2	$r_{KB} = K_B(\dot{\gamma})(r_k)^3(n_k)^2$
Case V		1.25	3	2	$r_{KB} = K_B(\dot{\gamma})^{1.25}(r_k)^3(n_k)^2$
Case VI		2	3	1	$r_{KB} = K_B(\dot{\gamma})^2(r_k)^3(n_k)^1$

Kramer and Clark rigorously reviewed contemporary break-up theories on floc aggregates formed during orthokinetic coagulation and proposed a uniform discrete random particle fragmentation model as (Kramer and Clark 1999),

$$\left.\frac{\mathrm{dn}_k}{\mathrm{dt}}\right|_{\mathrm{Breakup}} = \sum_{i=k+1}^{\max} \phi(\mathrm{i})\mathrm{K_B}(\dot{\gamma})^{\mathrm{b}}(\mathrm{r}_i)^{\mathrm{s}}(\mathrm{n}_i)^{\eta} - \mathrm{K_B}(\dot{\gamma})^{\mathrm{b}}(\mathrm{r}_k)^{\mathrm{s}}(\mathrm{n}_k)^{\eta} \tag{2.31}$$

where $\phi(i)$ is a random distribution function to account for the various daughter fragments of size class k. The first term on the right hand side of Eq. (2.31) represents the gain to the size class k concentration by the fracture of larger size class aggregates and the second term is the loss of size class k aggregates due to facture.

Binary particle break-up has been proposed by other researchers (Chen et al. 1990; Kramer 2000; Vanni 2000) and is represented as,

$$\left.\frac{\mathrm{dn}_k}{\mathrm{dt}}\right|_{\mathrm{Breakup}} = \mathrm{K}_{\mathrm{B},k+1}\left(\dot{\gamma}\right)^{\mathrm{b}}\left(\mathrm{r}_{k+1}\right)^{\mathrm{s}}\left(\mathrm{n}_{k+1}\right)^{2} - \mathrm{K}_{\mathrm{B},k}\left(\dot{\gamma}\right)^{\mathrm{b}}\left(\mathrm{r}_{k}\right)^{\mathrm{s}}\left(\mathrm{n}_{k}\right)^{2} \tag{2.32}$$

Binary break-up theory has the assumption that only daughter fragments of equal size result from the break-up of floc aggregates or $\mathrm{r}_{k+1} = 2\mathrm{r}_k$. Note that the binary break-up reaction given by Eq. (2.32) has a second order reaction rate ($\eta = 2$).

The evolution of particle size distribution was simulated using the model of Eq. (2.13). Figure 2.12 represents particle size distributions for polydisperse orthokinetic coagulation with a random break-up kernel (see Eq. (2.31)) and was generated using particle diameters between 1.0 and 10.1 μm, $\alpha = 0.01$, $\mathrm{K_B} = 0.001$, and a fractal dimension of 3.0 at various flow strain-rates. At the range of particle size and viscosity conditions used for this study, one can expect to neglect effects of inertia, Brownian diffusion, and gravity (Chin et al. 1998; Kramer and Clark 2000). Thus, it is assumed that only hydrodynamic forces are considered in orthokinetic coagulation with break-up. Figure 2.12 shows that the evolution of particle size distribution is a function of reaction time and flow strain-rate. As time elapses, peak concentration is lowered and larger particles are developed. Flow strain-rate also enhances coagulation kinetics. The applied flow strain-rate promotes particle collision rates that could be expressed by (collision efficiency) × (collision frequency). However, stresses resulting from flow strain-rate can induce aggregate break-up and alter the particle size distribution.

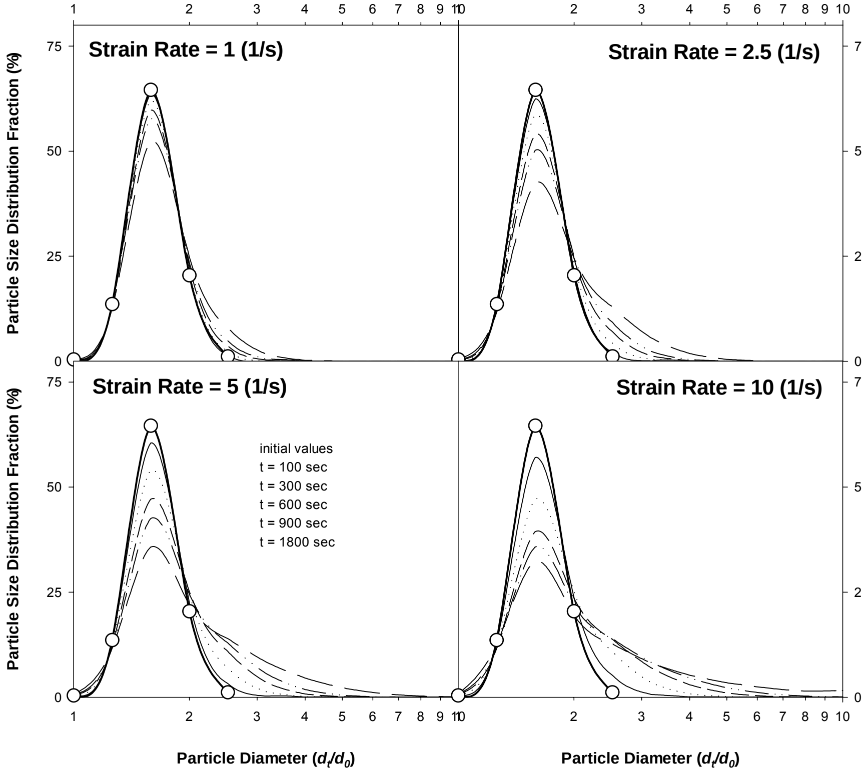

Figure 2.12 The evolution of particle size distribution for polydisperse orthokinetic coagulation at different strain-rate ($\alpha = 0.01$, $K_B = 0.001$, $D_f = 3.0$)

Orthokinetic coagulation modeling results using the varying break-up kernels are presented in Table 2.5 and Figs. 2.13 to 2.16 in terms of the mass conservation factor, particle cumulative percent and comparative statistical accuracy. Initially, monodisperse orthokinetic coagulation with random break-up (Case III-C) is shown in Figs. 2.13 and 2.14. Other results from various cases of Table 2.4 were not shown in the study due to the huge number of data sets. In the initially monodisperse case, the concentrations of particles in each size class had similar values using several break-up kernels (III-B, III-C, IV, V, and VI). However, mass was conserved only in the cases of III-B, III-C (see Table 2.4).

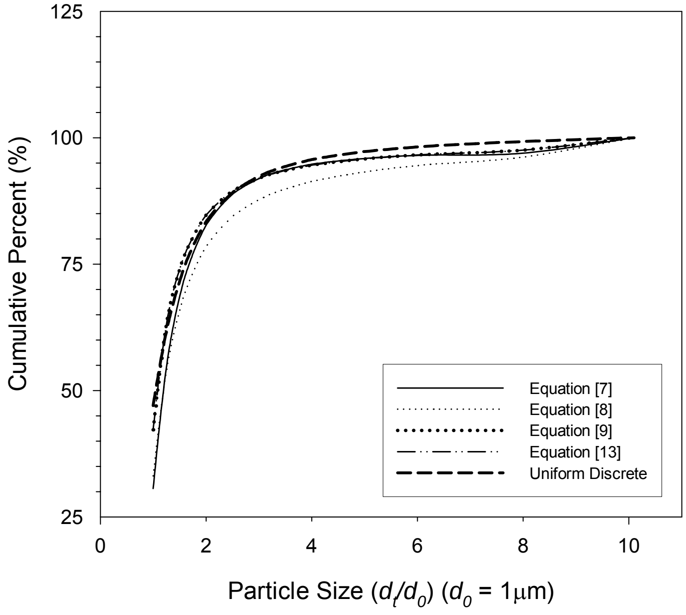

Figure 2.13 Monodisperse orthokinetic random break-up coagulation having the break-up kernel of $r_{KB}=K_B(\gamma)(r_k)^3(n_k)$ (α=0.1, K_B=0.005, γ=10 (1/s), D_f=3.0)

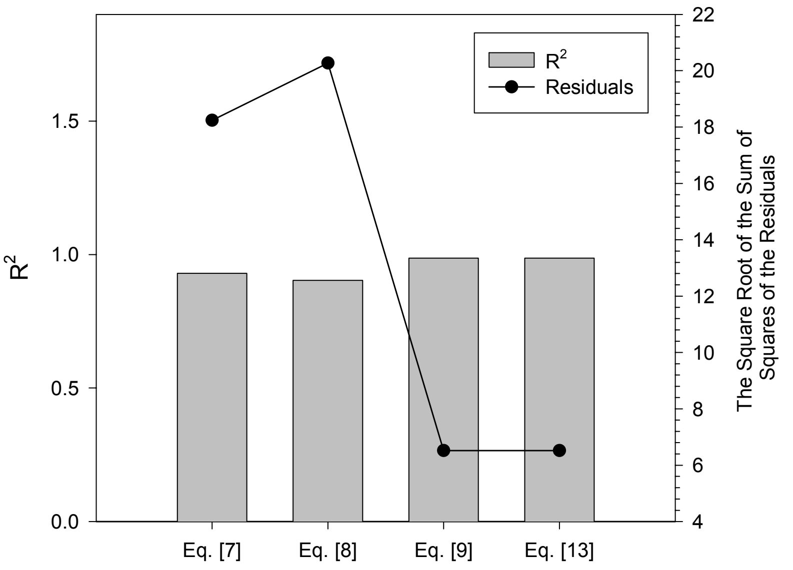

Figure 2.14 Statistical analysis for monodisperse orthokinetic coagulation models having random break-up kernel

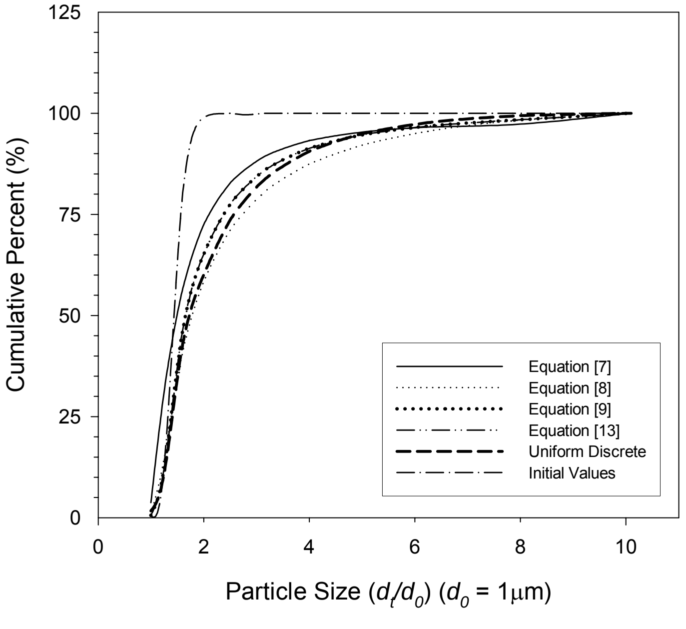

Figure 2.15 Polydisperse orthokinetic random break-up coagulation having the break-up kernel of $r_{KB}=K_B(\gamma)(r_k)^3(n_k)$ ($\alpha = 0.01$, $K_B = 0.005$, $\dot{\gamma}$ = 10 (1/s), $D_f = 3.0$)

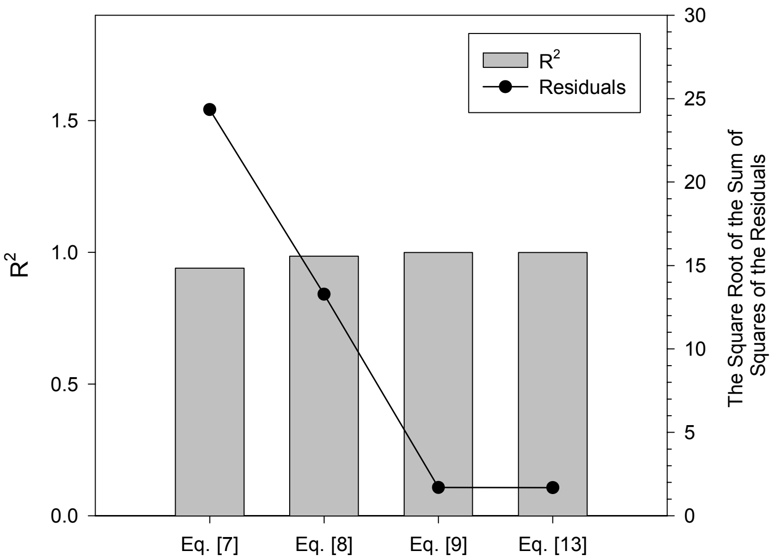

Figure 2.16 Statistical analysis for polydisperse orthokinetic coagulation models having random break-up kernel

These results imply that the optimum break-up kernel for initially monodisperse orthokinetic coagulation modeling is a first or second order reaction (η = 1 or 2) and break-up rate is proportional to the volume of the aggregates (s = 3), not the diameter of the aggregates (s = 1). Also, when the values of the break-up concentration exponent (η) and aggregate size exponent (s) is 1, 2 or 3, respectively, the break-up exponent (b) did not affect the overall coagulation modeling results. It should be noted that the simulation results of particle number concentration varied from each break-up kernel (see Table 2.4) and failed to conserve mass in the case of an aggregate size exponent (s) value of 1. Spicer and Pratsinis (1996a) proposed that break-up rate is related to aggregate size (s = 1), however, the findings of this study indicate that the break-up rate is a function of the area or volume of the aggregate.

Table 2.5 The Results of Mass Conservation Factor (After 30 min. of Coagulation)

Parameters		D_f	Eq. (2.7)	Eq. (2.8)	Eq. (2.9)	Eq. (2.13)	Eq. (2.17)	Eq. (2.29)
$\alpha = 0.1$ $K_B = 0.005$	M[1)]	3	0.99	1.00	1.00	1.00	1.00	1.00
$\alpha = 0.01$ $K_B = 0.005$	P[2)]	3	0.99	0.94	0.99	0.99	0.99	0.99
$\alpha = 0.01$	M	3	0.82	0.84	0.90	1.00	1.00	1.00
$K_B = 0.5$	M	2.5	0.80	0.82	0.89	0.39	1.00	0.99
	M	2.0	0.72	0.79	0.87	0.12	1.00	1.03

[1)] Monodisperse initial condition
[2)] Polydisperse initial condition

As shown in Table 2.5 and Figs. 2.15 and 2.16, initially polydisperse modeling has similar results when compared to the initially monodisperse cases (see Figs. 2.13 and 2.14). From Figs. 2.13 and 2.15, the model of Eq. (2.8) overestimates the coagulation intensity represented by the evolution of particle size distribution for both initial conditions, while the model of Eq. (2.7) underestimates the coagulation intensity for the polydisperse initial condition. The models of Eq. (2.9) and Eq. (2.13) represent very similar results with high numerical accuracy. Furthermore, random break-up kernels (Eq. (2.31)) have greater accuracy and stability than binary break-up kernels (Eq. (2.32)). From the Table 2.5, it is notable that as volume increases aggregate would be exposed to greater stress variance (i.e., increased collision efficiency or break-up coefficient), the three models (Eq. (2.7), Eq. (2.8), and Eq. (2.9)) have less stability while three new models of Eqs. (2.13), (2.17), and (2.29) have perfect mass conservation.

Statistical accuracy analyses are displayed in Figs. 2.14 and 2.16 and show that the models of Eq. (2.9) and Eq. (2.13) obtained higher numerical accuracy than the other models for random break-up case when compared to the uniform discrete model. Also, initial mono- and poly-disperse particle populations have similar numerical accuracy, showing that the accuracy of polydisperse coagulation is slightly higher than that of the initially monodisperse modeling. As mentioned in the orthokinetic coagulation modeling section, the model of Eq. (2.8) having a break-up kernel failed to achieve higher numerical accuracy for the relatively higher stiffness (monodisperse initial condition) (see Figs. 2.14 and 2.16). The application of a random break-up kernel having a functional relationship of aggregate area or volume achieves perfect conservation of mass for all coagulation models.

Numerical stability tests in terms of the mass conservation factor for both initial monodisperse and polydisperse conditions were conducted and displayed in Table 2.5. All models could achieve perfect numerical stability for the monodisperse condition. However, for the polydisperse condition, the model of Eq. (2.8) failed to conserve mass. That is, in the case of the polydisperse condition, the increased relative magnitude of the break-up coefficient due to the decreased collision efficiency (α) (from 0.1 to 0.01) caused the mass conservation deviation for the model of Eq. (2.8). Thus, the model of Eq. (2.8) should not be used as a coagulation model when high levels of break-up exist in the colloid system.

2.4.7 Parameter Sensitivity Analysis

Sensitivity analysis was conducted to obtain a more detailed understanding of the dependence between both collision efficiency (α) and break-up rate constant (K_B) using an orthokinetic coagulation model for a monodisperse initial particle concentration. For this study the aggregation model given by Eq. (2.13) with random discrete break-up kernels given by Eq. (2.31) was used. The model of Eq. (2.13) has higher stability and numerical accuracy than the other aggregation models. Further, the random break-up kernels had better stability than the binary break-up kernel.

The modeling parameters of flow strain-rate ($\dot{\gamma}$) of 10 s^{-1}, fractal dimension (D_f) of 3.0, various collision efficiencies (α) and break-up rate constants (K_B) of 0.01 to 1.0 were examined and results are displayed in Figs 2.17 and 2.18 as contour plots. At the region of high collision efficiency and low break-up rate constant (right bottom area in both figures), coagulation pileup is expected where all particles exist at the maximum size class considered.

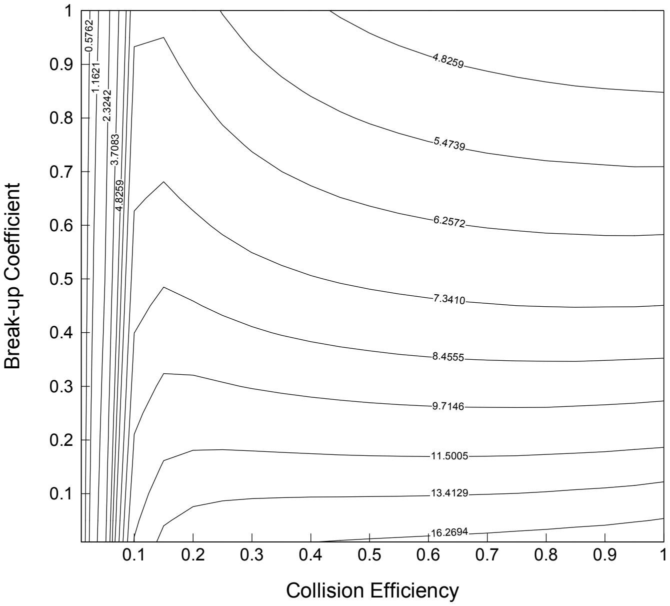

Figure 2.17 Parameter sensitivity analysis of collision efficiency and break-up coefficient as respect to maximum size class concentration (n_{max}) (× 10^5 no./cm^3, strain-rate = 10 s^{-1}, D_f = 3.0)

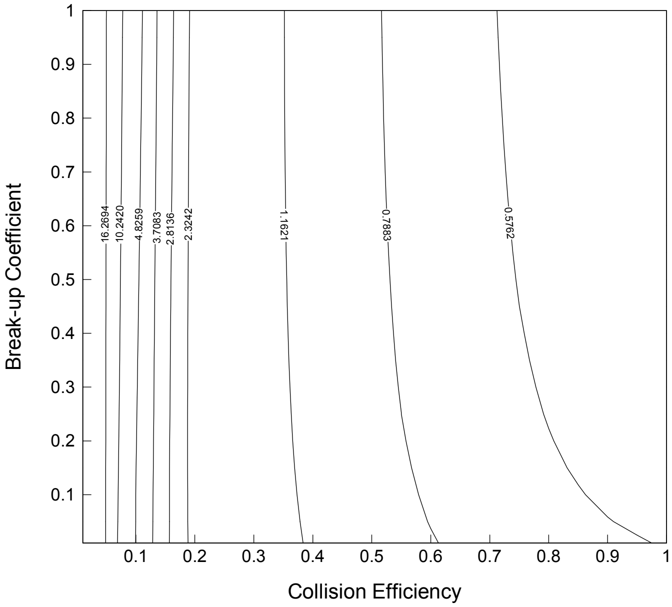

Figure 2.18 Parameter sensitivity analysis of collision efficiency and break-up coefficient as respect to total particle concentration (n_{total}) (× 10^7 no./cm^3, strain-rate = 10 s^{-1}, D_f = 3.0)

If the collision efficiency (α) is less than 0.1, regardless of the break-up coefficient, moderate coagulation patterns could be found. Also, at the collision efficiency value of 0.1, slow coagulation can be expected. As shown in Fig. 18 (representing total particle concentration (N_{total})) there is no effect of the break-up rate constant on total particle concentration. That is, within the limited range of having the break-up coefficient less than the collision efficiency, the breakup coefficient does not influence the total particle concentration, only the collision efficiency affects the total particle concentrations. These results indicate that aggregate break-up has importance to the particle size distribution and coagulation patterns. The contours in Fig. 2.17, representing particle number concentration of the maximum size class, indicate that collision efficiency and break-up rate constant are negatively correlated. That is, as collision efficiency is increased and break-up coefficient is decreased, one can expect increased particle number concentration of the maximum size class. However, as shown in Fig. 2.18, total particle concentration is dependent on collision efficiency having a negative relationship, not depending on the break-up coefficient.

2.4.8 Fractal Aggregation

The effects of aggregate fractal dimension on various coagulation models were also examined. The fractal analysis focused on particle size distribution and mass conservation. The Hounslow model (Eq. (2.9)) was excluded in this fractal dimension modeling due to the low stability discussed previously. The orthokinetic coagulation model having a random break-up kernel given by Eq. (2.31) with break-up parameters of b=1, s=3, and η=2 (see the Case IV of Table 2.4) was adopted for the initially monodisperse simulations. Incorporating Eq. (6) into Eq. (31) produces an orthokinetic coagulation model for fractal aggregates. Thus, this fractal aggregation and break-up equation can predict the effects of fractal dimension on the behavior of particle coagulation. Initially monodisperse modeling conditions of $\alpha = 0.01$, $K_B = 0.5$, $\dot{\gamma} = 10$ (1/s) and a theoretical elapsed time of 30 (min) were used. The results of the aggregate fractal dimension effects are represented in Table 5 and Figs. 19 to 22. New probabilities were considered in Eqs. (17) and (29) and compared with the uniform discrete models for fractal aggregation modeling.

As shown in Figs. 2.19 and 2.20, the model of Eq. (2.7) shows largest deviation from the uniform discrete model in particle size distribution and the total particle concentration results for all three different fractal dimension conditions. However, as the fractal dimension is decreased to 2.0, the differences between the model of Eq. (2.7) and uniform discrete models decrease. Although the model of Eq. (2.8) shows the least deviation from the uniform discrete model at larger particle size ranges, this model underestimated the total particle concentration. From the Figs. 2.19 and 2.20, the new models of Eqs. (2.17) and (2.29) show good agreement at various aggregate fractal dimensions ranging from 2 to 3. Shown in Fig. 2.20, total particle concentration is proportional to the aggregate fractal dimension. The reduction of total particle concentration is lowest with the model of Eq. (2.7) having the decreases of 40.08, 38.36, and 37.72 % for D_f values of 3.0, 2.5 and 2.0, respectively. For the model of Eq. (2.8), the total particle reduction is in the range of 78.15 % to 79.18 % for three different fractal dimension conditions. Results using the models of Eq. (2.9), Eq. (2.17), and Eq. (2.29), and the uniform discrete model are within the deviation range of 98.79 % to 103.15%.

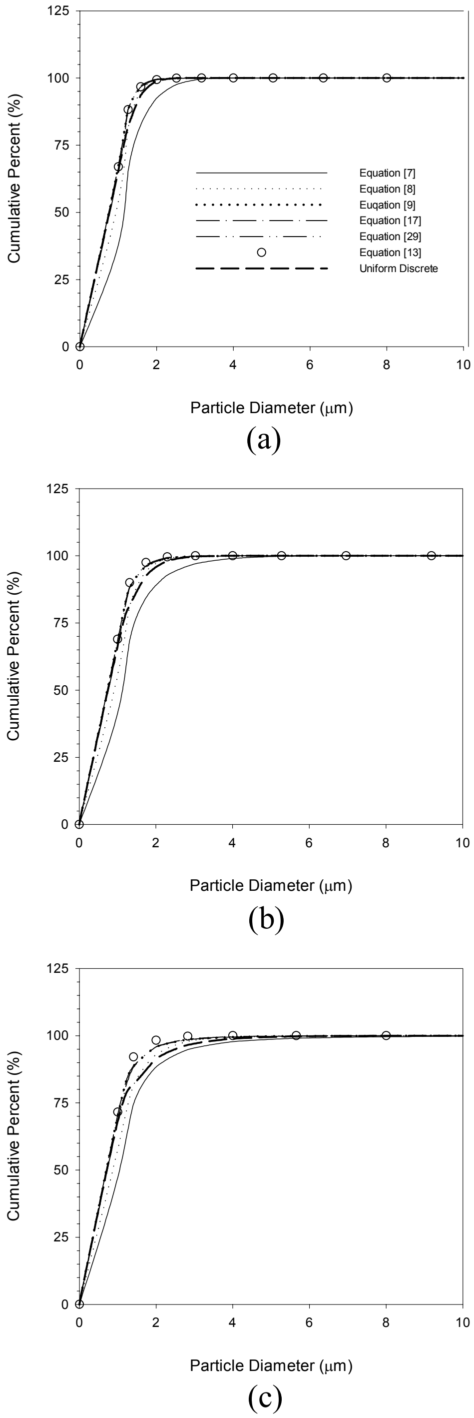

(a)

(b)

(c)

Figure 2.19 Particle cumulative percent for various models with different D_f values. (a) $D_f = 3.0$, (b) $D_f = 2.5$, and (c) $D_f = 2.0$

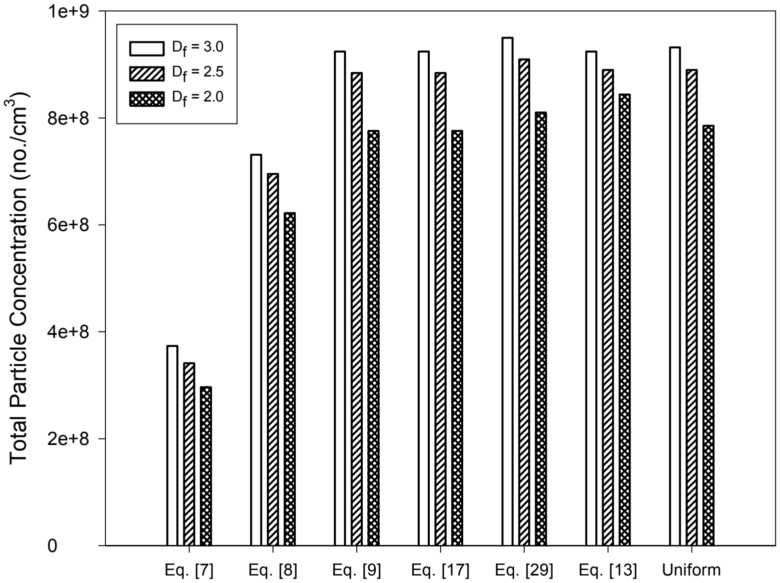

Figure 2.20 The effect of fractal dimension on total particle concentration

From the Figs. 2.21 and 2.22, the new model of Eq. (2.13) shows good agreement only when the fractal dimension value is 3. As the fractal dimension is decreased to 2.0, however, the differences increase due to lower stability (see Fig. 2.21). In the stability test for various fractal dimensions ranging from 2 to 3 (see Table 2.5 and Fig. 2.21), the three models (Eq. (2.7), Eq. (2.8), Eq. (2.9)) and Eq. (2.13) with break-up kernels fail to conserve mass. Although the model of Eq. (2.9) results have excellent agreement with the results from the new model of Eq. (2.17) (see Figs. 2.19, 2.20, and 2.22), the model of Eq. (2.9) failed to conserve mass especially when a low fractal dimension was used. The new model of Eq. (2.13) was applicable only when a fractal dimension value of 3 with a break-up kernel is used (see Figs. 2.21 and 2.22).

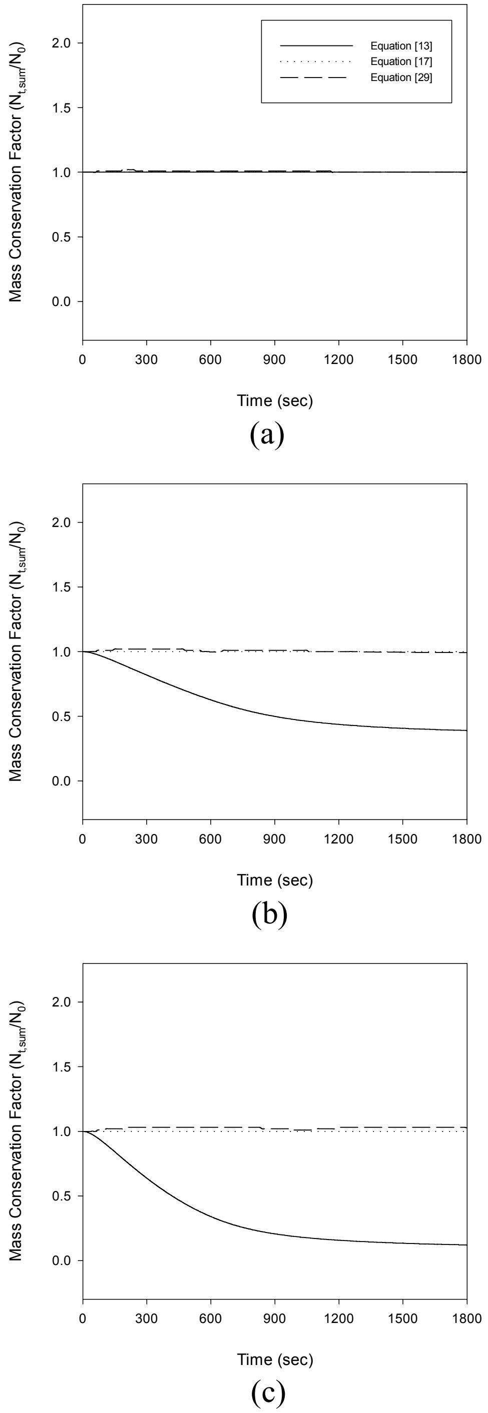

Figure 2.21 Mass conservation for fractal aggregation having random discretized break-up kernels with different D_f values. (a) $D_f = 3.0$, (b) $D_f = 2.5$, and (c) $D_f = 2.0$

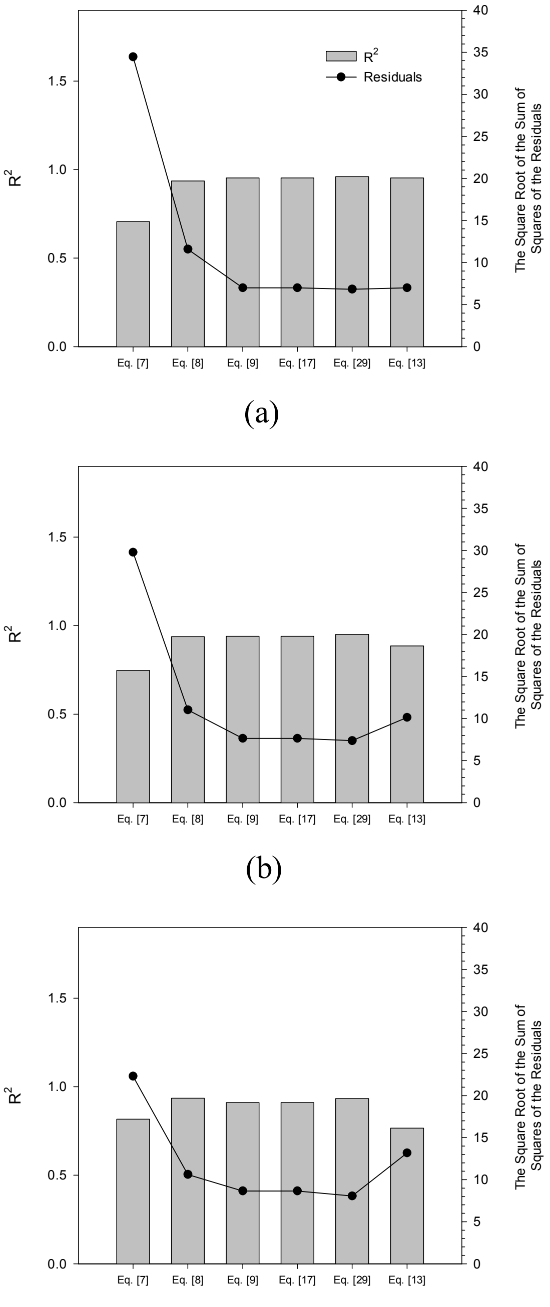

(a)

(b)

(c)

Figure 2.22 Statistical analysis for fractal aggregate coagulation models having random break-up kernel with different D_f values. (a) $D_f = 3.0$, (b) $D_f = 2.5$, and (c) $D_f = 2.0$

Furthermore, as fractal dimension is decreased, the model of Eq. (2.13) has lower accuracy and fails to achieve mass conservation. However, other two new probability functions (probability II and III) developed in this study (Eqs. (2.17) and (2.29)) conserved mass at all fractal dimension conditions. In the model of Eq. (2.13) the relationship, $\upsilon_{k+1} = 2\upsilon_k$, having a geometric size interval of 2, could not predict particle coagulation resulting from a variation in fractal dimension. Solid particle aggregates are found to be fractal (Table 2.1), thus fractal aggregate coagulation modeling is needed for realistic simulation. The new probability functions given by Eqs. (2.17) and (2.29) can be readily applied to population balance equations that include various fractal dimensions and break-up kernels.

2.4.9 Computational Efficiency

In examining the computational efficiency, several techniques were used and these results are displayed in Table 2.6 in terms of the number of steps, number of subroutine calls, and CPU time. These measurements were based on the commercial FORTRAN program IVPAG, one of the IMSL programs. All the computations were conducted using the same conditions for orthokinetic coagulation modeling having a random break-up kernel (α = 0.01, $\dot{\gamma}$ = 10 s^{-1}, D_f = 3.0, $r_{KB}=K_B(\dot{\gamma})(r_k)^3(n_k)$, K_B = 0.001) using the computer hardware of a 1.9 GHz Pentium IV having 1.0 GB of memory. Table 2.6 shows that the models of Eq. (2.13) and (2.17) have the best computational efficiency on the basis of number of steps, subroutine calls, and CPU time. These seven coagulation models demonstrate computational efficiency in the order of the models of

Eq. (2.17), Eq. (2.13), Eq. (2.8), Eq. (2.9), Eq. (2.7), Eq. (2.29), and uniform discrete models.

Table 2.6 Computational Efficiency Comparisons for Improved Coagulation Model

Models	Number of steps taken	Number of subroutine calls with IVPAG	CPU time (sec)
Equation (2.7)	471	554	6.2500×10^{-2}
Equation (2.8)	267	331	4.6875×10^{-2}
Equation (2.9)	241	370	5.2500×10^{-2}
Equation (2.13)	184	230	3.1250×10^{-2}
Equation (2.17)	184	230	3.1250×10^{-2}
Equation (2.29)	4654	5845	0.5938
Uniform Discrete	501	693	525.7640

The model of Eq. (2.29) makes many steps and subroutine calls due to the calculation of population differences (Δn_k) for each time step. Further, during the uniform discrete model test, as fractal dimension was decreased from 3.0 to 2.0, the number of steps and subroutine calls, and CPU time greatly increased. Thus, the uniform discrete model has low computational efficiency (long processing time) compared with the non-uniform discrete coagulation models as expected.

2.5 Conclusions

A variety of modeling techniques for the population balances resulting from particle coagulation were examined. The simplified models using non-uniform discretization schemes were compared to uniform discrete models. There is a large influence on the stability (conservation of mass) and accuracy (good statistical comparisons to the uniform discrete model) of these coagulation ordinary differential equations. However, in this study, an aggregation and break-up algorithm that can simulate variable kernels based on particle size were used, as these kernels represent the physical process of coagulation and are derived from basic mass transport principles. Under spherical particle conditions, having the fractal dimension of 3.0 (i.e., droplet coalescence), all of the coagulation models examined could conserve mass and had high accuracy. Although the model of Eq. (2.13) that has new probability function I had higher accuracy and stability than the other models, all models failed to conserve mass as the fractal dimension was decreased to 2.0. After introducing other new algorithms of Eqs. (2.17) and (2.29), these new two approaches made it possible to simulate fractal aggregate coagulation with high accuracy and perfect mass conservation. With respect to computational efficiency, the new algorithms of Eqs. (2.13) and (2.17) had the lowest computational time. Also, the results of the parameter sensitivity analysis showed that the addition of a break-up kernel does not effect total particle concentration within the limited range of having the break-up coefficient less than the collision efficiency. However, a break-up kernel does influence the particle size distributions. In the break-up study, the random discrete break-up kernel was introduced and compared with the binary break-up kernel. The binary break-up represents similar simulation results with the random break-up and slightly higher stability than random break-up when break-up concentration exponent (η) is 2 (see Table 2.4). However, the random break-up kernel has greater applicability to various break-up parameter conditions than the binary break-up kernel with higher stability and less computational limitations. Spicer and Pratsinis proposed that break-up rate is related to aggregate size (s = 1) (Spicer and Pratsinis 1996a), however, the results from the analysis of the various break-up kernel parameters indicate that the break-up rate is a function of volume (s = 3) of the aggregates. Also, when the values of the break-up concentration exponent (η) and aggregate size exponent (s) are 1 and 2 or 3, respectively, break-up exponent (b) did not affect the overall coagulation model. It should be noted that the simulation results of particle number concentration were different from each break-up kernel (see Table 2.4) and failed to conserve mass in the case of aggregate size exponent (s) value of 1. The new model of Eq. (2.17) has been shown in the investigation to be superior to all of the other models and can be used to develop predictive capability for coagulation in computational fluid dynamics (CFD) and reaction algorithms resulting from superior efficiency and accuracy.

CHAPTER III

IMPROVED ORTHOKINETIC COAGULATION MODEL FOR FRACTAL COLLOIDS: AGGREGATION AND BREAK-UP

3.1 Overview

An improved discretized population balance equation (PBE) is proposed in this study. This improved discretized population balance equation has new probability distribution functions for aggregates produced in non-uniform discrete coagulation modeling. The authors extended an improved particle coagulation model previously developed to an adjustable geometric size interval (*q*), where *q* is a volume ratio of class *k*+1 particles to class *k* particles ($\upsilon_{k+1}/\upsilon_k = q$). This model was compared with exact numerical solutions of continuous (uniform discretized) population balance equations and applied to simulate the particle aggregation and breakup with fractal dimensions lower than 3. Further, comparisons were made using the fractal aggregate collision mechanisms of orthokinetic coagulation with the inclusion of flow induced breakup.

In the course of the investigation the new algorithm was found to be a substantial improvement in terms of numerical accuracy, stability, and computational efficiency over the continuous model. This new algorithm makes it possible to solve fractal particle aggregation and breakup problems with high accuracy, perfect mass conservation and exceptional computational efficiency, thus the new model can be used to develop predictive simulation techniques for the coupled coagulation using computational fluid dynamics (CFD) and chemical reaction modeling.

3.2 Introduction

Coagulation is the multi-step process of producing larger aggregates by collisions and subsequent bonding or coalescing of smaller particles contained in a fluid. The particles can be either solid or fluid materials suspended in a gas or liquid. Particle collisions are induced by inter particle motions that have been attributed to three basic mechanisms: fluid motion or orthokinetic coagulation, Brownian diffusion or perikinetic coagulation and buoyancy or differential sedimentation. Fluid motion also creates disruptive stresses that can cause fracture of the agglomerates.

In recent years, numerous studies have attempted to solve the particle aggregation problem consisting of the continuous population balance equations (PBE), where the continuous PBE can be expressed as an uniform discretized equation (Smoluchowski 1917) (Eq. (3.1)) or a continuous integro-partial-differential equation (Drake 1972; Ramkrishna 1985) (Eq. (3.2)),

$$\left(\frac{\mathrm{dn}_k}{\mathrm{dt}}\right)_{\mathrm{Agg}} = \frac{1}{2}\sum_{i+j=k} \alpha\beta\left(\mathrm{r}_i, \mathrm{r}_j\right)\mathrm{n}_i\mathrm{n}_j - \mathrm{n}_k\sum_{l=1}^{\infty}\alpha\beta\left(\mathrm{r}_l, \mathrm{r}_k\right)\mathrm{n}_l \tag{3.1}$$

or

$$\left(\frac{\mathrm{dn}(\upsilon,\mathrm{t})}{\mathrm{dt}}\right)_{\mathrm{Agg}} = \frac{1}{2}\int_0^{\upsilon}\alpha\beta\left(\upsilon\text{-}w, w\right)\mathrm{n}(\upsilon\text{-}w,\mathrm{t})\mathrm{n}(w,\mathrm{t})\mathrm{d}w - \int_0^{\infty}\alpha\beta\left(\upsilon, w\right)\mathrm{n}(\upsilon,\mathrm{t})\mathrm{n}(w,\mathrm{t})\mathrm{d}w \tag{3.2}$$

where n is the number concentration of particles, r is the particle or aggregate radius, α is a collision efficiency, υ and *w* are particle volume, *i*, *j*, *k*, and *l* refer to particle size class indices, and t is time. The quantity β is termed the collision frequency kernel and is dependent on particle size, the particle movement mechanism, and collision geometry.

To obtain exact numerical solutions of the continuous PBE (Eq. (3.1) or (3.2)), extensive computation time and hardware are required. A realistic maximum size used in coagulation modeling would therefore produce an unmanageable number of simultaneous equations to solve. To overcome this computational non-efficiency of the continuous PBE (or uniform discretized PBE), various non-uniform discrete schemes have been introduced (Gelbard and Seinfeld 1978; Gelbard et al. 1980; Batterham et al. 1981; Hounslow et al. 1988; Marchal et al. 1988; Litster et al. 1995; Hill and Ng 1996; Kumar and Ramkrishna 1996a; Kramer 2000; Vanni 2000).

Relatively little attention has been paid to fractal particle coagulation modeling. Spherical particle coalescence applies only to ideal bubbles and droplets and most particle aggregates are found to be fractal, especially in solid colloidal particle coagulation. Thus, fractal coagulation modeling is needed for realistic simulation. This paper will examine an improved technique of PBE discretization and compare them to exact numerical solution of uniform discretized PBE. Further, modifications and comparisons are made to incorporate breakup in the orthokinetic population balances with the inclusion of flow induced fracture. Finally, model comparisons are made using simulation data of particle size distributions, mass conservation, and computational time.

3.3 Discretization of the Population Balance Equation

3.3.1 Particle Aggregation

Hill and Ng produced a discretized PBE based on probability density functions in each interval *k* for aggregation (Hill and Ng 1996) and breakup (Hill and Ng 1995).

The aggregation rate equation of Hill and Ng can be expressed as,

$$\begin{aligned}\left(\frac{\mathrm{dn}_k}{\mathrm{dt}}\right)_{\mathrm{Agg}} &= \sum_{j=1}^{k-2} \alpha\beta(\mathrm{r}_{k-1},\mathrm{r}_j)\mathrm{C}_{k\text{-}1,j,k}\mathrm{n}_{k-1}\mathrm{n}_j + \sum_{j=1}^{k-1} \alpha\beta(\mathrm{r}_k,\mathrm{r}_j)\mathrm{G}_{k,j,k}\mathrm{n}_k\mathrm{n}_j \\ &+ \frac{1}{2}\alpha\beta(\mathrm{r}_{k-1},\mathrm{r}_{k-1})\mathrm{C}_{k\text{-}1,k\text{-}1,k}(\mathrm{n}_{k-1})^2 + \frac{1}{2}\alpha\beta(\mathrm{r}_k,\mathrm{r}_k)\mathrm{G}_{k,k,k}(\mathrm{n}_k)^2 - \sum_{i=1}^{\max}\alpha\beta(\mathrm{r}_i,\mathrm{r}_k)\mathrm{n}_i\mathrm{n}_k\end{aligned} \tag{3.3}$$

where, $\mathrm{C}_{i,j,k}$ and $\mathrm{G}_{i,j,k\text{-}1}$ are collision probability functions. $\mathrm{C}_{i,j,k}$ predicts whether collisions between particles from intervals *i* and *j* will fall into interval *k* and $\mathrm{G}_{i,j,k\text{-}1}$ terms predict that the *i* and *j* interval particles will form a particle of a size in the range of interval $k-1$. Furthermore, a 100% probability exists that particles from intervals *i* and *j* will fall into either *k* or $k-1$, having the relation of $\mathrm{C}_{i,j,k}$ + $\mathrm{G}_{i,j,k\text{-}1}$ = 1. Hill and Ng concluded that the volume of particles removed from intervals *i* and *j* must be equal to the particle volume added to intervals *k* and $k-1$. However, it is not possible to know the volume or number of particles removed from a discrete interval or contributed to the larger intervals *a priori* during each iteration. A possible solution is to equate the probability density functions in terms of the volume ranges of each interval. Thus, the probability that a collision pair will fall into a given size class range increases as the range of the interval increases. For the adjustable interval scheme and an average volume concept, $\upsilon_{k+1} = q\upsilon_k$ and $\overline{\upsilon}_k = 0.5(\upsilon_k + \upsilon_{k-1})$, is used and Eq. (3.3) can be expressed in terms of the particle radii with volume based probabilities as,

$$\begin{aligned}\left(\frac{\mathrm{dn}_k}{\mathrm{dt}}\right)_{\mathrm{Agg}} &= \sum_{j=1}^{k-2} \alpha\beta(\mathrm{r}_{k-1},\mathrm{r}_j)\left(\frac{q}{q-1}\right)\left(\frac{\mathrm{r}_j}{\mathrm{r}_k}\right)^3 \mathrm{n}_{k-1}\mathrm{n}_j + \sum_{j=1}^{k-1} \alpha\beta(\mathrm{r}_k,\mathrm{r}_j)\left\{1-\left(\frac{1}{(q-1)}\right)\left(\frac{\mathrm{r}_j}{\mathrm{r}_k}\right)^3\right\}\mathrm{n}_k\mathrm{n}_j \\ &+ \frac{1}{2}\alpha\beta(\mathrm{r}_{k-1},\mathrm{r}_{k-1})\left(\frac{1}{q-1}\right)(\mathrm{n}_{k-1})^2 + \frac{1}{2}\alpha\beta(\mathrm{r}_k,\mathrm{r}_k)\left(\frac{q-2}{q-1}\right)(\mathrm{n}_k)^2 - \sum_{i=1}^{\max}\alpha\beta(\mathrm{r}_i,\mathrm{r}_k)\mathrm{n}_i\mathrm{n}_k\end{aligned} \tag{3.4}$$

3.3.2 Aggregate Break-Up

Aggregate breakup mechanisms have been applied to various fields, such as floc disintegration, droplet fragmentation, and comminution of particle solids (Vanni 1999). Population balance equations related to a breakup reaction can be expressed by continuous and discrete approaches (Patil et al. 2001). Few analytical solutions using either method are available under limited conditions (Ziff and McGrady 1985; Peterson 1986). Thus, numerical solutions are required for these breakup models. A pure breakup reaction in the form of a continuous breakup PBE can be expressed by Eq. (3.5) (Prasher 1987; Randolph and Larson 1988),

$$\left(\frac{\mathrm{dn}(\upsilon,\mathrm{t})}{\mathrm{dt}}\right)_{\mathrm{Break}} = \int_0^{\infty} \mathrm{b}(\upsilon, w)\mathrm{s}(w)\mathrm{n}(w,\mathrm{t})\mathrm{d}w - \mathrm{s}(\upsilon)\mathrm{n}(\upsilon,\mathrm{t}) \tag{3.5}$$

where $\mathrm{b}(\upsilon, w)$ is the breakup distribution function, and $\mathrm{s}(\upsilon)$ is the breakup rate coefficient. Also, Eq. (3.5) can be discretized

$$\left(\frac{\mathrm{dn}_k}{\mathrm{dt}}\right)_{\mathrm{Break}} = \sum_{j=k+1}^{\infty} \mathrm{b}_{k,j}\mathrm{s}_j\left(\mathrm{n}_j\right)^{\eta} - \mathrm{s}_k\left(\mathrm{n}_k\right)^{\eta} \tag{3.6}$$

where, η is a break-up concentration exponent, $\mathrm{b}_{k,j}$ is the breakup distribution function (or probability function), and s_k is the breakup rate coefficient.

Researchers have proposed the breakup distribution function (or probability function), $\mathrm{b}_{k,j}$ using several approaches (Coulaloglou and Tavlarides 1977; Pandya and Spielman 1982; Lu and Spielman 1985; Kusters 1991; Ziff 1991; Hill and Ng 1995; Spicer and Pratsinis 1996a; Kramer and Clark 1999). To solve the breakup distribution function an adjustable improved probability function was derived from the breakup function of Hill and Ng (Hill and Ng 1995) by adding the adjustable interval scheme, $\upsilon_{k+1} = q\upsilon_k$ and the average volume concept, $\overline{\upsilon}_k = 0.5(\upsilon_k + \upsilon_{k-1})$ producing,

$$\mathrm{b}_{k,j} = \frac{3(q-1)}{2}\left(\frac{\mathrm{r}_k}{\mathrm{r}_j}\right)^3 \tag{3.7}$$

Further, the breakup distribution function can be described using a random breakup distribution function, $\phi(j)$ (Kramer and Clark 1999) as,

$$\mathrm{b}_{k,j} = \phi(j) \tag{3.8}$$

The breakup rate coefficient, s_k has been proposed by several researchers (Chen et al. 1990; Kusters 1991; Spicer and Pratsinis 1996a; Serra and Casamitjana 1998a; Kramer and Clark 1999; Zhang and Li 2003). The most common approach to aggregate breakup is the use of flow strain-rate as the primary breakup parameter. The breakup rate coefficient can be expressed as,

$$\mathrm{s}_k = \mathrm{K_B}(\dot{\gamma})^{\mathrm{b}}(\mathrm{r}_k)^{\mathrm{s}} \tag{3.9}$$

where $\mathrm{K_B}$ is the breakup rate constant, b is a breakup rate exponent, s is an aggregate size exponent, and $\dot{\gamma}$ is the flow strain-rate. Equation (3.9) indicates that the breakup coefficient is a function of flow strain-rate resulting from energy input and the geometric properties of the aggregate (i.e., size, area, or volume). As populations of the aggregates are exposed to increasing levels of flow strain-rate (or stress), thus it is expected that increasing amounts of breakup will occur. Adding Eqs. (3.9) and (3.7) or (3.8) into Eq. (3.6), yields an improved discretized breakup population balance as,

$$\left(\frac{\mathrm{dn}_k}{\mathrm{dt}}\right)_{\mathrm{Break}} = \sum_{j=k+1}^{\infty} \frac{3(q-1)}{2}\left(\frac{\mathrm{r}_k}{\mathrm{r}_j}\right)^3 \mathrm{K_B}(\dot{\gamma})^{\mathrm{b}}(\mathrm{r}_j)^{\mathrm{s}}(\mathrm{n}_j)^{\eta} - \frac{1}{2}\mathrm{K_B}(\dot{\gamma})^{\mathrm{b}}(\mathrm{r}_k)^{\mathrm{s}}(\mathrm{n}_k)^{\eta} \tag{3.10}$$

or

$$\left(\frac{\mathrm{dn}_k}{\mathrm{dt}}\right)_{\mathrm{Break}} = \sum_{j=k+1}^{\infty} \phi(j)\mathrm{K_B}(\dot{\gamma})^{\mathrm{b}}(\mathrm{r}_j)^{\mathrm{s}}(\mathrm{n}_j)^{\eta} - \mathrm{K_B}(\dot{\gamma})^{\mathrm{b}}(\mathrm{r}_k)^{\mathrm{s}}(\mathrm{n}_k)^{\eta} \tag{3.11}$$

In a straightforward manner, a final coagulation population balance model can be obtained from the combination of aggregation and breakup, yielding an overall population balance equation. Thus, an overall continuous population balance equation with aggregation and breakup reactions can be expressed by Eq. (3.12) after summation of Eqs. (3.2) and (3.5) (Ramkrishna 1985; Randolph and Larson 1988).

$$\begin{aligned}\left(\frac{\mathrm{dn}(\upsilon,\mathrm{t})}{\mathrm{dt}}\right)_{\mathrm{Total}} &= \frac{1}{2}\int_0^{\upsilon} \alpha\beta\left(\upsilon\text{-}w, w\right)\mathrm{n}(\upsilon\text{-}w,\mathrm{t})\mathrm{n}(w,\mathrm{t})\mathrm{d}w - \int_0^{\infty} \alpha\beta\left(\upsilon, w\right)\mathrm{n}(\upsilon,\mathrm{t})\mathrm{n}(w,\mathrm{t})\mathrm{d}w \\ &\quad + \int_0^{\infty} \mathrm{b}\left(\upsilon, w\right)\mathrm{s}(w)\mathrm{n}(w,\mathrm{t})\mathrm{d}w - \mathrm{s}(\upsilon)\mathrm{n}(\upsilon,\mathrm{t})\end{aligned} \tag{3.12}$$

Also, the discretized form of Eq. (3.12) is represented by Eq. (3.13) using the summation of Eqs. (3.1) and (3.6).

$$\left(\frac{\mathrm{dn}_k}{\mathrm{dt}}\right)_{\mathrm{Total}} = \frac{1}{2}\sum_{i+j=k} \alpha\beta\left(\mathrm{r}_i,\mathrm{r}_j\right)\mathrm{n}_i\mathrm{n}_j - \mathrm{n}_k\sum_{l=1}^{\infty}\alpha\beta\left(\mathrm{r}_l,\mathrm{r}_k\right)\mathrm{n}_l + \sum_{j=k+1}^{\infty}\mathrm{b}_{k,j}\mathrm{s}_j\left(\mathrm{n}_j\right)^{\eta} - \mathrm{s}_k\left(\mathrm{n}_k\right)^{\eta} \tag{3.13}$$

Adding Eqs. (3.4) and (3.10) or (3.11) into Eq. (3.13), produces an overall improved discretized coagulation model including aggregation and breakup. Although Eq. (3.13) with Eqs. (3.4) and (3.10) or (3.11) has improved probability functions that can predict particle aggregation and breakup, Eq. (3.13) is applicable for only perfect spherical aggregates with fractal dimension D_f of 3.

3.3.3 Improved Coagulation Modeling for Fractal Agglomeration

In both continuous and discrete modeling the volume and/or radii of the particles are significant parameters. In droplet coalescence conservation of the volumes will produce a new droplet radius and is easily computed. In terms of a size class, such a radius is given by,

$$\mathrm{r}_k = \sqrt[3]{\frac{3k\upsilon_1}{4\pi}} \tag{3.14}$$

with υ_1 the volume of the primary size class droplet. Amorphous aggregates comprised of solid particles can be treated using a fractal dimension, D_f. The effective radius of a size class k aggregate comprised of primary particles of radius r_1 can be calculated using a fractal dimension (Meakin 1988) as,

$$\mathrm{r}_k = \mathrm{r}_1 (k)^{1/D_f} \tag{3.15}$$

The adjustable geometric size interval ($q = \upsilon_{k+1} / \upsilon_k$) is determined using an aggregate maximum size class computation incorporating a fractal dimension given as,

$$\mathrm{r}_{k,\mathrm{d}} = \mathrm{r}_1 (k_\mathrm{d})^{1/D_f} = \mathrm{r}_1 (q^{k_\mathrm{d}-1})^{1/D_f} \tag{3.16}$$

where $\mathrm{r}_{k,\mathrm{d}}$ is the aggregate radius of size class k for the discretized model and k_d is the number of the size class interval for discretized model. By letting Eq. (3.15) be equal to Eq. (3.16), the equation for the calculation of the adjustable geometric size interval (q) becomes,

$$q = (k_\mathrm{c})^{\{1/(k_\mathrm{d}-1)\}} \tag{3.17}$$

where, k_c is the number of size class intervals for the uniform discrete distribution model ($q = 1$).

Furthermore, coagulation simulation using Eq. (3.4) can not be directly applied to fractal aggregates based on the model's inability to conserve mass when modeling fractal aggregation. That is, the model of Eq. (3.4) is stable only for spherical particle aggregation, due to applying an average volume approach. To obtain solutions for the fractal aggregate coagulation problem it must be assumed that the probability functions are proportional to aggregate size having an exponent of a fractal dimension. Thus, an improved discretized aggregation model for fractal particles was derived as,

$$\begin{aligned}\left(\frac{\mathrm{dn}_k}{\mathrm{dt}}\right)_{\mathrm{Agg}} &= \sum_{j=1}^{k-2} \alpha\beta(\mathrm{r}_{k-1},\mathrm{r}_j)\left(\frac{q}{q-1}\right)\left(\frac{\mathrm{r}_j}{\mathrm{r}_k}\right)^{D_f} \mathrm{n}_{k-1}\mathrm{n}_j + \sum_{j=1}^{k-1} \alpha\beta(\mathrm{r}_k,\mathrm{r}_j)\left\{1-\left(\frac{1}{(q-1)}\right)\left(\frac{\mathrm{r}_j}{\mathrm{r}_k}\right)^{D_f}\right\}\mathrm{n}_k\mathrm{n}_j \\ &+ \frac{1}{2}\alpha\beta(\mathrm{r}_{k-1},\mathrm{r}_{k-1})\left(\frac{1}{q-1}\right)(\mathrm{n}_{k-1})^2 + \frac{1}{2}\alpha\beta(\mathrm{r}_k,\mathrm{r}_k)\left(\frac{q-2}{q-1}\right)(\mathrm{n}_k)^2 - \sum_{i=1}^{\max} \alpha\beta(\mathrm{r}_i,\mathrm{r}_k)\mathrm{n}_i\mathrm{n}_k\end{aligned} \tag{3.18}$$

Also, in the same manner, a new discretized breakup model for fractal particles was obtained as,

$$\left(\frac{\mathrm{dn}_k}{\mathrm{dt}}\right)_{\mathrm{Break}} = \sum_{j=k+1}^{\infty} \frac{3(q-1)}{2}\left(\frac{\mathrm{r}_k}{\mathrm{r}_j}\right)^{D_f} \mathrm{K_B}(\dot{\gamma})^{\mathrm{b}}(\mathrm{r}_j)^{\mathrm{s}}(\mathrm{n}_j)^{\eta} - \frac{1}{2}\mathrm{K_B}(\dot{\gamma})^{\mathrm{b}}(\mathrm{r}_k)^{\mathrm{s}}(\mathrm{n}_k)^{\eta} \tag{3.19}$$

By assuming Eqs. (3.18) and (3.19) or (3.11) to be additive, the overall improved discretized coagulation population balance model having fractal aggregate applicability is given as,

$$\begin{aligned}\left(\frac{\mathrm{dn}_k}{\mathrm{dt}}\right)_{\mathrm{Total}} &= \sum_{j=1}^{k-2} \alpha\beta(\mathrm{r}_{k-1},\mathrm{r}_j)\left(\frac{q}{q-1}\right)\left(\frac{\mathrm{r}_j}{\mathrm{r}_k}\right)^{D_f} \mathrm{n}_{k-1}\mathrm{n}_j + \sum_{j=1}^{k-1} \alpha\beta(\mathrm{r}_k,\mathrm{r}_j)\left\{1-\left(\frac{1}{(q-1)}\right)\left(\frac{\mathrm{r}_j}{\mathrm{r}_k}\right)^{D_f}\right\}\mathrm{n}_k\mathrm{n}_j \\ &+ \frac{1}{2}\alpha\beta(\mathrm{r}_{k-1},\mathrm{r}_{k-1})\left(\frac{1}{q-1}\right)(\mathrm{n}_{k-1})^2 + \frac{1}{2}\alpha\beta(\mathrm{r}_k,\mathrm{r}_k)\left(\frac{q-2}{q-1}\right)(\mathrm{n}_k)^2 - \sum_{i=1}^{\max}\alpha\beta(\mathrm{r}_i,\mathrm{r}_k)\mathrm{n}_i\mathrm{n}_k \\ &+ \sum_{j=k+1}^{\infty}\frac{3(q-1)}{2}\left(\frac{\mathrm{r}_k}{\mathrm{r}_j}\right)^{D_f}\mathrm{K_B}(\dot{\gamma})^{\mathrm{b}}(\mathrm{r}_j)^{\mathrm{s}}(\mathrm{n}_j)^{\eta} - \frac{1}{2}\mathrm{K_B}(\dot{\gamma})^{\mathrm{b}}(\mathrm{r}_k)^{\mathrm{s}}(\mathrm{n}_k)^{\eta}\end{aligned} \tag{3.20}$$

or

$$\begin{aligned}\left(\frac{\mathrm{dn}_k}{\mathrm{dt}}\right)_{\mathrm{Total}} &= \sum_{j=1}^{k-2} \alpha\beta(\mathrm{r}_{k-1},\mathrm{r}_j)\left(\frac{q}{q-1}\right)\left(\frac{\mathrm{r}_j}{\mathrm{r}_k}\right)^{D_f} \mathrm{n}_{k-1}\mathrm{n}_j + \sum_{j=1}^{k-1} \alpha\beta(\mathrm{r}_k,\mathrm{r}_j)\left\{1-\left(\frac{1}{(q-1)}\right)\left(\frac{\mathrm{r}_j}{\mathrm{r}_k}\right)^{D_f}\right\}\mathrm{n}_k\mathrm{n}_j \\ &+ \frac{1}{2}\alpha\beta(\mathrm{r}_{k-1},\mathrm{r}_{k-1})\left(\frac{1}{q-1}\right)(\mathrm{n}_{k-1})^2 + \frac{1}{2}\alpha\beta(\mathrm{r}_k,\mathrm{r}_k)\left(\frac{q-2}{q-1}\right)(\mathrm{n}_k)^2 - \sum_{i=1}^{\max}\alpha\beta(\mathrm{r}_i,\mathrm{r}_k)\mathrm{n}_i\mathrm{n}_k \\ &+ \sum_{j=k+1}^{\infty}\phi(j)\mathrm{K_B}(\dot{\gamma})^{\mathrm{b}}(\mathrm{r}_j)^{\mathrm{s}}(\mathrm{n}_j)^{\eta} - \mathrm{K_B}(\dot{\gamma})^{\mathrm{b}}(\mathrm{r}_k)^{\mathrm{s}}(\mathrm{n}_k)^{\eta}\end{aligned} \tag{3.21}$$

3.3.4 Orthokinetic Coagulation Modeling for Fractal Agglomeration

The collision frequency kernel, $\beta(\mathrm{r}_i, \mathrm{r}_j)$ in orthokinetic kinetic coagulation was rigorously analyzed using the coalescencing particle collisions created by a laminar shear flow (Kramer and Clark 1997) to be,

$$\beta(\mathrm{r}_i, \mathrm{r}_j) = \frac{4}{3}\pi\dot{\gamma}(\mathrm{r}_i + \mathrm{r}_j)^3 \tag{3.22}$$

To improve the computational efficiency and compatibility of Eqs. (3.20) or (3.21) when coupled with other modeling (i.e., computational fluid dynamics (CFD) and chemical reactions), a dimensionless scheme is very effective. For these purpose, dimensionless constants for concentration N_i, time τ, time increment $\mathrm{d}\tau$, and breakup κ can be introduced as:

For dimensionless concentration,

$$\mathrm{n}_i = \mathrm{N}_i(\mathrm{n}_0) \tag{3.23}$$

For dimensionless time,

$$\tau = \frac{4\pi}{3}\dot{\gamma}(\mathrm{r}_1)^3\mathrm{n}_0\mathrm{t} \tag{3.24}$$

and

$$\mathrm{d}\tau = \frac{4\pi}{3}\dot{\gamma}(\mathrm{r}_1)^3\mathrm{n}_0\mathrm{dt} \tag{3.25}$$

For dimensionless break-up,

$$\kappa = \frac{3\mathrm{K_B}(\dot{\gamma})^{\mathrm{b}-1}(\mathrm{r}_1)^{\mathrm{s}-3}}{4\pi\mathrm{n}_0^{2-\eta}} \tag{3.26}$$

Substituting Eqs. (3.23), (3.24), (3.25), and (3.26) into Eq. (3.21), produces the final dimensionless population balance equation for orthokinetic coagulation using the new probability distribution functions, yields

$$\begin{aligned}\frac{\mathrm{dN}_k}{\mathrm{d}\tau} = &\left[\left(\sum_{j=1}^{k-2}\alpha((k-1)^{1/\mathrm{D}_f} + j^{1/\mathrm{D}_f})^3\left(\frac{q}{q-1}\right)\left(\frac{j}{k}\right)\mathrm{N}_{k\text{-}1}\mathrm{N}_j\right) + \left(\sum_{j=1}^{k-1}\alpha(k^{1/\mathrm{D}_f} + j^{1/\mathrm{D}_f})^3\left\{1-\left(\frac{1}{(q-1)}\right)\left(\frac{j}{k}\right)\right\}\mathrm{N}_k\mathrm{N}_j\right)\right.\\ &\left.+\left(0.5\alpha\left(\frac{1}{q-1}\right)(k-1)^{3/\mathrm{D}_f}(\mathrm{N}_{k-1})^2\right) + \left(0.5\alpha\left(\frac{q-2}{q-1}\right)(k)^{3/\mathrm{D}_f}(\mathrm{N}_k)^2\right) - \left(\sum_{i=1}^{\max}\alpha(k^{1/\mathrm{D}_f} + i^{1/\mathrm{D}_f})^3\mathrm{N}_k\mathrm{N}_i\right)\right]\\ &+\kappa\left[\left(\sum_{j=k+1}^{\infty}\phi(j)(j)^{\mathrm{s}/\mathrm{D}_f}(\mathrm{N}_j)^{\eta}\right) - \left((k)^{\mathrm{s}/\mathrm{D}_f}(\mathrm{N}_k)^{\eta}\right)\right]\end{aligned} \tag{3.27}$$

3.4 Results and Discussion

3.4.1 Numerical Methods

Equation (3.27) generates a set of ordinary differential equations (ODEs) to predict the population n_k of all size classes k = 1 to maximum. Solutions to the PBE of

Eq. (3.27) were obtained using FORTRAN ODE integrating method (IVPAG) with Gear's method. IVPAG is applicable to numerically stiff problems such as the population balance equations where extreme ranges in particle population and size class exist. The error tolerance was 10^{-6} for all numerical solutions during coagulation modeling.

The PBM of Eq. (3.27) was computed over time using the monodisperse initial conditions as follows; primary particle concentration of 1.0×10^{8} no/cm^3 and primary particle diameter of 1.0 μm. For each computation a maximum size class of 1024 was used. Although it would be desirable to have an unlimited size class such that the aggregate growth would be unbounded, computationally this is not possible. Thus, a reasonable maximum size class must be selected. Further, a theoretical coagulation modeling time of 30 minutes was used in this study. The selection of 30 minutes was based on conventional practice in the water treatment field (Letterman et al. 1999).

3.4.2 Fractal Agglomeration

The effects of aggregate fractal dimension (D_f) on orthokinetic coagulation modeling results were examined. The fractal analysis focused on the response variables of mass conservation and cumulative oversize particle distribution of Eq. (3.28), not particle size distribution.

$$\left(\mathrm{CPSDO}_k\right)_t = 1-\left(\mathrm{CPSD}_k\right)_t = 1-\sum_{j=1}^{k}\frac{\left(n_j\right)_t}{\left(n_{Total}\right)_t} \tag{3.28}$$

where CPSDO is defined as cumulative oversize particle distribution and CPSD is cumulative particle size distribution or cumulative undersize particle distribution which is commonly used. Particle size distribution analysis can not be used directly to compare two different solutions resulting from uniform and non-uniform discretized modeling studies due to the different size classes and number of variables (this will be discussed in later section of this study).

Using the improved discretized population balance model of Eq. (3.21) or (3.27) with initially monodisperse modeling conditions of $\alpha = 0.1$, $K_B = 0.0$, $\dot{\gamma} = 20$ (1/s) and a theoretical elapsed time of 30 min, produces the results of fractal dimension influences on orthokinetic PBM. Further, these results were compared with the exact solution from uniform discretized (continuous) PBM of Eq. (3.13) (see Figs. 3.1 to 3.3). From Figs. 3.1 to 3.3, it was found that as the q value was decreased, solution accuracy was increased for all fractal dimension cases. That is, at a lower q value, the improved discretized model approaches the uniform discretized (continuous) as expected. As fractal dimension decreased from 3.0 to 2.0, smaller q values should be used to obtain a higher accuracy population balance model. Although it is interesting that fractal dimension may not be constant during coagulation (Jung et al. 1996; Kostoglou and Konstandopoulos 2001; Chakraborti et al. 2003), variable fractal dimension is beyond the scope of this study. Furthermore, a mass conservation factor (MCF) concept was used for evaluating the model numerical stability and is given as,

$$\left(\mathrm{MCF}\right)_t = \frac{\sum_{j=1}^{\max} j\left(\mathrm{n}_j\right)_t}{\left(\mathrm{n}_1\right)_{t=0}} \tag{3.29}$$

In the stability tests, all modeling results generated perfect mass conservation during the theoretical coagulation time of 30 min (not displayed in this study).

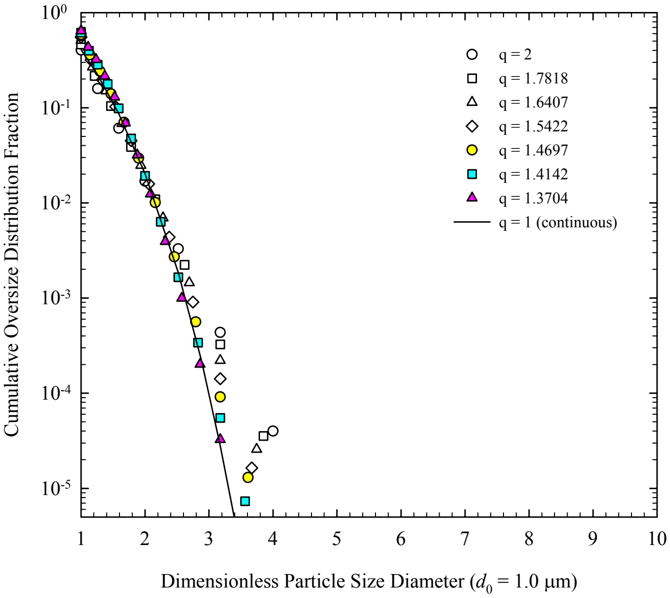

Figure 3.1 Cumulative oversize distribution for fractal agglomeration ($D_f = 3.0$)

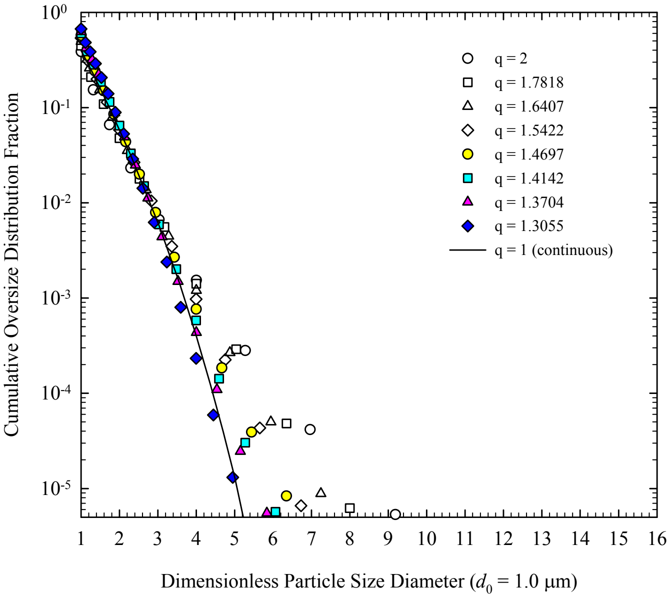

Figure 3.2 Cumulative oversize distribution for fractal agglomeration (D_f =2.5)

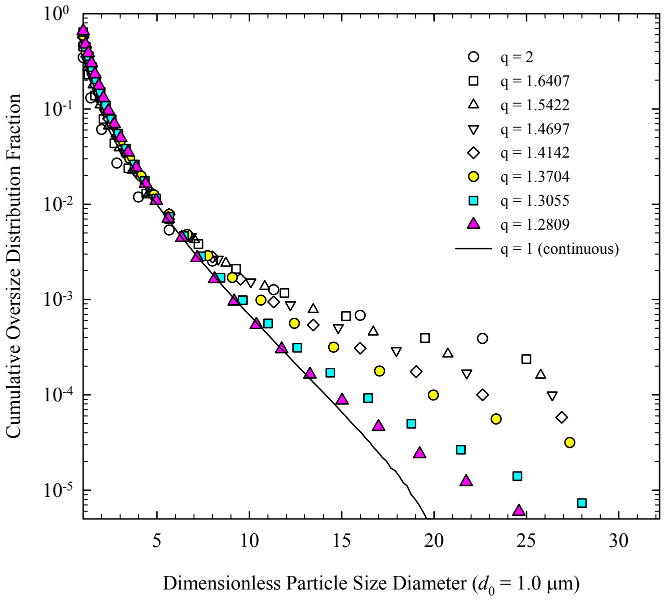

Figure 3.3 Cumulative oversize distribution for fractal agglomeration (D_f =2.0)

3.4.3 Orthokinetic Coagulation of Fractal Agglomeration

Incorporating Eqs. (3.11) and (3.22) into Eq. (3.18), produces an orthokinetic coagulation model for fractal particle aggregation and breakup (Eq. (3.21) or (3.27)). Thus, this fractal aggregation and breakup equation can predict the effects of the ratio of collision efficiency (α) to breakup coefficient (K_B) as well as fractal dimension on the behavior of particle coagulation. The improved orthokinetic fractal aggregate coagulation model (given by Eq. (3.21) or (3.27)) having a fractal dimension (D_f) of 2.5, a random break-up kernel with breakup parameters of b = 1, s = 3, and η = 2 (Kramer and Clark 1999) in a laminar flow field (strain-rate $\dot{\gamma}$ of 20 $\sec^{-1}$) was adopted for the initially monodisperse simulations during a theoretical elapsed time of 30 (min) and the results are displayed in Figs. 3.4 to 3.9.

In Fig. 3.4, the results from the orthokinetic coagulation of fractal aggregates are represented by the particle size distribution. Unfortunately, particle size distribution analysis is not applicable to compare directly two identical solutions resulting from non-uniform discretized and uniform discretized (continuous) models due to the different class size intervals or the number of variables. That is, due to the different class size intervals, it is impossible to compare two different results from a non-uniform discretized model to uniform discretized model by putting these two methods together on the same particle size distribution graph. Thus, an alternative comparison method should be developed. As shown in Fig. 3.5, for various ratios of aggregation to breakup (α/K_B of 0.1 to 10.0), the cumulative oversize particle distribution curves can be used as a direct comparison method. After converting the particle size distribution data (see Fig. 3.4) to a cumulative oversize particle distribution (see Fig. 3.5), it is possible to compare a set of solutions resulting from various size class intervals consisting of the improved discretized model (Eq. (3.21) or (3.27)) and the uniform discretized (continuous) model (Eq. (3.13)) (see Figs. 3.6 to 3.9). Further, the results for large size classes produce important information about particle evolution patterns during the experience of aggregation and breakup (Kramer and Clark 1999). Although, cumulative undersize particle distribution has been commonly used as one of the coagulation results analysis tools, this curve often fails to obtain valuable information of the large size class solutions.

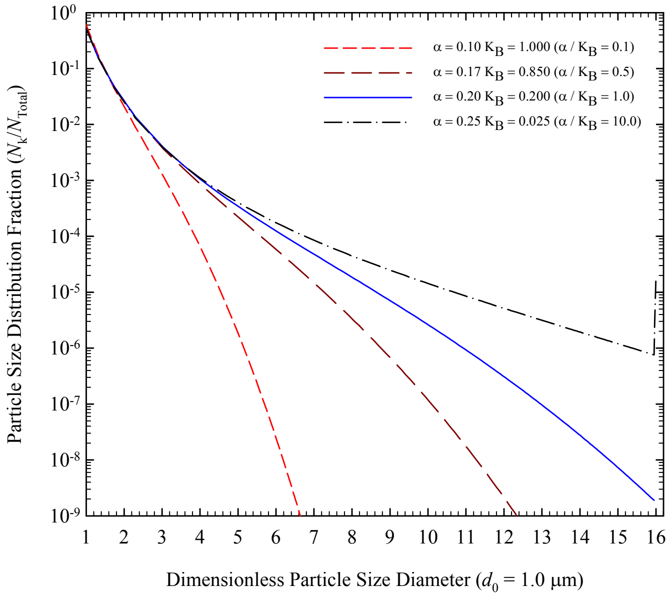

Figure 3.4 Particle size distributions for fractal agglomeration (D_f 2.5) using the continuous orthokinetic coagulation model

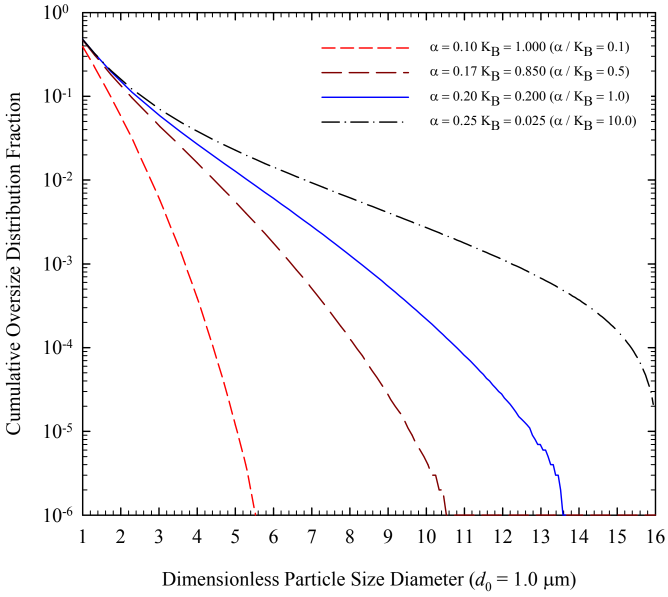

Figure 3.5 Cumulative oversize particle distribution for fractal agglomeration (D_f 2.5) using the continuous orthokinetic coagulation model

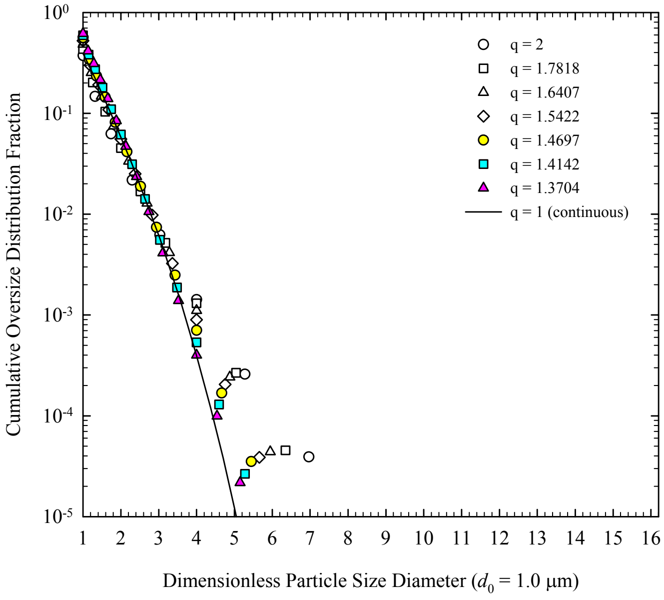

Figure 3.6 Cumulative oversize distribution for fractal agglomeration (D_f 2.5) using the orthokinetic coagulation; $\alpha/K_B = 0.1$

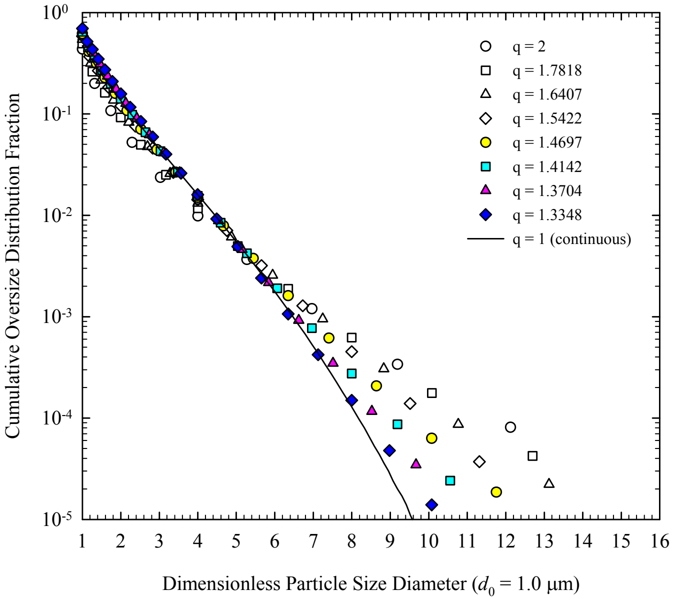

Figure 3.7 Cumulative oversize distribution for fractal agglomeration (D_f 2.5) using the orthokinetic coagulation; $\alpha/K_B = 0.5$

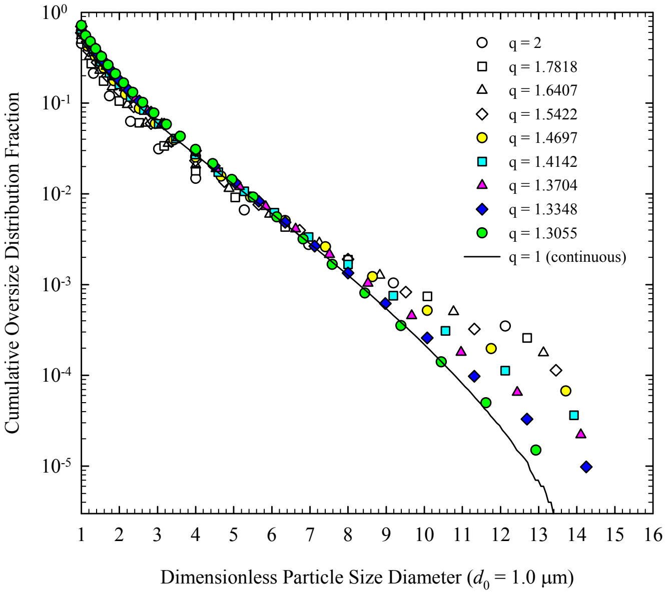

Figure 3.8 Cumulative oversize distribution for fractal agglomeration (D_f 2.5) using the orthokinetic coagulation; $\alpha/K_B = 1.0$

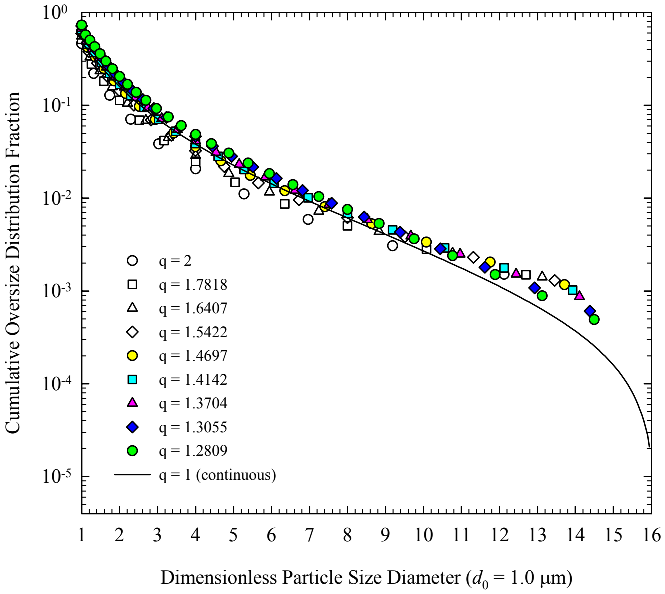

Figure 3.9 Cumulative oversize distribution for fractal agglomeration (D_f 2.5) using the orthokinetic coagulation; $\alpha/K_B = 10.0$

From Figs. 3.6 to 3.9, as *q* value is decreased, the improved discretized coagulation model approaches uniform discretized (continuous) model. Further, it was found that as the ratio of α/K_B changed from 0.1 to 10.0, a smaller value of geometric size interval (*q*) was required to achieve higher numerical accuracy, especially for larger size class solutions. That is, when the ratio of α/K_B increased, larger particles could exist due to the higher influence of aggregation which would overshadow aggregate breakup. In addition, perfect mass conservation was achieved throughout all of the modeling results during the theoretical coagulation time (not displayed in this study).

3.4.4 Computational Efficiency of Improved Orthokinetic Coagulation Model

In examining the computational efficiency, the continuous PBM (Eq. (3.13)) and two adjustable geometric size interval (q = 2.000 and 1.2089) of the discretized PBM (Eq. (3.21)) were used and these results are displayed in Table 1 and Fig. 10 in terms of the CPU time. All of the computations were conducted using the same conditions for orthokinetic coagulation including aggregation and breakup modeling (a monodisperse initial condition, an orthokinetic kernel, a random breakup kernel, $n_0 = 1.0\times10^8$ no/cm^3, $\alpha = 0.2$, $K_B = 0.2$, $\dot{\gamma} = 20$ sec^{-1}, $d_0 = 1.0$ μm, $D_f = 3.0 \sim 2.0$, elapsed time = 1800 sec) using the computer hardware of a 2.4 GHz Pentium IV CPU having 1.0 GB of memory.

Comparing CPU time, the improved discretized PBM has a much higher computational efficiency than the continuous model. Further, as expected, CPU time is inversely proportional to the magnitude of both *q* value (ranging 2.0 to 1.0) and the fractal dimension (ranging 3.0 to 2.0). For example, an improved discretized population balance model having *q* value of 1.2809 has approximately 1,000 and 5,000 times greater computational efficiency than the continuous population balance model for a fractal dimension of 3.0 and 2.0, respectively.

Table 3.1 Computational Efficiency Comparisons for Orthokinetic Coagulation

PBE Models	Fractal Dimension (D_f)	CPU time (sec)
Improved Discrete Model	3.0	1.5625×10^{-2}
(*q* = 2.000, *k* = 11)	2.5	2.8815×10^{-2}
	2.0	3.1250×10^{-2}
Improved Discrete Model	3.0	1.719×10^{-1}
(*q* = 1.2809, *k* = 29)	2.5	2.031×10^{-1}
	2.0	2.188×10^{-1}
Uniform Discrete Model	3.0	3.484×10^{2}
(*q* = 1.0000, *k* = 1024)	2.5	1.253×10^{3}
	2.0	1.440×10^{4}

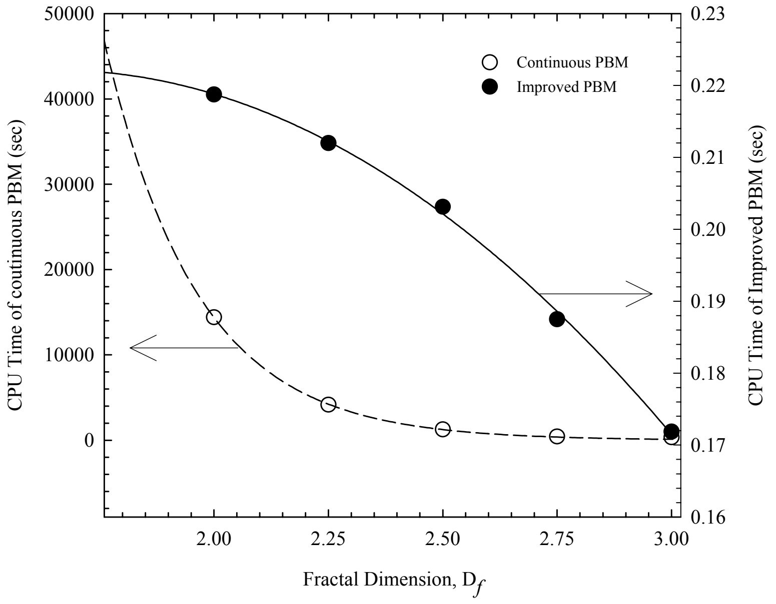

Figure 3.10 The relationship between fractal dimension and CPU time for continuous PBM and improved discretized PBM (*q* = 1.2809)

Computational efficiency is a direct relationship to the number of size intervals or the number of variables. As shown in Table 1, the discretized model, having the reduced number of size intervals (i.e., q = 1.2809), has only 29 size intervals or variables resulting in the lower number of steps and subroutine calls which greatly reduce computational time. Otherwise, there are 1024 size intervals considered for the continuous model (q = 1) having 1024 size intervals or variables. It may be impossible to use the continuous model (Eq. (3.13)) when coupled with CFD using fractal agglomeration. These results indicate that the discretized population balance equations developed in this study can be used in coupling coagulation population balance equation (PBE) with computational fluid dynamics (CFD) due to the low computational time required.

3.5 Conclusions

For the purpose of fractal aggregate coagulation modeling, the authors improved the discretized population balance equations having an aggregation and breakup kernel. After direct numerical simulation, the accuracy of this model was verified using the lowered geometric size interval (q), where q is a volume ratio of class $k+1$ particle to class k particle ($q = \upsilon_{k+1} / \upsilon_k$). Perfect mass conservation was achieved in all modeling cases. The proposed model was converted to a dimensionless orthokinetic coagulation form including an aggregation and breakup kernel to enhance computational efficiency. Furthermore, the authors attempted to find an optimum graphical method for representing the two different results (discretized and continuous populations) on an identical 2D plane and found that the cumulative oversize particle distribution is convenient to compare these results due to different aggregate class size scales.

As a result, this proposed discretized population balance equation can be used for fractal aggregate orthokinetic coagulation model on the basis of numerical accuracy, stability, and computational efficiency.

CHAPTER IV

ADJUSTABLE DISCRETIZED POPULATION BALANCE EQUATIONS: NUMERICAL SIMULATION AND PARAMETER ESTIMATION FOR FRACTAL AGGREGATION AND BREAK-UP

4.1 Overview

Improved adjustable discretized population balance equations (PBEs) are proposed in this study. The authors extended an improved particle coagulation model previously developed to an adjustable geometric size interval (*q*), where *q* is a volume ratio of class *k+1* particle to class *k* particle ($\upsilon_{k+1}/\upsilon_k = q$). This model was verified with the time derivative of the zero and first moments to show mass conservation and compared with previous analytical and numerical solutions. Also, the self-preserving distribution test was conducted by using size-independent and size-dependent kernels. After direct numerical simulations (DNS), the proposed model was found to have excellent agreement with the analytical and continuous numerical solutions. In addition, this proposed model was converted to a dimensionless form to enhance computational efficiency in order to be coupled with computational fluid dynamic solutions in the future. Furthermore, a parameter estimation scheme was created to computationally determine the two key parameters, the collision efficiency (α) and the break-up coefficient (K_B), from orthokinetic experimental data. This parameter estimation scheme was able to compute the coefficients in the coagulation model rapidly, especially in particle systems having a fractal aggregate structure. In addition, the authors attempted to find an optimum graphical method for representing the two different results (non-uniform discretized and continuous populations) on an identical 2D plane and the results indicate that the particle cumulative population distribution curve is convenient to compare these results due to different aggregate class size scales. Using the reproduction of a continuous distribution from discrete data, it was concluded that this method has close agreement between non-uniform discretized and continuous data.

4.2 Introduction

Coagulation is the growth of small particles (i.e. droplets, bubbles, or solid particles) into larger aggregates by the collision-inducing mechanisms: orthokinetic, perikinetic, and differential sedimentation. For droplet or bubble coalescence, the agglomeration between particles of volume υ and w has been described by a continuous nonlinear integro-partial-differential equation as (Drake 1972; Ramkrishna 1985),

$$\frac{\mathrm{dn}(\upsilon,\mathrm{t})}{\mathrm{dt}} = \frac{1}{2}\int_0^{\upsilon} \alpha\beta\left(\upsilon - w, w\right)\mathrm{n}(\upsilon - w,\mathrm{t})\mathrm{n}(w,\mathrm{t})\mathrm{d}w - \int_0^{\infty} \alpha\beta\left(\upsilon, w\right)\mathrm{n}(\upsilon,\mathrm{t})\mathrm{n}(w,\mathrm{t})\mathrm{d}w \quad (4.1)$$

where, α is the collision efficiency, β is the collision frequency or kernel, n is the particle concentration, and t is time. Although numerous studies have attempted to solve the classical coalescence equation (Eq. (4.1)), it is impossible to compute an exact analytical solution. Only limited analytical solutions exist with the assumptions of monodisperse initial conditions and simplified collision kernels (β). A numerical scheme converting the continuous particle size distribution into discretized particle-size domains (a histogram) is a useful approach to the solution of Eq. (4.1). Coagulation of droplets or bubbles is often treated as the coalescence of a continuous distribution, while the agglomeration of solid particles is discrete. Smoluchowski derived a uniform discrete population balance equation (Eq. (4.2)) for the coagulation of discrete particles having the class size interval value of 1 ($\upsilon_{k+1}/\upsilon_k = 1$) and this equation has been used extensively in modeling agglomeration (Smoluchowski 1917),

$$\left[\frac{\mathrm{dn}_k}{\mathrm{dt}}\right]_{\mathrm{Agg}} = \frac{1}{2}\sum_{i+j=k} \alpha\beta(\mathrm{r}_i,\mathrm{r}_j)\mathrm{n}_i\mathrm{n}_j - \sum_{l=1}^{\infty}\alpha\beta(\mathrm{r}_l,\mathrm{r}_k)\mathrm{n}_l\mathrm{n}_k \tag{4.2}$$

where r is the particle or agglomerate size, and *i*, *j*, *k*, and *l* refer to particle size class indices. To obtain a numerical solution of Eq. (4.2), extensive computation time is required for a realistic range of particle sizes. Thus, to overcome this computational non-efficiency of the uniform discrete model (Eq. (4.2)), various non-uniform discrete schemes ($\upsilon_{k+1}/\upsilon_k = q$, where q is greater than 1) have been introduced (Gelbard and Seinfeld 1978; Gelbard et al. 1980; Batterham et al. 1981; Hounslow et al. 1988; Marchal et al. 1988; Litster et al. 1995; Hill and Ng 1996; Kumar and Ramkrishna 1996a). Gelbard et al. developed a sectional balance method that could predict the total particle number or volume (Gelbard and Seinfeld 1978; Gelbard et al. 1980). Batterham et al. proposed a non-uniform discretized population balance equation having class size intervals or geometric-size intervals of 2 ($\upsilon_{k+1}/\upsilon_k = 2$), and the Batterham model scheme has half the number of products formed added to each possible class size interval (Batterham et al. 1981). Hounslow et al. improved the Batterham model using the concept that the scheme of arbitrarily dividing agglomerates between size classes incorrectly predicts coagulation rate (Hounslow et al. 1988). The model of Hounslow et al. (geometric-size interval of 2) differs from the Batterham model by considering continuous intervals rather than discrete boundaries (Hounslow et al. 1988). Marchal et al. improved the agglomeration model between class size intervals by assuming that coagulation behaves as a chemical reaction between species using the concept that stoichiometric coefficients of those chemical species should be adjusted to preserve mass (Marchal et al. 1988). Litster et al. extended the model of Hounslow el al. (Hounslow et al. 1988) to improve accuracy using an adjustable geometric size interval scheme given as $\upsilon_{k+1}/\upsilon_k = 2^{1/p}$ with arbitrary p values (Litster et al. 1995). In the case of a p value equal to 1, the Litster model is equivalent to the Hounslow model. Hill and Ng produced an improved population balance equation based on probability density functions for the particle population contributions in each interval k (Hill and Ng 1996). To account for the possibility of products from the collisions of two intervals producing aggregates that may fall into two larger size intervals, probability distributions are assumed. Kumar and Ramkrishna developed an overall coagulation modeling technique consisting of agglomeration and break-up using the fixed pivot method by adopting arbitrary size class grids (Kumar and Ramkrishna 1996a). Moreover, Kumar and Ramkrishna extended the fixed pivot scheme to a moving pivot technique (Kumar and Ramkrishna 1996b). The adjustable sectional method with arbitrary class size refinement capability has been examined by several researchers (Gelbard et al. 1980; Marchal et al. 1988; Kumar and Ramkrishna 1996a; Vanni 2000). Often modeling requires a much finer discretized class size interval to accurately predict real particle systems. For example, experimental devices to measure particle size distributions can obtain measurements with a greater resolution than the non-uniform discretization used by agglomeration modeling with class size interval ratio q of 2 (i.e. the Batterham and Houslow models). Furthermore, for a large class size range, the class size resolution is too broad to obtain high accuracy at the larger size class intervals. That is, between the class size of n = 1024 and n = 2048, there is only one class size interval in the non-uniform model with a q of 2, however, 1024 class size intervals exist in the continuous or uniform discrete model. Thus, to obtain higher coagulation modeling accuracy, especially when large size aggregates exist, the adjustable sectional method with arbitrary class size refinement capacity should be applied.

In this study, the authors extend an improved particle coagulation model (Kim and Kramer 2005) having particle size dependent agglomeration and break-up kernels with the addition of an adjustable geometric size interval (q), where q is a volume ratio of class $k+1$ particle to class k particle ($q = \upsilon_{k+1} / \upsilon_k$). This improved coagulation model overcomes the two limitations mentioned earlier; the large number of variable domain sizes for the uniform discrete model and the poor resolution at larger aggregate size classes for the non-uniform discrete model with a fixed class size interval. The improved adjustable discretized model was also expressed in a dimensionless form to enhance computational efficiency (CPU time). Further, the particle size distribution prediction from the results of the non-uniform discretized model to that of uniform discrete model to obtain continuous particle size distributions were rigorously compared.

The new model was verified with the time derivative of the zero and first moment methods and compared to previously obtained analytical and numerical solutions. Also, the self-preserving distribution test was conducted by using size-independent and size-dependent coagulation rate kernels. Furthermore, two key parameters in the new model, the collision efficiency (α) and break-up coefficient (K_B), were calculated from experimental data using a parameter estimation scheme.

4.3 Background

4.3.1 Adjustable Discretized Population Balance

Hill and Ng produced a discretized population balance equation based on probability density functions in each interval *k* for agglomeration (Hill and Ng 1996) and break-up (Hill and Ng 1995). The agglomeration rate equation of Hill and Ng can be expressed as,

$$\begin{aligned}\left[\frac{\mathrm{dn}_k}{\mathrm{dt}}\right]_{\mathrm{Agg}} &= \sum_{j=1}^{k-2} \alpha\beta(\mathrm{r}_{k-1},\mathrm{r}_j)\left(\frac{\overline{\upsilon}_j}{\overline{\upsilon}_k-\overline{\upsilon}_{k-1}}\right)\mathrm{n}_{k-1}\mathrm{n}_j + \sum_{j=1}^{k-1} \alpha\beta(\mathrm{r}_k,\mathrm{r}_j)\left(\frac{\overline{\upsilon}_{k+1}-\overline{\upsilon}_k-\overline{\upsilon}_j}{\overline{\upsilon}_{k+1}-\overline{\upsilon}_k}\right)\mathrm{n}_k\mathrm{n}_j \\ &+ \frac{1}{2}\alpha\beta(\mathrm{r}_{k-1},\mathrm{r}_{k-1})\left(\frac{\overline{\upsilon}_{k-1}}{\overline{\upsilon}_k-\overline{\upsilon}_{k-1}}\right)(\mathrm{n}_{k-1})^2 + \frac{1}{2}\alpha\beta(\mathrm{r}_k,\mathrm{r}_k)\left(\frac{\overline{\upsilon}_{k+1}-2\overline{\upsilon}_k}{\overline{\upsilon}_{k+1}-\overline{\upsilon}_k}\right)(\mathrm{n}_k)^2 - \sum_{i=1}^{\max} \alpha\beta(\mathrm{r}_i,\mathrm{r}_k)\mathrm{n}_i\mathrm{n}_k\end{aligned} \tag{4.3}$$

where, the over bar ($\overline{\upsilon}$) represents the particle volume removed from an interval and the probability functions expressed by the four functions of $\overline{\upsilon}$ on the right hand side of Eq. (4.3). However, it is not possible to know the volume or number of particles removed from a discrete interval or contributed to the larger intervals *a priori* during each iteration. A possible solution is to equate the probability density functions in terms of the volume ranges of each interval. Thus, the probability that a collision pair will fall into a given size class range increases as the range of the interval increases. For the interval scheme of $\upsilon_{k+1} = 2\upsilon_k$, using an average volume concept of $\overline{\upsilon}_k = 0.5(\upsilon_k + \upsilon_{k-1})$ and the definition of $\upsilon_k \propto (r_k)^3$, Eq. (4.3) can be modified in terms of the particle radii as,

$$\begin{aligned}\left[\frac{\mathrm{dn}_k}{\mathrm{dt}}\right]_{\mathrm{Agg}} &= \sum_{j=1}^{k-2} \alpha\beta(\mathrm{r}_{k-1}, \mathrm{r}_j)\left(\frac{2\mathrm{r}_j}{\mathrm{r}_k}\right)^3 \mathrm{n}_{k-1}\mathrm{n}_j + \sum_{j=1}^{k-1} \alpha\beta(\mathrm{r}_k, \mathrm{r}_j)\left(\frac{\mathrm{r}_k{}^3 - \mathrm{r}_j{}^3}{\mathrm{r}_k{}^3}\right)\mathrm{n}_k\mathrm{n}_j \\ &+ \frac{1}{2}\alpha\beta(\mathrm{r}_{k-1}, \mathrm{r}_{k-1})(\mathrm{n}_{k-1})^2 - \sum_{i=1}^{\max} \alpha\beta(\mathrm{r}_i, \mathrm{r}_k)\mathrm{n}_i\mathrm{n}_k\end{aligned} \tag{4.4}$$

Furthermore, to apply Eq. (4.4) into fractal aggregate coagulation, it must be assumed that the probability functions are proportional to aggregate size having an exponent of a fractal dimension of D_f. Meakin proposed the relationship between fractal dimension and particle size as (Meakin 1988),

$$\mathrm{r}_k = \mathrm{r}_1 (k)^{1/D_f} \tag{4.5}$$

By using Meakin's relationship between fractal dimension (D_f) and the radius (r_k) of a size class k aggregate (composed of k primary particles of radius r_1), the particle aggregation probability functions can be developed as,

$$\frac{2\mathrm{r}_j^3}{\mathrm{r}_k^3} = \frac{2\left(\mathrm{r}_1 (j)^{1/D_f}\right)^3}{\left(\mathrm{r}_1 (k)^{1/D_f}\right)^3} = \frac{2(j)^{3/D_f}}{(k)^{3/D_f}} = 2\left(\frac{j}{k}\right)^{3/D_f} \tag{4.6}$$

and

$$\frac{\mathrm{r}_k{}^3 - \mathrm{r}_j{}^3}{\mathrm{r}_k{}^3} = 1 - \frac{\mathrm{r}_j{}^3}{\mathrm{r}_k{}^3} = 1 - \frac{\left(\mathrm{r}_1 (j)^{1/D_f}\right)^3}{\left(\mathrm{r}_1 (k)^{1/D_f}\right)^3} = 1 - \frac{(j)^{3/D_f}}{(k)^{3/D_f}} = 1 - \left(\frac{j}{k}\right)^{3/D_f} \tag{4.7}$$

Further, when the fractal dimension value is 3, these probability functions can be replaced as,

$$\frac{2\mathrm{r}_j^{\,3}}{\mathrm{r}_k^{\,3}} = 2\left(\frac{j}{k}\right) \tag{4.8}$$

and

$$\frac{\mathrm{r}_k^{\,3} - \mathrm{r}_j^{\,3}}{\mathrm{r}_k^{\,3}} = 1 - \left(\frac{j}{k}\right) \tag{4.9}$$

Otherwise, applying the aggregate volume conservation scheme of Eq. (4.10) into new probability functions, the new probability functions can be rewritten as,

$$\upsilon_k = 2^{k-1} \cdot \upsilon_1 \tag{4.10}$$

$$\frac{2\mathrm{r}_j^{\,3}}{\mathrm{r}_k^{\,3}} = \frac{2\upsilon_j}{\upsilon_k} = \frac{2(2^{j-1} \cdot \upsilon_1)}{(2^{k-1} \cdot \upsilon_1)} = 2^{j-k+1} \tag{4.11}$$

and

$$\frac{\mathrm{r}_k^{\,3} - \mathrm{r}_j^{\,3}}{\mathrm{r}_k^{\,3}} = \frac{\upsilon_k - \upsilon_j}{\upsilon_k} = 1 - \frac{\upsilon_j}{\upsilon_k} = 1 - \frac{(2^{j-1} \cdot \upsilon_1)}{(2^{k-1} \cdot \upsilon_1)} = 1 - 2^{j-k} \tag{4.12}$$

As shown in the two sets of new probability functions (Eqs. (4.8)/(4.9) and (4.11)/(4.12)), two unique probability functions could be obtained. Thus, using the two unique probability functions, Eq. (4.4) can be modified when the fractal dimension value is 3, as

$$\begin{aligned}\left[\frac{d\mathrm{n}_k}{dt}\right]_{\mathrm{Agg}} &= \sum_{j=1}^{k-2} \alpha\beta(\mathrm{r}_{k-1}, \mathrm{r}_j)\left(2\frac{j}{k}\right)\mathrm{n}_{k-1}\mathrm{n}_j + \sum_{j=1}^{k-1} \alpha\beta(\mathrm{r}_k, \mathrm{r}_j)\left(1 - \left(\frac{j}{k}\right)\right)\mathrm{n}_k\mathrm{n}_j \\ &+ \frac{1}{2}\alpha\beta(\mathrm{r}_{k-1}, \mathrm{r}_{k-1})(\mathrm{n}_{k-1})^2 - \sum_{i=1}^{\max} \alpha\beta(\mathrm{r}_i, \mathrm{r}_k)\mathrm{n}_i\mathrm{n}_k\end{aligned} \tag{4.13}$$

or

$$\begin{aligned}\left[\frac{d\mathrm{n}_k}{dt}\right]_{\mathrm{Agg}} &= \sum_{j=1}^{k-2} \alpha\beta(\mathrm{r}_{k-1}, \mathrm{r}_j)(2^{j-k+1})\mathrm{n}_{k-1}\mathrm{n}_j + \sum_{j=1}^{k-1} \alpha\beta(\mathrm{r}_k, \mathrm{r}_j)\left(1 - 2^{j-k}\right)\mathrm{n}_k\mathrm{n}_j \\ &+ \frac{1}{2}\alpha\beta(\mathrm{r}_{k-1}, \mathrm{r}_{k-1})(\mathrm{n}_{k-1})^2 - \sum_{i=1}^{\max} \alpha\beta(\mathrm{r}_i, \mathrm{r}_k)\mathrm{n}_i\mathrm{n}_k\end{aligned} \tag{4.14}$$

Comparing Eq. (4.14) to the Hounslow's equation of Eq. (4.15) that is a conventional and popular discretized solution for population balance equations (Hounslow et al. 1988), the new probability functions proposed in this study are not the same as those of Hounslow's original model, but rather a novel approach.

$$\begin{aligned}\left[\frac{\mathrm{dn}_k}{\mathrm{dt}}\right]_{\mathrm{Agg}} &= \mathrm{n}_{k-1}\sum_{j=1}^{k-2}\alpha(2^{j-k+1})\beta(\mathrm{r}_{k-1},\mathrm{r}_j)\mathrm{n}_j + \frac{1}{2}\alpha\beta(\mathrm{r}_{k-1},\mathrm{r}_{k-1})(\mathrm{n}_{k-1})^2 \\ &\quad -\mathrm{n}_k\sum_{j=1}^{k-1}\alpha(2^{j-k})\beta(\mathrm{r}_k,\mathrm{r}_j)\mathrm{n}_j - \mathrm{n}_k\sum_{j=k}^{\max}\alpha\beta(\mathrm{r}_k,\mathrm{r}_j)\mathrm{n}_j\end{aligned} \tag{4.15}$$

Furthermore, in the application of the probability functions, it may be more convenient to apply these new probability functions into for systems with fractal aggregate coagulation. Introducing the new probability functions of Eq. (4.6) and (4.7) into improved coagulation model of Eq. (4.3) and using an adjustable interval scheme ($\upsilon_{k+1} = q\upsilon_k$) and an average volume concept ($\bar{\upsilon}_k = 0.5(\upsilon_k + \upsilon_{k-1})$), yields improved adjustable discretized population balance equations (PBEs) expressed in terms of the particle radii with volume based probabilities as,

$$\begin{aligned}\frac{\mathrm{dn}_k}{\mathrm{dt}} &= \sum_{j=1}^{k-2}\alpha\beta(\mathrm{r}_{k-1},\mathrm{r}_j)\left(\frac{q}{q-1}\right)\left(\frac{\mathrm{r}_j}{\mathrm{r}_k}\right)^{D_f}\mathrm{n}_{k-1}\mathrm{n}_j + \sum_{j=1}^{k-1}\alpha\beta(\mathrm{r}_k,\mathrm{r}_j)\left\{1-\left(\frac{1}{(q-1)}\right)\left(\frac{\mathrm{r}_j}{\mathrm{r}_k}\right)^{D_f}\right\}\mathrm{n}_k\mathrm{n}_j \\ &\quad +\frac{1}{2}\alpha\beta(\mathrm{r}_{k-1},\mathrm{r}_{k-1})\left(\frac{1}{q-1}\right)(\mathrm{n}_{k-1})^2 + \frac{1}{2}\alpha\beta(\mathrm{r}_k,\mathrm{r}_k)\left(\frac{q-2}{q-1}\right)(\mathrm{n}_k)^2 - \sum_{i=1}^{\max}\alpha\beta(\mathrm{r}_i,\mathrm{r}_k)\mathrm{n}_i\mathrm{n}_k\end{aligned} \tag{4.16}$$

or

$$\begin{aligned}\frac{\mathrm{dn}_k}{\mathrm{dt}} &= \sum_{j=1}^{k-2}\alpha\beta(\mathrm{r}_{k-1},\mathrm{r}_j)\left(\frac{q}{q-1}\right)\left(\frac{j}{k}\right)^{3/D_f}\mathrm{n}_{k-1}\mathrm{n}_j + \sum_{j=1}^{k-1}\alpha\beta(\mathrm{r}_k,\mathrm{r}_j)\left\{1-\left(\frac{1}{(q-1)}\right)\left(\frac{j}{k}\right)^{3/D_f}\right\}\mathrm{n}_k\mathrm{n}_j \\ &\quad +\frac{1}{2}\alpha\beta(\mathrm{r}_{k-1},\mathrm{r}_{k-1})\left(\frac{1}{q-1}\right)(\mathrm{n}_{k-1})^2 + \frac{1}{2}\alpha\beta(\mathrm{r}_k,\mathrm{r}_k)\left(\frac{q-2}{q-1}\right)(\mathrm{n}_k)^2 - \sum_{i=1}^{\max}\alpha\beta(\mathrm{r}_i,\mathrm{r}_k)\mathrm{n}_i\mathrm{n}_k\end{aligned} \tag{4.17}$$

4.3.2 Moment Conservation of Particle Mass with the New Agglomeration Model

The time derivative of the zero moment, corresponding to the total number of particles, can be rewritten in the discrete form of Eq. (4.18) as,

$$\frac{\mathrm{d}m_0}{\mathrm{dt}} = \sum_{k=1}^{\infty} \frac{\mathrm{dn}_k}{\mathrm{dt}} = -\frac{1}{2}\sum_{k=1}^{\infty}\sum_{j=1}^{\infty} \mathrm{A}_{k,j}\mathrm{n}_k\mathrm{n}_j \tag{4.18}$$

where, $\mathrm{A}_{k,j}$ represents the agglomeration rate coefficient which is the product of α and $\beta(\mathrm{r}_k, \mathrm{r}_j)$. Substituting Eq. (4.16) into Eq. (4.18), produces Eq. (4.19) consisting of terms (4.19.1) through (4.19.5),

$$\frac{\mathrm{d}m_0}{\mathrm{dt}} = \sum_{k}^{\infty} \frac{\mathrm{dn_k}}{\mathrm{dt}} = \sum_{k}^{\infty} \left\{ \begin{array}{ll} \displaystyle\sum_{j=1}^{k-1} \mathrm{A}_{k,j} \left(\frac{q}{q-1}\right)\left(\frac{\mathrm{r}_j}{\mathrm{r}_k}\right)^{D_f} \mathrm{n}_k\mathrm{n}_j & (4.19.1) \\ \displaystyle +\sum_{j=1}^{k-1} \mathrm{A}_{k,j} \left\{1-\left(\frac{1}{(q-1)}\right)\left(\frac{\mathrm{r}_j}{\mathrm{r}_k}\right)^{D_f}\right\} \mathrm{n}_k\mathrm{n}_j & (4.19.2) \\ \displaystyle +\frac{1}{2}\mathrm{A}_{k,k}\left(\frac{1}{q-1}\right)(\mathrm{n}_k)^2 & (4.19.3) \\ \displaystyle +\frac{1}{2}\mathrm{A}_{k,k}\left(\frac{q-2}{q-1}\right)(\mathrm{n}_k)^2 & (4.19.4) \\ \displaystyle -\sum_{j=1}^{\infty} \mathrm{A}_{k,j}\mathrm{n}_k\mathrm{n}_j & (4.19.5) \end{array} \right. \tag{4.19}$$

where (4.19.1) + (4.19.2) yields,

$$\sum_{j=1}^{k-1} \mathrm{A}_{k,j}\left\{1+\left(\frac{\mathrm{r}_j}{\mathrm{r}_k}\right)^{D_f}\right\}\mathrm{n}_k\mathrm{n}_j = \sum_{j=1}^{k-1} \mathrm{A}_{k,j}\mathrm{n}_k\mathrm{n}_j + \sum_{j=1}^{k-1} \mathrm{A}_{k,j}\left(\frac{j}{k}\right)^{3/D_f} \mathrm{n}_k\mathrm{n}_j \tag{4.20}$$

and adding terms (4.19.3) and (4.19.4), obtains

$$\text{Eq. (4.19.3)} + \text{Eq. (4.19.4)} = \frac{1}{2}\mathrm{A}_{k,k}(\mathrm{n}_k)^2 \tag{4.21}$$

The terms of Eq. (4.19.5) can be rewritten as,

$$\text{Eq. (4.19.5)} = -\sum_{j=k}^{\infty} \mathrm{A}_{k,j}\mathrm{n}_k\mathrm{n}_j - \sum_{j=1}^{k-1} \mathrm{A}_{k,j}\mathrm{n}_k\mathrm{n}_j \tag{4.22}$$

and after adding all terms into Eq. (4.19), the time derivative of the zero moment is obtained as,

$$\frac{\mathrm{d}m_0}{\mathrm{dt}} = \sum_{k}^{\infty}\left\{\sum_{k=1}^{\infty}\frac{1}{2}\mathrm{A}_{k,k}(\mathrm{n}_k)^2 + \sum_{j=1}^{k-1}\mathrm{A}_{k,j}\left(\frac{\mathrm{r}_j}{\mathrm{r}_k}\right)^{D_f}\mathrm{n}_k\mathrm{n}_j - \sum_{j=k}^{\infty}\mathrm{A}_{k,j}\mathrm{n}_k\mathrm{n}_j\right\} \tag{4.23}$$

For the condition where $\mathrm{r}_j = \mathrm{r}_k$, then Eq. (4.23) can be rewritten as,

$$\frac{\mathrm{d}m_0}{\mathrm{dt}} = \sum_{k}^{\infty}\left\{\sum_{k=1}^{\infty}\frac{1}{2}\mathrm{A}_{k,k}(\mathrm{n}_k)^2 - \sum_{j=1}^{\infty}\mathrm{A}_{k,j}\mathrm{n}_k\mathrm{n}_j\right\} \tag{4.24}$$

and, the time derivative of the zero moment is,

$$\begin{aligned}
\frac{\mathrm{d}m_0}{\mathrm{dt}} = \sum_{k}^{\infty}\frac{\mathrm{dn_k}}{\mathrm{dt}} &= \sum_{k=1}^{\infty}\left(\frac{1}{2}\mathrm{A}_{k,k}(\mathrm{n}_k)^2 - \sum_{j=1}^{\infty}\mathrm{A}_{k,j}\mathrm{n}_k\mathrm{n}_j\right) \\
&= \sum_{k=1}^{\infty}\left(\frac{1}{2}\mathrm{A}_{k,k}(\mathrm{n}_k)^2 - \sum_{j=k}^{\infty}\mathrm{A}_{k,j}\mathrm{n}_k\mathrm{n}_j - \mathrm{A}_{k,k}(\mathrm{n}_k)^2\right) \\
&= \sum_{k=1}^{\infty}\left(-\frac{1}{2}\mathrm{A}_{k,k}(\mathrm{n}_k)^2 - \sum_{j=k}^{\infty}\mathrm{A}_{k,j}\mathrm{n}_k\mathrm{n}_j\right) \\
&= -\frac{1}{2}\sum_{k=1}^{\infty}\left(\mathrm{A}_{k,k}(\mathrm{n}_k)^2 + 2\sum_{j=k+1}^{\infty}\mathrm{A}_{k,j}\mathrm{n}_k\mathrm{n}_j\right) \\
&= -\frac{1}{2}\sum_{k=1}^{\infty}\sum_{j=1}^{\infty}\mathrm{A}_{k,j}\mathrm{n}_k\mathrm{n}_j
\end{aligned} \tag{4.25}$$

Thus, Eq. (4.16) can conserve particle mass.

The time derivative of the first moment, corresponding to total particle volume, can be rewritten in a discrete form of Eq. (4.26) as,

$$\frac{\mathrm{d}m_1}{\mathrm{dt}} = \sum_{k=1}^{\infty} \bar{\upsilon}_k \frac{\mathrm{dn}_k}{\mathrm{dt}} = 0 \tag{4.26}$$

Substituting Eq. (4.16) into Eq. (4.26), yields Eq. (4.27).

$$\frac{\mathrm{d}m_1}{\mathrm{dt}} = \sum_{k}^{\infty} \bar{\upsilon}_k \frac{\mathrm{dn}_k}{\mathrm{dt}} = \sum_{k}^{\infty} \bar{\upsilon}_k \left\{ \begin{array}{ll} \displaystyle\sum_{j=1}^{k-1} \mathrm{A}_{k,j} \left(\frac{q}{q-1}\right)\left(\frac{\mathrm{r}_j}{\mathrm{r}_k}\right)^{D_f} \mathrm{n}_k \mathrm{n}_j & (4.27.1) \\ \displaystyle +\sum_{j=1}^{k-1} \mathrm{A}_{k,j} \left\{1-\left(\frac{1}{(q-1)}\right)\left(\frac{\mathrm{r}_j}{\mathrm{r}_k}\right)^{D_f}\right\} \mathrm{n}_k \mathrm{n}_j & (4.27.2) \\ \displaystyle +\frac{1}{2}\mathrm{A}_{k,k}\left(\frac{1}{q-1}\right)(\mathrm{n}_k)^2 & (4.27.3) \\ \displaystyle +\frac{1}{2}\mathrm{A}_{k,k}\left(\frac{q-2}{q-1}\right)(\mathrm{n}_k)^2 & (4.27.4) \\ \displaystyle -\sum_{j=1}^{\infty} \mathrm{A}_{k,j} \mathrm{n}_k \mathrm{n}_j & (4.27.5) \end{array} \right. \tag{4.27}$$

By adding terms (4.27.1) and (4.27.2) yields,

$$\sum_{j=1}^{k-1} \mathrm{A}_{k,j} \left\{\left(\frac{\mathrm{r}_j}{\mathrm{r}_k}\right)^{D_f} + 1\right\} \mathrm{n}_k \mathrm{n}_j = \sum_{j=1}^{k-1} \mathrm{A}_{k,j} \mathrm{n}_k \mathrm{n}_j + \sum_{j=1}^{k-1} \mathrm{A}_{k,j} \left(\frac{r_j}{r_k}\right)^{D_f} \mathrm{n}_k \mathrm{n}_j \tag{4.28}$$

and by adding terms (4.27.3) to (4.27.4), produces Eq. (4.29).

$$\text{Eq. (4.27.3)} + \text{Eq. (14.27.4)} = \frac{1}{2}\mathrm{A}_{k,k}(\mathrm{n}_k)^2 \tag{4.29}$$

The terms of Eq. (4.27.5) can be rewritten as,

$$\text{Eq. (4.27.5)} = -\sum_{j=k}^{\infty} \mathrm{A}_{k,j} \mathrm{n}_k \mathrm{n}_j - \sum_{j=1}^{k-1} \mathrm{A}_{k,j} \mathrm{n}_k \mathrm{n}_j \tag{4.30}$$

and after combining all terms, Eq. (4.27) can be rewritten as

$$\frac{\mathrm{d}m_1}{\mathrm{dt}} = \sum_k^{\infty} \bar{\upsilon}_k \frac{\mathrm{dn}_k}{\mathrm{dt}} = \sum_k^{\infty} \bar{\upsilon}_k \left\{ \sum_{j=1}^{k-1} \mathrm{A}_{k,j} \left(\frac{\mathrm{r}_j}{\mathrm{r}_k} \right)^{D_f} \mathrm{n}_k \mathrm{n}_j - \sum_{j=k+1}^{\infty} \mathrm{A}_{k,j} \mathrm{n}_k \mathrm{n}_j \right\} \tag{4.31}$$

For the situation where $\mathrm{r}_j = \mathrm{r}_k$, two terms of Eq. (4.31) may be shown to be identical and Eq. (4.31) can be used for the steady-state time derivative of first moment, representing volume conservation.

$$\frac{\mathrm{d}m_1}{\mathrm{dt}} = \sum_{k=1}^{\infty} \bar{\upsilon}_k \frac{\mathrm{dn}_k}{\mathrm{dt}} = 0 \tag{4.32}$$

4.3.3 Improved Orthokinetic Coagulation Models for Fractal Aggregate

The improved adjustable discretized model having agglomeration and break-up kernels was converted to a dimensionless form to enhance computational efficiency. Fractal aggregate break-up mechanisms have also been incorporated in the agglomeration modeling phenomenon to predict phenomenon such as floc disintegration, droplet break-up, and the comminution of solid particles (Vanni 1999). Population balance equations in terms of a break-up reaction can be modeled by continuous and discrete approaches (Patil et al. 2001). The discrete aggregate break-up equation can be expressed as

$$\left[\frac{\mathrm{dn}_k}{\mathrm{dt}} \right]_{\mathrm{Break}} = \sum_{j=k+1}^{\infty} \mathrm{b}_{k,j} \mathrm{s}_j (\mathrm{n}_j)^{\eta} - \mathrm{s}_k (\mathrm{n}_k)^{\eta} \tag{4.33}$$

where, η is a break-up concentration exponent, $\mathrm{b}_{k,j}$ is the break-up distribution function, and s_k is the break-up rate coefficient. Thus, an overall population balance equation with both aggregation and break-up reactions is expressed by the summation of Eqs. (4.2) and (4.33) or,

$$\left[\frac{\mathrm{dn}_k}{\mathrm{dt}}\right]_{\mathrm{Overall}} = \frac{1}{2}\sum_{i=1}^{k-1}\alpha\beta(\mathrm{r}_i,\mathrm{r}_{k-i})\mathrm{n}_i\mathrm{n}_{k-i} - \sum_{j=1}^{\infty}\alpha\beta(\mathrm{r}_k,\mathrm{r}_j)\mathrm{n}_k\mathrm{n}_j + \sum_{j=k+1}^{\infty}\mathrm{b}_{k,j}\mathrm{s}_j(\mathrm{n}_j)^{\eta} - \mathrm{s}_k(\mathrm{n}_k)^{\eta} \quad (4.34)$$

where, the first term on the right hand side represents the rate of creation of all size class *k* aggregates from the collisions of all possible combinations of the smaller size class *i* and *j* particles. The second term on the right hand side is the loss in concentration of size class *k* particles due to growth into larger aggregates by collisions with all possible size classes. The third term is the gain to the size class *k* concentration by the fracture of larger size class aggregates. The last term on the right side is the loss of size class k aggregates due to fracture. Often, colloid aggregates pose a fractal geometry, as opposed to spherical droplets or bubbles (Kim and Kramer 2005). The break-up rate coefficient s_k and break-up distribution function $b_{k,j}$ are summarized in Table 5.1 and 5.2.

Table 4.1 The Summary of Break-Up Rate Coefficient, s_k

Expression	Reference
$s_k = K_B(\dot{\gamma})^{\mathrm{b}}(r_k)^{\mathrm{s}}$	
s = 1	Chen et al. (1990)
s = 1 b = 1.6 $K_B = 4.7\times10^{-3}$	Spicer and Pratsinis (1996a)
s = 1 b = 1.6 $K_B = 7.0\times10^{-4}$	Flesch et al. (1999)
s = 1 b = 1.89~5.62 $K_B = 2.0\times10^{-8}$~0.02	Serra and Casamitjana (1998a)
s = 3 b = 1.25	Kramer and Clark (1999)
$s_k = \left(\frac{2}{\pi}\right)^{1/2}\frac{\Delta u_{rms}}{a_k}\exp\left(-\frac{\Delta u_{critical}^2}{\Delta u_{rms}^2}\right)$	Delichatsios and Probstein (1975)
$s_k = \left(\frac{4}{15\pi}\right)^{1/2}\left(\frac{\varepsilon}{\nu}\right)^{1/2}\exp\left(-\frac{\varepsilon_{k,critcal}}{\varepsilon}\right)$	Kusters (1991)
$s_k = K_B c\left(\frac{\pi}{6}\right)^{1/3}\left(\frac{1}{\rho_p}\right)^{1/D_f}(\dot{\gamma})^{1.6}(\mathrm{mass}_k)^{1/D_f}$	Zhang and Li (2003)

Table 4.2 The Summary of Break-Up Distribution Functions, $b_{k,j}$

Expression	Reference
$b_{k,j} = c\dfrac{\upsilon_j}{\upsilon_k}$	Spicer and Pratsinis (1996a)
$b_{k,j} = \dfrac{\upsilon_j}{\upsilon_k}\displaystyle\int_{c_{i=1}}^{c_i} \dfrac{1}{\sqrt{2\pi}\log\sigma}\exp\left[-\left(\dfrac{\log(\upsilon/\upsilon_m)}{\log\sigma}\right)^2\right]d\upsilon$	Pandya and Spielman (1982) Lu and Spielman (1985)
$b_{k,j} = \dfrac{\upsilon_j}{\upsilon_k}\displaystyle\int_{c_{i=1}}^{c_i} \dfrac{1}{\sqrt{2\pi\sigma}}\exp\left[-\dfrac{(\upsilon-\upsilon_m)^2}{2\sigma^2}\right]d\upsilon$	Coulaloglou and Tavlarides (1977) Spicer and Pratsinis (1996a)
$b_{k,j} = \dfrac{ab}{3\upsilon_j}\left(\dfrac{\upsilon_k}{\upsilon_j}\right)^{(b/3)-2} + \dfrac{(1-a)c}{3\upsilon_j}\left(\dfrac{\upsilon_k}{\upsilon_j}\right)^{(c/3)-2}$	Hill and Ng (1995)
$b_{k,j} = -\dfrac{b^2}{\upsilon_j}\left(\dfrac{\upsilon_k}{\upsilon_j}\right)^{b-2}\ln\left(\dfrac{\upsilon_k}{\upsilon_j}\right)$	Hill and Ng (1995)
$b_{k,j} = \dfrac{ab}{\upsilon_j}\left(\dfrac{\upsilon_k}{\upsilon_j}\right)^{b-2} + \dfrac{(1-a)d}{\upsilon_j}\left(\dfrac{\upsilon_k}{\upsilon_j}\right)^{d-2}$	Ziff (1991)
$b_{k,j} = \dfrac{2\exp\left[-(\upsilon_k-\upsilon_j/2)^2/2\sigma^2\right]\upsilon_j}{\sqrt{2\pi}\sigma\left[\mathrm{erf}\left(\upsilon_j/(2\sqrt{2}\sigma)\right)\right]}$	Pandya and Spielman (1982)
$b_{k,j} = \dfrac{3}{2}\left(\dfrac{\upsilon_k-\upsilon_{k-1}}{\upsilon_{j-1}}\right)$	Hill and Ng (1995)
$b_{k,j} = \phi(\text{random number})$	Kramer and Clark (1999)
$b_{k,j} = \dfrac{3(q-1)}{2}\left(\dfrac{r_k}{r_j}\right)^3$	Kim and Kramer (2005)

To solve the break-up model equation of Eq. (4.33), the equation was modified by adding the adjustable interval scheme ($\upsilon_{k+1} = q\upsilon_k$) and the average volume concept ($\overline{\upsilon}_k = 0.5(\upsilon_k + \upsilon_{k-1})$) producing,

$$\left[\frac{dn_k}{dt}\right]_{\text{Break}} = \sum_{j=k+1}^{\infty}\frac{3(q-1)}{2}\left(\frac{r_j}{r_k}\right)^{D_f} s_k(n_j)^{\eta} - \frac{1}{2}s_k(n_k)^{\eta} \tag{4.35}$$

Researchers have proposed particle fragmentation (break-up) models based on five basic categories; limiting strength, strain-rate or flow stress dependence, limiting size, reaction rate, and stochastic dependence (Kramer and Clark 1999). The most common approach to aggregate break-up is the use of flow strain-rate as the primary break-up parameter (Thomas 1964; Argaman and Kaufman 1970; Parker et al. 1972; Kao and Mason 1975; Tambo and Watanabe 1979a; Lu and Spielman 1985; Ray and Hogg 1986; Sonntag and Russel 1987; Spicer and Pratsinis 1996a; Kramer and Clark 1999; Serra and Casamitjana 1999). The break-up rate coefficient, s_k can be summarized as,

$$\mathrm{s}_k = \mathrm{K_B}(\dot{\gamma})^{\mathrm{b}}(\mathrm{r}_k)^{\mathrm{s}} \tag{4.36}$$

where $\mathrm{K_B}$ is the break-up rate constant (the reversible coagulation rate), b is a break-up rate exponent, s is an aggregate size exponent, and $\dot{\gamma}$ is the fluid strain-rate (non-rotational velocity gradient). Equation (4.36) indicates that the break-up coefficient is a function of fluid strain-rate resulting from energy input and the geometric properties of the aggregate (i.e., size, area, or volume). As populations of the aggregates are exposed to increasing levels of fluid strain-rate (or stress), thus it is expected that increasing amounts of break-up will be seen. Adding Eq. (4.36) into Eq. (4.35), yields an improved break-up kinetic model as,

$$\left[\frac{\mathrm{dn}_k}{\mathrm{dt}}\right]_{\mathrm{Break}} = \sum_{j=k+1}^{\infty} \frac{3(q-1)}{2}\left(\frac{\mathrm{r}_j}{\mathrm{r}_k}\right)^{D_f} \mathrm{K_B}(\dot{\gamma})^{\mathrm{b}}(\mathrm{r}_j)^{\mathrm{s}}(\mathrm{n}_j)^{\eta} - \frac{1}{2}\mathrm{K_B}(\dot{\gamma})^{\mathrm{b}}(\mathrm{r}_k)^{\mathrm{s}}(\mathrm{n}_k)^{\eta} \tag{4.37}$$

Further, a general expression for the break-up kinetics can be described using a random break-up distribution function, $\phi(j)$ (Kramer and Clark 1999):

$$\left[\frac{\mathrm{dn}_k}{\mathrm{dt}}\right]_{\mathrm{Break}} = \sum_{j=k+1}^{\infty} \phi(j)\mathrm{K_B}(\dot{\gamma})^{\mathrm{b}}(\mathrm{r}_j)^{\mathrm{s}}(\mathrm{n}_j)^{\eta} - \mathrm{K_B}(\dot{\gamma})^{\mathrm{b}}(\mathrm{r}_k)^{\mathrm{s}}(\mathrm{n}_k)^{\eta} \tag{4.38}$$

In a straightforward manner, a final coagulation kinetic model can be obtained from the combination of agglomeration of Eq. (4.16) and break-up (Eq. (4.37) or (4.38)), yielding an overall population balance equation.

Kramer and Clark rigorously analyzed the coalescencing particle collisions created by a laminar shear flow in orthokinetic coagulation (Kramer and Clark 1997) and found $\beta(\mathrm{r}_i, \mathrm{r}_j)$ to be,

$$\beta(\mathrm{r}_i, \mathrm{r}_j) = \frac{4}{3}\pi\dot{\gamma}(\mathrm{r}_i + \mathrm{r}_j)^3 \tag{4.39}$$

By assuming Eqs. (4.16) and (4.37) or (4.38) to be additive, the overall coagulation rate equation having the fractal aggregate applicability of Eq. (4.5) and an orthokinetic coagulation kernel of Eq. (4.39) becomes,

$$\begin{aligned}
\left[\frac{\mathrm{dn}_k}{\mathrm{dt}}\right] = & \sum_{j=1}^{k-2} \alpha\left(\frac{4\pi}{3}\dot{\gamma}(\mathrm{r}_{k\text{-}1} + \mathrm{r}_j)^3\right)\left(\frac{q}{q-1}\right)\left(\frac{\mathrm{r}_j}{\mathrm{r}_k}\right)^{D_f} \mathrm{n}_{k\text{-}1}\mathrm{n}_j \\
& + \sum_{j=1}^{k} \alpha\left(\frac{4\pi}{3}\dot{\gamma}(\mathrm{r}_k + \mathrm{r}_j)^3\right)\left\{1 - \left(\frac{1}{(q-1)}\right)\left(\frac{\mathrm{r}_j}{\mathrm{r}_k}\right)^{D_f}\right\}\mathrm{n}_k\mathrm{n}_j \\
& + \frac{1}{2}\alpha\left(\frac{4\pi}{3}\dot{\gamma}(\mathrm{r}_{k\text{-}1} + \mathrm{r}_{k\text{-}1})^3\right)\left(\frac{1}{q-1}\right)(\mathrm{n}_{k\text{-}1})^2 + \frac{1}{2}\alpha\left(\frac{4\pi}{3}\dot{\gamma}(\mathrm{r}_k + \mathrm{r}_k)^3\right)\left(\frac{q-2}{q-1}\right)(\mathrm{n}_k)^2 \\
& - \sum_{i=1}^{\max} \alpha\left(\frac{4\pi}{3}\dot{\gamma}(\mathrm{r}_k + \mathrm{r}_i)^3\right)\mathrm{n}_k\mathrm{n}_i \\
& + \sum_{j=k+1}^{\infty} \frac{3(q-1)}{2}\left(\frac{\mathrm{r}_j}{\mathrm{r}_k}\right)^{D_f} \mathrm{K_B}(\dot{\gamma})^{\mathrm{b}}(\mathrm{r}_j)^{\mathrm{s}}(\mathrm{n}_j)^{\eta} - \frac{1}{2}\mathrm{K_B}(\dot{\gamma})^{\mathrm{b}}(\mathrm{r}_k)^{\mathrm{s}}(\mathrm{n}_k)^{\eta}
\end{aligned} \tag{4.40}$$

Equation (4.5) can be substituted for all values of r_i, r_j, and r_k, then the total orthokinetic coagulation rate equation (Eq. (4.40)) becomes

$$\begin{aligned}\left[\frac{\mathrm{dn}_k}{\mathrm{dt}}\right] &= \alpha\frac{4\pi}{3}\dot{\gamma}(\mathrm{r}_1)^3\sum_{j=1}^{k-2}\left((k-1)^{1/\mathrm{D}_f}+j^{1/\mathrm{D}_f}\right)^3\left(\frac{q}{q-1}\right)\left(\frac{j}{k}\right)\mathrm{n}_{k\text{-}1}\mathrm{n}_j\\ &+\alpha\frac{4\pi}{3}\dot{\gamma}(\mathrm{r}_1)^3\sum_{j=1}^{k}\left(k^{1/\mathrm{D}_f}+j^{1/\mathrm{D}_f}\right)^3\left\{1-\left(\frac{1}{(q-1)}\right)\left(\frac{j}{k}\right)\right\}\mathrm{n}_k\mathrm{n}_j\\ &+\alpha\frac{2\pi}{3}\dot{\gamma}(\mathrm{r}_1)^3\left(\frac{1}{q-1}\right)\left(k-1\right)^{3/\mathrm{D}_f}(\mathrm{n}_{k\text{-}1})^2\\ &+\alpha\frac{2\pi}{3}\dot{\gamma}(\mathrm{r}_1)^3\left(\frac{q-2}{q-1}\right)\left(k\right)^{3/\mathrm{D}_f}(\mathrm{n}_k)^2-\alpha\frac{4\pi}{3}\dot{\gamma}(\mathrm{r}_1)^3\sum_{i=1}^{\max}\left(k^{1/\mathrm{D}_f}+i^{1/\mathrm{D}_f}\right)^3\mathrm{n}_k\mathrm{n}_i\\ &+\frac{3}{2}\mathrm{K}_\mathrm{B}(\dot{\gamma})^\mathrm{b}(\mathrm{r}_1)^\mathrm{s}\sum_{j=k+1}^{\infty}(q-1)\left(\frac{k}{j}\right)(i)^{\mathrm{s}/\mathrm{D}_f}(\mathrm{n}_j)^\eta-\frac{1}{2}\mathrm{K}_\mathrm{B}(\dot{\gamma})^\mathrm{b}(\mathrm{r}_1)^\mathrm{s}(k)^{\mathrm{s}/\mathrm{D}_f}(\mathrm{n}_k)^\eta\end{aligned}\tag{4.41}$$

Next, introduce a dimensionless concentration N_i defined as,

$$\mathrm{n}_i=\mathrm{N}_i(\mathrm{n}_0)\tag{4.42}$$

and

$$\sum_{i=1}^{\max}i(\mathrm{N}_i)=1\tag{4.43}$$

By substituting Eq. (4.42) into Eq. (4.41) and rearranging the following non-dimensional overall orthokinetic fractal aggregation rate equation results in,

$$\begin{aligned}\frac{3}{4\pi\dot{\gamma}(\mathrm{r}_1)^3\mathrm{n}_0}\frac{\mathrm{dN}_k}{\mathrm{dt}} &= \left[\left(\sum_{j=1}^{k-2}\alpha((k-1)^{1/\mathrm{D}_f}+j^{1/\mathrm{D}_f})^3\left(\frac{q}{q-1}\right)\left(\frac{j}{k}\right)\mathrm{N}_{k\text{-}1}\mathrm{N}_j\right)\right.\\ &+\left(\sum_{j=1}^{k-1}\alpha(k^{1/\mathrm{D}_f}+j^{1/\mathrm{D}_f})^3\left\{1-\left(\frac{1}{(q-1)}\right)\left(\frac{j}{k}\right)\right\}\mathrm{N}_k\mathrm{N}_j\right)\\ &+\left(0.5\alpha\left(\frac{1}{q-1}\right)(k-1)^{3/\mathrm{D}_f}(\mathrm{N}_{k-1})^2\right)+\left(0.5\alpha\left(\frac{q-2}{q-1}\right)(k)^{3/\mathrm{D}_f}(\mathrm{N}_k)^2\right)\\ &\left.-\left(\sum_{i=1}^{\max}\alpha(k^{1/\mathrm{D}_f}+i^{1/\mathrm{D}_f})^3\mathrm{N}_k\mathrm{N}_i\right)\right]\\ &+\frac{3\mathrm{K}_\mathrm{B}(\dot{\gamma})^\mathrm{b}(\mathrm{r}_1)^\mathrm{s}}{8\pi\dot{\gamma}(\mathrm{r}_1)^3(\mathrm{n}_0)^{2-\eta}}\left[\left(\sum_{i=k+1}^{\infty}3(q-1)\left(\frac{k}{i}\right)(i)^{\mathrm{s}/\mathrm{D}_f}(\mathrm{N}_i)^\eta\right)-\left((k)^{\mathrm{s}/\mathrm{D}_f}(\mathrm{N}_k)^\eta\right)\right]\end{aligned}\tag{4.44}$$

$$\tau = \frac{4\pi}{3}\dot{\gamma}\left(\mathrm{r}_1\right)^3 \mathrm{n}_0 \mathrm{t} \tag{4.45}$$

$$\mathrm{d}\tau = \frac{4\pi}{3}\dot{\gamma}\left(\mathrm{r}_1\right)^3 \mathrm{n}_0 \mathrm{dt} \tag{4.46}$$

$$\kappa = \frac{3\mathrm{K}_\mathrm{B}\left(\dot{\gamma}\right)^{\mathrm{b}-1}\left(\mathrm{r}_1\right)^{\mathrm{s}-3}}{8\pi \mathrm{n}_0^{2-\eta}} \tag{4.47}$$

Further, by defining a dimensionless time constant (Eq. (4.45)), a dimensionless time increment (Eq. (4.46)), and a dimensionless break-up constant (Eq. (4.47)), yields a new dimensionless orthokinetic coagulation rate equation using the new probability distribution functions, producing

$$\begin{aligned}\frac{\mathrm{dN}_k}{\mathrm{d}\tau} = & \left[\left(\sum_{j=1}^{k-2} \alpha((k-1)^{1/\mathrm{D}_f} + j^{1/\mathrm{D}_f})^3 \left(\frac{q}{q-1}\right)\left(\frac{j}{k}\right)\mathrm{N}_{k\text{-}1}\mathrm{N}_j\right)\right. \\ & + \left(\sum_{j=1}^{k-1} \alpha(k^{1/\mathrm{D}_f} + j^{1/\mathrm{D}_f})^3 \left\{1 - \left(\frac{1}{(q-1)}\right)\left(\frac{j}{k}\right)\right\}\mathrm{N}_k\mathrm{N}_j\right) \\ & + \left(0.5\alpha\left(\frac{1}{q-1}\right)(k-1)^{3/\mathrm{D}_f}(\mathrm{N}_{k-1})^2\right) + \left(0.5\alpha\left(\frac{q-2}{q-1}\right)(k)^{3/\mathrm{D}_f}(\mathrm{N}_k)^2\right) \\ & \left. - \left(\sum_{i=1}^{\max} \alpha(k^{1/\mathrm{D}_f} + i^{1/\mathrm{D}_f})^3 \mathrm{N}_k\mathrm{N}_i\right)\right] \\ & + \kappa\left[\left(\sum_{i=k+1}^{\infty} 3(q-1)\left(\frac{k}{i}\right)(i)^{\mathrm{s}/\mathrm{D}_f}(\mathrm{N}_i)^\eta\right) - \left((k)^{\mathrm{s}/\mathrm{D}_f}(\mathrm{N}_k)^\eta\right)\right]\end{aligned} \tag{4.48}$$

The first, second, third, and fourth terms on the right hand side of Eq. (4.48) represent the rate of creation of all size class *k* aggregates from the collisions of all possible combinations of the smaller size classes *i* and *j*. The fifth term on the right hand side in Eq. (4.48) is the loss in concentration of size class *k* due to growth into larger aggregates by collisions with all possible size classes. The sixth term is the gain to the size class *k* concentration by the fracture of larger size class aggregates. The last term is the loss of size class k aggregates due to fracture. Equation (4.48) generates a set of ordinary differential equations for the population n_k of all size classes $k = 1$ to max. The set of coupled equations defined by Eq. (4.40) or (4.48) can not be solved analytically, therefore, a numerical technique must be used.

4.4 Results and Discussion

4.4.1 Modeling Conditions

Several ODE solvers can be used to solve Eqs. (4.40) or (4.48). However, it should be noted that the stiffness problem exists when attempting to solve these population balance equations. That is, extremely large ranges exist among the values of all size class variables during each differential equation solution time step. For example, the maximum and minimum values of n_k are 1.0×10^{10} and 1.0×10^{0} in the initial conditions. In this study, a Fortran IVPAG subprogram based on Gear's method was used to simulate coagulation modeling and conduct parameter estimation (collision efficiency and break-up coefficient). The error tolerance selected was 1.0×10^{-6} for all numerical solutions. Also, a user-supplied subroutine (collision frequency, break-up kernel, probability functions, and random number generation) was developed and coupled to calculate the kernels for particle agglomeration and break-up in the population balance equations. In addition, various coagulation kernels used in this study (i.e., size-independent, size-dependent, self-preserving, and orthokintic) are summarized in Table 4.3.

Table 4.3 The Kernels Used as Coagulation Modeling Verification

Kernels	Formula
Size-independent (constant)	$\beta\left(\mathrm{r}_i, \mathrm{r}_j\right)=\beta_0$
Size-dependent (linear)	$\beta\left(\mathrm{r}_i, \mathrm{r}_j\right)=\beta_0\left(\mathrm{r}_i+\mathrm{r}_j\right)$
Self-Preserving (Friedlander)	$\beta\left(\mathrm{r}_i, \mathrm{r}_j\right)=\beta_0\left((\mathrm{r}_i)^{D_f}+(\mathrm{r}_j)^{D_f}\right)\left(\frac{1}{(\mathrm{r}_i)^{D_f}}+\frac{1}{(\mathrm{r}_j)^{D_f}}\right)$
Orthokinetic	Equation (4.39)

4.4.2 Comparison with Analytical and Uniform Discrete Numerical Solutions

Numerical accuracy of the improved population balance equations were verified using the solution results and analytical equations having constant (size-independent) and linear (size-dependent) agglomeration kernels (see Table 4.3). In this test, various model cases having different values of q were compared with respect to particle size distributions. Scott and Gelbard and Seinfeld developed analytical solutions for various agglomeration kernels (Eqs. (4.49) and (4.50)) (Scott 1968; Gelbard and Seinfeld 1978). For a size-independent kernel case ($\beta(\mathrm{r}_i,\mathrm{r}_j)=\beta_0$, constant kernel), analytical solution is

$$n(\upsilon,t)=\frac{4n_{total}}{\upsilon_0(\tau_1+2)^2}\exp\left(-\frac{2\overline{\upsilon}}{\tau_1+2}\right) \tag{4.49}$$

where, n_{total} is the total particle number concentration, υ_0 is the initial particle mean volume, $\tau_1=n_{total}\beta_0 t$, and $\overline{\upsilon}=\upsilon/\upsilon_0$. The solution for a size-dependent kernel (linear kernel) case, $\beta(\mathrm{r}_i,\mathrm{r}_j)=\beta_0(\mathrm{r}_i+\mathrm{r}_j)$, is

$$n(\upsilon, t) = \frac{n_{total}(1-T)}{\upsilon\sqrt{T}}\exp[-(1+T)\overline{\upsilon}]I_1(2\overline{\upsilon}\sqrt{T}) \tag{4.50}$$

where, $T = 1 - \exp(-\tau_2)$, $\tau_2 = n_{total}\upsilon_0\beta_0 t$, and I_1 is the modified Bessel function of the first kind of order one.

The adjustable geometric size interval ($q = \upsilon_{k+1}/\upsilon_k$) was determined by an aggregate maximum class size calculation having a fractal dimension (see Eq. (4.5)),

$$\mathrm{r}_{k,\mathrm{d}} = \mathrm{r}_1(k_\mathrm{d})^{1/D_f} = \mathrm{r}_1(q^{k_\mathrm{d}-1})^{1/D_f} \tag{4.51}$$

where, $\mathrm{r}_{k,\mathrm{d}}$ is the aggregate radius of size class k for discretized model and k_d is the number of the size class interval for discretized model. By letting Eq. (4.51) be equal to Eq. (4.5), the equation for the calculation of the adjustable geometric size interval (q) becomes,

$$q = (k_\mathrm{c})^{\{1/(k_\mathrm{d}-1)\}} \tag{4.52}$$

where, k_c is the number of size class intervals for the uniform discrete distribution model (q = 1). The numerical solutions, obtained from the particle agglomeration model (Eq. (4.16)) with various geometric size interval values (q) for the size-independent kernel case ($\beta(\mathrm{r}_i, \mathrm{r}_j) = \beta_0$), were represented by a cumulative particle size distribution and compared with the analytical solution (Eq. (4.49)) in Figure 4.1(a).

Also, deviations between each result and the analytical solution were compared using an R^2 computation and the square root of the sum-of-squares of the residuals analyses (see Fig. 4.1(b)). As the q value was decreased from 2.0 to 1.3348, higher numerical accuracy was found (R^2 of 0.9936 and residuals of 0.1616). This result indicate that as the q value decreases from 2.0 and falls into 1.0, the solution resulting from improved adjustable discretized coagulation model approaches the exact solution of size independent (or constant) kernel case calculated from analytical solution of Eq. (4.49).

Similar results were obtained using a size-dependent kernel ($\beta(r_i, r_j) = \beta_0(r_i + r_j)$) (see Fig. 4.2). In this case, the cumulative particle size distribution results were compared with the analytical (Eq. (4.50)) and numerical accuracy test were conducted in terms of an R^2 and the sum of residuals using statistical analyses and displayed in in Figs. 4.2(a) and 4.2(b).

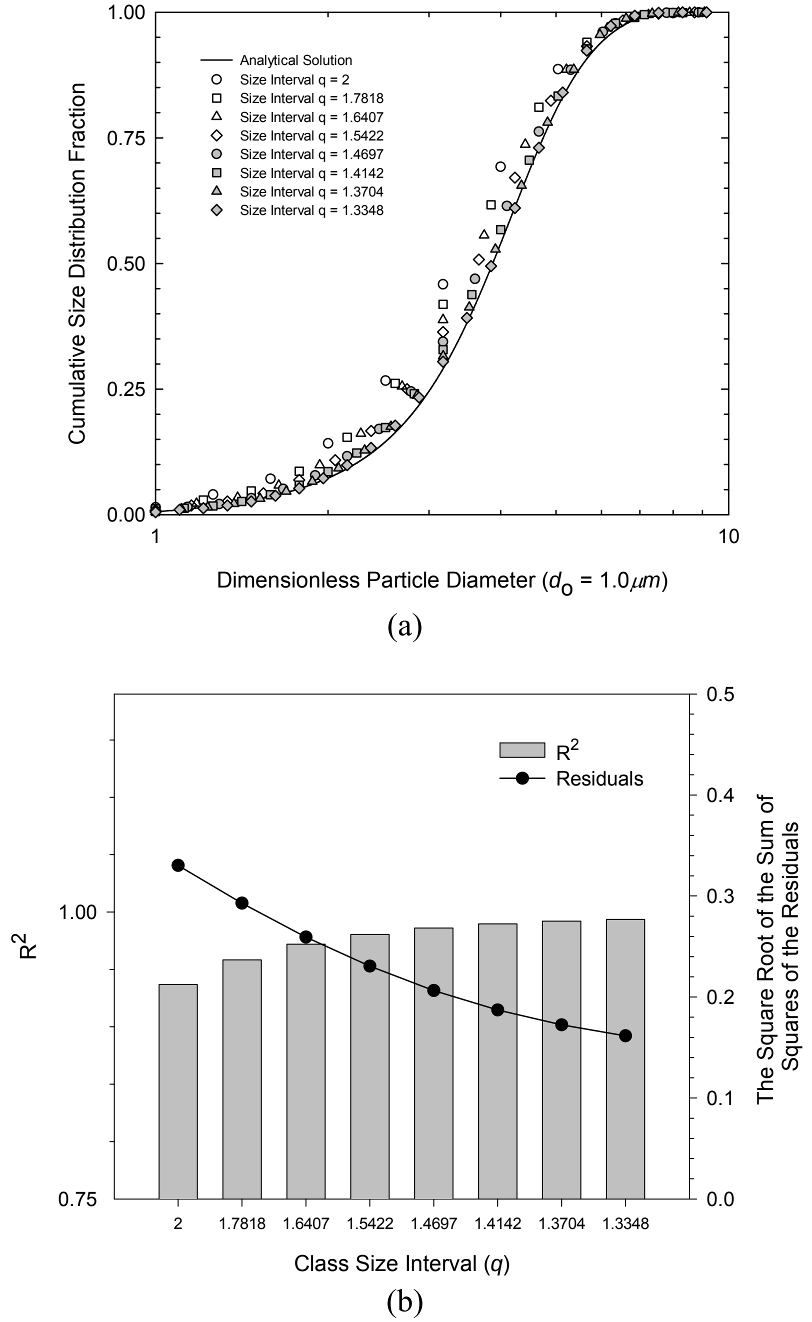

(a)

(b)

Figure 4.1 Size-independent particle size distributions for various geometric size intervals ($\beta_o = 1.0\times10^{-9}$ cm^3/sec, $K_B = 0.0$, $d_o = 1$ μm, $D_f = 3.0$)

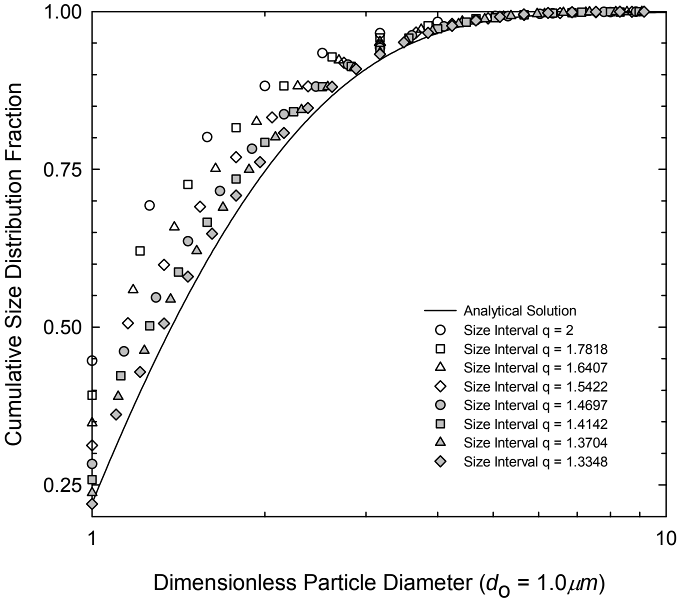

(a)

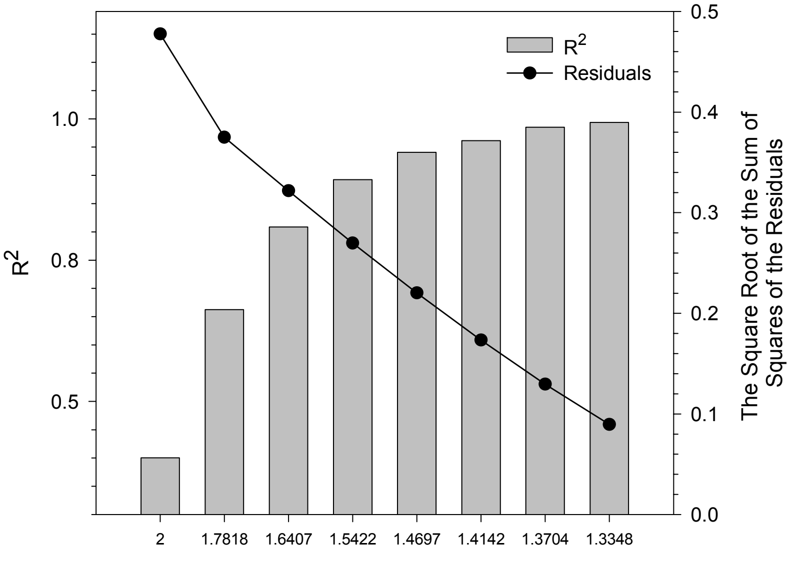

(b)

Figure 4.2 Size-dependent particle size distributions for various geometric size intervals ($\beta_o = 1.0\times10^2$ cm^2/sec, $K_B = 0.0$, d_o = 1 μm, $D_f = 3.0$)

Higher numerical accuracy could be obtained by a decreasing q from 2.0 to 1.3348 (R^2 of 0.9978 and residuals of 0.0557). These numerical accuracy tests for the results from the agglomeration model having the size-independent and size-dependent kernels indicate that numerical accuracy can be obtained with introducing fine resolution of class size interval q value (i.e., smaller q value but larger than 1.0). At a smaller q value, the solution deviation was minimized and converged to the exact results from analytical solutions when both size-independent and size-dependent kernels are used.

4.4.3 Self-Preserving Distribution Test

A self-preserving distribution method can also be used to evaluate the accuracy of the population balance equation (Eq. (4.16)), which is associated with the agglomeration rate kernels such as a size-independent kernel and a size-dependent kernel. Friedlander suggested that in aerosol agglomeration the resulting particle size distribution approaches a form at long times, which is asymptotically independent of the initial particle size distribution (Friedlander 2000). These asymptotic particle size distributions are independent of time when results are plotted in a non-dimensional form and are termed self-preserving distributions. This self-preserving distribution method is based on scaling the density function as,

$$\psi(\eta_\upsilon) = \mathrm{n}(\upsilon)\bar{\upsilon} / \mathrm{m}_0 \tag{4.53}$$

where, $\psi(\eta_\upsilon)$ is a dimensionless particle number concentration, η_υ is a dimensionless particle volume expressed as $\eta_\upsilon = \upsilon / \bar{\upsilon}$, m_0 is the zero moment (see Eq. (4.54)), and $\bar{\upsilon}$ is average aggregate size calculated by the ratio of the third moment to the zero moment, $\bar{\upsilon} = \mathrm{m}_3 / \mathrm{m}_0$. The n^{th} moment can be obtained from the equation suggested by Hounslow,

$$\mathrm{m}_k = \sum_j (L_j)^k \mathrm{n}_j \tag{4.54}$$

where, *L* is an aggregate length in diameter (Hounslow et al. 1988). Litster derived a self-preserving method for a size-independent kernel (Litster et al. 1995). For the size-independent kernel, this self-preserving equation (Eq. (4.54)) can be rewritten as,

$$\psi(\eta) = \exp(-\eta) \tag{4.55}$$

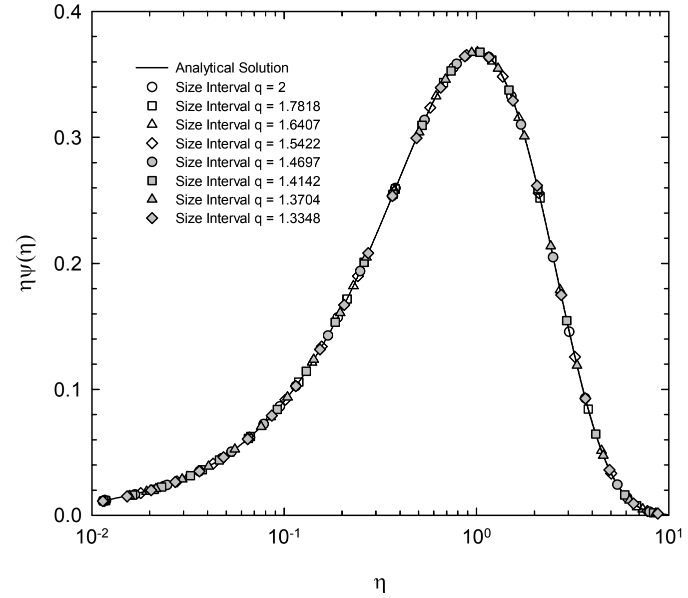

Figure 4.3 Size-independent self-preserving particle size distributions for various geometric size intervals ($\beta_o = 1.0\times10^{-9}$ cm^3/sec, $K_B = 0.0$, $d_o = 1$ μm, $D_f = 3.0$)

As shown in Figure 4.3, the self-preserving analysis of Eq. (4.16) having a size-independent kernel ($\beta(\mathrm{r}_i,\mathrm{r}_j) = \beta_0$) were conducted and compared with the analytical solution (Eq. (4.49)). In the *q* ranging from 2 to 1.4142 (the results of *q* values of 1.4697 and 1.4142 were not presented to avoid overlapping the symbols), all results were in excellent agreement (R^2 of 1 and residuals of 1.7719×10^{-7} to 2.5517×10^{-4}) with the analytical solution (Eq. (4.49)).

Friedlander provides a numerical solution for a size-dependent agglomeration kernel associated with an aggregate fractal dimension, D_f, (Friedlander 2000) as,

$$\beta(r_i, r_j) = \beta_0\left((r_i)^{1/D_f} + (r_j)^{1/D_f}\right)\left(\frac{1}{(r_i)^{1/D_f}} + \frac{1}{(r_j)^{1/D_f}}\right) \tag{4.56}$$

For self-preserving test for size-dependent kernel (Eq. (4.56)), the results from the improved adjustable discretized model (Eq. (4.16)) using an initially monodisperse particle population were compared with the uniform discrete model (Eq. (4.2)) and displayed in Fig. 4.4.

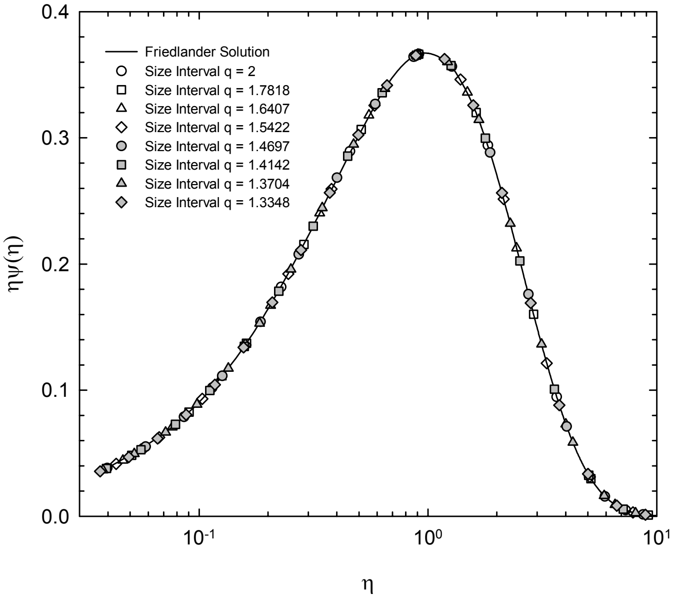

Figure 4.4 Size-dependent self-preserving particle size distributions for various geometric size intervals ($\beta_o = 1.0\times10^{-10}$ cm^3/sec, $K_B = 0.0$, $d_o = 1$ μm, $D_f = 3.0$)

As seen in Fig. 4.4, excellent agreement was found among the self-preserving distributions computed by the various techniques (R^2 of 1 and residuals of 4.5942×10^{-3} to 6.6578×10^{-3} with q ranging from 2 to 1.4142 and the results of q values of 1.4697 and 1.4142 were not presented to avoid overlapping the symbols). After comparing these self-preserving results (see Figs. 4.3 and 4.4), it can be concluded that the self-preserving distribution analysis may not be the proper way to verify a coagulation model. Thus, in addition to the self-preserving distribution analysis, the resulting particle size distributions using various collision frequencies (or kernels) should be considered to evaluate numerical coagulation accuracy.

4.4.4 Coagulation Parameter Estimation

A parameter estimation scheme was created to computationally determine the two key coagulation constants, the collision efficiency (α) and the break-up coefficient (K_B). To verify the estimation procedure the fractal aggregate orthokinetic experimental data of Li and Zhang was used (Li and Zhang 2003). Li and Zhang obtained their orthokinetic data by using batch coagulation experiments having initial conditions of; a latex primary particle size of 2.8 μm in diameter with a density of 1.05 g/cm^3, initial number concentration $n_o = 2.0\times10^6$ /mL, using a jar-test device with a flat paddle mixer, 3.5% NaCl as a electrolyte, 10 mg/L $Al_2(SO_4)_3\cdot18H_2O$ as a flocculant, and the pH maintained at 7.5 using 0.1M $NaHCO_3$. A microscopic technique was used for the measurement of the particle size class concentrations.

The improved adjustable discretized model was converted to the dimensionless form of Eq. (4.48) to improve computational efficiency. Parameter estimation was performed to optimize the two best fit values of collision efficiency (α) and break-up coefficient (K_B), two crucial coefficients in orthokinetic coagulation model. The function used for this parameter estimation was the Gauss-Newton least-square method (Eq (4.58)) by minimizing the sum of squared residuals (SSR) between the experimental and model results for the change in number concentrations with time (Constantinides and Mostoufi 1999),

$$\mathrm{SSR}=(\mathrm{n}_{\exp}-\mathrm{n}_{\mathrm{mod}}-\mathrm{J}\Delta\mathrm{p})^{T}(\mathrm{n}_{\exp}-\mathrm{n}_{\mathrm{mod}}-\mathrm{J}\Delta\mathrm{p}) \tag{4.57}$$

where, $\mathrm{n}_{\exp}$ is the experimental data, $\mathrm{n}_{\mathrm{mod}}$ is the predicted value using the model, p is a parameter vector, J is the Jacobian matrix, and the superscript *T* implies the transpose operation. The algorithm of the Gauss-Newton least square method is converts a nonlinear problem into a linear one by applying a Taylor series expansion as,

$$\mathrm{n}(\mathrm{t},\,\mathrm{p})=\mathrm{n}(\mathrm{t},\,\mathrm{p}^{(\mathrm{m})}+\Delta\mathrm{p})=\mathrm{n}(\mathrm{t},\,\mathrm{p}^{(\mathrm{m})})+\left.\frac{\partial\mathrm{n}}{\partial\mathrm{p}}\right|_{\mathrm{p}^{(\mathrm{m})}}\Delta\mathrm{p}=\mathrm{n}+\mathrm{J}\Delta\mathrm{p} \tag{4.58}$$

where, the Taylor series has been truncated after the second term. Therefore, the problem has been transformed from finding the parameter to one of finding the correction to the parameter through minimizing the sum of squared residuals using the addition of $\Delta\mathrm{p}$ into an estimated p. The Gauss-Newton scheme is a simplified classical Newton method in that this scheme contains the first and second derivatives of the matrix of sum of squared residuals (Ernest et al. 1991). The algorithm of the Gauss-Newton method adopted in this study is represented by the flow chart shown in Fig. 4.5. The parameter estimation conditions used were; a primary particle size of 2.8 μm in diameter, a fractal aggregate dimension D_f of 2.0, a fluid strain-rate of 15 (1/s), a break-up exponent b of 1, an aggregate size exponent s of 3, and a break-up concentration exponent η of 2, and particle size interval q value of 1.5422.

These results are shown in Fig. 4.6 and Table 4.4, with collision efficiency α of 0.3938 and aggregate break-up coefficient K_B of 4.4105. Li and Zhang compared their model simulation results to experimental data and did not achieve an accurate prediction in terms of the time evolution of particle size distribution (Li and Zhang 2003). This discrepancy between the experimental and modeling data resulted from inaccurately assuming the collision efficiency (α) and not considering aggregate break-up. Li and Zhang simulated the time evolution of the particle size distributions with only two modeling coefficients, collision efficiency α of 1.0 and curvilinear collision frequency β developed by Han and Lawler (Han and Lawler 1992), and excluded an aggregate break-up kernel.

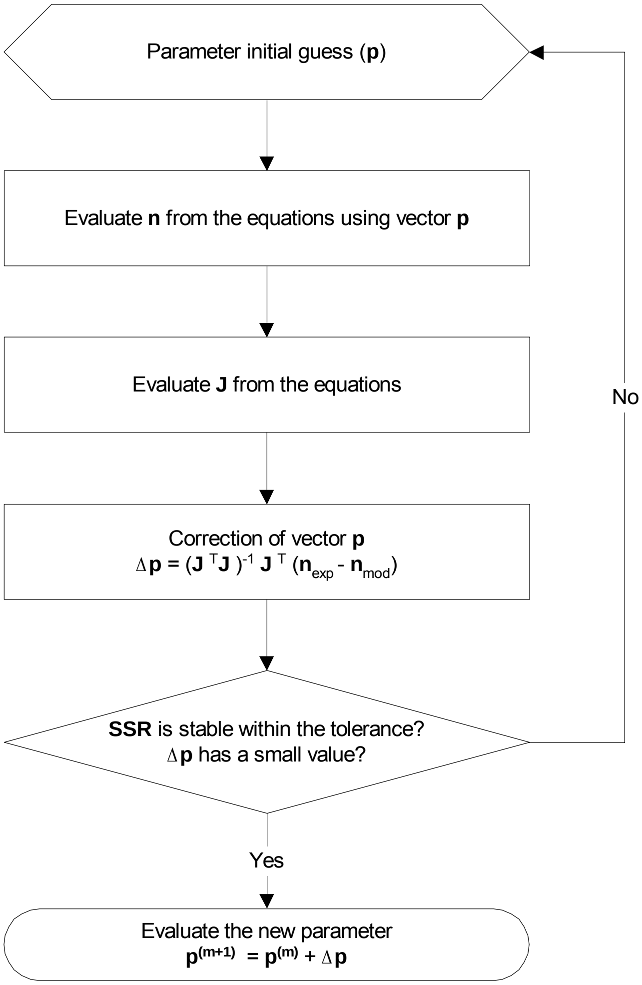

Figure 4.5 The algorithm of parameter estimation scheme

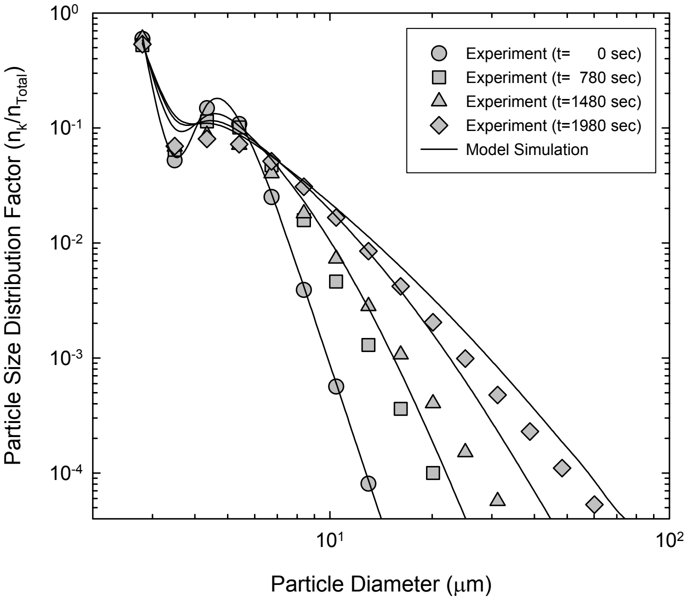

Figure 4.6 Particle concentration evolution during orthokinetic coagulation ($n_o = 2.0\times10^6$ cm^{-3}, $\dot{\gamma}$ = 15 (1/s), $D_f = 2.0$)

Table 4.4 Parameter Estimation Results for Fitting the Experimental Data

Parameter	Value	Standard Deviation	95% Confidence Levels	
			Lower	Upper
α	0.3938	6.5678×10^{-3}	0.38074	0.40697
K_B	4.4105	1.0598	2.2946	6.5264

4.4.5 Reproduction of Continuous Distribution from Discrete Data

Although the particle size distributions resulting from experimental data and discretized coagulation modeling mentioned in the above sections are represented by histograms due to the convenient depiction of the data (see Fig. 4.7), a continuous representation is required when modeling experimental data (Hiemenz and Rajagopalan

1997). As shown in Fig. 4.8, due to the different class size intervals (q values of 1.5422 and 1), it is impossible to compare two different results from non-uniform discrete population balance models to uniform discrete models by putting these two methods together on the same graph. There are 1024 size intervals (or variables) in the uniform discrete model (q = 1), however, there are only 17 size intervals in the corresponding non-uniform discrete model (q = 1.5422), which is based on maximum class size interval of 1024 (see Eq. (4.52)). For example, with the non-uniform discrete model having q = 2, only one class size value of n = 1024 represents all population values ranging from n = 512 to n = 1024, while the uniform discrete model produces population values at each size class. Obviously, one population value in the non-uniform discrete model (N_{NU}) represents several values of the uniform discrete model results (N_U) (N_{NU} is always larger than N_U) (see Fig. 4.7). By using the cumulative distribution curve, one can directly compare both results without any data conversion. The particle cumulative population distribution is a convenient way to compare these data having different class size intervals; non-uniform and uniform discrete data. Further, the particle size distribution can be derived easily from the cumulative population distribution curve using a data reproduction procedure with statistic scheme. After converting the discretized particle size distribution data into a cumulative size distribution, it is possible to regenerate a synthetic continuous particle size distribution using a statistical nonlinear regression analysis (see Fig. 4.9). As shown in Fig. 4.8, at a particle geometric size d_k, the particle cumulative size distribution corresponds to C_k and

$$C_k = \sum_{j=1}^{k} \frac{n_j}{n_{total}} \tag{4.59}$$

so

$$n_{total} C_k = n_1 + n_2 + n_3 + \ldots\ldots + n_k \tag{4.60}$$

and

$$n_k = n_{total} C_k - \sum_{j=1}^{k-1} n_j \tag{4.61}$$

thus at d_1, $n_1 = n_{total} C_1$, then $n_2 = n_{total} C_2 - n_1$ and on, for all class size *k*. Thus, from any cumulative distribution one can compute a continuous (uniform discretized) particle size distributions. As shown in Fig. 4.9, this method shows good agreement between the discretized and continuous data except at the larger particle size classes. This difference, especially in the larger size classes, results from different size class interval scales. Furthermore, particle concentrations for the larger size classes have relative smaller fraction than those for smaller class size.

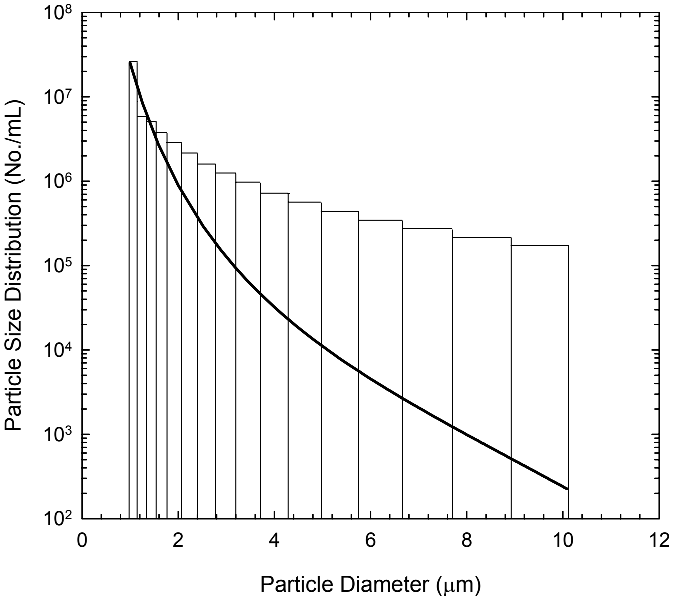

Figure 4.7 Particle size distributions for discretized data (histogram) and continuous data (line plot)

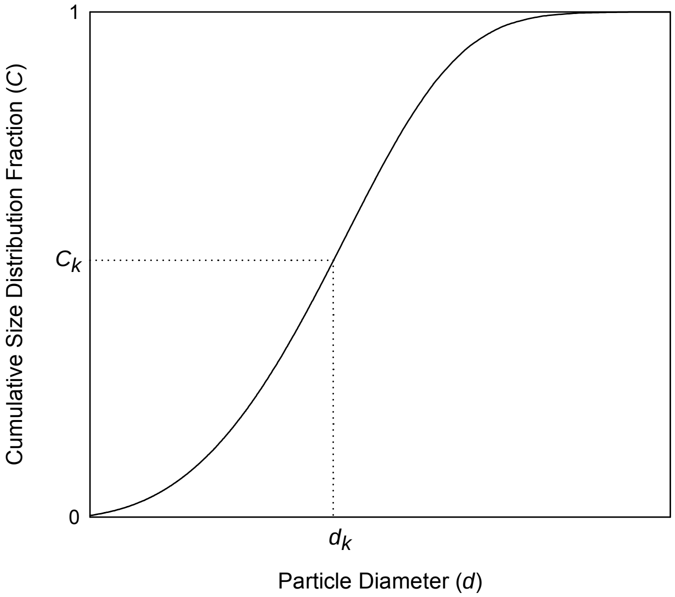

Figure 4.8 The reproduction of continuous particle size distribution from discretized data using cumulative size distribution curve

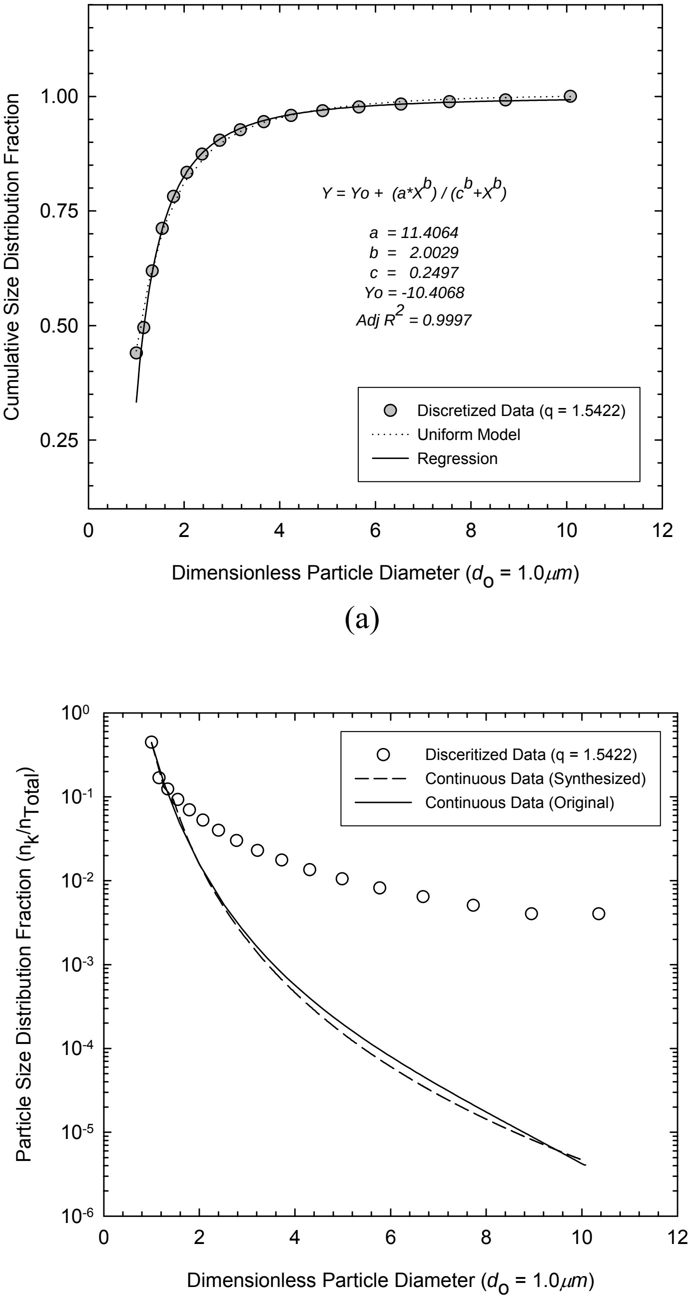

(a)

(b)

Figure 4.9 Particle size distributions for various geometric size intervals (Monodisperse initial condition, orthokinetic kernel, $n_o = 1.0\times10^8$ cm^{-3}, $\alpha = 0.1$, $\dot{\gamma} = 15$ 1/s, $K_B = 0.01$, $D_f = 3.0$)

4.5 Conclusions

In this study, the authors extended their improved particle coagulation model having an agglomeration and break-up kernel to an adjustable geometric size interval (*q*), where *q* is a volume ratio of class *k+1* particle to class *k* particle ($q = \upsilon_{k+1} / \upsilon_k$). The accuracy of this model was verified using several methods; direct numerical simulations (DNS) comparing to analytical exact solutions, the derivative of moments, and self-preserving distributions. The proposed model was converted to a dimensionless form to enhance computational efficiency. Furthermore, a parameter estimation scheme was created to computationally determine the two key parameters in the new model, the collision efficiency (α) and the break-up coefficient (K_B), from orthokinetic experimental data. This parameter estimation scheme can be readily applied to establish coefficients in a variety of coagulation systems, especially those having fractal aggregate structure. In addition, the authors attempted to find an optimum graphical method for representing the two different results (discretized and continuous populations) on an identical 2D plane and found that the particle cumulative population distribution curve is convenient to compare these results due to different aggregate class size scales. Using the reproduction of continuous distribution from discrete data, it was concluded that this method has close agreement between discretized and continuous data except at the larger particle size classes.

CHAPTER V

ARSENIC SORPTION ONTO HYDROUS FERRIC OXIDE

5.1 Overview

To enhance the predictive capability for arsenic sorption onto metal oxy-hydroxide surfaces, a surface complexation equilibrium model using a thermodynamic equilibrium database and a sorption kinetic model using diffusion mass transport would be a useful tool especially for small scale arsenic sorption removal systems.

A surface complexation model was introduced to predict arsenic sorption equilibrium behaviors (i.e., pH envelop and isotherm). A set of equations representing surface complexation model, which are related to the arsenic acid-base reactions, hydrous ferric oxide (HFO) surface protonation/deprotonation, and inner-sphere monodentate surface complexations for arsenic sorption on HFO surfaces, was solved with a public domain computer program. Further, the surface complexation model was coupled with an arsenic sorption kinetic model based on the diffusion mass transport mechanism using the sorption local equilibrium assumption to provide easy to use software that establishes predictive capability for the water treatment community.

The improved arsenic sorption modeling technique coupled with arsenic sorption kinetics and equilibrium could provide enhanced predictive capability for the exact arsenic sorption behavior especially related to arsenic sorption kinetics, equilibrium, and HFO surface charge/potential evolution with reaction time, as well as required sorption process design parameters, sorption media capacity, sorption media doses, sorption media operation life-times, residuals production, and sorption process operating costs. Furthermore, the surface charge/potential evolution with reaction time would be used to couple two models of arsenic sorption and coagulation (details will be addressed in the next chapter). That is, a unified coagulation model will be coupled with arsenic sorption model using surface charge/potential which is one of major variable parameters in collision efficiency calculation.

5.2 Introduction

5.2.1 Arsenic Sorption onto Freshly Precipitated Hydrous Metal Oxy-Hydroxides

In the engineering field of water treatment, one of the most practical methods for removing major toxic metals (arsenic, chromium, and lead) is sorption onto amorphous hydrous ferric oxides (HFO, am-$Fe(OH)_{3(s)}$, or 2-line ferrihydrite ($Fe_pO_r(OH)_s \cdot nH_2O$)), which are precipitates generated during the coagulation process. It should be noted that this 2-line ferrihydrite is commonly but incorrectly called “hydrous ferric oxide (HFO)” or “amorphous iron oxide” in various fields (Schwertmann and Cornell 2000). Although many researchers have proposed a chemical formula for ferrihydrite, neither the single formula nor the structure of ferrihydrite has been fully established (Robinson et al. 1981; Cornell et al. 1989; Schwertmann et al. 1999). The disagreement results from the rate and conditions of hydrolysis; solution pH, temperature, aging time, [OH]/[Fe] ratios, and the co-existence of impurities. The physical and chemical properties of the hydrous ferric oxy-hydroxides, consisted of amorphous ferric hydroxide (am-$Fe(OH)_{3(s)}$), ferrihydrite ($Fe_pO_r(OH)_s \cdot nH_2O$), goethite (α-FeOOH), lepidocrocite (γ-FeOOH), and hematite (α-Fe_2O_3), can affect the sorption capacity for both metals and coagulation index due to different porosity, specific surface area, diffusion coefficient, particle size, pH_{zpc} and aggregate fractal dimension.

A number of researchers have reported on the sorption of arsenic onto the hydrous metal oxy-hydroxide solids that precipitate during coagulation process when the metal salts of Fe and Al (e.g., $FeCl_3$, alum) are added to the solutions. Often, the processes in which these reagents are added are considered to be coagulation rather than sorption, but the reaction between arsenic and the precipitated solids can be viewed as adsorption or some related reaction (Gulledge and O'Connor 1973; Shen 1973; Anderson et al. 1976; Gupta and Chen 1978; Sorg and Logsdon 1978; Leckie et al. 1980; Pierce and Moore 1982; Ghosh and Yuan 1987; Fuller et al. 1993; Waychunas et al. 1993). The first studies on the behavior of arsenic in these types of systems indicated that both As(III) and As(V) could be removed by coagulation and sorption onto freshly precipitated hydrous iron and aluminum oxides in the suspension phase, with iron hydroxide being a somewhat stronger adsorbent than aluminum hydroxide on a weight basis (comparing $FeCl_3$ and alum) and arsenate binding more strongly than arsenite (Sorg and Logsdon 1978; Leckie et al. 1980; Pierce and Moore 1982). It was reported that significantly more arsenic can bind to the solids if they are freshly formed in situ than if they are preformed and that either type of solid has a very large affinity and capacity for As(V) (Edwards 1994; Hering et al. 1997). It was found that arsenic removal in the practical systems using alum coagulation was not as good as expected based on the laboratory studies. In some cases, the differences could be attributed to incomplete precipitation of the added aluminum as a hydrous solid or incomplete removal of the solids that formed (McNeill and Edwards 1995). Also, it was found that As(V) was adsorbed somewhat more strongly than As(III), that binding of As(III) to the solid was more susceptible to competition from sulfate than the binding of As(V), and that As(V) removal could be enhanced by the presence of calcium in the system due to cooperative effect of calcium by changing the surface charge to be positive at high pH and enhancing anion sorption at high pH (Hering et al. 1996; Wilkie and Hering 1996). It was reported that the removal of arsenic via coagulation by $FeCl_3$ was much more effective than by alum, even when equivalent molar doses of iron and aluminum were compared. Arsenic removal efficiency by conventional treatment (coagulation, sedimentation, and filtration) was consistently over 80% at $FeCl_3$ doses of 3 to 10mg/L (Cheng et al. 1994; Scott et al. 1995).

5.2.2 Arsenic Sorption onto Pre-Synthesized Metal Oxy-Hydroxides

Previous investigations have studied the sorption of arsenate and arsenite onto pre-synthesized aluminum oxides and hydroxides (Ferguson and Anderson 1974; Anderson et al. 1976; Anderson and Malotky 1979; Ghosh and Yuan 1987; Manning and Goldberg 1997; Arai et al. 2001; Goldberg et al. 2001), iron oxides and hydroxides (Ferguson and Anderson 1974; Anderson and Malotky 1979; Pierce and Moore 1980; Harrison and Berkheiser 1982; Pierce and Moore 1982; Hsia et al. 1992; Fuller et al. 1993; Waychunas et al. 1993; Hsia et al. 1994; Hering et al. 1996; Waychunas et al. 1996; Wilkie and Hering 1996; Hering et al. 1997; Raven et al. 1998; Suarez et al. 1998; Jain et al. 1999; Meng et al. 2000; Goldberg and Johnston 2001), goethite (Lumsdon et al. 1984; Waychunas et al. 1995; Sun and Doner 1996; Fendorf et al. 1997; Grossl et al. 1997; Matis et al. 1997; Manning et al. 1998; Hiemstra and van Riemsdijk 1999; Matis et al. 1999; Grafe et al. 2001), goethite and gibbsite (Manning and Goldberg 1996), goethite, akageneite, and lepidocrocite (Manceau 1995), goethite, hematite, and lepidocrocite (Bowell 1994), akageneite (Driehaus et al. 1998), gibbsite (Weerasooriya et al. 2003), manganese oxides and hydroxides (Oscarson et al. 1983; Thanabalasingam and Pickering 1986; Driehaus et al. 1995), alumina, hematite, quartz, and kaolin (Xu et al. 1988; Xu et al. 1991), kaolinite and montmorillonite (Frost and Griffin 1977), granular activated alumina (Lin and Wu 2001), activated alumina, bauxite, and carbon (Gupta and Chen 1978), and activated carbon (Huang and Fu 1984), activated alumina (Rosenblum and Clifford 1982), and clay minerals (Manning and Goldberg 1997). Recently, to enhance arsenic sorption capacity, other alternative adsorbents have been developed; silica gel impregnated with ferric hydroxide, basic yttrium carbonate, lanthanum, lanthanum impregnated saw dust carbon, hydrate zirconium oxide, porous resin loaded with crystalline hydrous zirconium oxide, hydrotalcite, Ce(IV)-doped iron oxide, and iron impregnated sand (Yoshida et al. 1976; Suzuki et al. 2000; Vaishya and Gupta 2003; Zhang et al. 2003). The arsenic sorption studies using various adsorbents are summarized in Table 5.1.

A number of studies have indicated that various complexes are formed in the adsorption of As(V) on ferrihydrite (Manceau 1995; Sun and Doner 1996; Fendorf et al. 1997). EXAFS studies on arsenic bearing ferrihydrite formed at pH > 7, have shown that As(V) is adsorbed onto ferrihydrite as a strongly bonded inner-sphere surface complex with either monodentate or bidentate attachment (Waychunas et al. 1993; Waychunas et al. 1995).

Table 5.1 Arsenic Sorption onto Various Adsorbents

Adsorbent	Loading Ratio	Comment	Reference
2-line ferrihydrite	As(V,III) 5.34×10^{-4} M – 2.67×10^{-2} M Fe(III) 2.25×10^{-2} M (0.025–1.187 : 1)	As(V,III) sorption (pH 4.6 and 9.2, 0.1M NaCl, N_2) Kinetic, isotherm, and envelop (pH 3.8–10). Diffusion controlled reaction. Adsorption density 0.60 (V) 0.25 (III) for pH 4.6 and 0.58 (V) 0.16 (III) for pH 9.2. * 0.25(V) for Fuller, 0.11(V) for Ferguson, 5.0 (III/V) for Pierce (As/Fe=15:1).	Raven et al. 1998
2-line ferrihydrite	As(V,III) $5.3–16\times10^{-4}$ M Fe(III) 2.25×10^{-2} M (0.025–0.071 : 1)	ZPC of ferrihydrite is 8.5, decreasing with increasing adsorbed As. As(III) and As(V) adsorption and OH^- release/uptake. As(V) at pH 9.2 released up to 1mol OH^- per mol As adsorbed whereas As(III) released <0.25 mol As per mol Fe. At pH 4.6, OH^- release was much less for As(V) adsorption and under these conditions there was a net release of H+ by arsenite.	Jain et al. 1999
2-line ferrihydrite FeOOH / $Fe_2O_3\cdot H_2O$	As(V) 1.0×10^{-4} M Fe(III) 5.0×10^{-4} M (0.2 : 1)	As(V) sorption (pH 7.5– 9.0, 0.1M $NaNO_3$, O_2-N_2-Air). At pH = 8.0, adsorption density was 0.70 (V) in coprecipitate and 0.25 (V) in post-synthesis adsorbent. No surface precipitations. For Dzombak and Morel (1990), sorption density of 0.205(V), specific surface area 600 m^2/g, and molecular weight 89g HFO/mol Fe.	Fuller et al. 1993
2-line ferrihydrite FeOOH / $Fe_2O_3\cdot H_2O$	As(V) 1.0×10^{-4} M Fe(III) 5.0×10^{-4} M (0.2 : 1)	As(V) sorption (pH 7.5– 9.0, 0.1M $NaNO_3$, O_2-N_2-Air) on ferrihydrite. FTIR, EXAFS, and Raman spectroscopy analysis. As(V) adsorbs on ferrihydrite as inner-sphere surface complexes that are attached predominantly via bidentate linkages with some monodentate linkages.	Waychunas et al. 1993
am-FeOOH am-$Al(OH)_3$	As(V,III) 1.0×10^{-3} M Fe(III) $7.7–8.6\times10^{-4}$ M Al(III) $1.3–1.7\times10^{-2}$ M (1.16 : 1) & (0.06 : 1)	As(V,III) sorption (pH 6–8) on synthesized HFOs. Kinetic, pH effect, and isotherm experiments (not enough information). Adsorption density 0.034 for Al and 0.13 for Fe based on 99.5% As(III) removal.	Ferguson and Anderson 1974
am-$Fe(OH)_3$ (Ferrihydrite)	As(V,III) 6.67×10^{-7} M – 13.30×10^{-4} M Fe(III) 4.16×10^{-5} M (0.016–31.97 : 1)	As(V,III) sorption (pH 4–10, 0.01M $NaNO_3$) on synthesized HFO. Adsorption density 5.34 (V,III) at pH 4.0, [As]=6.67×10^{-4} M, and [Fe]=4.16×10^{-5} M. Fitted to Langmuir isotherm at low concentrations and linear isotherm at higher concentrations. Heterogeneous surface site model concept.	Pierce and Moore 1982
am-$Fe(OH)_3$ (Ferrihydrite)	As(III) $6.67–66.7\times10^{-7}$ M Fe(III) 5×10^{-5} M (0.013–0.13 : 1)	As(III) sorption (pH 4–10, 0.01M $NaNO_3$) on synthesized HFO. Sorption envelop, isotherms, ZPC experiment. Linear isotherm indicates that the sorption reactions are reversible and coverage is monolayer. The Maximum sorption occurs at pH 7. Specific adsorption and electrostatic interactions are important mechanisms.	Pierce and Moore 1980
2-line ferrihydrite	As(V) 0.01–0.1 M Fe(III) 0.1 M (0.1–1.0 : 1)	A wide angle X-ray scattering (and EXAFS) study of 2-line ferrihydrite co-precipitated with varying amounts of As(V) suggested that the As reduced crystallite size because of the formation of strongly bound inner sphere complex between As(V) and edge sharing $Fe(O,OH)_6$ octahedra. Saturation at As/Fe mol ratio of 0.68	Waychunas et al. 1996
2-line ferrihydrite	As $53–210\times10^{-6}$ M Fe(III) 1.7×10^{-3} M (0.03–0.12 : 1)	Adsorption and polymerization of silicic acid (H_4SiO_4)on ferrihydrite and its effect on As(V,III) adsorption (pH 4–12, 0.1M $NaNO_3$). Modified intrinsic adsorption constant. [As(V) (log K_1=0.0 log K_2=6.12 log K_3=-0.76 log K_4=-9.079)]. [As(III) (log K_1=5.74 log K_2=-2.88 log K_3=-10.95)].	Swedlund and Webster 1999
am-$Fe(OH)_3$ (Ferrihydrite)	As(V) $0.5–2.0\times10^{-4}$ M Fe(III) 1.0×10^{-3} M (0.05–0.2 : 1)	As(V) sorption (pH 4–10, 0.01M $NaNO_3$, N_2) on am-HFO. EDAX, FTIR, zeta potential, pH and ionic strength analysis. An inner-sphere complexation was identified from the results of the ionic strength effect and the shift in isoelectric point of the system. As(V) was chemisorbed on the iron oxide surface with specific adsorption.	Hsia et al. 1994

Table 5.1 (Continued)

Adsorbent	Loading Ratio	Comment	Reference
am-$Fe(OH)_3$ (Ferrihydrite)	As(V) 0.5–2.0$\times10^{-4}$ M Fe(III) 1.0–2.0$\times10^{-3}$ M (0.025–0.2 : 1)	As(V) sorption (pH 4–10, 0.01M $NaNO_3$, N_2) on am-HFO. Single and combined model using outer sphere (surface ionization or ion-pair form) and inner sphere (electrolyte binding or surface coordination occur). Inner sphere model fits well data than inner + outer sphere and outer sphere models. Inner sphere complexation for surface species $=Fe(H_2AsO_4)$, $=Fe(HAsO_4)^-$ and $=Fe(AsO_4)^{2-}$ is the reaction mechanism.	Hsia et al. 1992
am-$Fe(OH)_3$ (Ferrihydrite)	–	As(V) sorption on freshly prepared HFO. Infrared analysis. Monovalent and divalent anion bonding behavior. Without exception, each bidentate bridging complex forms by replacement of protonated and unprotonated hydroxyls. With anion geometry and the charge being equal, pH determines sorption capacity.	Harrison and Berkheiser 1982
am-$Fe(OH)_3$ am-$Al(OH)_3$	As 0.01–1.0$\times10^{-3}$ M Me 4.0, 0.5g/L	As(V,III) sorption (pH 2–12, 0.01–1.0M NaCl) on am-HFO and am-HAO. FTIR, EM, pH, ionic strength analysis. As(V) forms inner-sphere surface complexes on both am-HFO and am-HAO. As(III) forms both inner- and outer sphere surface complexes on am-HFO and outer-sphere surface complexes on am-HAO.	Goldberg and Johnston 2001
am-$Fe(OH)_3$ am-$Al(OH)_3$	As(V) 6.67$\times10^{-7}$ M Me(III)4.4–22$\times10^{-5}$ M (0.003–0.015 : 1)	As(V) sorption (pH 5–8) during coagulation, sedimentation, and filtration. Main factors are pH and coagulation dose. Ferric sulfate achieved better removal than alum and was less sensitive to increases in pH.	Gulledge and O'Connor 1973
am-$Fe(OH)_3$ am-$Al(OH)_3$	As(V,III)2.7–133$\times10^{-5}$ M Fe(III) 3.00$\times10^{-5}$ M (0.89–44.3 : 1)	As(V,III) sorption (pH 4–9, 0.01M $NaNO_3$) on coprecipitate and synthesized HFO & HAO. Competition with NOM, SO_4^{2-}, PO_4^{3-}. PO_4^{3-} decrease ZPC (inner sphere complex), SO_4^{2-} increase ZPC (outer sphere complex). Arsenic was much more efficiently removed by coprecipitate than post-synthesis HFO.	Hering et al. 1997
am-$Fe(OH)_3$	As(V) 4.7$\times10^{-7}$ M Fe(III) 5.0$\times10^{-5}$ M (0.01 : 1)	As(V,III) sorption (pH 4–9) on coprecipitate and synthesized HFO. Effects of Ca^+, SO_4^{2-}, PO_4^{3-}. For ferric chloride, stoichiometric conversion to the hydroxide solid (HFO) yields 0.55 mg/L per mg/L $FeCl_3$ added.	Hering et al. 1996
am-$Fe(OH)_3$	As 1.3μM(5) 0.7μM(3) Fe(III) 18μM(5) 54μM(3) (0.07:1(5), 0.01:1(3))	As(V,III) sorption (pH 4–9, 0.04M KNO_3, N_2-Air) on co-precipitated am-$Fe(OH)_3$ in 60mL. Monodentate inner sphere surface complexation. The effect of anions (silicate, sulfate, carbonate). Silicate has negative effect on As sorption but sulfate and carbonate has negligible effects. Sorption maxima (pH 6.8 & 9.2) was 0.65(V) & 0.1(III), 72%(V) & 11%(III) of Fe-OH site density (0.9mol/mol Fe).	Meng et al. 2000
am-$Fe(OH)_3$	As(V,III)3.3–133$\times10^{-8}$ M Fe(III) 5.00$\times10^{-5}$ M (6.6$\times10^{-4}$–2.7$\times10^{-2}$: 1)	As(V,III) sorption (pH 4–9, 0.01M $NaNO_3$) on synthesized HFO. SO_4^- decreased adsorption of As(V) and As(III), especially at low pH, while Ca^+ increased As(V) adsorption at high pH. 1mM bicarbonate did not affect either As(V) or As(III) adsorption greatly. ZPC of am-$Fe(OH)_3$ is 8.1	Wilkie and Hering 1996
am-$Fe(OH)_3$	As(V,III) 1– 100$\times10^{-5}$ M Fe(III) 1.87$\times10^{-3}$ M (0.005–0.5 : 1)	As(V,III) sorption (pH 3–11, 0.01M NaCl) on synthesized HFO. ZPC 8.5 by EM. ZPC large negative shift occurs as initial As(V) increased. The hydroxyl release (OH released/As(V) adsorbed) was 0.19 and 1.03 for pH 5 and pH 8 respectively. The ZPC shift vs. hydroxyl release. ATR-FTIR analysis.	Suarez et al. 1999
am-$Fe(OH)_3$	As(V) 0.05–1.33$\times10^{-5}$ M Fe(III) 0.05–1.0$\times10^{-3}$ M	As(V,III) sorption on hydrous ferric oxide. Modeling the experimental data from literatures.	Dzombak and Morel 1990
am-$Fe(OH)_3$ Goethite Magnetite	As(V) 10–100$\times10^{-6}$ M Fe(III) 3.4–56.2$\times10^{-4}$ M (0.0018– 0.30: 1)	As(V,III) sorption (pH 4–11, 0.01M $NaClO_4$,) on fresh HFO, goethite, and magnetite. Reduction of As(V) in the presence of HFO had only minor effects on or even decrease its mobility at neutral pH range. As(V,III) similar surface site densities on 3 oxides. Decrease in specific surface area and hence sorption site density that accompanies transformation of am-HFO to more crystalline phases could increase As mobility.	Dixit and Hering 2003
am- $Al(OH)_3$	As(V,III) 1.0$\times10^{-3}$ M Al(III) 1.3$\times10^{-3}$ M (0.77 : 1)	As(V,III) sorption (pH 2.5–10.5, 0.1M NaCl) on synthesized am-HAO. Sorption envelop experiment at various surface area. Surface area of HAO < 15m^2/g, HFO > 200m^2/g.	Goldberg et al. 2001
CHFO	As(V,III) 6.67$\times10^{-4}$ M Fe(III) 2.25$\times10^{-3}$ M (0.3 : 1)	As(V,III) sorption (pH 6) in 50mL vessel on synthesized CHFO. Batch and packed column test. Particle size was 0.14–0.29 mm. Various aging time, anions, and regeneration of As-rich CHFO.	Manna et al. 2003

Table 5.1 (Continued)

Adsorbent	Loading Ratio	Comment	Reference
Goethite	As/Goethite = 0–400 µmol / g (As : Fe = 0–0.036 : 1)	As(V,III) sorption (pH 3–8.5) on goethite. T-FTIR and ATR-FTIR analysis. Extraction experiment. As(V) has two A-type and one B-type OH groups. As(III) has two A-type and one C-type OH groups. Both As(V) and As(III) form bidentate Inner-sphere surface complexes (A-type bond) with Fe on goethite surface. Adsorption maxima was 200 µmole As / g goethite (0.02 mole As / mole Fe) at pH 5.5.	Sun and Doner 1996
Goethite	As(V,III) 1.0×10^{-3} M Fe(III) 2.8×10^{-2} M (0.036 : 1)	As(V,III) sorption (pH 3–11, 0.01M $NaNO_3$) on α-FeOOH in 100mL vessel. pH of kinetic was 6.5 for As(V) and 5.0 for As(III). Sorption kinetic and edge experiments at various DOCs co-existence.	Grafe et al. 2001
Goethite	As(V,III) 1.33×10^{-4} M Fe(III) $5.6–11.2\times10^{-2}$ M (0.0012–0.0024 : 1)	Shows pH edge at about pH 9 (pH 2–11). Adsorption density was 40 mg As/g goethite (0.05 mole As/mole Fe), 10.5 (Samaras (1994)). Isotherms relevant to anion sorption are typically pseudo-Langmuirian at all sorbate/sorbent ratios, indicating one dominant type of binding site (ligand exchange), Dzombak 1990)	Matis et al. 1997
Goethite	As(V) 1.07×10^{-3} M Goethite 223 m^2/L	Successfully applied the CD-MUSIC SCM to literature data for anion adsorption to goethite including As(V)-P competition. The CD-MUSIC is the most promising of the SCM for modeling complex natural systems.	Hiemstra and van Riemsdijk 1999
Goethite	As(V) 1.34×10^{-4} M Fe(III) 0.011M (1g/L)	As(V) adsorption on synthetic goethite primarily for a study of impact on flocculation and electrokinetics. Final pH varied but not defined. Average particle size was 2.5µm (80% of particles were less than 16µm).	Matis et al. 1999
Goethite	As(V) 0.001 M Fe(III) 0.112 M (10 g/L) (0.0088 : 1)	Kinetic study by pressure jump relaxation technique. I = 0.1–0.01 M $NaNO_3$. Monodentate (XH_2AsO_4, $XHAsO_4^-$ or $XHAsO_4^{2-}$) and bidentate (X_2HAsO_4 or $X_2AsO_4^-$) surface species were observed. First step is initial ligand exchange of aqueous oxyanion with goethite, forming an inner-sphere monodentate surface complex. Second step involves a second ligand exchange, resulting an inner-sphere bidentate surface complex.	Grossl et al. 1997
Goethite	As(V) 0.001 M Fe(III) 0.112 M (10 g/L)	EXAFS study of As(V) sorption (pH 3–11, 0.1M $NaNO_3$) on goethite. Monodentate binding favored at low surface coverages of As(V), bidentate at high surface coverages. Three different inner-sphere As(V)-goethite complexes characterized by As-Fe distance of 0.285, 0.323, and 0.360 nm.	Fendorf et al. 1997
Goethite	As(III) $1.3–2.6\times10^{-1}$ M Fe(III) 2.8×10^{-2} M (4.6–9.2 : 1)	As(III) sorption (pH 3–11) on α-FeOOH. As(V,III). Adsorption envelope. An EXAFS and XANES study of As(III) adsorption to a α-FeOOH indicates bidentate inner-sphere complexation (As-Fe distance was 0.338 nm), showing little pH or concentration dependence at surface coverages ranging from 1.9 to 4.6 µmol/m^2	Manning et al. 1998
Goethite Ferrihydrite	As/Fe = 0.001–0.6	EXAFS study of As(V). At larger As(V) concentrations on goethite surface the concentration of monodentate As(V) was found to be decreased. Three different inner-sphere As(V)-goethite complexes characterized.	Waychunas et al. 1995
Goethite	As/Goethite = 50–200 µmole/g (As:Fe = 0.005–0.02:1)	Infrared spectroscopy. As(V) as the acidic $HAsO_4^{2-}$ ion replaced singly coordinate surface OH groups. In this respect, As(V) is analogous to phosphate, but its larger size apparently causes it to interact more strongly with some of the OH groups that remain on the surface.	Lumsdon et al. 1984
Goethite	As(V) $8.8–34\times10^{-6}$ M Fe(III) 2.6×10^{-3} M (0.0034–0.013)	Arsenate & Phosphate sorption on goethite (pH 3–10 in 0.1–0.7 M NaCl solution). Arsenate shows a similar sorption pattern but a higher affinity than phosphate. The model prediction overestimates As(V) sorption at low initial As/Fe ratio (0.0034). Study of anion sorption competition modeling.	Gao and Mucci 2001
Goethite Lepidocrocite Hematite	As(V,III) 1.0×10^{-6} M Mineral 0.28M (25 g/L) (3.57×10^{-6} : 1)	As(V,III), MMAA and DMAA sorption on natural minerals (coarse-grained and very low He-Ar surface area). As sorption: generally goethite > lepidocrocite > hematite (pH 2–12, maximum often pH 5–8). Sorption: As(V) > DMAA=MMAA > As(III) below pH 7 and As(V) > As(III) > DMAA=MMAA above pH 7. FA decreases As sorption	Bowell 1994
α-,β-,γ-FeOOH Ferryhydrite HFO	Comparison of EXAFS results obtained at the As K-edges	The difference of structural behavior is not supported by the experimental data. The reason for this discrepancy is shown to result from a mistaken determination by Waychynas et al. (1993) of the As-Fe distance. Changes of the ferrihydrite structure at increasing As loading and ageing time are important.	Manceau 1995

Table 5.1 (Continued)

Adsorbent	Loading Ratio	Comment	Reference
GFH (Akageneite)	As(V) 1×10^{-5}–0.01M Fe(III) 0.011M (1g/L) (9×10^{-5}–0.9 : 1)	As(V) sorption (pH 5–9, 0.01 M NaCl) on co-precipitated and granular ferric hydroxide. Granulation dose not lead to a considerable decrease in adsorption density (1.0mmol As/g Fe). SO_4^- competition significant at mM concentrations below pH 7 only; phosphate competition at natural groundwater concentrations	Driehaus et al. 1998
Goethite, gibbsite, am-$Al(OH)_3$	As 0.27–1.07×10^{-3} M Me ?	As(V) sorption modeling using the data of Hingston (1970,1971) and Anserson and Malotky (1979). CCM was able to As-phospate competition results.	Goldberg 1986
Goethite Gibbsite	As(V) 1.33–2.66×10^{-4} M Me 0.028 M (2.5 g/L) (0.0048–0.0096 : 1)	Effects of pH (2–10)and competing anions (P, Mo) on As(V) sorption on α-FeOOH and γ-$Al(OH)_3$. Two model approaches of one-site (monodentate) and two-site (monodentate + bidentate) gave comparable fits to experimental sorption data and were consistent with competitive sorption observed in binary sorption envelops.	Manning and Goldberg 1996
Gibbsite	As(III) 13.4×10^{-3} M Me 20 g/L	As(III) sorption (pH 4–8, $NaNO_3$ 0.001-0.1M) on gibbsite. The As(III) exhibits weak affinity toward gibbsite. The heat of adsorption (ΔH_r was 20 kJ/mol) indicates surface physical bonding. The CD-MUSIC/TPM model combination described data well when initial As(III) < 10^{-5} M.	Weerasooriya et al. 2003
am-$Al(OH)_3$	As(V) 6.7–160×10^{-5} M Al(III) 0.002 M (0.16g/L) (0.0034–0.8 : 1)	As(V) sorption (pH 3.5–10.5) on post-precipitated $Al(OH)_3$. Kinetic, sorption envelop, EM, isotherm tests. Adsorption density was 1600μmol/g (1.6 mol As / mol Al) at pH 4.6. Fitted data to pH dependent Langmuir isotherm.	Anderson et al. 1976
Gibbsite (γ-$Al(OH)_3$)	As(III) 2.69–40×10^{-5} M Me 0.26 M (20 g/L) (1×10^{-5}–1.5×10^{-4} : 1)	As(III) sorption (pH 4–10, 0.01–0.1 M NaCl, N_2) on gibbsite. As(III) showed a weak affinity for gibbsite surface. Maximum sorption occurs around pH 8.2. As(III) sorption data was quantified by CD MUSIC model using the surface complexation postulated (outer-sphere complexation).	Weerasooriya et al. 2003
Clay minerals am-$Al(OH)_3$	As(V,III) 4.0×10^{-7} M Al(III) 3.2×10^{-2} M (1.25×10^{-5} : 1)	As(V,III) sorption (pH 2–11, 0.1M NaCl) on kaolinite, illite, montmorillonite, and am-$Al(OH)_3$ (post-synthesized) in 20mL vessel. Adsorption and desorption test. Oxidation of As(III) to As(V) was enhanced by heterogeneous oxidation on clay surfaces.	Manning and Goldberg 1977
Activated Alumina (Granular)	As(V,III) 2.67×10^{-7} M – 1.60×10^{-4} M Al(III) 9.8–49×10^{-4} M (5.5×10^{-5}– 0.16 : 1)	As(V,III) sorption (pH 2.5–12) on am-GAA. Properties of GAA. Equilibrium isotherm and kinetic experiment at various GAA size (mesh) and As/Al rations. Tortuosity analysis was conducted. ZPC of GAA is 8.4–9.1	Lin and Wu 2001
Aluminum oxide (γ-Al_2O_3)	As(V,III) 7.0×10^{-4} M Al(III) 9.8×10^{-2} M (0.007 : 1)	As(V,III) sorption (pH 3–9, 0.013–0.8M $NaNO_3$). XAS, sorption envelop, EM. Ionic strength and pH effects on sorption. EXAFS data indicate that As(VI) form inner-sphere complexes with a bidentate binuclear configuration, however, for As(III) inner- and outer-sphere adsorption coexist.	Arai et al. 2001
Aluminum oxide (γ-Al_2O_3)	As(V,III) 1–20×10^{-3} M Al(III) 1–5×10^{-2} M (0.02–2.0 : 1)	As(V,III) sorption (pH 3–10, 0.1M NaCl) on γ-Al_2O_3 in 125mL vessel. Sorption kinetic, ion strength, temperature, pH, equilibrium, fixed bed experiments. ZPC of γ-Al_2O_3 7.92, BET surface area 218m^2/g, intrinsic acidity constants, and N_t 4.6×10^{14} site/cm2. Adsorption of As is enhanced by the cation presence.	Ghosh and Yuan 1987
Activated Alumina (γ-Al_2O_3)	As(V) 6.67×10^{-5} M Alumina 0.067–1.0 g/L	As(V) from the artificial groundwater by sorption on activated alumina (γ-Al_2O_3). As(V) adsorption is extremely dependent on pH due to AA surface charge and As species and valence.	Rosenblum and Clifford 1982
Activated Alumina Activated Bauxite Activated Carbon	As(V,III) 5.0×10^{-6} M – 1.3×10^{-4} M Al(III) 2.0×10^{-2} M (2.5×10^{-4}–6.5×10^{-3} : 1)	As(V,III) sorption (pH 2–12, I = 0–0.67M). These isotherms indicate that the reactions are reversible phenomena and the coverage is monolayer. As(V,III) sorption capacity is in the order of alumina > bauxite > carbon. As(V) sorption efficiency was reduced in the presence of high ionic strength (Ca^{2+} and Na^+) at pH 7–8, less effect in As(III).	Gupta and Chen 1978
Alumina (α-Al_2O_3) Hematite (α-Fe_2O_3) Quartz (SiO_2)	As(V,III) 1.0×10^{-6} M Minerals 25 g/L	On natural alumina, sorption was As(V)>As(III)>MMAA=DMAA (pH>6). Maximum adsorption at pH 5 for As(V) and pH 7 for As(III). As(V) but not As(III) sorption decreased rapidly above pH 6. Log K_d (l kg^{-1}) at micromolar concentrations (pH 7) was 2.5–3.5 for As(V) and about 1.5 for As(III). FA decreased sorption.	Xu et al. 1991
Alumina, hematite, Kaolin, quartz	As(V) 1.0×10^{-6} M Minerals 25 g/L	As(V) sorption (pH 2–10) on natural minerals. Sorption decreases with pH; alumina=kaolin > hematite > quartz. Gives K_d values and isotherms at low concentrations. Some SO_4^{2-} competition especially below pH 7. FA (>10 mg/L) generally reduced sorption at pH 5–7 but not above pH 7 where FA is not adsorbed	Xu et al. 1988

Table 5.1 (Continued)

Adsorbent	Loading Ratio	Comment	Reference
Manganese oxide (δ-MnO_2)	As(III) 6.7×10^{-5} M Mn 92×10^{-5} M (0.073 : 1)	As(V,III) removal by $MnO_2(s)$ is similar, up to say 5 mmol As mol^{-1} Mn. Kinetic and Freundlich isotherm. As(III) oxidized to As(V). Rapid oxidation (minutes) and adsorption of As(III). Monitored Mn release and effect of pH, Ca^{2+}, phosphate and sulphate.	Driehaus et al. 1995
Manganese oxides (α-,β-,δ-MnO_2)	As(III) 1.33×10^{-3} M MnO_2 0.016 M (1.4 g/L) (0.083 : 1)	As(III) oxidation and As(V,III) sorption in presence of various MnO_2. As(III) adsorption (per unit weight of oxide): cryptomelane(α) > birnessite(δ) > pyrolusite(β) whereas for As(V) cryptomelane(α) > pyrolusite(β) > birnessite(δ) (not detectable). No isotherms given. First-order of As(III) depletion (oxidation+sorption)	Oscarson et al. 1983
Manganese oxides	As(III) 1.0×10^{-5} M Minerals 0.6 g/L	As(III) oxidation and As(V) sorption by MnOOH, α-MnO2, β-MnO2 and retention of oxidation products varies with pH.	Thanabalasingam and Pickering 1986
Pyrite (FeS_2)	As(III) 5.06×10^{-4} M As(V) 1.58×10^{-4} M FeS_2 0.85–8.35×10^{-2} M (0.002–0.012 : 1)	As(III,V) removal (pH 2–12, I = ? M) by pyrite fines (average diameter of 15µm, specific area of 4.67 m^2/g). pH envelop and sorption kinetic experiments were conducted. Further, lime and NaOH were added into the arsenic and pyrite suspension.	Zouboulis et al. 1993
Troilite (FeS) Pyrite (FeS_2)	As(III) 0–2.5×10^{-4} M Mineral	As(III) removal (pH 4–9, I = 0.005–0.5 M NaCl, buffer = 0.002 M acetate, MOPS, borate, and initial sulfide = 0–0.002 M). XAS, XANES, XPS experiments. Batch and flow-cell experiments.	Bostick and Fendorf 2003
Kaolinite Montmorillonite	As(V) 1.3–25×10^{-4} M Clays 1–4 g/L	Sorption of As(V,III), Se(IV) from municipal landfill leachate by clay minerals. Montmorillonite adsorbed more As and Se than kaolinite (higher edge surface area). Under alkaline conditions, As and Se are quite mobile	Frost and Griffin 1977
Activated Carbon		As(V) sorption (pH 3–11, I = 0.01 M) on various types of activated carbons. Adsorption density was 100 µmole As / g AC. Maximum As(V) removal occurs at pH 4.5. Electrostatic attraction and formation of specific chemical bond were major sorption mechanisms (the reversal of surface charge).	Huang and Fu 1984
Other Adsorbents		Silica gel impregnated with ferric hydroxide Porous resin loaded with crystalline hydrous zirconium oxide Ce(IV)-doped iron oxide Iron impregnated sand AC, Zr-AC, Absorptionsmittel 3, Fe^0, iron hydroxide granulates	Yoshida et al. 1976 Suzuki et al. 2000 Zhang et al. 2003 Vaishya and Gupta 2003 Daus et al. 2004
Engineering Fields	As(V) 2.67×10^{-7} M Fe(III) 6.2–18.5×10^{-5} M (0.001–0.004 : 1)	Enhanced coagulation for As(V) & turbidity removal (pH 5.5–7.0) using $FeCl_3$. As(V) was removed better in the $H_2AsO_4^-$ form than in the $HAsO_4^{2-}$ form (agreed with Gulledge & O'Conner). Although no correlation between turbidity and arsenic removal was found, turbidity removal is a prerequisite for arsenic removal.	Cheng et al. 1994
Engineering Fields		As(V) adsorption occurs during the rapid mixing stage, taking only a few minutes, and the As(III) fraction remaining soluble. Oxidation of As(III) to As(V) prior to coagulation is recommended (EPA,1998).	Gregor 2001
Engineering Fields	As(T) 1.3×10^{-4} M Fe(III) 9–18×10^{-3} M (0.007–0.014 : 1)	Arsenic removal from wastewater using ferric chloride, hydrated lime, sodium sulfide, and alum. $Ca(OH)_2/FeCl_3$ (pH 10) was able to remove over 99% of arsenic.	Harper and Kingham 1992
Engineering Fields		Arsenic removal from wastewater. The pH 6.5 and the ratio of As/Fe 0.2 can reduce residual arsenic to near or below analytical detection limits. Electro-chemical cell and H_2O_2 are recommended.	Brewster 1992
Engineering Fields	As(T) 1.85×10^{-7} M – 4.08×10^{-5} M	POU (point-of-use) treatment techniques for arsenic removal from drinking water. RO, ion exchange, GAA process.	Fox 1989
Engineering Fields	As(T) 2.1×10^{-8} M Fe(III) 1.9–6.2×10^{-5} M (0.00034–0.0011 : 1)	Arsenic removal with ferric chloride and alum from drinking water treatment. This utility's goal of 90% arsenic removal was attained through treatment with 6.5 mg/L $FeCl_3$.	Scott et al. 1995
Engineering Fields	As(V) 6.7×10^{-7} M As(III) 4.0×10^{-6} M Me 30 mg/L	As(V,III) removal (pH 5–9). Significant removal of arsenic with conventional drinking water treatment and superior performance by the ferric coagulant (ferric sulfate) than aluminum coagulant (alum).	Sorg and Logsdon 1978
Engineering Fields	As(T) 2.0×10^{-3} M	Arsenic (organic and inorganic) removal form groundwater. Fenton oxidation + coprecipitation was best. Four type adsorbent were tested (AC, AA, ferrous sulfide, resin). TCLP test. UV and ozone oxidation tested.	Kuhlmeier and Sherwood 1996
Engineering Fields	As 6.7(5)/ 67(3)$\times10^{-7}$ M Me 5–40×10^{-6} M	As(V,III) removal (pH 6–9.5) on HFO and HAO during coagulation. Two metals are equivalent in As(V) removal on the based on molar concentration at pH < 7.5.	Edwards 1994

Table 5.1 (Continued)

Adsorbent	Loading Ratio	Comment	Reference
Engineering Fields		First to survey soluble arsenic removal at full-scale water treatment (coagulation, Fe-Mn oxidation, softening). Alum coagulation was not as effective as expected. During coagulation As(V) removal was limited by small size HFO(HAO) (under 0.45μm, filter pore size) that adsorbed arsenic.	McNeill and Edwards 1995
Engineering Fields		Arsenic removal during coagulation or Fe-Mn oxidation. Importance of particulate arsenic. At the low sorbate/sobent ratios common in water treatment, a simple linear isotherm may be derived either a Langmuir isotherm or a diffuse-layer model using a mass balance on As and on sorption sites on the metal surface.	McNeill and Edwards 1997

HFO = hydrous ferric oxide, amorphous ferric hydroxide, amorphous ferric oxy-hydroxide
CHFO = crystalline hydrous ferric oxide
HAO = hydrous aluminum oxide
GFH = granular ferric hydroxide
AA = activated alumina
AC = activated carbon
GAA = granular activated alumina
IIS = iron impregnated sand
IOCS = iron oxide coated sand
SCM = surface complexation model
EXAFS = extended X-ray absorption fine structure
XANES = X-ray absorption near-edge structure
EDAX = energy dispersive analysis of X-rays
XAS = X-ray absorption spctroscopy
FTIR = Fourier transform infrared
T-FTIR = Transmission-Fourier transform infrared
ATR-FTIR = Attenuated Total Reflectance-Fourier transform infrared
MMAA = monomethylarsonic acid, $CH_3AsO(OH)_2$
DMAA = dimethylarsinic acid, $(CH_3)_2AsO(OH)$
DOC = dissolved organic compound
NOM = natural organic material
FA = fulvic acid
CD-MUSIC = charge distribution-multisite complexation model
DLM = diffuse layer model (double layer model)
CCM = constant capacitance model
TLM = triple layer model
EM = electrophoretic mobility

5.3 Background

5.3.1 Characterization of Hydrous Ferric Oxide

Hydrous ferric oxide (HFO) is generated during rapid ferric iron hydrolysis and also called amorphous ferric hydroxide, amorphous iron oxyhydroxide, and 2-line ferrihydrite ($Fe_pO_r(OH)_s{\cdot}nH_2O$) (Schwertmann and Cornell 2000). Although many researchers have proposed the chemical formula of ferrihydrite, neither the single formula nor the structure of ferrihydrite has been fully established (Robinson et al. 1981; Cornell et al. 1989; Schwertmann et al. 1999). The disagreement results from the rate and conditions of hydrolysis; temperature, aging time, [OH]/[Fe] ratios, and the co-existence of impurities. Measurements of HFO density are in the range of 2.2 to 4.0 g/cm^3, with an average density of 3.5 g/cm^3 and the formula weight of HFO is reported as 89 g HFO/mol Fe (Dzombak and Morel 1990).

Freshly generated hydrous ferric oxide particles are reported to be fractal (fractal dimension D_f of 1.7 to 2.3), which is mainly dependent of [OH]/[Fe] ratios (Lagavankar and Gemmell 1968; Wiesner and Mazounie 1987; Lo and Waite 2000). Furthermore, it is reported that the size of colloidal hydrous ferric oxide ranges from 10 nm at low [OH]/[Fe] ratio to 700 nm at high [OH]/[Fe] ratio (Tchoubar et al. 1991). It should be noted that these HFO colloid particle size values were determined below the flocculation threshold. However, once flocculation is induced (for example, by reduction in surface charge through pH increase), HFO aggregates are easily formed and can be reached to maximum aggregate size depending on flocculation conditions; fluid strain-rate, mixing device, electrolyte concentration, and solution pH. According to an experimental study for freshly precipitated HFO flocculation (Lo and Waite 2000), the initial colloid particle size distribution of freshly generated HFO ranges from 0.8 to 33.7 μm, with the volume average diameter of 5.2 μm.

A theoretical surface area of HFO is reported to be 840 m^2/g assuming 2-nm-diameter spheres and its density of 3.57 g/cm^3 (Davis and Leckie 1978). On the other hand, according to the experimental studies, measurements of HFO surface area are in the range of 159 to 750 m^2/g. This lower experimental value of HFO surface area than theoretical calculation results from experimental technique such as nitrogen gas adsorption with BET analysis which is the most popular experimental method. However, the method is not applicable to porous solids such as HFO due to low reproducibility and strong dependency of the outgassing procedure. This low reliability of the method is induced from surface decomposition during the drying step for gas adsorption measurements. This surface decomposition can lead to significant underestimates of surface area. Resulting from this disadvantage of nitrogen gas adsorption with BET analysis, the experimental measurements of the specific surface area of HFO may be lower than the actual value. Thus, it is commonly accepted that the HFO surface area be 600 m^2/g, which actual HFO surface area value is less than 840 m^2/g and more than 200 to 300 m^2/g (Davis and Leckie 1978).

Sorption site density (mole site/ mole Fe) of HFO are divided into two types; a small set of high-affinity strong sites and a large set of low-affinity weak sites. A weak site is the total reactive site to adsorb proton, cation and anion, whose site density is determined from experimental sorption maxima (also called maximum sorption capacity). A strong site corresponds to a cation-HFO binding site and its site density is determined from a sorption isotherm. In general, the value of the two types of site densities (strong and weak site density) on HFO are accepted as 0.005 and 0.1 ~ 0.3 mol site/mol Fe, respectively, from the arithmetic mean of the various experimental data (Dzombak and Morel 1990).

The point of zero charge (ZPC or pH_{ZPC}) for HFO can be measured by acid-base titration, electrophoresis, and salt titration. According to the experimental studies, the ZPC values are in the range of 7.9 to 8.2. Further, when sufficient parameters (HFO properties and acid-base reaction coefficient) for surface complexation modeling are provided, the theoretical ZPC value can be calculated (details will be discussed in next section).

5.3.2 Surface Complexation Modeling

Metal containing mineral surfaces become hydrated by reacting with water. The water coordinately reacts with metal ions at the surface by donation of lone electron pairs followed by chemical dissociation of the hydrogen resulting in the surface functional groups defined as $\equiv XOH$, where $\equiv X$ represents a metal ion of the oxy-hydroxide mineral surface bound to reactive hydroxyl group (Schindler and Stumm 1987). These surface functional groups exhibit acid-base behavior by donating or accepting protons and altering the surface charge.

Five different electrostatic double layer equilibrium models can be used for surface complexation modeling; CCM (Constant Capacitance Model), DLM (Diffuse Layer Model), TLM (Triple Layer Model), BSM (Basic Stern Model), and Triple Plane Model (TPM). These five models are closely related by considering a surface charge (σ) using columbic correction factor ($\exp(-F\psi_i / RT)$), where ψ_i is the surface potential (volt) in the *i*th surface plane, F is the Faraday constant (C $\mathrm{mol_c}^{-1}$), R is the molar gas constant (8.314 J mol^{-1} K^{-1}), and T is the absolute temperature (K)) to account for the effect of surface charge on surface complexation (Table 5.2 and Fig. 5.1). Each surface complexation model treats sorption as a surface complexation reaction (that is, the reaction is treated as analogous to a solution phase complexation reaction governed by a mass action equation) and accounts for the electrostatic potentials at the charged surface. Although these models may be expressed with similar mass law and material balance equations, each surface complexation model involves different descriptions of the electric double layer in the way that electrostatics is included. Surface charge results from protonation, dissociation, and/or surface complexation reactions of reactive surface hydroxyl groups at solid surfaces. The pH and ionic strength of solution determines the sign and magnitude of the solid surface charge.

Huang, Stumm, and Jenkins (Huang and Stumm 1973) first applied the diffuse layer model to the surface complexation model and Dzombak and Morel (Dzombak and Morel 1990) extended the diffuse layer model to the generalized two-layer model (DLM). Like the CCM, DLM assumes that all surface complexes are inner-sphere complexes as shown in Figs. 5.2 and 5.3. The DLM assumption greatly simplifies the surface charge balance as Eq. (5.1).

$$\sigma_P = \sigma_H + \sigma_{is} \tag{5.1}$$

were, σ_P represents the total net surface charge density and σ_H (adsorbed proton charge density) is established through association and dissociation reactions of H^+ as described by Eqs. (5.2) and (5.3), and σ_{is} (inner-sphere complex charge density) generated from the metal/ligand sorption onto the HFO surfaces.

The diffuse layer model proposed by Huang, Stumm, and Jenkins (Huang and Stumm 1973) can lead to very high surface charge. To prevent this extreme charge on the solid surface Dzombak and Morel divided the diffuse layer into two planes of charge used to represent the surface (Dzombak and Morel 1990). That is, all surface complexes are placed into the surface *o*-plane and the diffuse layer commences at the *d*-plane and extends into solution phase (see Fig. 5.4). Furthermore, unlike the CCM, no capacitance parameters are required in the DLM. This simplicity can make it easy to handle the input of model parameters in surface complexation modeling.

Table 5.2 Surface Complexation Model Matrix (Venema et al. 1996)

Interface Model	Complexation Model	
	1 pK $\equiv XOH^{-1/2} + H^{+} \Leftrightarrow \equiv XOH_2^{+1/2}$ pK_1	2 pK $\equiv XO^{-} + H^{+} \Leftrightarrow \equiv XOH^{o}$ pK_{H1} $\equiv XOH^{o} + H^{+} \Leftrightarrow \equiv XOH_2^{+}$ pK_{H2}
Diffuse Double Layer Only		Constant Capacitance Model (CCM) Diffuse Layer Model (DLM)
Diffuse Double Layer + one charge-free layer	Basic Stern Model (BSM)	
Diffuse Double Layer + Two charge-free layers	Three Plane Model (TPM)	Triple Layer Model (TLM)

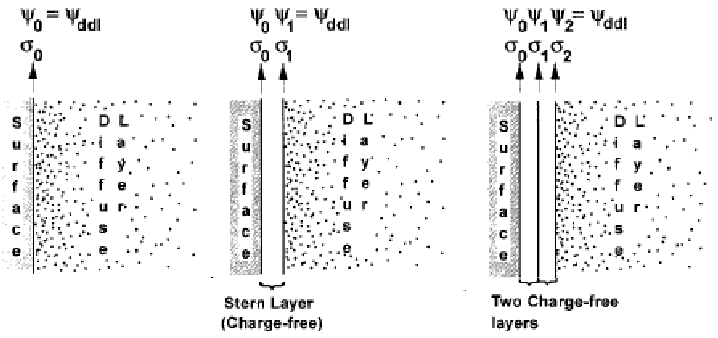

a) DLM (b) BSM (c) TPM/TLM

Figure 5.1 The diagram of various surface complexation models (Venema et al. 1996)

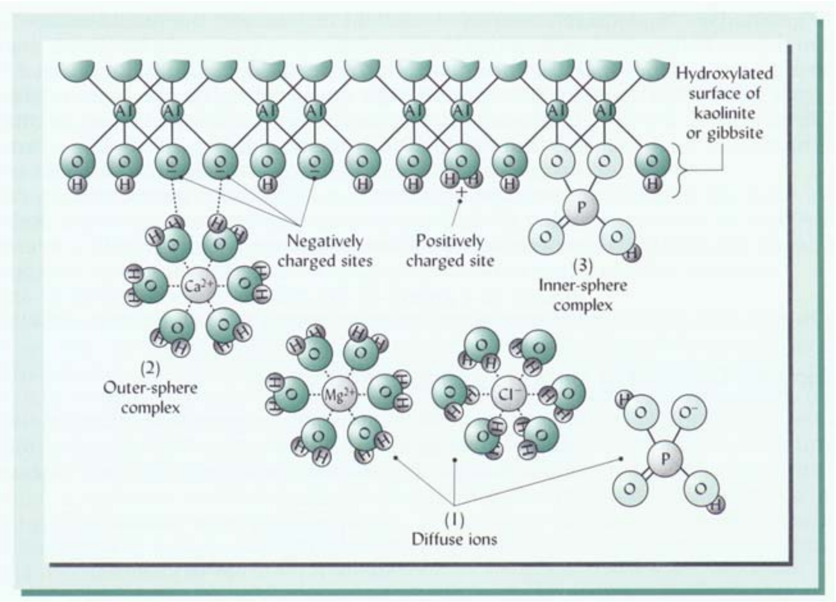

Figure 5.2 A diagrammatic representation of the adsorption of ions on a HFO surface by the formation of outer-sphere and inner-sphere complexes (Brady and Weil 2002)

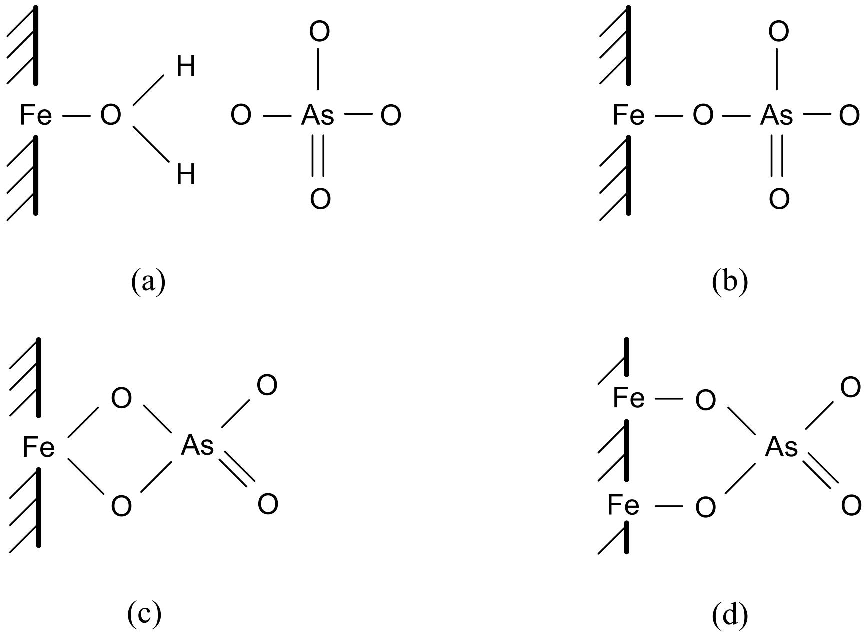

Figure 5.3 Arsenate sorption on a HFO surface by the formation of surface complex ((a) outer-sphere complex, (b) inner-sphere monodentate complex, (c) inner-sphere bidentate complex (mono-nuclear), and (d) inner-sphere bidentate complex (bi-nuclear)

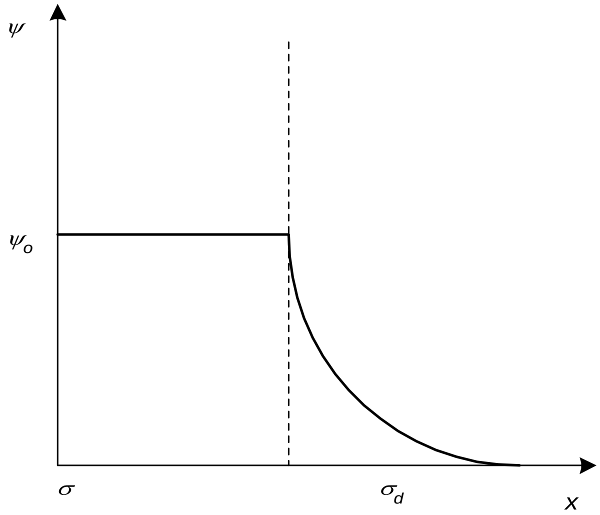

Figure 5.4 Generalized two-layer model (DLM)

In DLM, metal ion sorption is considered to occur on two types of sites: a small set of high-affinity strong sites (*s*) and a large set of low-affinity weak sites (*w*). Application of the DLM to systems containing both metal and ligand species is difficult because the pool of binding sites for protonation-dissociation and ligand adsorption is split into two sets of binding sites of different affinity for metal adsorption. For this reason, mass balance and charge balance equations are provided separately for metal and ligand adsorption.

Table 5.3 The Reactions Related to the Surface Complexation Model (DLM)

Reactions	Equilibrium Constants	
$\equiv \mathrm{XOH} + \mathrm{H}^+ \Leftrightarrow\ \equiv \mathrm{XOH}_2^+$	$K_{+(\mathrm{int})} = \dfrac{[\equiv \mathrm{XOH}_2^+]}{[\equiv \mathrm{XOH}][\mathrm{H}^+]}\exp[F\psi / RT]$	(5.2)
$\equiv \mathrm{XOH} \Leftrightarrow\ \equiv \mathrm{XO}^- + \mathrm{H}^+$	$K_{-(\mathrm{int})} = \dfrac{[\equiv \mathrm{XO}^-][\mathrm{H}^+]}{[\equiv \mathrm{XOH}]}\exp[-F\psi / RT]$	(5.3)
$\equiv \mathrm{X^sOH} + \mathrm{M^{m+}} \Leftrightarrow\ \equiv \mathrm{X^sOM}^{(m-1)} + \mathrm{H}^+$	$K_{M(\mathrm{int})}^{s} = \dfrac{[\equiv \mathrm{X^sOM}^{(m-1)}][\mathrm{H}^+]}{[\equiv \mathrm{X^sOH}][\mathrm{M}^{m+}]}\exp[(m-1)F\psi / RT]$	(5.4)
$\equiv \mathrm{X^wOH} + \mathrm{M^{m+}} \Leftrightarrow\ \equiv \mathrm{X^wOM}^{(m-1)} + \mathrm{H}^+$	$K_{M(\mathrm{int})}^{w} = \dfrac{[(\equiv \mathrm{X^wO})_2\mathrm{M}^{(m-2)}][\mathrm{H}^+]^2}{[\equiv \mathrm{X^wOH}]^2[\mathrm{M}^{m+}]}\exp[(m-2)F\psi / RT]$	(5.5)
$\equiv \mathrm{XOH} + \mathrm{H}^+ + \mathrm{L}^{l-} \Leftrightarrow\ \equiv \mathrm{XL}^{(l-1)-} + \mathrm{H_2O}$	$K_{L(\mathrm{int})}^{1} = \dfrac{[\equiv \mathrm{XL}^{(l-1)-}]}{[\equiv \mathrm{XOH}][\mathrm{H}^+][\mathrm{L}^{l-}]}\exp[-(l-1)F\psi / RT]$	(5.6)
$\equiv \mathrm{XOH} + 2\mathrm{H}^+ + \mathrm{L}^{l-} \Leftrightarrow\ \equiv \mathrm{XHL}^{(l-2)-} + \mathrm{H_2O}$	$K_{L(\mathrm{int})}^{2} = \dfrac{[\equiv \mathrm{XHL}^{(l-2)-}]}{[\equiv \mathrm{XOH}][\mathrm{H}^+]^2[\mathrm{L}^{l-}]}\exp[-(l-2)F\psi / RT]$	(5.7)

For metal surface complexation these equations are:

$$[\equiv \mathrm{X^sOH}]_\mathrm{T} = [\equiv \mathrm{X^sOH}] + [\equiv \mathrm{X^sOH_2^+}] + [\equiv \mathrm{X^sO^-}] + [\equiv \mathrm{X^sOM}^{(m-1)}] \tag{5.8}$$

$$[\equiv \mathrm{X^wOH}]_\mathrm{T} = [\equiv \mathrm{X^wOH}] + [\equiv \mathrm{X^wOH_2^+}] + [\equiv \mathrm{X^wO^-}] + [\equiv \mathrm{X^wOM}^{(m-1)}] \tag{5.9}$$

$$\sigma = \frac{F}{2a}\left\{\begin{array}{l}[\equiv \mathrm{X^sOH_2^+}] + [\equiv \mathrm{X^wOH_2^+}] + (m-1)[\equiv \mathrm{X^sOM}^{(m-1)}] \\ +(m-1)[\equiv \mathrm{X^wOM}^{(m-1)}] - [\equiv \mathrm{X^sO^-}] - [\equiv \mathrm{X^wO^-}]\end{array}\right\} \tag{5.10}$$

For ligand surface complexation the equations are:

$$[\equiv \mathrm{XOH}]_\mathrm{T} = [\equiv \mathrm{XOH}] + [\equiv \mathrm{XOH_2^+}] + [\equiv \mathrm{XO^-}] + [\equiv \mathrm{XL}^{(l-1)-}] + [\equiv \mathrm{XHL}^{(l-2)-}] \tag{5.11}$$

$$\sigma = \frac{F}{2a}\left\{[\equiv \mathrm{X^wOH_2^+}] - [\equiv \mathrm{XO^-}] - (l-1)[\equiv \mathrm{XL}^{(l-1)-}] - (l-2)[\equiv \mathrm{XHL}^{(l-2)-}]\right\} \tag{5.12}$$

Further, according to the Gouy-Chapman theory, the surface charge density σ_P (C m^{-2}) is related to the surface potential ψ_0 (volt) as

$$\sigma_P = \sqrt{(8RT\varepsilon\varepsilon_o c)\times 10^3}\,\sinh\left(\frac{zF\psi_0}{2RT}\right) \qquad (5.13)$$

where ε is the relative dielectric constant of water (78.5 at 25°C), ε_o is the permittivity of free space (8.854×10^{-12} C^2 J^{-1} m^{-1}), c is the molar electrolyte concentration (M), and z is the ionic charge (Stumm and Morgan 1996).

This set of equations (Eqs. (5.2)～(5.13)) can be solved with a computer program (i.e., MINTEQA, FITEQL, MINEQL, and PHREEQ) using the mathematical approach outlined by Westall and Hohl (1980). Several applications of the surface complexation to arsenic sorption are summarized on Table 5.4.

Table 5.4 Surface Complexation Modeling for Arsenic

Adsorbent	Ratio	Model	Reference
am-Fe(OH)$_3$ Goethite Magnetite	As(V) $10–100\times10^{-6}$ M Fe(III) $3.4–56.2\times10^{-4}$ M As/Fe = 0.0018– 0.3	DLM by FITEQL	Dixit and Hering 2003
am-Fe(OH)$_3$	As(V,III)$3.3–133\times10^{-8}$ M Fe(III) 5.00×10^{-5} M As/Fe = $6.6\times10^{-4}–2.7\times10^{-2}$	DLM by MINEQL$^+$	Wilkie and Hering 1996
2-line ferrihydrite	As $53–210\times10^{-6}$ M Fe(III) 1.7×10^{-3} M As/Fe = 0.03–0.12	DLM by FITEQL	Swedlund and Webster 1999
am-Fe(OH)$_3$	As(V) $0.05–1.33\times10^{-5}$ M Fe(III) $0.05–1.0\times10^{-3}$ M As/Fe = 0.0266–50	DLM (generalized two layer model)	Dzombak and Morel 1990
am-Fe(OH)$_3$ (Ferrihydrite)	As(V) $0.5–2.0\times10^{-4}$ M Fe(III) $1.0–2.0\times10^{-3}$ M As/Fe = 0.025–0.2	TLM Modified Langmuir isotherm Equilibrium partition	Hsia et al. 1992
am-Fe(OH)$_3$	As 1.3μM(5) 0.7μM(3) Fe(III) 18μM(5) 54μM(3) As/Fe = 0.07 (V), 0.01 (III)	TLM by MINEQA2 Langmuir isotherm	Meng et al. 2000
am-Fe(OH)$_3$ am-Al(OH)$_3$	As $0.01–1.0\times10^{-3}$ M Me 4.0, 0.5g/L	TLM & CCM by FITEQL	Goldberg and Johnston 2001
Goethite	As(V) $8.8–34\times10^{-6}$ M Fe(III) 2.6×10^{-3} M As/Fe = 0.0034–0.013	BSM,TLM,CCM, by FITEQL	Gao and Mucci 2001
Goethite	As(V) 0.001 M Fe(III) 0.112 M (10 g/L) As/Fe = 0.0088	CCM by FITEQL	Grossl et al. 1997
Goethite	As(III) $1.3–2.6\times10^{-1}$ M Fe(III) 2.8×10^{-2} M As/Fe = 4.6–9.2	CCM by FITEQL	Manning et al. 1998

Table 5.4 (Continued)

Adsorbent	Ratio	Model	Reference
Goethite Gibbsite	As(V) 1.33–2.66×10^{-4} M Me 0.028 M (2.5 g/L) As/Fe = 0.0048–0.0096	CCM by FITEQL	Manning and Goldberg 1996
Goethite, gibbsite, am-Al$(OH)_3$	As 0.27–1.07×10^{-3} M Me ?	CCM by FITEQL	Goldberg 1986
Goethite	As(V) 1.07×10^{-3} M Goethite 223 m^2/L	CD-MUSIC	Hiemstra and van Riemsdijk 1999
Gibbsite	As(III) 13.4×10^{-3} M Me 20 g/L	CD-MUSIC/TPM	Weerasooriya et al. 2003
Clay minerals am-Al$(OH)_3$	As(V,III) 4.0×10^{-7} M Al(III) 3.2×10^{-2} M As/Al = 1.25×10^{-5}	CCM by FITEQL	Manning and Goldberg 1977
am-Fe$(OH)_3$	As(V) 4.7×10^{-7} M Fe(III) 5.0×10^{-5} M As/Fe = 0.0094	SCM by MINEQL$^+$ Simple isotherm model	Hering et al. 1996
Aluminum oxide (γ-Al_2O_3)	As(V,III) 1–20×10^{-3} M Al(III) 1–5×10^{-2} M As/Al = 0.02–2.0	SCM (for proton) Langmuir isotherm	Ghosh and Yuan 1987

5.3.3 Arsenic Sorption Kinetics

The thermodynamic sorption equilibrium model (surface complexation model) can predict the final equilibrium state of the system. However, this equilibrium model cannot predict the pathway or rate of sorption toward the equilibrium state. The sorption kinetic model allows the prediction of reaction rates and provides insight to the reaction pathway or mechanism. Especially, with respect to coupling this sorption model with a coagulation kinetic model, the sorption kinetic model should be developed to provide surface charge evolution versus time, which is related to a collision efficiency parameter in coagulation modeling.

Both transport and chemical reaction processes can affect the sorption rates at the solid-liquid interface. Transport processes include: (a) transport in the solution phase, (b) transport across the liquid film at the solid-liquid interface (film diffusion), (c) transport in liquid-filled macropores, and (d) particle diffusion processes. The processes of (a) to (c) are nonactivated diffusion processes and occur in mobile regions. The process (d) includes diffusion of sorbate occluded in micropores (pore diffusion) and along pore-wall surfaces (surface diffusion) and diffusion processes in the bulk of the solid, all of which are activated diffusion processes (Crittenden et al. 1987; Tien 1994). Pore and surface diffusion within the immediate region can be referred to as intraparticle diffusion and diffusion in the solid can be called interparticle diffusion (Tien 1994).

The slowest of the chemical reactions and transport processes is the rate limiting step (Sparks 1999). In this study, it is assumed that the limiting step of arsenic sorption onto hydrous ferric oxide is the transport process of intraparticle diffusion through particle pores or surfaces (Fuller et al. 1993). That is, transported arsenic can be rapidly adsorbed on particle effective sites and reaches equilibrium state with local concentrations of arsenic. The traditional simplified sorption kinetic models include: the ordered models (i.e., zero-, first-, and second-order), the Elovich equation, and the Parabolic equation (Sparks 1999). Recently, enhanced computational equipment and numerical schemes have been developed and applied to the diffusion models based on the numerical solution of partial differential equations. In a number of studies, it has been shown that several simplified kinetic models describe rate data well, based on correlation coefficients and standard errors of the estimate. Despite this advantage of the simplified sorption kinetic models, there is often not a consistent relationship between the equation and physicochemical properties of the adsorbents (i.e., size, porosity, density, initial concentration, volume, mass, and a surface diffusion coefficient) and adsorbate (i.e., liquid film mass transfer coefficient). Another problem with some of the simplified kinetic models is that they are empirical and no meaningful universal rate parameters can be obtained.

The finding that slower reactions at the particle/liquid interface can be described by diffusion models indicates that the kinetics of chemical processes cannot be considered separately from physically limited transport phenomena. Thus, such a combination of processes cannot be treated using simplified sorption kinetic models. If one assumes that there are sites that cannot be reached directly from the liquid phase, but can be reached after the adsorbate has undergone adsorption and desorption at other sites, one cannot separate chemical kinetics from diffusion limited kinetics. The overall kinetic process obeys a diffusion equation since diffusion is the rate limiting process.

Pore Diffusion Model (PDM)

A pore diffusion model operates if the intraparticle mass transfer is due only to the diffusion of adsorbates through the pore fluid. Assuming the simple case of single species adsorption, Fick's law application, and spherical shape of adsorbent, the macroscopic conservation equation is derived as,

$$\varepsilon_p \frac{\partial c}{\partial t} + \rho_p \frac{\partial q}{\partial t} = \frac{1}{r_p^2} \frac{\partial}{\partial r_p}\left(D_p r_p^2 \frac{\partial c}{\partial r_p} \right) \qquad (5.14)$$

Initial condition $c = 0$ $t = 0,\ 0 \le r_p \le a_p$ (5.15)

Boundary conditions $\dfrac{\partial c}{\partial r_p} = 0$ $t > 0,\ r_p = 0$ (5.16)

$$k_f (c_b - c) = D_p \frac{\partial c}{\partial r_p} \qquad t > 0, r_p = a_p \qquad (5.17)$$

where c is the adsorbate concentration in the pore fluid and q is the adsorbate concentration of the adsorbed phase corresponding to any given point within the particle, k_f is the liquid film mass transfer coefficient, D_p is the pore diffusion coefficient, and c_b is the concentration in bulk aqueous phase. It should be noted that the equation of the PDM still requires that one specify appropriate initial and boundary conditions as well as an additional relationship between c and q.

In the diffusion kinetic models (i.e., PDM and SDM), q is assumed to be in equilibrium with c in the adjacent pore water with the isotherm. The equations are often used to describe the relationship between c and q including the Langmuir isotherm (Eq. (5.18)) and the Freundlich isotherm (Eq.(5.19)),

$$q = \frac{x}{m} = \frac{q_m b c_{eq}}{1 + b c_{eq}} \tag{5.18}$$

and

$$q = \frac{x}{m} = K c_{eq}^{1/n} \tag{5.19}$$

where x (μg) is the mass of adsorbate sorbed at time t, m (g) is the mass of adsorbent, c_{eq} (μ/L) is the adsorbate equilibrium concentration, q_m (μg/g) is a constant indicating the adsorbate sorbed completely required to saturate a unit mass of adsorbent, b (L/μg) is a constant related to the energy of adsorption, K (L/μg) is an experimental constant indicating the adsorption capacity of adsorbent, and n (dimensionless) is an experimental constant indicating the sorption intensity of adsorbent. Considered together with the mass balance of adsorbate (c) in the solid-liquid system, Eq. (5.14) is combined with Eqs. (5.15) to (5.17) and either Eq. (5.18) or (5.19) for solving c and c_b at different time using various numerical methods (i.e., finite difference method using explicit or implicit scheme and orthogonal collocation method).

Surface Diffusion Model (SDM)

In the case in which the intraparticle mass transfer is effected through the diffusion of the adsorbed molecules along pore-wall surfaces, for single species adsorption with spherical particles and assuming that Fick's law applies, the intraparticle mass transfer is described as,

$$\left(\frac{\varepsilon_p}{\rho_p}\right)\frac{\partial c}{\partial t}+\frac{\partial q}{\partial t}=\frac{1}{r_p^2}\frac{\partial}{\partial r_p}\left(D_s r_p^2\frac{\partial q}{\partial r_p}\right) \tag{5.20}$$

In the previous pore diffusion model scheme, Eq. (5.14) can be replaced by Eq. (5.20) in the surface diffusion model (SDM). Similar to PDM, the SDM equation can be readily solved with several conditions such as an initial condition (Eq. (5.15)), boundary conditions (Eqs. (5.16) and (5.17)), and a relationship between *c* and *q* (Eq. (5.18) or (5.19)).

5.4 Results and Discussion

5.4.1 Arsenate Sorption Equilibrium

A surface complexation model, generalized two-layer model (DLM), was used to predict the As(V) sorption pH envelops (Dzombak and Morel 1990). Characteristic parameters for HFO (i.e., stoichiometry, specific surface area, site density, and As(V) sorption density) were used as recommended by several researchers (Dzombak and Morel 1990; Wilkie and Hering 1996; Dixit and Hering 2003) and these parameters are displayed as Table 5.5. In addition to the HFO physico-chemical parameters, two sets of thermodynamic data were provided in this surface complexation modeling; aqueous protonation constants and intrinsic surface complexation constants. A generalized two-layer model (DLM) has two advantages to use as a surface complexation modeling tool; compared to other surface complexation models, the least modeling parameters are needed and the surface potential can be easily determined from the diffuser layer boundary as shown in Figs. 5.1 and 5.4.

For surface complexation modeling, VMINTEQ/MINTEQA, FITEQL, and PHREEQC can be introduced for this purpose. VMINTEQ/MINTEQA and PHREEQC are widely used as public domain programs and FITEQL is the most popular commercial software in surface complexation modeling due to a parameter estimation technique for determining equilibrium constants using experimental data. In this study, PHREEQC was introduced to couple the surface complexation model with sorption kinetic model. Furthermore, although both MINTEQ/VMINTEQ and FITEQL have various surface complexation model techniques (i.e., CCM, BSM, TLM, DLM, TPM), it is impossible to access these program with external input and output files to interface with other programs (i.e., MATLAB and FORTRAN). Using PHREEQC, one can access external programs with user-made data file and obtain results with user-selected output file. Thus, to accomplish coupling, PHREEQC is necessary to combine surface complexation model with a sorption kinetic model and a coagulation model.

According to an EXAFS study for As(V) sorption onto goethite (Fendorf et al. 1997), it was reported that the monodentate complex was mostly found at low

As(V)/surface ratio while the bidentate complex was prevalent at high As(V)/surface ratio. In addition, the bidentate-binuclear complexes were found to be in the greatest proportion at the highest As(V)/surface ratio. Furthermore, surface complexation process between arsenate and goethite surface could be subdivided into two steps; a relative fast step forming an inner-sphere monodentate surface complex and the subsequent slow step resulting an inner-sphere bidentate surface complex. Thus, although both inner-sphere monodentate and bidentate complexes binding As(V) onto HFO surface species has been found by experimental studies using EXAFS (Extended X-ray Absorption Fine Structure) spectroscopy (Waychunas et al. 1993; Manceau 1995; Fendorf et al. 1997), inner-sphere bidentate surface complexation reactions (Eqs. (5.31) and (5.32) in Table 5.6) were excluded and only monodentate complexations were considered in this study as sufficient information on the proportion of monodentate and bidentate surface species was not available. However, the equilibrium constants for the inner-sphere bidentate complexation can be estimated through a numerical parameter estimation scheme (i.e., least square error method) with sufficient experimental data but this is beyond scope of this study.

Table 5.5 HFO Surface Parameters for Surface Complexation Modeling (DLM)

Parameter	Value
Stoichiometry	89g HFO/mol Fe
Specific surface area	600 m^2/g
As(V) sorption density	0.24 mol As(V)/mol Fe 2.6 sites/nm^2
Weak sorption sites ($\equiv X^wOH$)	0.20 mol sites/mol
Strong sorption sites ($\equiv X^sOH$)	0.005 mol sites/mol Fe

Table 5.6 Reaction of As(V) Surface Complexation Modeling onto the HFO

[1] Aqueous protonation constant	Log k	
Acid-Base Reactions		
$H_3AsO_4 + 2H^+ + 2e^- \Leftrightarrow H_3AsO_3 + H_2O$	18.90	(5.21)
$HAsO_4^{-2} \Leftrightarrow AsO4^{-3} + H^+$	-11.60	(5.22)
$H_2AsO_4^- \Leftrightarrow AsO_4^{-3} + 2H^+$	-18.35	(5.23)
$H_3AsO_4 \Leftrightarrow AsO_4^{-3} + 3H^+$	-20.60	(5.24)
[2] Intrinsic surface complexation constant	Log k	
Surface protonation constant		
$\equiv XOH + H^+ \Leftrightarrow \equiv XOH_2^+$	7.29	(5.25)
$\equiv XOH \Leftrightarrow \equiv XO^- + H^+$	-8.93	(5.26)
Monodentate As(V) sorption		
$\equiv XOH + AsO_4^{-3} + 3H^+ \Leftrightarrow \equiv XH_2AsO_4 + H_2O$	29.98	(5.27)
$\equiv XOH + AsO_4^{-3} + 2H^+ \Leftrightarrow \equiv XHAsO_4^- + H_2O$	24.43	(5.28)
$\equiv XOH + AsO_4^{-3} + H^+ \Leftrightarrow \equiv XAsO_4^{-2} + H_2O$	18.10	(5.29)
$\equiv XOH + AsO_4^{-3} \Leftrightarrow \equiv XAsO_4^{-3}$	10.58	(5.30)
Bidentate As(V) Sorption		
$2\equiv XOH + AsO_4^{-3} + 3H^+ \Leftrightarrow \equiv X_2HAsO_4 + 2H_2O$	38.69$^{a)}$	(5.31)
$2\equiv XOH + AsO_4^{-3} + 2H^+ \Leftrightarrow \equiv X_2AsO_4^- + 2H_2O$	30.71$^{a)}$	(5.32)

$^{a)}$ Data from As(V) sorption onto goethite study (Grossl et al. 1997)

5.4.2 ZPC Calculation Using a Surface Complexation Model

Surface protonation reactions of Eqs. (5.25) and (5.26) define the charging behavior of mineral surfaces. The point of zero charge (ZPC) for hydrous ferric oxide in the absence of specific adsorption is defined as the pH where the concentration of $\equiv XOH_2^+$ species equals the concentration of $\equiv XO^-$ and the surface is neutrally charged. In the absence of adsorption, solutions of pH less than the ZPC will be positively charged while solutions of pH greater than ZPC will be negatively charged.

By using a surface complexation model, each surface species concentration ($[\equiv XOH_2^+]$ and $[\equiv XO^-]$) was calculated for various ionic strength conditions ($0.01M < I < 0.1M$) (see Figs. 5.5 to 5.7) and the point of zero charge (pH_{ZPC}) was determined by Eq. (5.33).

$$\sigma = \frac{F}{2a}\left\{[\equiv X^{w}OH_2^+] - [\equiv XO^-]\right\} \tag{5.33}$$

As a result, the pH_{ZPC} of freshly generated HFO was found to be 8.15 (see Fig. 5.8) and this pH_{ZPC} value was in the range of 7.9 ~ 8.2, reported by several experimental studies. Also, the point of zero charge for HFO can be calculated by a simple formula (Eq. (5.34)) with two acid-base equilibrium constants in the Eqs. (5.25) and (5.26) (Stumm and Morgan 1996) and the ZPC value was determined to be 8.11.

$$\mathrm{pH}_{ZPC} = \frac{1}{2}(pK_{+(\mathrm{int})} + pK_{-(\mathrm{int})}) \tag{5.34}$$

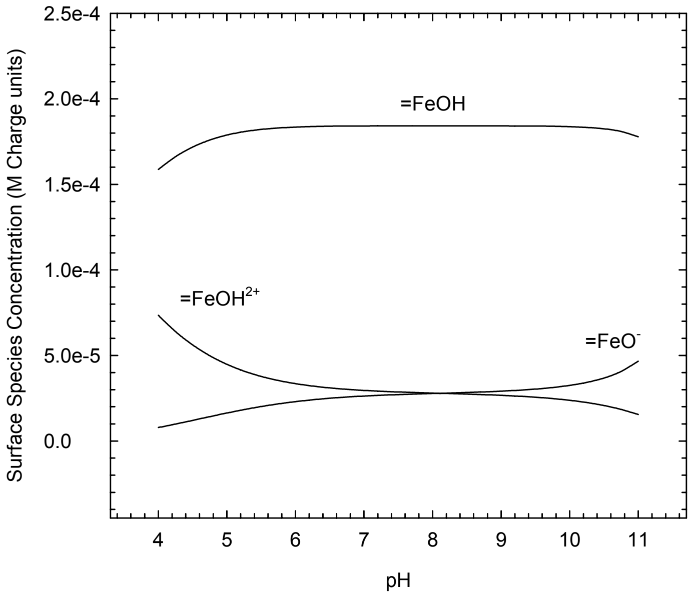

Figure 5.5 pC-pH diagram for HFO surface species at various ionic strength using PHREEQC (I = 0.1M)

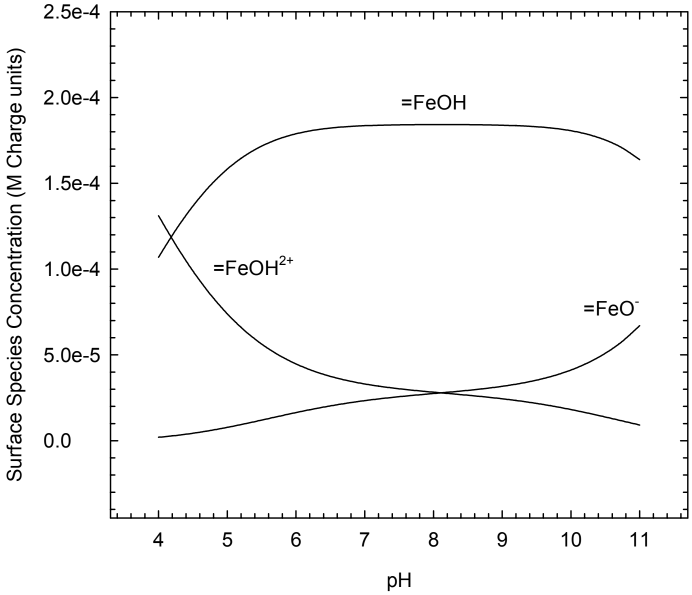

Figure 5.6 pC-pH diagram for HFO surface species at various ionic strength using PHREEQC (I = 0.01M)

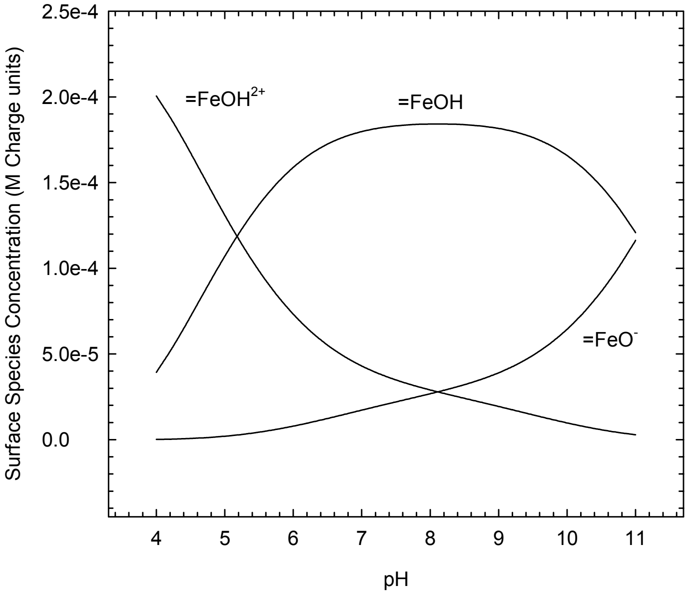

Figure 5.7 pC-pH diagram for HFO surface species at various ionic strength using PHREEQC (I = 0.001M)

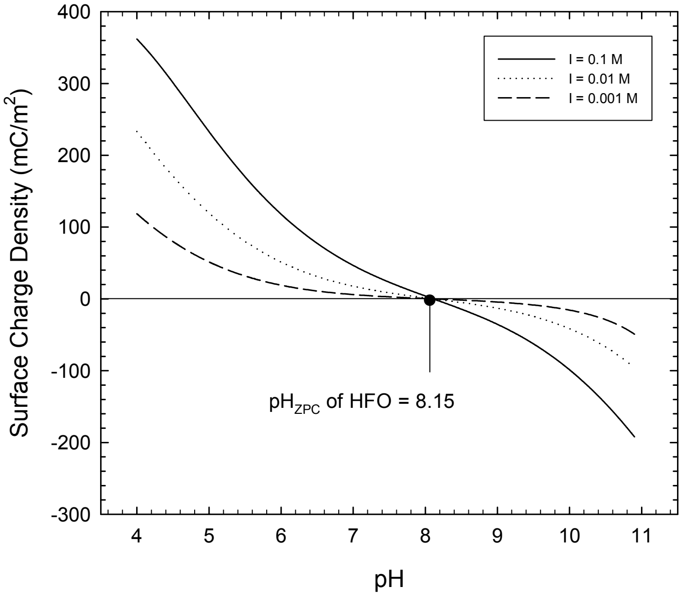

Figure 5.8 pC-pH diagram for HFO surface charge density at various ionic strength using PHREEQC

5.4.3 As(V) Sorption pH Envelop Simulation Using Surface Complexation Model

The sorption surface complexation modeling of As(V) onto HFO surface was conducted using PHREEQC public domain software. The sorption results using a surface complexation model were compared to literature data (Hsia et al. 1992) and displayed in Figs. 5.9 to 11. For this surface complexation modeling, a generalized two-layer model (DLM) was used with model parameters of Table 5.5 and equilibrium constants of Table 5.6. These results were displayed as As(V) sorption edge (pH envelop) diagram for the initial sorption conditions; As(V) concentrations ranging from 5×10^{-5} M to 2×10^{-4} M, HFO concentration of 1×10^{-3} M, and ionic strength (I) of 1×10^{-2} M. The arsenate loading ratio, [As]/[Fe] for this sorption equilibrium modeling was in the range of 0.05 to 0.2, which range represents a moderate As(V) sorption loading condition as reported by other sorption studies in Table 5.4.

Recently, the metal and/or ligand sorption modeling studies using a surface complexation model have been conducted and well predicted under a moderate adsorbate loading rate, ionic strength, and pH range. However, when the sorption loading rate increased, a surface complexation model may be not available to use as a sorption prediction technique due to surface precipitation. Although a general surface complexation model exhibits a saturation in sorption capacity at mono-layer surface coverage, some sorption experimental data show a continuous increase in sorption density instead of showing the saturation in sorption capacity (Farley et al. 1985). Thus, the As(V) sorption simulation using surface complexation modeling in this study (moderate sorption conditions of initial [As]/[Fe] ratio of 0.05 ~ 0.2 and ionic strength (I) of 0.001 ~ 0.1) was used to predict the As(V) sorption behavior without a surface precipitation.

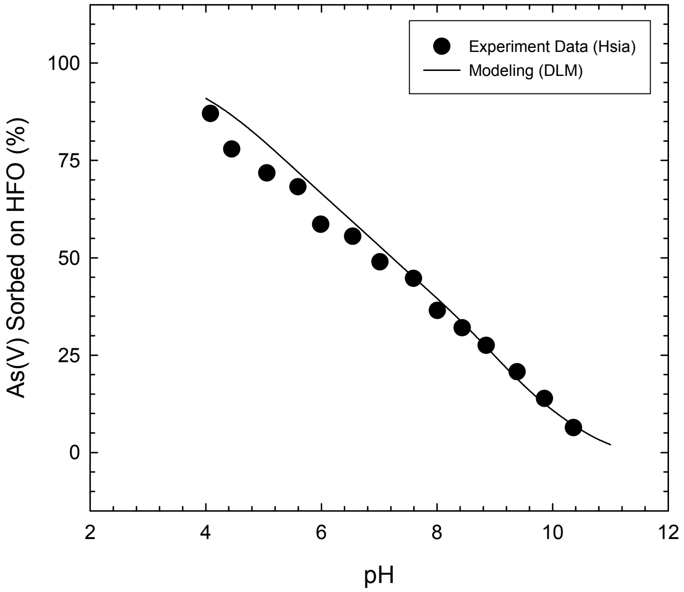

Figure 5.9 As(V) sorption envelop modeling using DLM ([As]=2.0×10^{-4} M, [Fe]=1.0×10^{-3} M, I=0.01M) (Data from Hsia (1992))

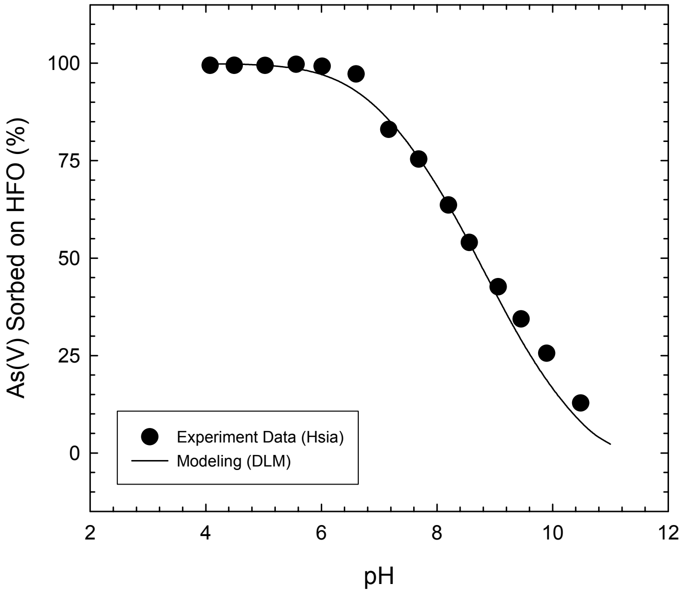

Figure 5.10 As(V) sorption envelop modeling using DLM ([As]=1.0×10^{-4} M, [Fe]=1.0×10^{-3} M, I=0.01M) (Data from Hsia (1992))

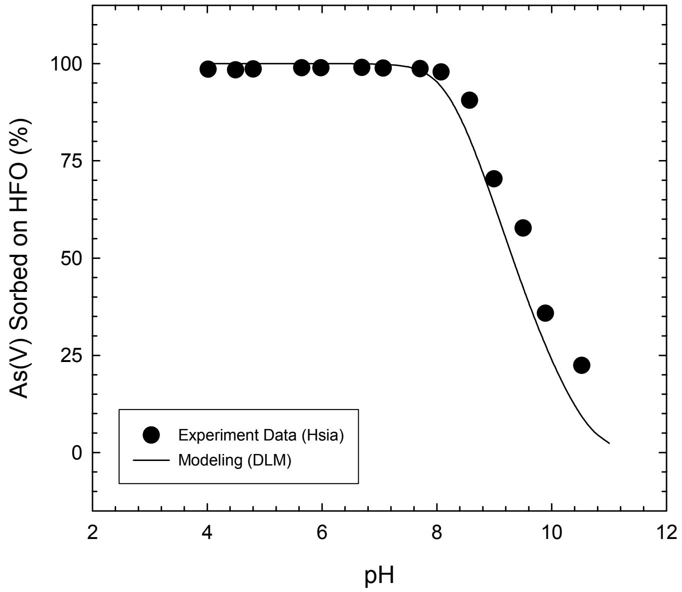

Figure 5.11 As(V) sorption envelop modeling using DLM ([As]=0.5×10^{-4} M, [Fe]=1.0×10^{-3} M, I=0.01M) (Data from Hsia (1992))

5.4.4 ZPC Evolution during As(V) Sorption onto HFO Surface

HFO surface species and their concentrations of As(V) sorption equilibrium state was derived via surface complexation modeling which was described in the above section. As shown in Table 5.6, theoretical HFO surface species can be expected as, $\equiv XOH_2^+$, $\equiv XOH$, $\equiv XO^-$, $\equiv XH_2AsO_4$, $\equiv XHAsO_4^-$, $\equiv XAsO_4^{-2}$, $\equiv XAsO_4^{-3}$, $\equiv X_2AsO_4^-$, and $\equiv X_2HAsO_4$. The pC-pH diagrams for surface species of HFO at various As(V) sorption loading conditions are displayed in Figs. 5.12 to 5.14. The bidentate surface complexation reactions (see Eqs. (5.31) and (5.32)) between HFO surface and As(V) were excluded in this surface complexation modeling as the monodentate complex is dominant in the moderate arsenic loading ratios adopted in this study. It was found that the surface species concentrations were dependent on the initial As(V) loading conditions and the charged surface species ($\equiv XOH_2^+$, $\equiv XO^-$, $\equiv XHAsO_4^-$, $\equiv XAsO_4^{-2}$, and $\equiv XAsO_4^{-3}$) played a key role in determining the surface charge density or charge potential. For a general As(V) sorption equilibrium modeling study, the surface charge density could be determined by using these surface species that affect the surface charge or surface potential as,

$$\sigma = \frac{F}{2a}\left\{\begin{aligned}&[\equiv \mathrm{XO}^-]+[\equiv \mathrm{XOH}_2^+]+[\equiv \mathrm{XAsO}_4^{-3}]+[\equiv \mathrm{XAsO}_4^{-2}]\\&+[\equiv \mathrm{XHAsO}_3^-]+[\equiv \mathrm{X}_2\mathrm{AsO}_4^-]\end{aligned}\right\} \tag{5.35}$$

After excluding the bidentate complexation, the surface charge density of HFO on which As(V) is adsorbed can be calculated as,

$$\sigma = \frac{F}{2a}\left\{[\equiv \mathrm{XO}^-]+[\equiv \mathrm{XOH}_2^+]+[\equiv \mathrm{XAsO}_4^{-3}]+[\equiv \mathrm{XAsO}_4^{-2}]+[\equiv \mathrm{XHAsO}_3^-]\right\} \tag{5.36}$$

Using the Eq. (5.36), the surface charge density curves for various As(V) sorption loading conditions (initial [As]/[Fe] ratio of 0 ~ 0.2) were calculated and displayed in Fig. 5.15. The ZPC values of HFO were determined by letting the surface charge density of Eq. (5.36) be zero. From the Fig. 5.15, the ZPC value of HFO was shifted to the left side on the x-axis having lower pH_{ZPC} value and the shifting magnitude was proportional to the amount of As(V) adsorbed onto the HFO surface. Similar ZPC reduction of HFO for anion sorption (As(III) and As(V)) has been reported by Jain et al. (1999). This ZPC reduction indicates that the inner-sphere complex mechanism is prevalent in the adsorption of As(V), rather than outer-sphere complex reactions of Eq. (5.37) and (5.38) in Table 5.7.

Table 5.7 As(V) Surface Complexation Mechanisms on HFO Surface

[1] Inner-sphere complexation	
$\equiv XOH + AsO_4^{-3} + 3H^+ \Leftrightarrow \equiv XH_2AsO_4 + H_2O$	(5.27)
$\equiv XOH + AsO_4^{-3} + 2H^+ \Leftrightarrow \equiv XHAsO_4^- + H_2O$	(5.28)
$\equiv XOH + AsO_4^{-3} + H^+ \Leftrightarrow \equiv XAsO_4^{-2} + H_2O$	(5.29)
$\equiv XOH + AsO_4^{-3} \Leftrightarrow \equiv XAsO_4^{-3}$	(5.30)
[2] Outer-sphere complexation	
$\equiv XOH + AsO_4^{-3} + 3H^+ \Leftrightarrow \equiv XOH_2^+ \cdots\cdots H_2AsO_4^-$	(5.37)
$\equiv XOH + AsO_4^{-3} + 2H^+ \Leftrightarrow \equiv XOH_2^+ \cdots\cdots HAsO_4^{-2}$	(5.38)

The outer-sphere complexation (low-affinity specific adsorption) of anions would result in increased pH_{ZPC} values. Physically adsorbed counter ions (As(V) anion) in the diffuse double layer would induce additional positive charge on the HFO surface by hydroxyl desoption (see Fig. 5.3 (a) and Table 5.7). Conversely, the inner-sphere complexation (high-affinity specific adsorption or chemisorption) of As(V) anion adsorption onto the HFO surface leads to lowering the pH_{ZPC} value, resulting in As(V) chemical coordination to the surface metal ion. That is, the adsorbed anion species becomes a part of the surface with high-affinity specific adsorption and translates its charge to the solid. Thus, the lowering of the pH_{ZPC} results from the inner-sphere complexation of an anion onto the HFO surface (Singh and Uehara 1998) (see Fig. 5.3 (b), (c), and(d) and Table 5.7). From the HFO ZPC reduction during the sorption of As(V) (one of the anionic species), it is expected during As(V) sorption onto HFO that surface charge or potential is altered, changing the stability of HFO colloidal particles, and impacting HFO colloid coagulation kinetics.

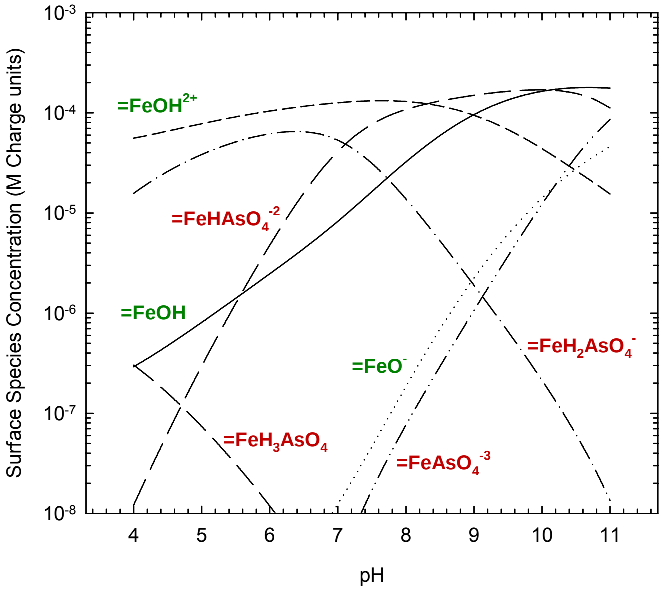

Figure 5.12 HFO surface species modeling after As(V) sorption using DLM ([As]=2.0×10^{-4} M, [Fe]=1.0×10^{-3} M, I=0.01M)

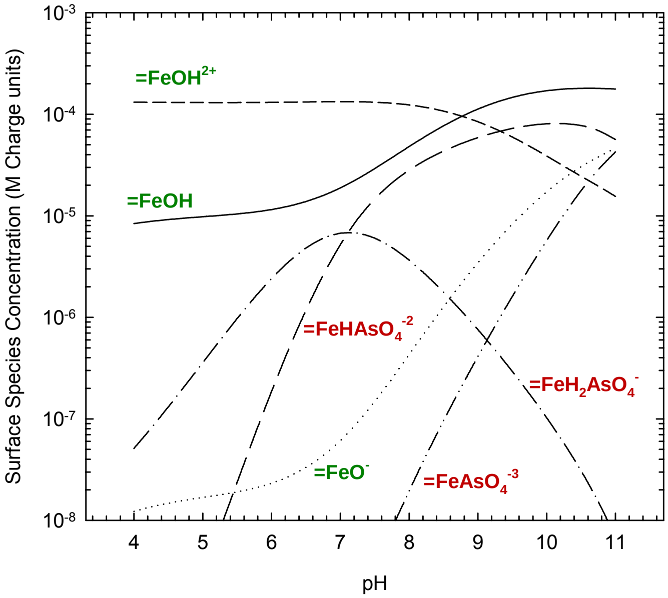

Figure 5.13 HFO surface species modeling after As(V) sorption using DLM ([As]=1.0×10^{-4} M, [Fe]=1.0×10^{-3} M, I=0.01M)

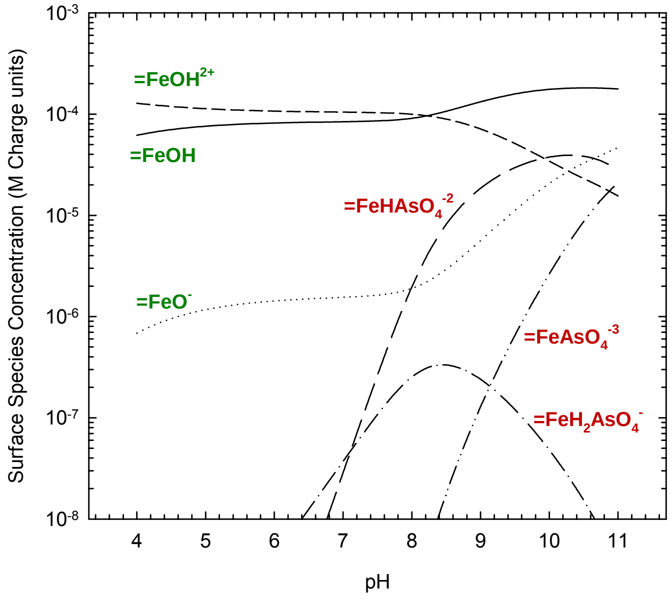

Figure 5.14 HFO surface species modeling after As(V) sorption using DLM ([As]=0.5×10^{-4} M, [Fe]=1.0×10^{-3} M, I=0.01M)

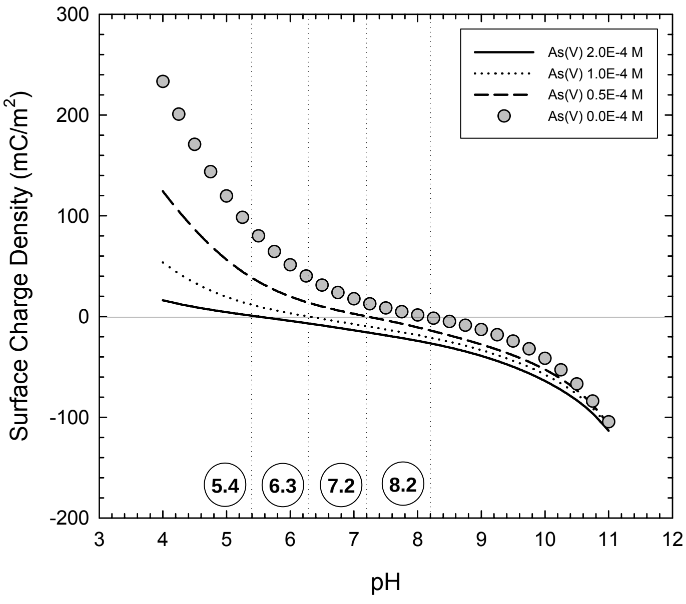

Figure 5.15 Surface charge evolution after As(V) sorption onto HFO using DLM ([Fe]= 1.0×10^{-3} M, I=0.01M)

5.4.5 Arsenate Sorption Kinetics

In this study, the intrapaticle transport expressed by the pore diffusion model of Eq. (5.14) and surface diffusion model of Eq. (5.20) were introduced to simulate arsenic sorption kinetics. These partial differential equations of Eqs. (5.14) and (5.20) can be solved by several numerical techniques such as the orthogonal collocation method and the finite difference method. To use the finite difference method, these partial differential equations were discretized by replacing the derivatives in the Eqs. (5.14) and (5.20) with finite difference approximations at each point in the interval of integration (Constantinides and Mostoufi 1999).

For pore diffusion model of Eq. (5.14), the discretization using an explicit scheme was derived as,

For $1 \le j \le N$

$$c^{+}_{j,m+1} = \frac{c_{b0}}{\rho_p q_0^*} \frac{\Delta t^{+}}{(\Delta r^{+})^2} \left\{ \left[1 + \frac{\Delta r^{+}}{r^{+}} \right] c^{+}_{j+1,m} - 2c^{+}_{j,m} + \left[1 - \frac{\Delta r^{+}}{r^{+}} \right] c^{+}_{j-1,m} \right\} \tag{5.39}$$

For $j = N + 1$

$$c^{+}_{N+1,m+1} = \frac{2c_{b0}}{\rho_p q_0^*} \frac{\Delta t^{+}}{(\Delta r^{+})^2} \left\{ -\left[1 + \frac{N+1}{N} (\Delta r^{+}) \frac{k_f a_p}{D_p} \right] c^{+}_{N+1,m} + c^{+}_{N,m} + \left[\frac{N+1}{N} (\Delta r^{+}) \frac{k_f a_p}{D_p} \right] \right\} \tag{5.40}$$

The dimensionless variables are defined as,

$$c^{+} = \frac{c}{c_{b0}}, \qquad c_b^{+} = \frac{c_b}{c_{b0}}, \qquad t^{+} = \frac{D_p t}{r_p^2}, \qquad r^{+} = \frac{r}{r_p},$$

$$q_0^* = f(c_{b0}), \quad q^{+} = F(c^{+})$$

where $f(c_{b0})$ is the sorption isotherm function of Eq. (5.18) or (5.19), and $F(c^+)$ is the dimensionless value of the isotherm function. Further, for the surface diffusion model of Eq. (5.20), the results of the explicit discretization were represented by the following equations,

For $j = 1$

$$q^+_{1,m+1} = -\left[6\frac{\Delta t^+}{(\Delta r^+)^2} - 1\right] q^+_{1,m} + \left[\frac{\Delta t^+}{(\Delta r^+)^2}\right] q^+_{2,m} \tag{5.41}$$

For $2 \le j \le N$

$$q^+_{j,m+1} = \frac{\Delta t^+}{(\Delta r^+)^2}\left[1 + \frac{\Delta r^+}{r^+}\right] q^+_{j+1,m} - \left[2\frac{\Delta t^+}{(\Delta r^+)^2} - 1\right] q^+_{j,m} + \frac{\Delta t^+}{(\Delta r^+)^2}\left[1 - \frac{\Delta r^+}{r^+}\right] q^+_{j-1,m} \tag{5.42}$$

For $j = N + 1$

$$q^+_{N+1,m+1} = -\left[2\frac{\Delta t^+}{(\Delta r^+)^2} - 1\right] q^+_{N+1,m} + \left[2\frac{\Delta t^+}{(\Delta r^+)^2}\right] q^+_{N,m} + \left[2\frac{k_f a_p}{D_s}\frac{c_{b0}}{\rho_p q_0^*}\Delta r^+ \frac{\Delta t^+}{(\Delta r^+)^2}\left(\frac{N+1}{N}\right)\right] \tag{5.43}$$

After the introduction of the finite difference scheme, the partial differential equations were converted to a set of simultaneous nonlinear algebraic equations and could be easily integrated.

To verify the As(V) sorption kinetic model adopted in this study, model simulation results were compared with experimental data from the literature (Thirunavukkarasu et al. 2003). These arsenate sorption kinetic experiments were conducted under the conditions of an initial As(V) concentration of 100 μg/L, granular ferric hydroxide of 2 g/L, particle size of 0.8 to 1.2 mm in diameter, and solution pH of 7.6. In addition, the model parameters used simulate sorption kinetics were particle porosity of 0.75 (Thirunavukkarasu et al. 2003), particle density of 1.32 g/cm^3 (Driehaus et al. 1998), and the Freundlich isotherm parameters of K = 10.3 L/μg and n = 1.5 at solution pH of 7.6 (Thirunavukkarasu et al. 2003). Further, from the parameter estimation technique based on a least-square error method, the liquid film mass transfer coefficient (k_f) and the pore diffusion coefficient (D_p) were found as 1.82×10^{-5} m/sec and 3.77×10^{-15} m^2/sec, respectively. The results of the model verification for arsenic sorption kinetics is displayed in Figure 5.16. Deviations between the experimental and model prediction data were compared using statistical analysis represented by the square of the correlation coefficient (R^2) and the square root of the sum-of-squares of the errors ($\sqrt{SSE}$), with $R^2 = 0.9385$ and $\sqrt{SSE} = 0.2496$.

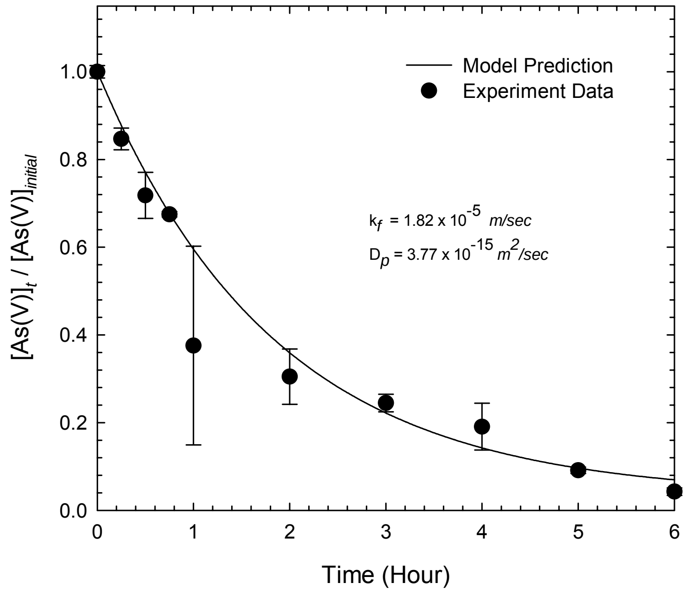

Figure 5.16 The verification of As(V) sorption kinetics with experiment data (As(V)$_0$ = 100 μg/L, granular ferric hydroxide = 2.0 g/L, pH = 7.6)

Another model verification was conducted by the comparison of model prediction values with the literature experimental data for arsenate adsorption onto the hydrous ferric oxide solid particles (Thirunavukkarasu 2002). The model parameters used were particle porosity of 0.5 (Axe and Anderson 1995), particle density of 3.57 g/cm^3 (Dzombak and Morel 1990), and the Freundlich isotherm parameters of K = 58.0 L/μg and n = 1.1 at solution pH of 7.6 (Thirunavukkarasu 2002). The liquid film mass transfer coefficient (k_f) and the pore diffusion coefficient (D_p) used in this arsenic sorption on hydrous ferric oxide study were 1.82×10^{-5} m/sec and 3.77×10^{-15} m^2/sec, respectively, which were derived from the previous arsenic sorption kinetic study using granular ferric hydroxide. The kinetic modeling results are displayed in Fig. 5.17.

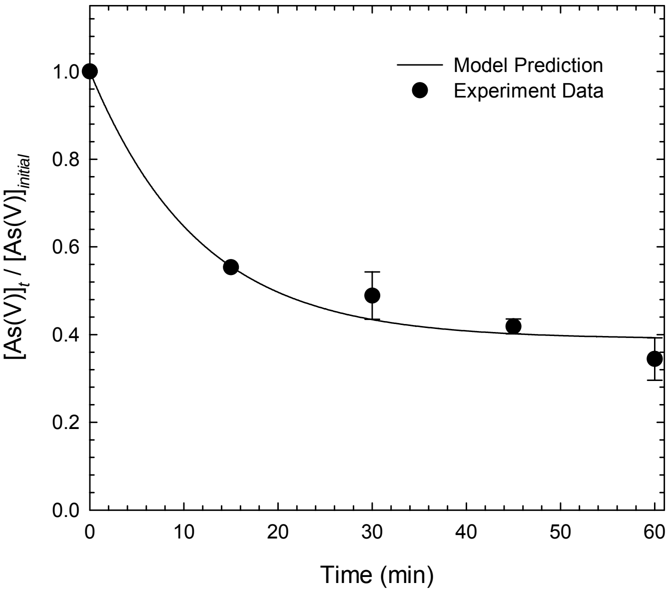

Figure 5.17 The verification of As(V) sorption kinetics with experiment data ($As(V)_0$ = 100 μg/L, hydrous ferric oxide = 0.2 g/L, pH = 7.6)

From the statistical analysis, the deviations between the experimental and simulation data were R^2 = 0.9789 and $\sqrt{SSE}$ = 0.0747. From these statistical analyses, the sorption kinetic model is shown to predict well the experimental data with high accuracy.

To apply and extend this arsenic sorption kinetic model to this study, model parameters were adopted from literature and summarized in Table 5.8. Two major parameters used in the sorption kinetic modeling are, the liquid-particle mass transfer coefficient k_f and the pore diffusion coefficient (D_p), which were 1.82×10^{-5} m/sec and 3.77×10^{-15} m^2/sec, respectively. These two parameters were derived from the previous arsenic sorption kinetic modeling studies using granular ferric hydroxide and hydrous ferric oxide. By assuming that q is to be in equilibrium with c in the adjacent pore water with the isotherm, c and q can be coupled with the sorption isotherm equation and the isotherm model parameters required to solve the As(V) sorption kinetics. In this study, the Freundlich isotherm of Eq. (5.19) was introduced and these two isotherm parameters derived from the literature (Pierce and Moore 1982).

Finally, As(V) sorption kinetic modeling was conducted by using Eqs. (5.14) /(5.20) and (5.18), and model parameters displayed in Table 5.8. The kinetic model results of As(V) sorption onto HFO for various initial As(V) loading ratios (As(V)/Fe) ranging in 0.05 ~ 0.2 were calculated and displayed in Fig. 5.18.

Table 5.8 Model Parameters Used for As(V) Sorption Kinetics

Parameters	Values	Reference
HFO porosity (ε_p)	0.5	(Axe and Anderson 1995)
HFO density (ρ_p)	3.57 (g/cm^3)	(Dzombak and Morel 1990)
Mass transfer coefficient (k_f)	1.82×10^{-5} (m/sec)	
Pore diffusion coefficient (D_p)	3.77×10^{-15} (m^2/sec)	
Freundlich isotherm parameters	K = 55.34 (L/μg)	(Pierce and Moore 1982)
	n = 3.67	

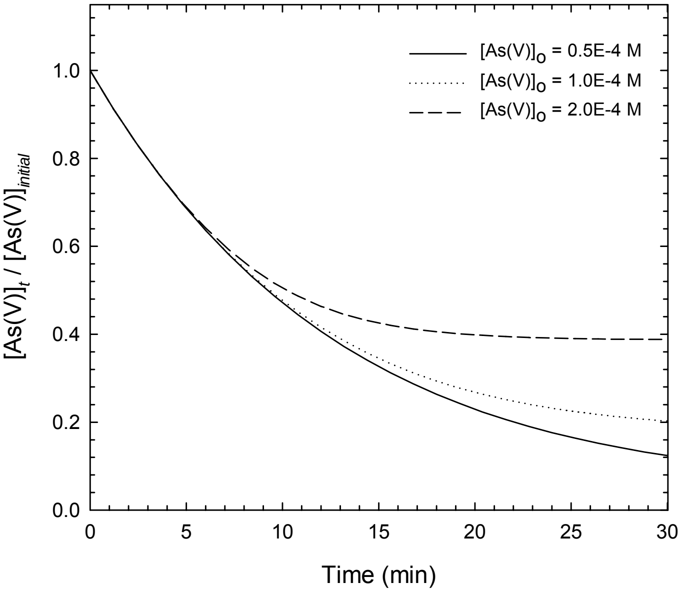

Figure 5.18 As(V) sorption kinetics for various initial As(V) concentrations ([Fe] = 1.0×10^{-3} M and pH = 7.0)

5.4.6 Surface Charge/Potential Evolution

During arsenic sorption on hydrous ferric oxide surface, the surface charge (potential) of the hydrous ferric oxide is altered due to protonation, deprotonation, and surface complexation of ionic species (see Table 5.6). Considering only the monodentate complexation mechanism between As(V) and hydrous ferric oxide surface, the surface charge (potential) is calculated from the summation of the surface charge determining ions using Eq. as,

$$\sigma = \frac{F}{2a}\left\{ [\equiv \mathrm{XO}^{-}]+[\equiv \mathrm{XOH_2}^{+}]+[\equiv \mathrm{XHAsO_4}^{-}]+[\equiv \mathrm{XAsO_4}^{-2}]+[\equiv \mathrm{XAsO_4}^{-3}]\right\} \quad (5.36)$$

Each species concentration in Eq. (5.36) can be determined by the surface complexation modeling between As(V) and HFO surface. Further, using the local equilibrium assumption, surface species concentrations at each time step can be derived by coupling the surface complexation equilibrium model with the As(V) sorption kinetic model mentioned in previous sections. The results of hydrous ferric oxide surface potential kinetic modeling during As(V) sorption for various initial As(V) loading ratio (As(V)/Fe) ranging in 0.05 ~ 0.2 were obtained and displayed in Figs. 5.19 to 22.

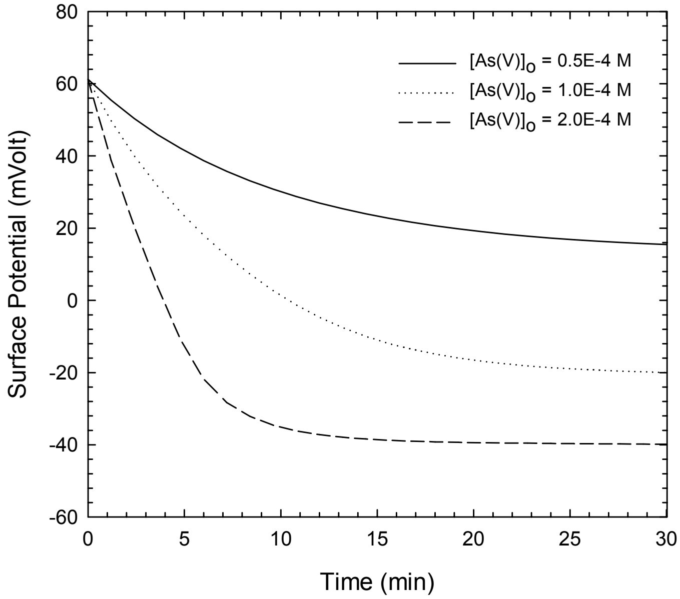

Figure 5.19 The surface potential kinetics for various initial As(V) concentrations ([Fe] = 1.0×10^{-3} M, pH = 7.0, I = 0.01)

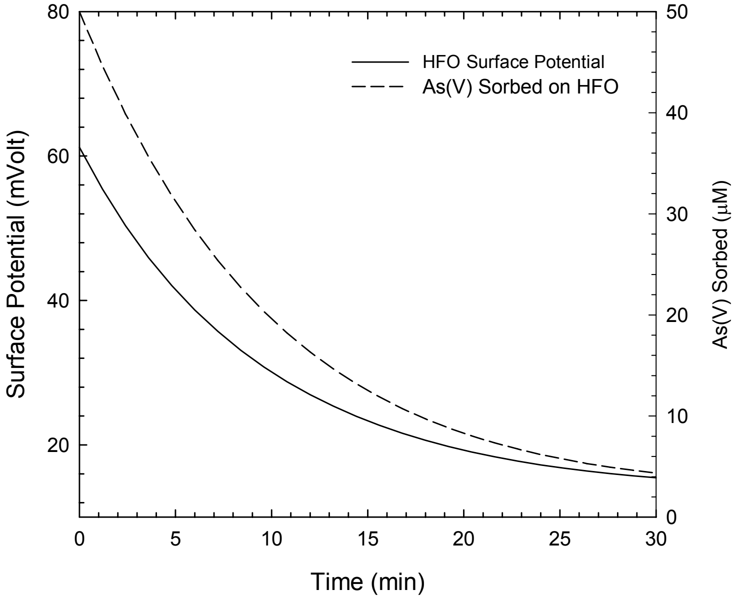

Figure 5.20 The kinetics of As(V) sorption and surface potential ([As(V)$_o$] = 0.5×10^{-4} M, [Fe] = 1.0×10^{-3} M, pH = 7.0, and I = 0.01)

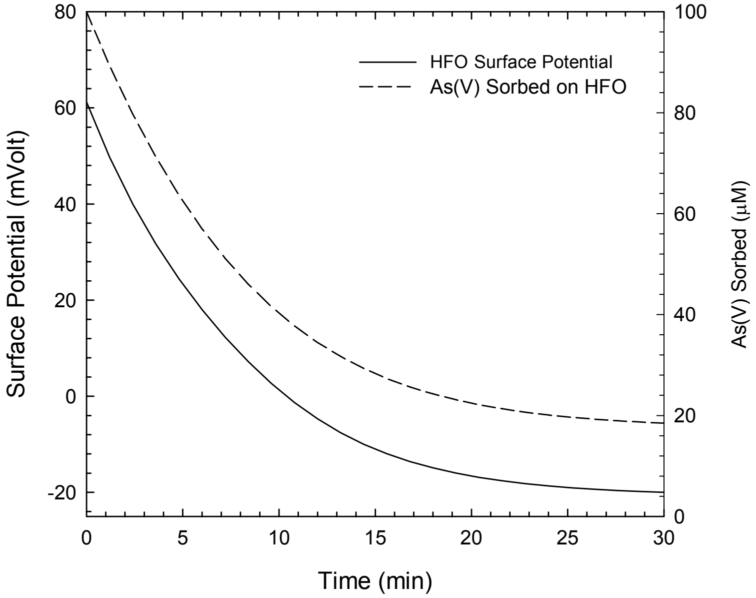

Figure 5.21 The kinetics of As(V) sorption and surface potential ($[As(V)_o] = 1.0\times10^{-4}$ M, $[Fe] = 1.0\times10^{-3}$ M, pH = 7.0, and I = 0.01)

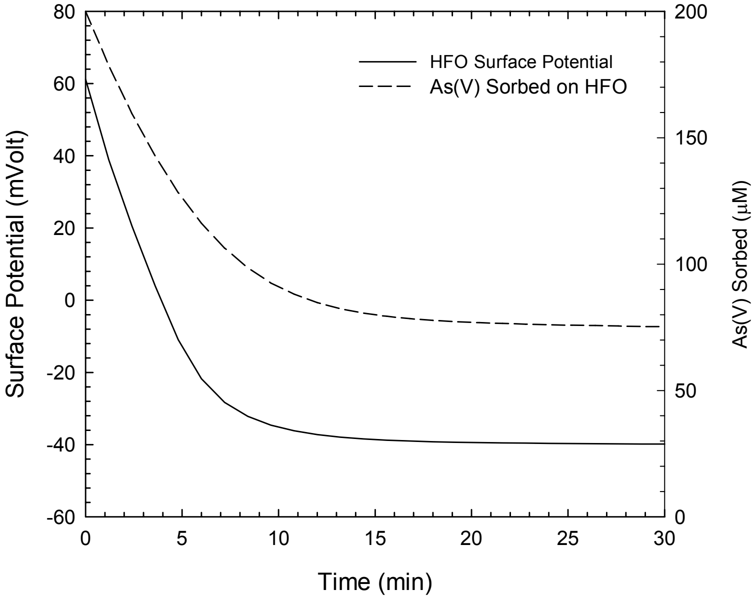

Figure 5.22 The kinetics of As(V) sorption and surface potential ($[As(V)_o] = 2.0\times10^{-4}$ M, $[Fe] = 1.0\times10^{-3}$ M, pH = 7.0, and I = 0.01)

As shown in Figs. 20 to 21, the HFO surface potential decreases with As(V) anion sorption time for all As(V) loading ratios. It was found that the surface potential for relatively low As(V) loading ratio, As(V)/Fe of 0.05 approached a minimum value but maintained a positive surface potential of 13.8 mVolt (see Fig. 5.20). However, for medium to high As(V) loading conditions ranging in 0.1 ~ 0.2 of As/Fe (see Figs. 5.21 to 22), the surface appeared to the negative surface potentials of -20.9 mVolt and -40.3 mVolt, respectively. It is expected that the surface potential kinetics affect the particle surface energy or surface force due to double-layer electrostatic repulsion which is directly related to the particle stability ratio (*W*).

To investigate the relationship between As(V) anion sorption on hydrous ferric oxide particle surface and particle interactions such as repulsive energy, attractive energy, and total energy, these particle interactions were theoretically calculated during As(V) anion sorption kinetics. For equal size spherical particles, the electrostatic diffuse double-layer repulsive energy (V_R) and van der Waals attractive energy (V_A) were calculated as (Stumm and Morgan 1996),

$$\mathrm{V_T} = \mathrm{V_R} + \mathrm{V_A} \tag{5.44}$$

$$\mathrm{V_R} = \frac{64\pi k_B T}{\kappa}\frac{(r_p+\delta)^2}{R_p}\left\{\tanh\left(\frac{ze\psi_d}{4k_BT}\right)\right\}^2 \mathrm{e}^{-\kappa(H-2\delta)} \tag{5.45}$$

$$\mathrm{V_A} = -\frac{A}{6}\left[\frac{2}{s^2-4}+\frac{2}{s^2}+\ln\frac{s^2-4}{s^2}\right] \tag{5.46}$$

with

$$\kappa = \sqrt{\frac{2F^2I\times10^3}{\varepsilon\varepsilon_0RT}} \tag{5.47}$$

$$s = \frac{R_p}{r_p} \tag{0.1}$$

where, k_B = Boltzmann constant T = absolute temperature
κ = reciprocal thickness of double layer
r_p = particle radius
R_p = distance between centers of two spheres
δ = thickness of (Stern) double layer, inner most layer of ions plastered against the surface of a particle
z = charge number
e = elementary charge
ψ_d = surface potential at the plane where the diffuse double layer begins
H = shortest interaction distance between two spherical particles
A = Hamaker constant

The surface potential (ψ) is directly related to double layer electrostatic repulsive energy (V_R) as shown in Eq. (5.45). In general, the double layer electrostatic repulsive energy (V_R) decreases in proportion to the separation distance and the V_R decreases approximately in proportion to the square of the surface potential (ψ^2) (Stumm and Morgan 1996). In addition, ionic strength and electrolyte charge number affect the repulsive energy which is directly proportional to net surface potential energy (V_T).

The surface potential energy versus particle separation distance at various arsenic loading ratios was calculated and is displayed in Figs. 5.23 to 5.28. The initial surface potential energy before As(V) sorption was calculated and the results displayed in Fig. 5.23. The initial particle interaction energy calculation was conducted under the conditions of, [Fe] = 1.0×10^{-3} M, pH = 7.0, I = 0.01 M, z = 1.0, particle diameter of 1 μm, and ψ_o = 61.2 mVolt. Other modeling conditions were $As(V)_O$ = 5×10-5 M, HFO = 1.0×10-3 M, pH = 7.0, I = 0.01 M, z = 1.0, particle diameter of 1 μm, and ψ_o = 13.8 ~ 42.1 mVolt.

The energy barrier is characterized by the maximum of the particle interaction energy curve ($V_{T,max}$) and the energy barrier or $V_{T,max}$ which is strongly related to the net repulsive energy (V_R). As shown in Figs. 5.23 to 5.28, the energy barrier or $V_{T,max}$ decreased as surface potential (ψ) decreased or the amount of As(V) anion sorbed on the particle surface increased. Further, as the sorption time elapsed 1800sec (see Fig. 5.26), the repulsive energy (V_R) was minimized and the net surface potential energy (V_T) is approached the same magnitude of van der Waals attractive energy (V_A). Thus, it was found that As(V) sorption on HFO particle surface can affect the surface potential evolution and thus the decreased surface potential/charge lowers the energy barrier height or the maximum of the particle interaction energy curve ($V_{T,max}$).

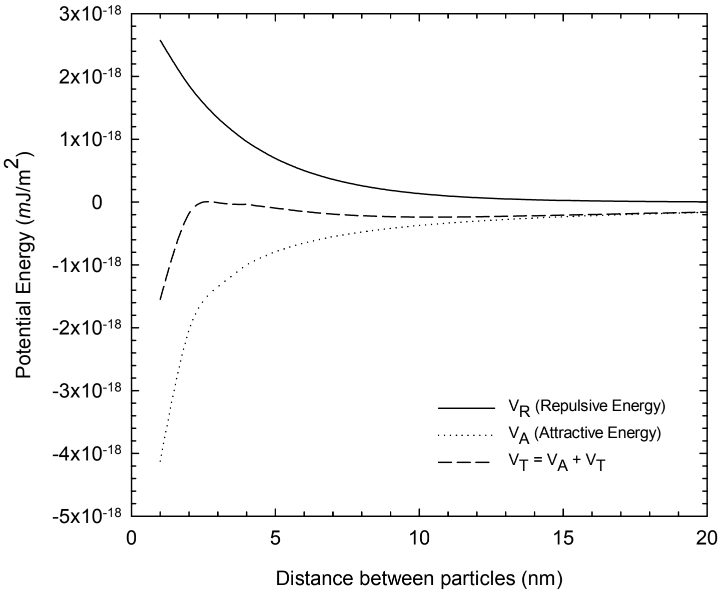

Figure 5.23 Surface energy evolution during As(V) sorption onto HFO at 0 sec ([Fe] = 1.0×10^{-3} M, pH = 7.0, I = 0.01 M, and ψ_o = 61.2 mVolt)

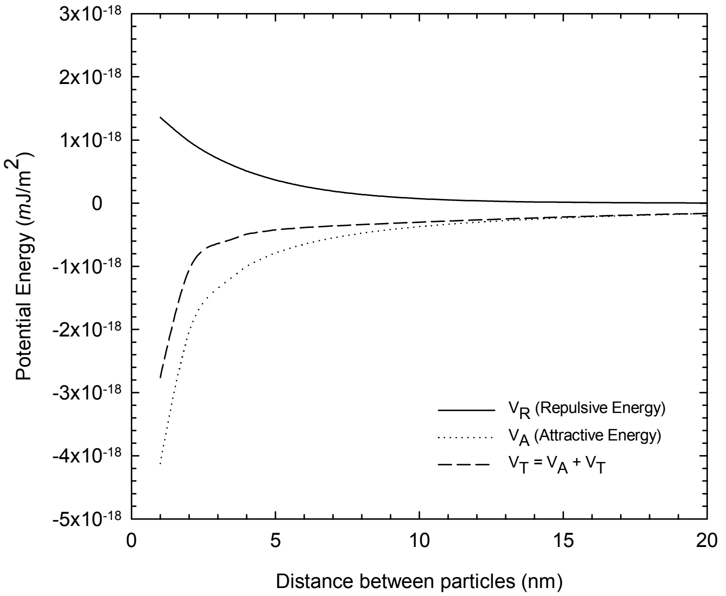

Figure 5.24 Surface energy evolution during As(V) sorption onto HFO at 360 sec ($[As(V)_o]$= 5×10^{-5} M, [Fe] = 1.0×10^{-3} M, pH = 7.0, I = 0.01 M, and ψ_o = 42.1 mVolt)

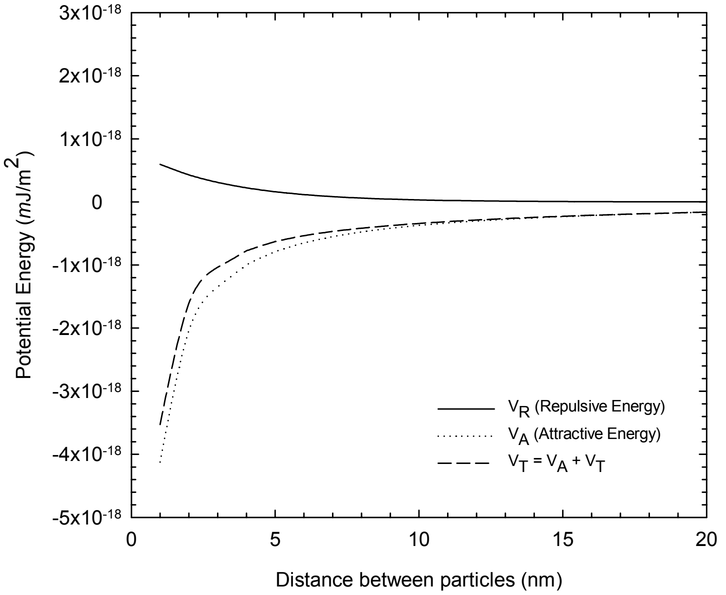

Figure 5.25 Surface energy evolution during As(V) sorption onto HFO at 900 sec ($[As(V)_o]$= 5×10^{-5} M, HFO = 1.0×10^{-3} M, pH = 7.0, I = 0.01 M, and ψ_o = 27.0 mVolt)

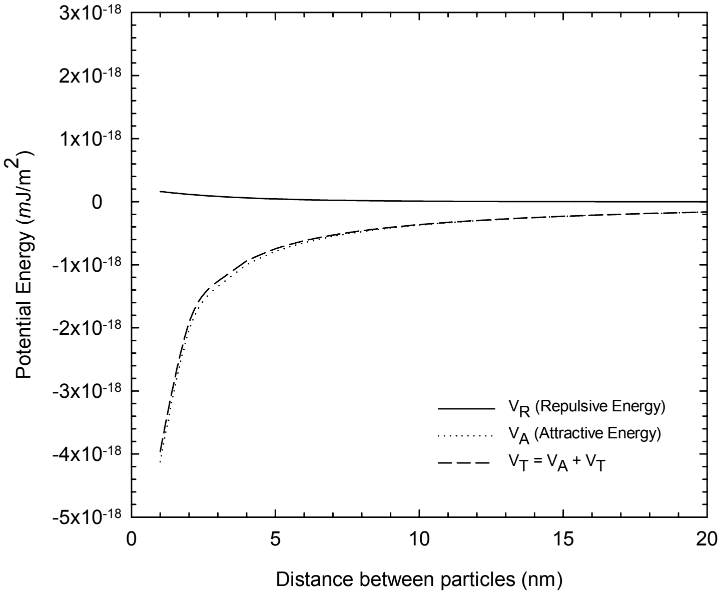

Figure 5.26 Surface energy evolution during As(V) sorption onto HFO at 1800 sec ([As(V)$_o$]= 5×10^{-5} M, [Fe] = 1.0×10^{-3} M, pH = 7.0, I = 0.01 M, and ψ_o = 13.8 mVolt)

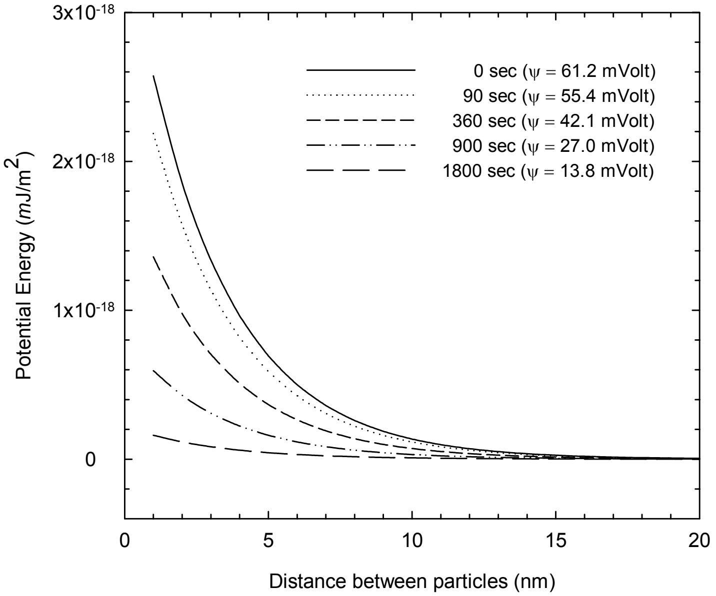

Figure 5.27 Repulsive energy (V$_R$) kinetics during As(V) sorption onto HFO ([As(V)$_o$]= 5×10^{-5} M, [Fe] = 1.0×10^{-3} M, pH = 7.0, and I = 0.01 M)

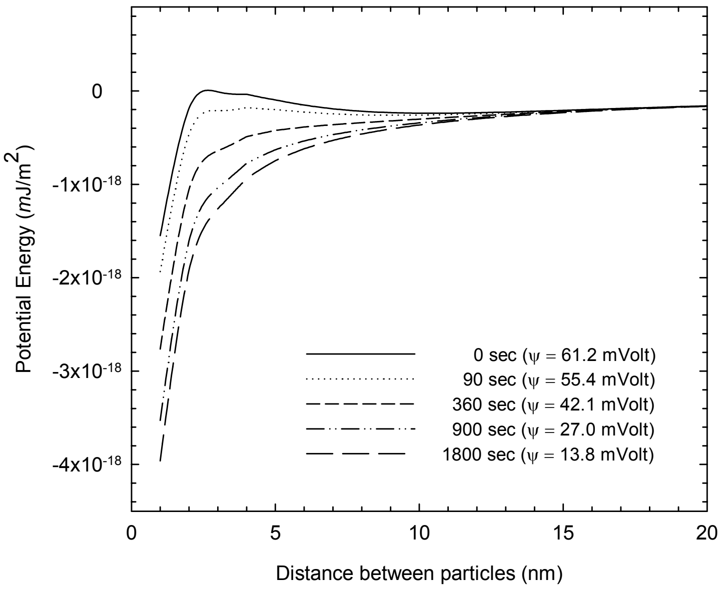

Figure 5.28 Total energy (V_T) kinetics during As(V) sorption onto HFO ($[As(V)_o]= 5\times10^{-5}$ M, [Fe] = 1.0×10^{-3} M, pH = 7.0, and I = 0.01 M)

Colloid stability (*W*) is characterized by the height of the net energy barrier (V_{max}) or by a repulsive interaction energy (V_R) and *W* is the factor by which particle collisions are slower than in the absence of an energy barrier (Stumm and Morgan 1995). Further, the conceptually defined colloid stability ratio (*W*) should correspond to the operationally determined particle collision efficiency α ($\alpha = 1/W$). It should be noted that the colloid stability ratio *W* or collision efficiency α is strongly related to the height of the potential energy barrier V_{max}. Thus, it is expected during As(V) sorption onto particle surface that surface charge (potential) is altered with kinetically controlled behavior and this change affects the stability of hydrous ferric oxide colloidal particles influencing colloid particle coagulation.

5.5 Conclusions

To enhance the predictive capability for arsenic sorption onto metal oxy-hydroxide surfaces, a surface complexation equilibrium model using a thermodynamic equilibrium database and a sorption kinetic model using diffusion mass transport were introduce and coupled with local equilibrium assumption. The unified sorption model was developed as follows; First, a surface complexation model was introduced to predict arsenic sorption equilibrium behaviors (i.e., pH envelop and isotherm). A set of equations representing surface complexation model was solved with a public domain computer program. Second, arsenic sorption kinetic model based diffusion mass transport mechanism was introduced to predict arsenic sorption rate. Finally, the introduced surface complexation model was coupled with an arsenic sorption kinetic model using sorption local equilibrium assumption. To verify two arsenic sorption equilibrium and kinetic models, the model results were compared to experimental data from literature such as arsenic pH envelop data for equilibrium model verification and arsenic sorption rate data for kinetic model.

The improved arsenic sorption modeling technique coupled with arsenic sorption kinetics and equilibrium could provide enhanced predictive capability for the exact arsenic sorption behavior especially related to arsenic sorption kinetics, equilibrium, and particle surface charge (potential) evolution over reaction time. Thus, it is expected during As(V) sorption onto particle surface that surface charge (potential) is altered with kinetically controlled behavior and this change affects the stability of hydrous ferric oxide colloidal particles influencing colloid particle coagulation. Furthermore, the surface charge (potential) evolution can be used to couple two models of arsenic sorption and coagulation model. That is, a unified coagulation model will be coupled with arsenic sorption model using surface charge (potential) which is one of major variable parameters in collision efficiency calculation.

CHAPTER VI

COUPLING THE COAGULATON MODEL WITH THE SORPTION MODEL

6.1 Overview

An improved discretized population balance equation (PBE) is proposed in this study. This improved discretized population balance equation has new probability distribution functions for aggregates produced in non-uniform discrete coagulation modeling. In this study, this model was found to be a substantial improvement in terms of numerical accuracy, stability, and computational efficiency over the continuous model. Further, this model was able to simulate the particle aggregation and breakup with fractal dimensions lower than 3. Moreover, comparisons were made using the fractal aggregate collision mechanisms of orthokinetic coagulation with the inclusion of flow induced breakup. This new algorithm makes it possible to solve fractal particle aggregation and breakup problems with high accuracy, perfect mass conservation and exceptional computational efficiency, thus the new model can be used to develop predictive simulation techniques for the coupled coagulation using computational fluid dynamics (CFD) and chemical reaction modeling.

In this study, this improved coagulation model developed was coupled with arsenic sorption equilibrium and kinetics on fractal colloids of hydrous ferric oxide (HFO). The model coupling was achieved by using the colloid stability factor of $\mathrm{W}(\mathrm{r}_i, \mathrm{r}_j)$ and/or particle collision efficiency $\alpha(\mathrm{r}_i, \mathrm{r}_j)$ as one component of the aggregation rate constant ($k_{agg} = \alpha\beta$) and a main function for coupling a coagulation model with chemical reactions such as arsenic sorption. The study reviewed the collision efficiency studies for perikientic and orthokientic mechanisms and provided the numerical algorithms to calculate collision efficiency for two different transport mechanisms, depending on two colliding particle geometric sizes and surface potentials or surface charges. Finally, unified model that is coupled coagulation modeling with arsenic sorption kinetics consisting of a sorption diffusion transport model and surface complexation model was developed. Using the coupled model developed in this study, it was possible to predict arsenic sorption (equilibrium and kinetics) and colloid particle collision (surface potential time evolution, coagulation kinetics and particle size distributions) during the arsenic sorption and coagulation, simultaneously.

6.2 Introduction

Coagulation is the multi-step process of producing larger agglomerates by collisions and subsequent bonding or coalescing of smaller particles contained in a fluid. Coagulation consists of two different reactions, aggregation and breakage. The colloidal particles can be either solid or fluid materials suspended in a gas or liquid. Particle collisions are induced by inter particle motions that have been attributed to three basic mass transport mechanisms: fluid motion or orthokinetic coagulation, Brownian diffusion or perikinetic coagulation and buoyancy or differential sedimentation. In other hand, fluid motion also creates disruptive stresses that can cause fracture of the agglomerates. Particle aggregation is primarily kinetic phenomena. For example the rate of coagulation of a suspension can be written as,

$$\frac{\mathrm{dn}}{\mathrm{dt}} = -k_{agg}\mathrm{n}^2 \tag{6.1}$$

where, n is particle concentration at time t and k_{agg} is a second order aggregation rate constant depending on physical and chemical properties of the system (O'Melia and Tiller 1993). Further, the aggregation rate constant k_{agg} can be expressed as,

$$k_{agg}(\mathrm{r}_i, \mathrm{r}_j) = \alpha(\mathrm{r}_i, \mathrm{r}_j)\beta(\mathrm{r}_i, \mathrm{r}_j) \tag{6.2}$$

where, r is the particle or agglomerate radius, *i* and *j* refers to colliding particle size class indices, $\alpha(\mathrm{r}_i, \mathrm{r}_j)$ is collision efficiency or dimensionless sticking coefficient ($0 \le \alpha \le 1$), and the quantity $\beta(\mathrm{r}_i, \mathrm{r}_j)$ is termed the collision frequency or mass transport coefficient with dimensions of $(\text{length})^3/\text{time}$.

The collision frequency or mass transport coefficient, $\beta(\mathrm{r}_i, \mathrm{r}_j)$ can be simple linear operators or obtained from mass balances of the colliding particles. Smoluchowski analyzed the particle collisions created by a laminar shear flow in orthokinetic coagulation (Smoluchowski 1917) and found $\beta(\mathrm{r}_i, \mathrm{r}_j)$ to be,

$$\beta_{\mathrm{shear}}(\mathrm{r}_i, \mathrm{r}_j) = \frac{4}{3}\frac{\partial \mathrm{u}_{\mathrm{x}}}{\partial \mathrm{y}}(\mathrm{r}_i + \mathrm{r}_j)^3 \tag{6.3}$$

where $\partial \mathrm{u}_{\mathrm{X}}/\partial \mathrm{y}$ is the flow rate of strain (non-rotational velocity gradient) in the x-y direction. Saffman and Turner considered homogeneous, isotropic turbulent flow and found (Saffman and Turner 1956),

$$\beta_{\mathrm{Turb}}(\mathrm{r}_i, \mathrm{r}_j) = \sqrt{\frac{8\pi\varepsilon}{15\mu}}(\mathrm{r}_i + \mathrm{r}_j)^3 \tag{6.4}$$

where ε is the turbulent eddy energy dissipation rate and μ is the fluid viscosity. A similar kernel was derived as (Levich 1962),

$$\beta_{\text{Turb}}(r_i, r_j) = \frac{12\pi}{\sqrt{15}}\sqrt{\frac{\varepsilon}{\mu}}(r_i + r_j)^3 \tag{6.5}$$

Kramer and Clark analyzed local straining flow and derived $\beta(r_i, r_j)$ due to multi-directional strain-rate induced collisions as (Kramer and Clark 1997),

$$\beta_{\text{shear}}(r_i, r_j) = \frac{4\pi}{3}|\dot{\gamma}'_{\max}|(r_i + r_j)^3 \tag{6.6}$$

where $|\dot{\gamma}'_{\max}|$ is the magnitude of the maximum principal component of the local flow strain-rate. Perikinetic coagulation is generated by random particle collisions induced by natural Brownian random motion. For the perikinetic mechanism, the collision frequency function was derived by Smoluchowski as,

$$\beta_{\text{Br}}(r_i, r_j) = \frac{2k_B T}{3\mu}\left(\frac{1}{r_i} + \frac{1}{r_j}\right)(r_i + r_j) \tag{6.7}$$

where k_B is Boltzmann's constant, T is the temperature, and μ is the fluid viscosity. Differential sedimentation occurs due to particles settling at a faster velocity than smaller and/or less dense particles, thus colliding and forming larger aggregates. The collision frequency function for differential sedimentation is,

$$\beta_{\text{ds}}(r_i, r_j) = \pi(r_i + r_j)^2 \left|v_i - v_j\right| = \frac{\pi g}{72\mu}(\rho_p - \rho_l)(d_i + d_j)^3 \left|d_i - d_j\right| \tag{6.8}$$

where v is the terminal settling velocity of each respective particle, ρ_p and ρ_l are the particle and fluid densities, d is the particle size in diameter, and g is the gravitational constant.

This chapter will discuss particle collision efficiency $\alpha(r_i, r_j)$ that is one component of the aggregation rate constant ($k_{agg} = \alpha\beta$) and a main function for coupling a coagulation model with chemical reaction kinetics such as arsenic sorption onto HFO (Hydrous Ferric Oxide). The chapter will begin with a review of the collision efficiency study for perikientic and orthokientic mechanisms, then provide the numerical algorithms to calculate collision efficiency for two different transport mechanisms, depending on two colliding particle geometric sizes and surface potentials (surface charges), and finally develop an unified model that is a coupling coagulation model with arsenic sorption kinetics consisting of sorption diffusion transport model and surface complexation model.

6.3 Collision Efficiency

The collision efficiency (α) is a dimensionless coefficient that is the fraction of total inter-particle collisions resulting in particle aggregation and has values ranging from 0 to 1. Smoluchowski developed the particle aggregation model (Eq. (6.9)) having the assumption that all particle collisions are successful in producing aggregates, that is, the collision efficiency (α) is 1.0 (Smoluchowski 1917).

$$\frac{dn_k}{dt} = \frac{1}{2}\sum_{i+j=k} \alpha\beta(r_i, r_j) n_i n_j - n_k \sum_{l=1}^{\max} \alpha\beta(r_l, r_k) n_l \tag{6.9}$$

In a real situation this assumption cannot be supported because not all of the collisions will bond and produce larger aggregates, thus leading to efficiency values less than one. The reduced collision efficiency is due to repulsive colloidal interactions resulting from double layer repulsive forces, steric interactions, and hydrodynamic or viscous interactions, which tends to hinder the approach of colliding particles (Filella and Buffle 1993; Elimelch et al. 1995).

The colloid stability ratio (W_{ij}) is the inverse of collision efficiency for two colliding particles *i* and *j* and can be expressed by the ratio of rapid aggregation rate constant (k_{rapid}), which is theoretically computed by Smoluchowski to the rate constant under the conditions of interest (k_{slow}).

$$W_{ij} = \frac{1}{\alpha_{ij}} = \frac{k_{\text{rapid}}}{k_{\text{slow}}} \tag{6.10}$$

Therefore, this colloid stability ratio (or collision efficiency) can be termed as collision delay factor having the ratio of the aggregation rate in the absence of colloidal interactions to that found when there is repulsion between particles. The retardation factor (W_{ij}) for slow coagulation is not constant but increases as the particles grow during coagulation and finally the barrier may become so high as to prevent any further agglomeration (Overbeek 1952). However, it has been impossible to calculate the retardation factor quantitatively because the agglomeration would have a very complicated form so that exact calculations on the particle interaction energy were not feasible. With the advance of colloid interface science and computational capability, the collision efficiency has being unveiled from perikinetic coagulation (Spielman 1970; Honig 1971; Valioulis and List 1984; Han and Lee 2002) and from orthokinetic coagulation (Curtis and Hocking 1969; van de Ven and Mason 1976; van de Ven and

Mason 1977; Zeichner and Schowalter 1977; Zeichner and Schowalter 1979; Adler 1981a; Adler 1981b; Higashitani et al. 1982).

6.3.1 Collision Efficiency in Brownian Random Motion (α_{Br})

Fuchs derived the colloid stability for Brownian motion having total interactive energy (V_T) between colliding particles where the interactive energy (V_T) is the summation of van der Waals attraction energy (V_A) and electrical repulsion energy (V_R) as (Fuchs 1934),

$$V_T = V_R + V_A \tag{6.11}$$

$$W_{Br} = \frac{1}{\alpha_{Br}} = 2\int_0^\infty \frac{\exp\left(V_T/k_B T\right)}{(S+2)^2}\,dS \tag{6.12}$$

with

$$S = \frac{2l}{r_i + r_j} \tag{6.13}$$

where, V_T is total interactive energy between two colliding particles, k_B is Boltzmann's constant, T is the absolute temperature, S is dimensionless separation distance, l is the distance between two colliding particle centers, r_i and r_j are spherical particle radii for size class i and j, respectively. Equation (6.12) must be evaluated numerically, using appropriate expressions for the electrical repulsive and van der Waals attractive interactions (Elimelch et al. 1995).

Several researchers considered the hydrodynamic force using Brenner's solution, as well as repulsive and attraction forces (Spielman 1970; Honig 1971; Valioulis and List 1984). They insisted that the diffusivity between two colliding particles in the viscous fluid condition is a function of particle size and size ratio, not the sum of the diffusivities of each particle resulting from the hydrodynamic interaction between the two particles.

$$W_{Br} = \frac{1}{\alpha_{Br}} = \left(1 + \frac{r_i}{r_j}\right) \int_{1+\frac{r_i}{r_j}}^{\infty} \left(\frac{D_{i,j}^{\infty}}{D_{i,j}}\right) \frac{\exp\left(V_T/k_B T\right)}{S^2} dS \tag{6.14}$$

or

$$W_{Br} = \frac{1}{\alpha_{Br}} = 2\int_{2}^{\infty} \left(\frac{1}{G(S,\lambda)}\right) \frac{\exp\left(V_T/k_B T\right)}{S^2} dS \tag{6.15}$$

with $D_i = k_B T/6\pi\mu r_i$ and $D_i = k_B T/6\pi\mu r_j$ where $D_{i,j}^{\infty}/D_{i,j}$ is a dimensionless value representing the viscous effects due to the fluid motion between the particles, and $D_{i,j}$ is the sum of D_i and D_j for each size class i and j particle, and $G(S,\lambda)$ is a function of the additional resistance due to the squeezing of the fluid between the two approaching particles.

Han and Lee (2002) modified the equation of Spielman using dimensionless variables, S and λ, considering electrostatic repulsive forces, van der Waals attractive forces and hydrodynamic forces,

$$W_{Br} = \frac{1}{\alpha_{Br}} = \left(1 + \frac{r_i}{r_j}\right) \int_{2}^{\infty} \left(\frac{1}{G^{*}(S,\lambda)}\right) \frac{\exp\left(V_T/k_B T\right)}{S^2} dS \tag{6.16}$$

where $G^{*}(S,\lambda)$ indicates the hydrodynamic function based on Jeffrey and Onishi's solution (Jeffrey and Onishi 1984). Equation (6.16) consists of two hydrodynamic functions, resistance function (Brenner and O'Neill 1972)) and mobility function (Batchelor 1976). As shown above, it is clear that the total particle interaction energy (V_T) is a major factor in particle collision efficiency, $\alpha(r_i, r_j)$ (or stability, W).

Consequently, in coagulation kinetics, it is essential to evaluate these interaction energies, properly.

Hamaker proposed the equation for the attractive energy between spherical particles with size ratio λ as,

$$V_A = -\frac{2A\lambda}{3(1+\lambda)^2}\left[\frac{2}{S^2-4}+\frac{2}{S^2-\frac{4(1-\lambda)^2}{(1+\lambda)^2}}+\frac{(1+\lambda)^2}{4\lambda}\ln\frac{S^2-4}{S^2-\frac{4(1-\lambda)^2}{(1+\lambda)^2}}\right] \tag{6.17}$$

where A is the Hamaker constant and S is dimensionless separation distance. The attractive energy expressed by the Hamaker summation method has been widely used to calculate the van der Waals-London interaction energy. For two unequal spherical particles having radii of r_i and r_j , respectively, the attractive energy between two particles is written as (Mahanty and Ninham 1976),

$$V_A = -\frac{A(h)}{6}\left[\frac{2r_ir_j}{l^2-(r_i+r_j)^2}+\frac{2r_ir_j}{l^2-(r_i-r_j)^2}+\ln\frac{l^2-(r_i+r_j)^2}{l^2-(r_i-r_j)^2}\right] \tag{6.18}$$

where l is the is the center to center separation between two spherical particles and A(h) effective Hamaker constant for two materials in a medium. A(h) is calculated from several methods (Mahanty and Ninham 1976; Pailthorpe and Russel 1982; Bowen and Jenner 1995). In the case of colliding between equal spherical particles ($r_i = r_j$), the Eq. (6.18) can be reduced to,

$$V_A = -\frac{A(h)}{6}\left[\frac{2}{S^2-4}+\frac{2}{S^2}+\ln\frac{S^2-4}{S^2}\right] \tag{6.19}$$

It should be noted that Eq. (6.17) overestimates the attractive forces due to the neglect of electromagnetic retardation, especially when particles are at large distances (the separation is larger than 10 nm). To consider the retardation effect on the attractive energy of Eq. (6.17), several researchers developed retarded van der Waals attraction energy (Schenkel and Kitchener 1960; Ho and Higuchi 1968). From the study of Ho and Higuchi (1968), the retarded attraction energy can be calculated as,

$$\mathrm{V_A} = -\frac{\mathrm{A}\lambda}{3(1+\lambda)^2}\frac{1}{(\mathrm{S}-2)}\left(\frac{2.45}{5p_0} - \frac{2.17}{15p_0^2} + \frac{0.59}{35p_0^3}\right) \qquad p_0 \geq 1.0 \tag{6.20}$$

$$\mathrm{V_A} = -\frac{\mathrm{A}\lambda}{3(1+\lambda)^2}\frac{1}{(\mathrm{S}-2)}\left(\frac{1}{1+1.7692p_0}\right) \qquad p_0 < 1.0 \tag{6.21}$$

with

$$p_0 = \frac{\pi[\max(\mathrm{r}_i, \mathrm{r}_j)](1+\lambda)(\mathrm{S}-2)}{\lambda_\mathrm{L}} \tag{6.22}$$

where, λ is colliding particles size ratio, S is the dimensionless separation distance, and λ_L is London wave length (typically 100 nm).

Particle interaction energy due to electrostatic repulsion (DLVO theory) for spherical particles cannot be obtained as easily as the parallel plate cases. Thus, only approximate methods are available for the spherical case (Kihira et al. 1992). One simplified approach is the Derjaguin approximation which is valid for $\kappa H_o > 10$,

$$\mathrm{V_R} = \frac{2\pi \mathrm{r}_i \mathrm{r}_j}{\mathrm{r}_i + \mathrm{r}_j}\int_{\mathrm{H}_0}^{\infty} \mathrm{V_{Overbeek}}\,d\mathrm{H} \tag{6.23}$$

$$\mathrm{V_{Overbeek}} = \Delta \mathrm{G(H)} - \Delta \mathrm{G}(\infty) \tag{6.24}$$

where, κ is Debye parameter (inverse of Debye-Huckel distance) and H_o is the shortest separation distance between two spherical particles. The expressions ΔG(H) and ΔG(∞) in Eq. (6.23) are well described and can be calculated by the study of Kihira et al. (1992) where Overbeek's expression was used for the double-layer interaction energy calculation. The Hog-Healy-Fuerstenau (HHF) analytical expression can be applied to the repulsive energy between spherical particles (Hogg et al. 1966),

$$\begin{aligned} V_R &= \varepsilon_0 \varepsilon_r \frac{\pi r_i r_j}{r_i + r_j}\left(\frac{k_B T}{e}\right) \times \\ &\left\{ 2\phi_i \phi_j \ln\left[\frac{1+\exp(-\kappa H_0)}{1-\exp(-\kappa H_0)}\right] + (\phi_i^2 + \phi_j^2)\ln\left[1-\exp(-2\kappa H_0)\right] \right\} \end{aligned} \tag{6.25}$$

where, e is proton charge, ϕ_i and ϕ_j are reduced Stern potentials for surfaces i and j potential ($\phi = e\psi / k_B T$), ε_0 and ε_r are permittivity, vacuum and in relative cases. For the same surface potential of $\phi_i = \phi_j$, electric repulsive energy between unequal spherical particles can be approximated as (Han and Lee 2002),

$$V_R = \frac{\varepsilon_r \lambda[\max(r_i, r_j)]}{1+\lambda} \psi_s^2 \ln\left\{1+\exp\left[-\kappa\left(\frac{2l}{r_i + r_j} - 2\right)\right]\right\} \tag{6.26}$$

where λ is particle size ratio (small to large). Other various equations are available to calculate the electrostatic energies (V_R) and forces (F_R) for different conditions, and these equations are listed in Table 6.1 (Russel et al. 1989).

Table 6.1 Electrostatic Repulsive Energies (V_R) and Forces (F_R) (Russel et al. 1989)

Geometry	Constraint	V_R	F_R
Flat plates	Superposition	$64k_B Tn_b \kappa^{-1} \tanh^2(0.25\psi_s)\exp(-\kappa H)$	$64k_B Tn_b \tanh^2(0.25\psi_s)\exp(-\kappa H)$
Spheres	Constant potential	$2\pi\varepsilon\varepsilon_0\left(\frac{k_B T}{ze}\right)^2 a\psi_s^2 \ln[1+\exp(-\kappa H)]$	$2\pi\varepsilon\varepsilon_0\left(\frac{k_B T}{ze}\right)^2 \kappa a\psi_s^2 \frac{\exp(-\kappa H)}{1+\exp(-\kappa H)}$
Spheres	Constant charge	$-2\pi\varepsilon\varepsilon_0\left(\frac{k_B T}{ze}\right)^2 aq^2 \ln[1-\exp(-\kappa H)]$	$2\pi\varepsilon\varepsilon_0\left(\frac{k_B T}{ze}\right)^2 \kappa aq^2 \frac{\exp(-\kappa H)}{1-\exp(-\kappa H)}$
Spheres	Linear superposition	$4\pi\varepsilon\varepsilon_0\left(\frac{k_B T}{ze}\right)^2 \frac{a^2}{H+2a}\psi_s^2 \exp(-\kappa H)$	$\pi\varepsilon\varepsilon_0\left(\frac{k_B T}{ze}\right)^2 \frac{1+\kappa(H+2a)}{(H/2a+1)^2}\psi_s^2 \exp(-\kappa H)$
Spheres	Superposition	$32\pi\varepsilon\varepsilon_0\left(\frac{k_B T}{ze}\right)^2 a \tanh^2(0.25\psi_s)\exp(-\kappa H)$	$32\pi\varepsilon\varepsilon_0\left(\frac{k_B T}{ze}\right)^2 \kappa a \tanh^2(0.25\psi_s)\exp(-\kappa H)$

Equation (6.15) can be integrated to investigate perikinetic collision efficiency resulting from Brownian random motion. As shown in Eq. (6.15), two interaction energy calculations that are representing van der Waals attraction energy (V_A) and electrostatic repulsive energy (V_R) are needed to obtain the collision efficiency (α_{Br}) between two colliding particles. These equations introduced to use as the perikientic collision efficiency calculation are rewritten as,

$$W_{Br}=\frac{1}{\alpha_{Br}}=2\int_2^\infty\left(\frac{1}{G(S,\lambda)}\right)\frac{\exp\left(V_T/k_B T\right)}{S^2}dS \tag{6.15}$$

$$V_T = V_R + V_A \tag{6.11}$$

$$V_A = -\frac{A\lambda}{3(1+\lambda)^2}\frac{1}{(S-2)}\left(\frac{2.45}{5p_0}-\frac{2.17}{15p_0^2}+\frac{0.59}{35p_0^3}\right) \qquad p_0 \geq 1.0 \tag{6.20}$$

$$V_A = -\frac{A\lambda}{3(1+\lambda)^2}\frac{1}{(S-2)}\left(\frac{1}{1+1.7692p_0}\right) \qquad p_0 < 1.0 \tag{6.21}$$

$$V_R = \frac{\varepsilon_r\lambda[\max(r_i, r_j)]}{1+\lambda}\psi_s^2 \ln\left\{1+\exp\left[-\kappa\left(\frac{2l}{r_i+r_j}-2\right)\right]\right\} \tag{6.26}$$

The attraction energy (V_A) of Eqs. (6.21)/(6.20) and the repulsive energy (V_R) of Eq. (6.26) were substituted into total energy total or net interaction energy (V_T) of perikinetic collision efficiency of Eq. (6.15). For the numerical modeling initial conditions, the Hamaker constant (A) was given as 4.14×10^{-20} J (Hiemenz and Rajagopalan 1997) and a moderate ionic strength value of 0.01 M was used. In this numerical modeling of perikinetic coagulation, the effect of hydrodynamic force on the collision efficiency (α_{Br}) was neglected by letting the hydrodynamic function of $G(S,\lambda)$ be 1 in Eq. (6.15). Thus, the numerical simplification in this study can overestimate the collision efficiency during perikientic coagulation rather than the exact value resulting from real particle collision.

The numerical modeling for perikinetic collision efficiency (α_{Br}) was conducted under main two categories; between two equal size colliding particles ($r_i = r_j$) and two unequal size colliding particles ($r_i \neq r_j$) at various particle surface potential conditions ($\psi_{s,i} = \psi_{s,j}$). For the study of perikinetic collision efficiency (α_{Br}) between equal size colliding particles, the particle size was selected in the range of 10 nm to 1 μm, in which Brownian random motion is the dominant colliding mechanism among the three basic mass transport mechanisms: fluid motion or orthokinetic coagulation, Brownian diffusion or perikinetic coagulation and buoyancy or differential sedimentation. The result from the collision efficiency simulation for the equal size colliding particles governed by Brwonian diffusion was represented by Fig. 6.1. As shown in Fig. 6.1, the perikinetic collision efficiency (α_{Br}) decreases as the colliding particle size increases under all surface potential regimes.

The collision between relatively large particles (200 < d < 1000 nm) can not be expected at the surface potential of less than -15 mV or larger than +15 mV. For the particle size range of 100 nm to 1000 nm, collision efficiency slightly increases, thus particle collision can be expected at the surface potential range of -25 mV to +25 mV. This result corresponds to the other perikinetic coagulation study (Subramaniam et al. 1998). In their study, only within the surface potential range of -20 mV to +20 mV, homogeneous HFO (hydrous ferric oxide) particles of size range of 220 nm to 600 nm were observed to be destabilized.

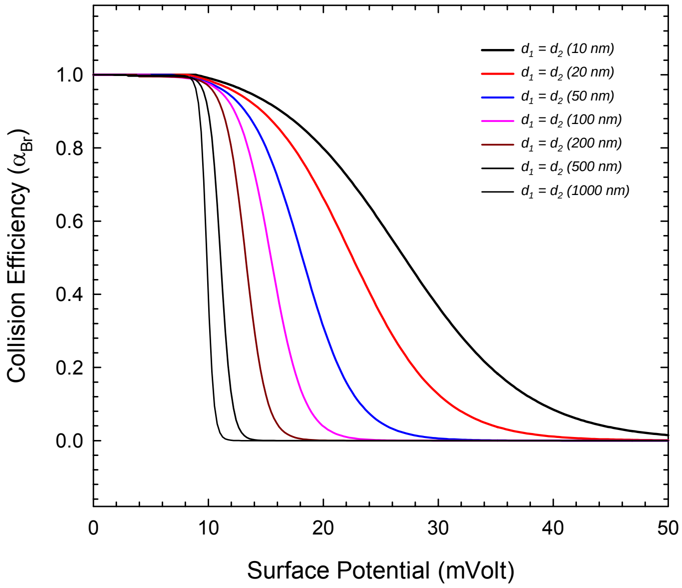

Figure 6.1 Perikinetic collision efficiency (α_{Br}) between two equal size colliding particles at various particle surface potential conditions

Moreover, it can be expected that nano-scale particle collisions (under 10 nm) occur even though the particle surface has the relatively high potential range of -50 mV to +50 mV. That is, these nano-scale particles can be easily destabilized under or over this surface potential magnitude limit (±50 mV) and lead to aggregate formation. Thus, it is expected that surface potential (charge) plays a key role in the nano-scale particle technologies. Without any surface potential (charge), the nano-scale particles are readily dispersed so that they form aggregate shape due to high perikinetic particle collision efficiency. In contrast, by letting the nano-size particles have surface potential (charge), the nano-size particles maintain their small size physico-chemical properties without forming aggregates. Furthermore, the large aggregate (i.e., 1000 nm in diameter) formed during perikinetic coagulation may not be found under the surface potential of less than -10 mV or larger than +10 mV. More details of the relationship between surface potential and aggregate formation will be discussed at the last section of coupled coagulation modeling with sorption kinetics and equilibrium modeling.

In addition, perikinetic collision efficiency (α_{Br}) between unequal size colliding particles was simulated and these results are displayed in Figs. 6.2 to 6.5. Particle size ratio (d_{max}/d_{min}) of 1 to 10 was applied to the unequal size particle collision study. For all cases, the collision efficiency decrease as size ratio (d_{max}/d_{min}) decrease from 10 to 1 at various particle surface potential conditions. Further, even though the particle size ratio range was fixed as 1 to 10 for all unequal size particle collision cases, the overall perikinetic collision efficiency (α_{Br}) has the higher at d = 10 ~ 100 nm rather than at d = 100 ~ 1000 nm. Like equal size particle collision, this result indicates that smaller particle between unequal size colliding particles is very important in the Brownian diffusion. Furthermore, as shown in Fig. 6.5, only within the surface potential range of -20 mV to +20 mV, particle colliding can be expected due to colloid destabilization.

As a result, perikinetic collision efficiency (α_{Br}) was not a universal constant but rather a function of geometric size and surface potential between colliding particles.

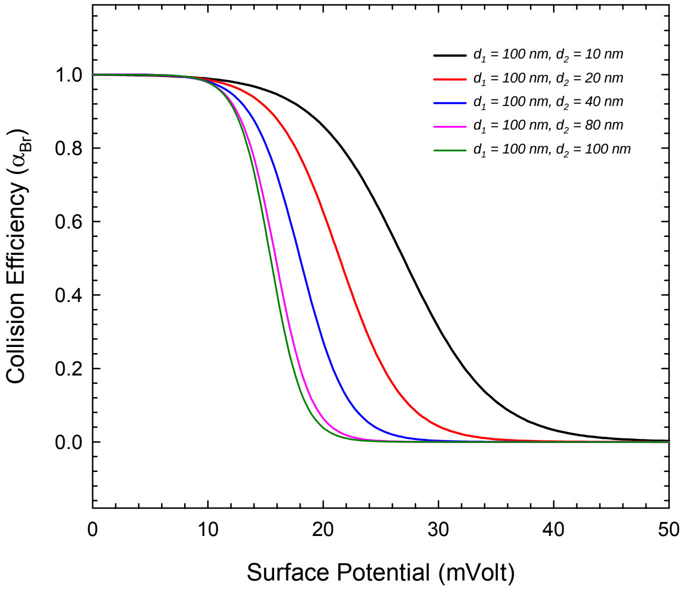

Figure 6.2 Perikinetic collision efficiency (α_{Br}) between two unequal size colliding particles at various particle surface potential conditions (d = 10~100 nm)

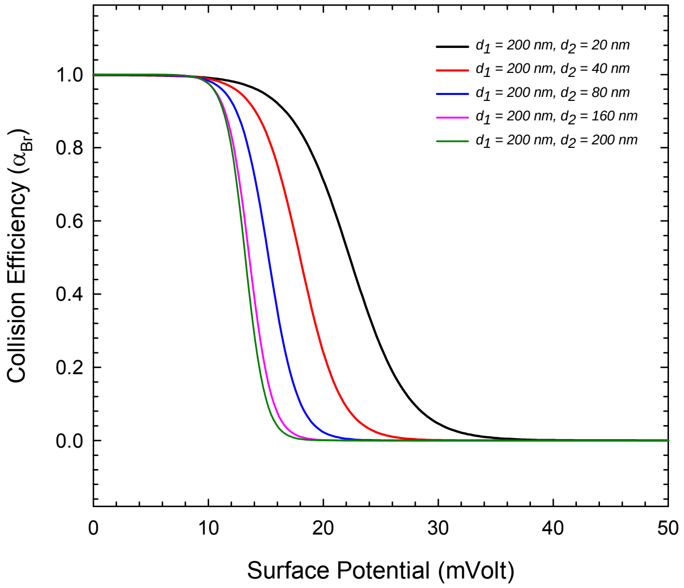

Figure 6.3 Perikinetic collision efficiency (α_{Br}) between two unequal size colliding particles at various particle surface potential conditions (*d* = 20~200 nm)

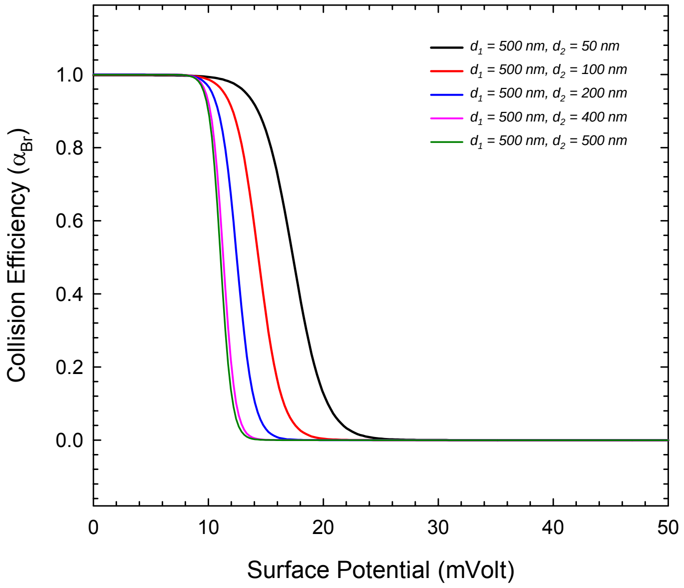

Figure 6.4 Perikinetic collision efficiency (α_{Br}) between two unequal size colliding particles at various particle surface potential conditions (*d* = 50~500 nm)

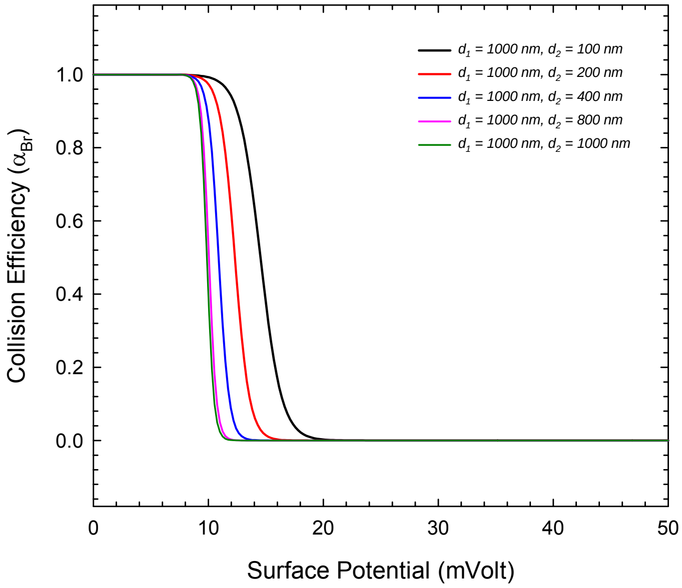

Figure 6.5 Perikinetic collision efficiency (α_{Br}) between two unequal size colliding particles at various particle surface potential conditions (*d* = 100~1000 nm)

6.3.2 Collision Efficiency in a Fluid Flow (α_{Sh})

Smoluchowski (1917) analyzed the collision of two particles transported by the movement of the surrounding fluid, considering non-interactive forces between two approaching particles in a simple shear flow field (α = 1.0). This collision theory was extended to a turbulent flow filed (Saffman and Turner 1956), assuming that "particles smaller than the smallest eddies move alike in a shear flow, whose rate of shear is related to the rate of energy dissipation through the Taylor micro-scale relations (Melis et al. 1999)". However, collision efficiency in a turbulent filed is not easily calculated from theoretical and experimental approaches. Thus, most of the existing studies on orthokinetic coagulation, especially in terms of theoretical collision efficiency, have been conducted for a simple shear flow (laminar regime), since pure laminar flow can be easily generated in the laboratory using co-axial rotating cylinders to generate a Couette flow which has a simple mathematical description (Vanni and Baldi 2002). Also, a number of authors have adopted the collision efficiency calculated for laminar flow to predict turbulent coagulation kinetics (Higashitani et al. 1983; Boer et al. 1989; Adachi et al. 1994; Kusters et al. 1997).

A simplified model was proposed to calculate orhokinetic collision efficiency (α_{Sh}) as functions of fluid shear/strain-rate and collision particle size (van de Ven and Mason 1976; van de Ven and Mason 1977), as

$$\alpha(\mathrm{r}_j, \mathrm{r}_j) = f(\lambda / \mathrm{r}_j)\frac{\mathrm{A}}{36\pi\mu\dot{\gamma}\mathrm{r}_j^3} \tag{6.27}$$

where $\dot{\gamma}$ is a flow strain-rate and $f(\lambda / \mathrm{r}_j)$ is a function of the dispersion wavelength (since retardation effects were included) and the particle size. From the study of van de Ven and Mason, in the case of a London characteristic wavelength of 100 nm (typical colloidal particles), $f(\lambda / \mathrm{r}_j)$ has 0.79, 0.87, and 0.95 for particles of radius 2, 1, and 0.5 μm, respectively. From Eq. (6.27) it can be found that collision efficiency decreases as the particle size and the shear rate increase due to the exponential relationship of $\dot{\gamma}^{0.82}$, rather than being linearly dependent on shear (strain-rate), as in the Smoluchowski result (Elimelch et al. 1995). Although there exists an inverse relationship between collision efficiency and flow strain-rate, however, the collision rate constant (collision efficiency(α)×collision frequency(β)) increases for large particles (see Eq. (6.6)). Unfortunately, this simplified model is only possible to apply in equal size particle collisions rather than unequal size particle collisions due to the main assumption of colliding between same size class particles. Thus, the advanced technique was needed to calculate the collision efficiency (α_{Sh}) for unequal size particle collision modeling.

Shear induced coagulation studies after the 1970's (Curtis and Hocking 1969; van de Ven and Mason 1976; van de Ven and Mason 1977; Zeichner and Schowalter 1977; Zeichner and Schowalter 1979; Adler 1981a; Adler 1981b; Higashitani et al. 1982) included two-sphere trajectory analysis to predict the effects of hydrodynamic interaction forces on collision efficiency.

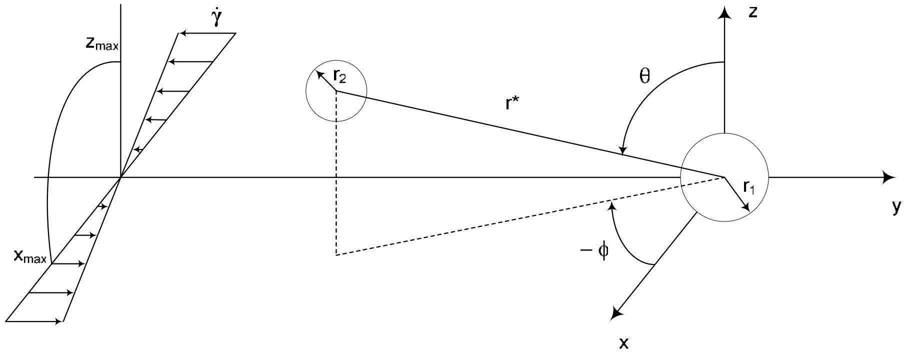

Figure 6.6 Trajectory analysis coordinate for two spheres in a simple shear flow

According to these trajectory studies, the relative motion of two spherical particles can be summarized in terms of polar coordinates (r^*, θ, ϕ), expressed by the ordinary differential equations,

$$\frac{dr^*}{dt} = \dot{\gamma} r^*(1-\mathcal{A})\sin^2\theta\sin\phi\cos\phi + \frac{\mathcal{C}}{6\pi\mu r_1^2}(F_T) \tag{6.28}$$

$$\frac{d\theta}{dt} = \dot{\gamma}(1-\mathcal{B})\sin\theta\cos\theta\sin\phi\cos\phi \tag{6.29}$$

$$\frac{d\phi}{dt} = \dot{\gamma}\left(\cos^2\phi - \frac{\mathcal{B}}{2}\cos 2\phi\right) \tag{6.30}$$

where the hydrodynamic parameters $\mathcal{A}$, $\mathcal{B}$ and $\mathcal{C}$ can be calculated from the trajectory studies (Batchelor and Green 1972; Zeichner and Schowalter 1977; Adler 1981b; Higashitani et al. 1982; Wang 1992). For large separations, the hydrodynamic parameters can be written as (Batchelor and Green 1972),

$$\mathcal{A} = \frac{\frac{5}{2}(1+\lambda^3)}{(\mathrm{r}^*)^3} - \frac{\frac{3}{2}(1+\lambda^5)+\frac{5}{2}\lambda^2(1+\lambda)}{(\mathrm{r}^*)^5} + \frac{25\lambda^3}{(\mathrm{r}^*)^6} \tag{6.31}$$

$$\mathcal{B} = \frac{1+\lambda^5+\frac{5}{3}\lambda^2(1+\lambda)}{(\mathrm{r}^*)^5} \tag{6.32}$$

$$\mathcal{C} = \frac{1+\lambda}{\lambda}\left[1 - \frac{6\lambda}{(1+\lambda)^2(\mathrm{r}^*)} + \frac{8(1+\lambda^2)\lambda}{(1+\lambda)^4(\mathrm{r}^*)^3} - \frac{60(1+\lambda^3)\lambda}{(1+\lambda)^5(\mathrm{r}^*)^4}\right] \tag{6.33}$$

$$\text{with } \lambda = \frac{\mathrm{r}_2}{\mathrm{r}_1} \text{ and } \mathrm{r}^* = \frac{l}{\mathrm{r}_1} \tag{6.34}$$

where l is the distance between colliding particle centers. Also, for very small separations, these hydrodynamic parameters hold as,

$$\mathcal{A} = 1 - 4.08\hat{h} \quad \mathcal{B} = 0.4060 + \frac{0.78}{\ln\hat{h}} \quad \mathcal{C} = 4\hat{h}(1+1.34\hat{h}\ln\hat{h}) \quad \text{for } \lambda = 1.0 \tag{6.35}$$

$$\mathcal{A} = 1 - 4.50\hat{h} \quad \mathcal{B} = 0.5830 + \frac{1.36}{\ln\hat{h}} \quad \mathcal{C} = 9\hat{h}(1+1.70\hat{h}\ln\hat{h}) \quad \text{for } \lambda = 0.5 \tag{6.36}$$

$$\mathcal{A} = 1 - 3.06\hat{h} \quad \mathcal{B} = 0.9104 + \frac{1.89}{\ln\hat{h}} \quad \mathcal{C} = 36\hat{h}(1+2.46\hat{h}\ln\hat{h}) \quad \text{for } \lambda = 0.2 \tag{6.37}$$

with

$$\hat{h} = (l - \mathrm{r}_1 - \mathrm{r}_2)/\mathrm{r}_1 \tag{6.38}$$

As shown in Eq. (6.28), total force (F_T) interacting between two colliding particles in fluid shear flow applied needs to be calculated as,

$$\mathrm{F}_\mathrm{T} = \mathrm{F}_\mathrm{A} + \mathrm{F}_\mathrm{R} \tag{6.39}$$

The interparticle forces can be obtained by differentiating the respective interparticle potential energies against particle separation distance as,

$$\mathrm{F} = \frac{d\mathrm{V}(h)}{dh} = \frac{d\mathrm{V}(h)}{d\mathrm{S}}\frac{d\mathrm{S}}{dh} \tag{6.40}$$

where h is separation distance defined as $h = l - \mathrm{r}_1 - \mathrm{r}_2$. The Schenkel-Kitchener formula (Schenkel and Kitchener 1960) has been mainly used for the van der Waals attractive potential energy accounting for the retardation effect. Further, the attractive force can be derived from Schenkel-Kitchener's attractive potential formula using the relationship between the energy and force of Eq. (6.40) (Wang 1992), as

$$\mathrm{F}_\mathrm{A} = -\frac{\mathrm{A}_{1,2}\mathrm{r}_2}{(1+\lambda)h^2}\left[\frac{2.45}{15p} - \frac{2.17}{30p^2} + \frac{1.18}{105p^3}\right] \qquad p \geq 1.0 \tag{6.41}$$

$$\mathrm{F}_\mathrm{A} = -\frac{\mathrm{A}_{1,2}\mathrm{r}_2}{(1+\lambda)h^2}\left[\frac{1+3.54p}{6(1+1.77p)^2}\right] \qquad p < 1.0 \tag{6.42}$$

with

$$p = 2\pi\mathrm{S}/\lambda_\mathrm{L} \tag{6.43}$$

Also, the electrostatic repulsive force can be obtained from the interparticle repulsive energy of Eq. (6.25) using the Eq. (6.40) (Wang 1992), as

$$\mathrm{F}_\mathrm{R} = \frac{\pi\varepsilon_0\varepsilon_r\kappa\mathrm{r}_2}{1+\lambda}\left[\frac{2\psi_1\psi_2 - (\psi_1^2+\psi_2^2)\exp(-\kappa h)}{\sinh(\kappa h)}\right] \tag{6.44}$$

From the trajectory studies, it can be assumed that the collision efficiency, $\alpha(\mathrm{r}_1, \mathrm{r}_2)$ is related to the profile of the collision cross-section x(z) (Vanni and Baldi 2002),

$$\alpha(r_1, r_2) = \frac{3/2}{(r_1 + r_2)^3} \int_0^{z_{max}} [x(z)]^2 dz \tag{6.45}$$

Equation (6.45) can be calculated by a consideration that compares an actual non-equatorial collision cross-section assumed by the Smoluchowski model (particles move like the fluid along straight streamlines until they collide with another particle) as shown in Fig. 6.7 (Vanni and Baldi 2002).

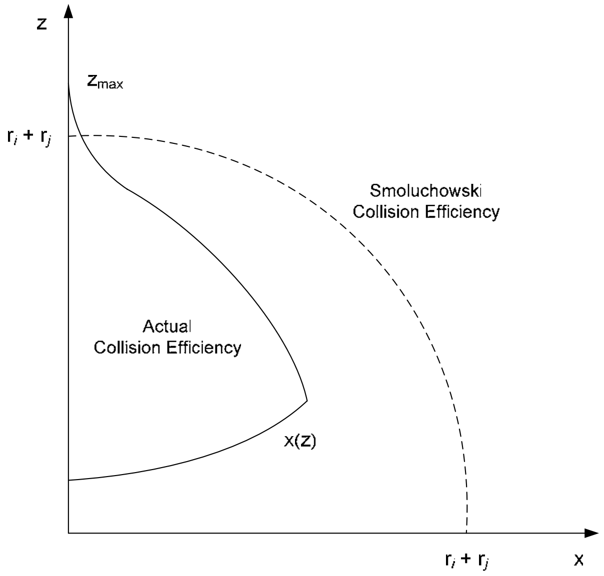

Figure 6.7 Collision efficiency related to the profile of the collision cross-section x(z) (Vanni and Baldi 2002)

The collision efficiency (α_{Sh}) in the applied fluid shear flow was calculated using trajectory analysis. The trajectory analysis could be achieved by integrating the set of ordinary differential equations of Eqs. (6.28) to (6.30). To solve the ordinary differential equation for particle trajectories in the applied flow field, three acting forces on the colliding particles were introduced into Eqs. (6.28) to (6.30); hydrodynamic effect of

Eqs. (6.31) to (6.38), van der Waals attractive force (F_A) of Eqs. (6.41) to (6.43), and electrostatic repulsive force (F_R) of Eq. (6.44).

The trajectory analysis for determining orthokinetic collision efficiency (α_{Sh}) in the shear flow was conducted under several computational conditions proposed by previous researchers (Higashitani et al. 1982; Wang 1992; Vanni and Baldi 2002). The numerical computation was initiated with the plane $y = -100(\mathrm{r}_1)$ for each trial ($x > 0$, $z > 0$). A 30×30 evenly spaced quadrant mesh was placed in the start plane to calculate the collision cross-section. The size of each side of the quadrant mesh placed on the plane of $y = -100(\mathrm{r}_1)$, $x > 0$, and $z > 0$ was set to $1.5(\mathrm{r}_1 + \mathrm{r}_2)$. Every quadrant mesh node was used as a release point for particle 2 (r_2) and after beginning the computation the trajectory of particle 2 was integrated to determine whether the collision occurs or not (collision efficiency). In addition, the computation was terminated when the numerical criteria (collision, orbit, or separation) yielded as (Vanni and Baldi 2002),

Collision $$\frac{\mathrm{r}^*}{\mathrm{r}_1} < 1 + \frac{\mathrm{r}_2}{\mathrm{r}_1} + \varepsilon_{allow} \tag{6.46}$$

Orbit $$\phi > \frac{\pi}{2} \tag{6.47}$$

Separation $$\frac{y}{r_1} > 10 \tag{6.48}$$

where, ε_{allow} is error tolerance. Solutions to the trajectory equations consist of a set of the ordinary differential equations of Eqs. (6.28) to (6.30) and were obtained using the FORTRAN ODE integrating method IVPAG. The error tolerance was 10^{-6} for all numerical solutions during the trajectory modeling. The parameter ε_{allow} of the collision criterion of the Eq. (6.46) was set to 10^{-7} as recommended by Vanni and Baldi (2002). To consider the hydrodynamic effect on the particle trajectory in the shear flow, the three hydrodynamic parameters ($\mathcal{A}$, $\mathcal{B}$, and $\mathcal{C}$) for far-field separation (or large separation) between the two colliding particles (Eqs. (6.31) to (6.34)) were introduced to the trajectory analysis, rather than the near-field separation (or small separation) of Eqs. (6.35) to (6.38). As the near-field separation formula could not be used for the unequal size colliding particles having a wide range of size ratio λ, far-field separation formula were introduced as the parameter calculation representing the hydrodynamic effect on the trajectory. To apply this orthokinetic collision efficiency using trajectory analysis into the unified coagulation model, various colliding particle size ratios should be required, rather than the small separation formula of Eqs. (6.35) to (6.37) having limited application for only colliding particle size ratios (λ) of 1.0, 0.5, and 0.2. Thus, large separation hydrodynamic parameters of Eqs. (6.31) to (6.33) were used in this study.

To investigate the effect of electrostatic force applied to two colliding particles on the orthokinetic collision efficiency in the applied shear flow, trajectory analysis was visualized in y-z 2D plane in Figs. 6.8 and 6.9. In this test, two spherical colliding particles of 1 μm and 10 μm in diameter was simulated in the shear flow of 15 1/sec in strain-rate. Like the perikinetic coagulation collision efficiency study, Hamaker constant (A) of 4.14×10^{-20} J (Hiemenz and Rajagopalan 1997) and a moderate ionic strength value of 0.01 M were introduced as numerical modeling initial conditions. The particle trajectory simulations in applied shear flow (strain-rate of 15 1/s) were conducted under two different particle surface potential conditions of 0 mV and 50 mV.

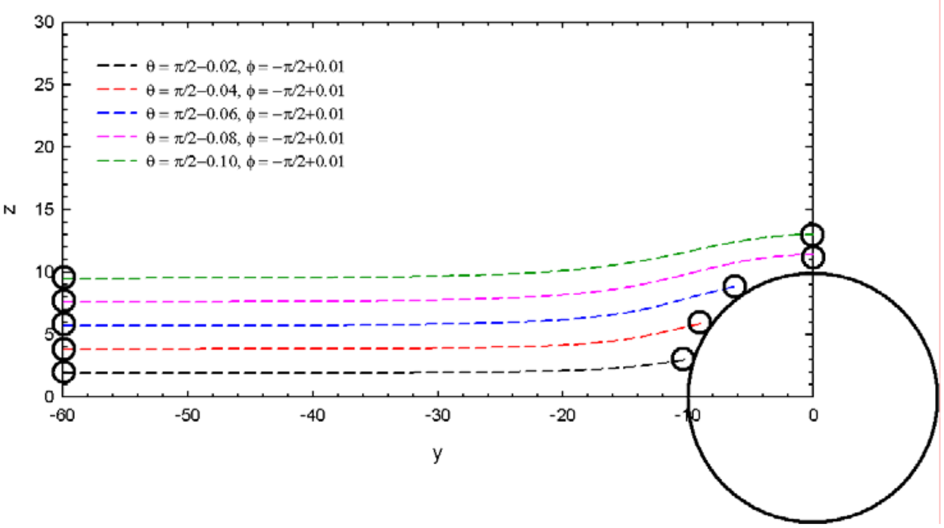

Figure 6.8 Collision trajectory (y-z) in absence of electrostatic repulsive force (surface potential = 0 mv, strain rate = 15 1/s)

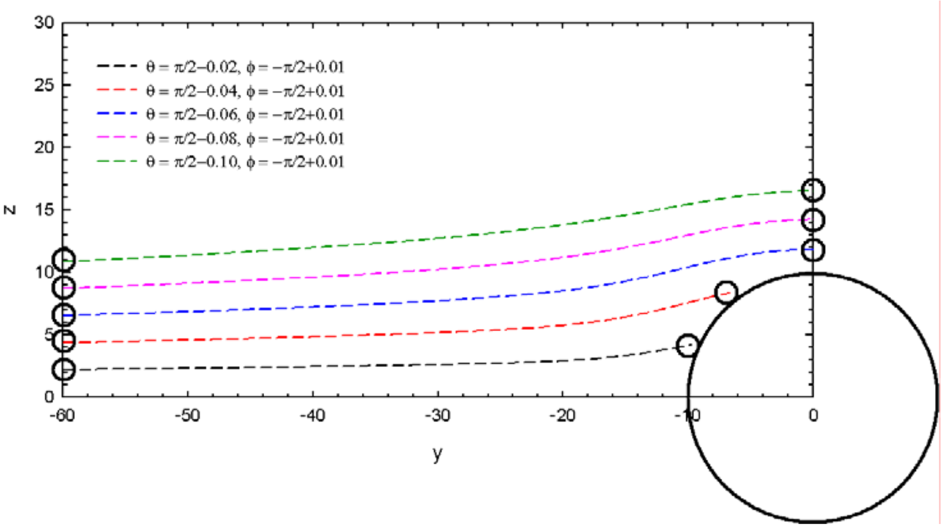

Figure 6.9 Collision trajectory (y-z) in presence of electrostatic repulsive force (surface potential = 50 mv, strain rate = 15 1/s)

As shown in Figs. 6.8 and 6.9, these results indicate that particle collision probability decreases as colliding particle surface potential increases. That is, the surface potential applied to the colliding particles plays a role in the determining orthokinetic collision efficiency as would be expected.

The orthokinetic collision efficiency (α_{sh}) was investigated under two main categories; between two equal size colliding particles ($r_i = r_j$) and two unequal size colliding particles ($r_i \neq r_j$) at various particle surface potential conditions ($\psi_{s,i} = \psi_{s,j}$) and flow strain-rates. The particle surface potential ranged from -30 mV to +30 mV and all numerical simulation was conducted at the flow strain-rates of 10, 25, and 50 1/sec. For the study of orthokinetic collision efficiency (α_{sh}) between equal and unequal size colliding particles at various flow strain-rate conditions, the primary and maximum particle sizes were selected as 1 and 8 μm, respectively. In these colliding particle size ranges, flow strain-rate is the dominant colliding mechanism among the three basic mass transport mechanisms mentioned above. The results from the orthokinetic collision efficiency simulation for the equal and unequal size colliding particles governed by fow strain-rate are represented in Figs. 6.10 to 15. As expected from the perikinetic collision efficiency study of section 6.3.1, the orthokinetic collision efficiency (α_{sh}) decreased as the colliding particle size increases from 1.0 μm to 8.0 μm under the conditions of the applied strain-rate ranges of 10 to 50 1/s and surface potential ranges of 0 to 30 mV. Further, it is found that the smaller colliding particles are more sensitive to magnitude of particle surface potential applied than the larger particles. Orthokinetic collision efficiencies of the small particles (1.0 μm) decreases as surface potentials increase from

0 to 30 mV. For the orthokinetic coagulation study, these results indicate that the collision between the smaller size particles is strongly governed by electrostatic repulsive force due to the surface potential applied to the colliding particle than in the collision between the large particles. However, orthokinetic collision is less dependent on the surface potential than in the case of perikinetic collision. It is evident that flow strain-rates increase the chance of colliding particles overcoming a potential energy barrier and being captured by a datum particle (Elimelch et al. 1995; Squires and Brenner 2000). Thus, it can be expected that particle collision is possible even when electrostatic repulsive force exists due to the surface potential applied to the colliding particle surface. As a result, orthokinetic collision efficiency (α_{sh}) was not a universal constant but rather a function of geometric size and surface potential between colliding particles and the fluid strain-rate applied to the coagulation system.

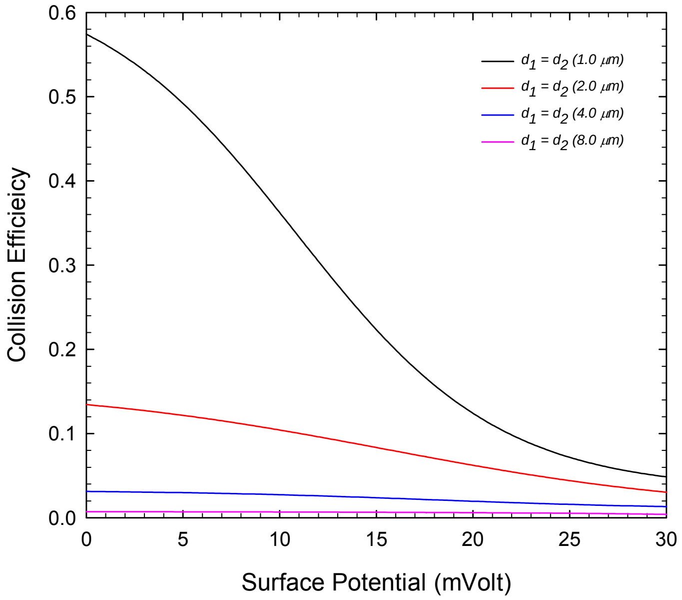

Figure 6.10 Orthokinetic collision efficiency between two equal size colliding particles at a strain-rate of 10 1/s

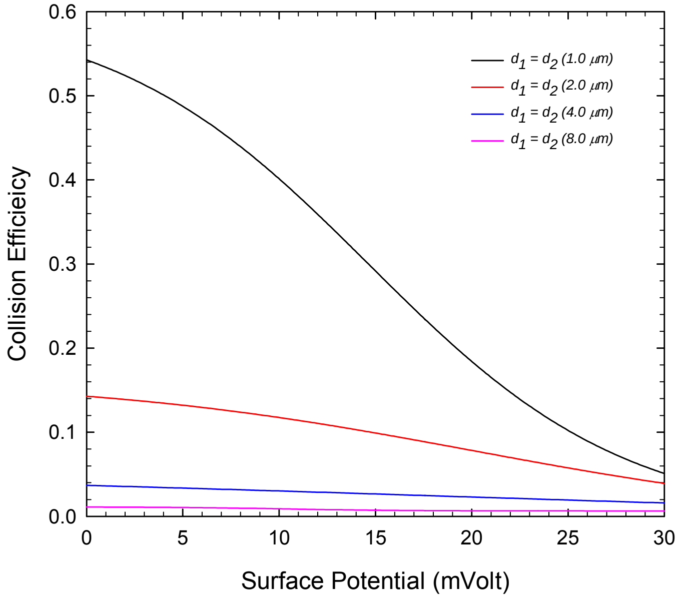

Figure 6.11 Orthokinetic collision efficiency between two equal size colliding particles at a strain-rate of 25 1/s

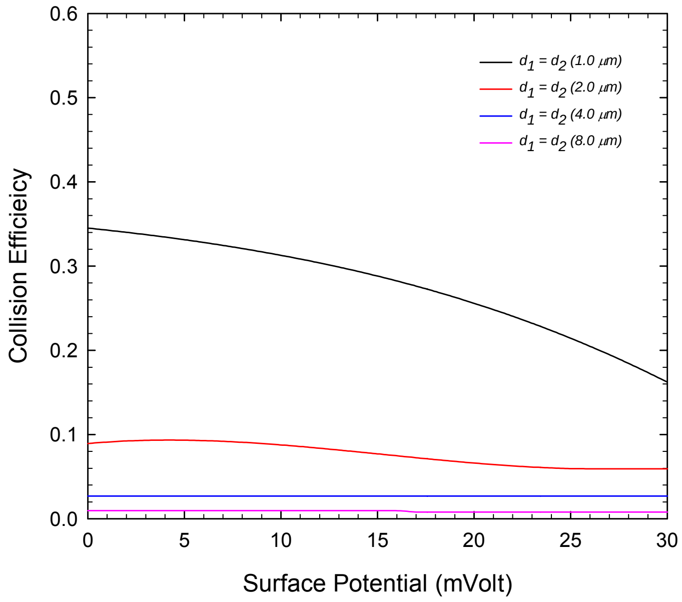

Figure 6.12 Orthokinetic collision efficiency between two equal size colliding particles at a strain-rate of 50 1/s

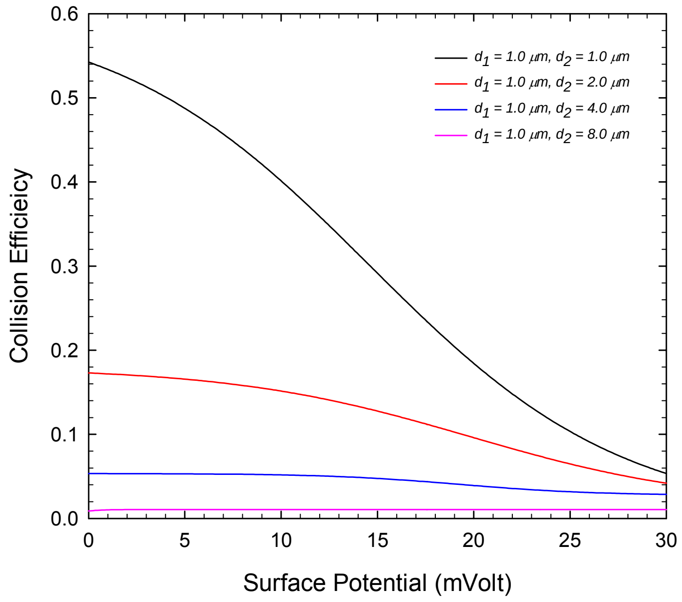

Figure 6.13 Orthokinetic collision efficiency between two unequal size colliding particles at a strain-rate of 10 1/s

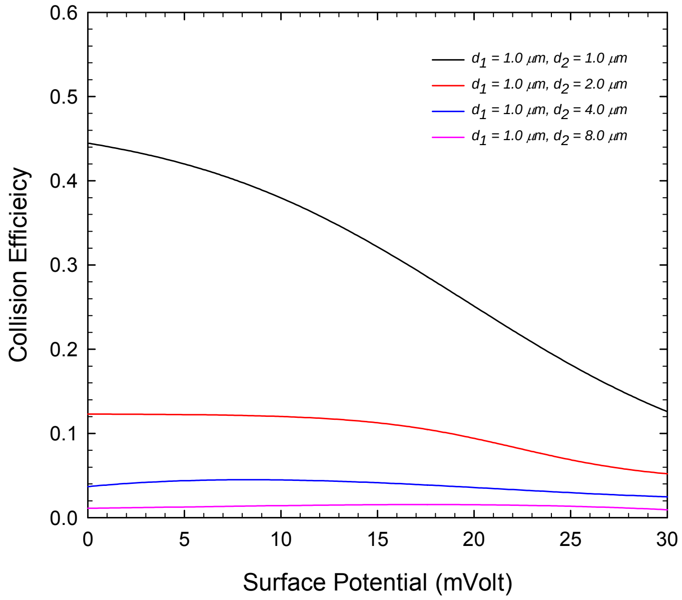

Figure 6.14 Orthokinetic collision efficiency between two unequal size colliding particles at a strain-rate of 25 1/s

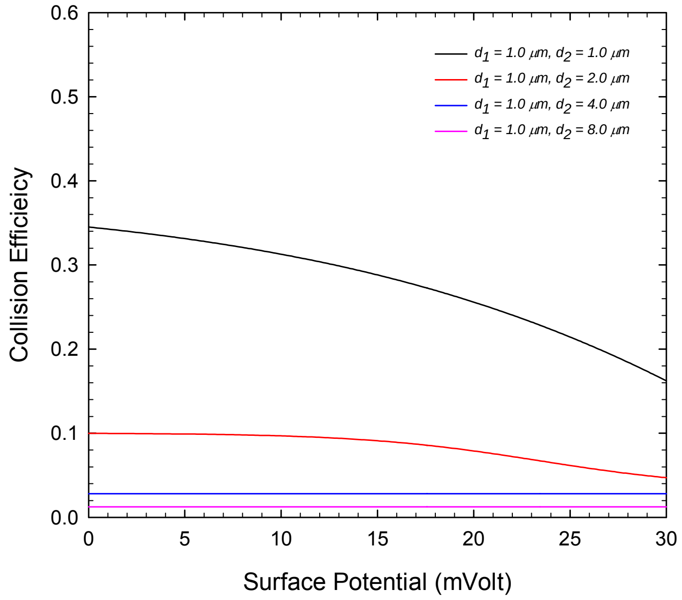

Figure 6.15 Orthokinetic collision efficiency between two unequal size colliding particles at a strain-rate of 50 1/s

6.4 Strain-Rate Calculation

To complete the orthokinetic coagulation model of Eq. (6.9) with the collision efficiency of $\alpha_{\mathrm{sh}}(\mathrm{r}_i, \mathrm{r}_j)$ derived from trajectory analysis in section 6.3 of this chapter and collision frequency $\beta_{\mathrm{sh}}(\mathrm{r}_i, \mathrm{r}_j)$ previously proposed (Kramer and Clark 1997), two hydrodynamic parameters of $\dot{\gamma}$ and $|\dot{\gamma}'_{\max}|$ are required, where $|\dot{\gamma}'_{\max}|$ is the magnitude of the maximum principal component of the local flow strain-rate and $\dot{\gamma}$ is local flow strain-rate. Maximum principle strain-rate ($|\dot{\gamma}'_{\max}|$) is substituted into the collision frequency, $\beta_{\mathrm{sh}}(\mathrm{r}_i, \mathrm{r}_j)$ represented by Eq. (6.6). In addition, this maximum principle strain-rate ($|\dot{\gamma}'_{\max}|$) is introduced into trajectory analysis for orthokinetic collision efficiency of Eqs. (6.28) to (6.30).

$$\frac{\mathrm{dn}_k}{\mathrm{dt}} = \frac{1}{2}\sum_{i+j=k} \alpha\beta(\mathrm{r}_i, \mathrm{r}_j)\mathrm{n}_i \mathrm{n}_j - \mathrm{n}_k \sum_{l=1}^{\max} \alpha\beta(\mathrm{r}_l, \mathrm{r}_k)\mathrm{n}_l \tag{6.9}$$

$$\beta_{\mathrm{sh}}(\mathrm{r}_i, \mathrm{r}_j) = \frac{4\pi}{3}|\dot{\gamma}'_{\max}|(\mathrm{r}_i + \mathrm{r}_j)^3 \tag{6.6}$$

$$\frac{\mathrm{d}l^*}{\mathrm{dt}} = |\dot{\gamma}'_{\max}|\mathrm{r}^*(1-\mathcal{A})\sin^2\theta\sin\phi\cos\phi + \frac{\mathcal{C}}{6\pi\mu\mathrm{r}_1^2}(\mathrm{F}_\mathrm{T}) \tag{6.28}$$

$$\frac{\mathrm{d}\theta}{\mathrm{dt}} = |\dot{\gamma}'_{\max}|(1-\mathcal{B})\sin\theta\cos\theta\sin\phi\cos\phi \tag{6.29}$$

$$\frac{\mathrm{d}\phi}{\mathrm{dt}} = |\dot{\gamma}'_{\max}|\left(\cos^2\phi - \frac{\mathcal{B}}{2}\cos 2\phi\right) \tag{6.30}$$

Substituting $\alpha_{\mathrm{sh}}(\mathrm{r}_i, \mathrm{r}_j)$ and $\beta_{\mathrm{sh}}(\mathrm{r}_i, \mathrm{r}_j)$ into a conventional discretized population balance equations of Eq. (6.9), yields an advanced coagulation model having variable collision efficiency depending on fluid strain-rate, particle size and surface potential, not constant collision efficiency, as

$$\frac{dn_k}{dt} = \frac{1}{2}\sum_{i+j=k} \alpha_{sh}(r_i, r_j)\beta_{sh}(r_i, r_j)n_i n_j - n_k \sum_{l=1}^{max} \alpha_{sh}(r_l, r_k)\beta_{sh}(r_l, r_k)n_l \quad (6.49)$$

As shown in Eq. (6.49), two major parameters of orthokinetic collision efficiency $\alpha_{sh}(r_i, r_j)$ and collision frequency $\beta_{sh}(r_i, r_j)$ are not constant but rather a function of the geometric size between two colliding particles and dependent on flow strain-rate.

In this section, the flow strain-rate will be redefined and these two hydrodynamic parameters in the applied shear flow system will be calculated using a CFD (Computational Fluid Dynamics) technique. Moreover, the calculated hydrodynamic parameter of $|\dot{\gamma}'_{max}|$ will be introduced in the next section of a unified model development with coagulation and sorption.

6.4.1 Strain-Rate and Maximum Principle Strain-Rate

To estimate a local strain-rate ($\dot{\gamma}$), the energy dissipation has been used (Camp and Stein 1943; Clark 1985; Graber 1994; Kramer and Clark 1997; Serra et al. 1997). The classical energy dissipation function can be derived from the First Law of Thermodynamics and the concepts of energy and work as they apply to fluid systems (the detailed derivation can be found in the literature (White 1991; Graber 1994)). The classical differential energy dissipation function at a point for ideal incompressible flow can be written as the summation of normal strain-rate and shear strain-rate,

$$\frac{\Phi}{\mu} = 2\left[\left(\frac{\partial u_x}{\partial x}\right)^2 + \left(\frac{\partial u_y}{\partial y}\right)^2 + \left(\frac{\partial u_z}{\partial z}\right)^2\right] + \left[\left(\frac{\partial u_x}{\partial y} + \frac{\partial u_y}{\partial x}\right)^2 + \left(\frac{\partial u_x}{\partial z} + \frac{\partial u_z}{\partial x}\right)^2 + \left(\frac{\partial u_y}{\partial z} + \frac{\partial u_z}{\partial y}\right)^2\right] \quad (6.50)$$

where Φ represents the dissipation of energy per unit volume brought about by viscous fluid motion. Equation (6.50) is only valid at a point in any incompressible fluid flow, laminar or turbulent. Equation (6.50) can be rewritten as,

$$\begin{array}{ccccc} \dot{\gamma}^2 & = & G'^2 & + & G''^2 \\ \text{Strain Rate} & = & \text{Normal Strain-Rate} & + & \text{Shear Strain-Rate} \end{array} \qquad (6.51)$$

with normal strain-rate (G') resulting from pure normal stress, and

$$G'^2 = 2\left[\left(\frac{\partial u_x}{\partial x}\right)^2 + \left(\frac{\partial u_y}{\partial y}\right)^2 + \left(\frac{\partial u_z}{\partial z}\right)^2\right] \qquad (6.52)$$

shear strain-rate (G'') resulting from pure shear stress

$$G''^2 = \left(\frac{\partial u_x}{\partial y} + \frac{\partial u_y}{\partial x}\right)^2 + \left(\frac{\partial u_x}{\partial z} + \frac{\partial u_z}{\partial x}\right)^2 + \left(\frac{\partial u_y}{\partial z} + \frac{\partial u_z}{\partial y}\right)^2 \qquad (6.53)$$

Substituting the terms of (6.52) and (6.53) into Eq. (6.51), yields overall local strain-rate (or rate of deformation) equations as,

$$\dot{\gamma}^2 = 2\left[\left(\frac{\partial u_x}{\partial x}\right)^2 + \left(\frac{\partial u_y}{\partial y}\right)^2 + \left(\frac{\partial u_z}{\partial z}\right)^2\right] + \left[\left(\frac{\partial u_x}{\partial y} + \frac{\partial u_y}{\partial x}\right)^2 + \left(\frac{\partial u_x}{\partial z} + \frac{\partial u_z}{\partial x}\right)^2 + \left(\frac{\partial u_y}{\partial z} + \frac{\partial u_z}{\partial y}\right)^2\right] \qquad (6.54)$$

The energy dissipation function represents the mechanical work done on an element of fluid by viscous forces (or internal frictions). Camp and Stein (1943) eliminated the normal components of the strain-rate from the Eq. (6.54) by extrapolating a two-dimensional case of fluid flow to a three-dimensional case. Their research implies that the strain-rate tensor can be transformed into a pure off-diagonal form, or

$$\left[\dot{\gamma}_{ij}\right] = \begin{bmatrix} \dot{\gamma}_{11} & \dot{\gamma}_{12} & \dot{\gamma}_{13} \\ \dot{\gamma}_{21} & \dot{\gamma}_{22} & \dot{\gamma}_{23} \\ \dot{\gamma}_{31} & \dot{\gamma}_{32} & \dot{\gamma}_{33} \end{bmatrix} = \begin{bmatrix} 0 & \dot{\gamma}'_{12} & \dot{\gamma}'_{13} \\ \dot{\gamma}'_{21} & 0 & \dot{\gamma}'_{23} \\ \dot{\gamma}'_{31} & \dot{\gamma}'_{32} & 0 \end{bmatrix} \qquad (6.55)$$

The transformation in Eq. (6.55) was used to justify the relationship for the energy dissipation function given in Eq. (6.54). In Eq. (6.54) only the shear components of strain-rate are included in the analyses. While the transformation conducted by Camp and Stein (Camp and Stein 1943) to obtain Eq. (6.55) is valid for a two-dimensional case of fluid flow, which is not possible to obtain the transformation in Eq. (6.55) for a general case of three-dimensional flow. Therefore, Eq. (6.55) is in general incorrect.

It might be supposed that the principal strain-rates could be used instead of the shear strain-rate in Eq. (6.54). However, this is also incorrect. If the local dissipation function is placed in terms of the principal strain-rates the energy dissipation function becomes

$$\Phi_L = 2\mu\left[(\dot{\gamma}'_{11})^2 + (\dot{\gamma}'_{22})^2 + (\dot{\gamma}'_{33})^2\right] \tag{6.56}$$

Then, for the local energy dissipation function Φ_L, Eq. (6.56) implies that a local strain-rate, $\dot{\gamma}_L$, could possibly be expressed as the Euclidean norm, or

$$a_L = \sqrt{(a'_{11})^2 + (a'_{22})^2 + (a'_{33})^2} = \sqrt{\frac{\Phi_L}{2\mu}} \tag{6.57}$$

Equation (6.57) is similar to Camp and Stein's equation, however the error associated with the use of Eq. (6.57) as an estimate for the collision frequency $\beta_{sh}(r_i, r_j)$ of particles must be considered. The Euclidean norm is always greater than the absolute value of any component of the strain-rate tensor and is always positive. This means that if Eq. (6.57) were to be used in place of velocity-gradient $\partial u_X/\partial y$ in the collision frequency function of Eq. (6.3) a collision frequency greater than what the flow would actually generate will result.

To generalize an orthokientic coagulation model, collision frequency $\beta_{\mathrm{sh}}(\mathrm{r}_i, \mathrm{r}_j)$ in Eq. (6.6) is substituted into the coagulation model of Eq. (6.49) and then one can obtain the orthokinetic coagulation model in applied fluid shear, as

$$\frac{\mathrm{dn}_k}{\mathrm{dt}} = \frac{1}{2}\sum_{i+j=k} \alpha_{\mathrm{sh}}(\mathrm{r}_i, \mathrm{r}_j)\frac{4\pi}{3}\dot{\gamma}(\mathrm{r}_i + \mathrm{r}_j)^3 \mathrm{n}_i \mathrm{n}_j - \sum_{l=1}^{\max} \alpha_{\mathrm{sh}}(\mathrm{r}_l, \mathrm{r}_k)\frac{4\pi}{3}\dot{\gamma}(\mathrm{r}_k + \mathrm{r}_l)^3 \mathrm{n}_k \mathrm{n}_l \tag{6.58}$$

A method must be established that properly relates the components of strain-rate without miscounting the number of collisions or collision frequency. If all nine components of the strain-rate tensor were incorporated into Eqs. (6.58) and integrated, the result would incorrectly estimate the total collision rate and yield an inaccurate population size-class balance. In a general case of three-dimensional fluid flow, some strain-rate must be positive valued in order to satisfy continuity. Therefore, only the strain-rates that induce velocity towards the datum sphere must be considered and the strain-rates causing movement away from the sphere must be eliminated from the coagulation collision frequency analysis.

Since the strain-rate tensor is symmetric, the number of equations can be reduced by diagonalizing the strain-rate tensor without a loss of information (Borisenko and Tarapov 1980).

$$\left[\dot{\gamma}_{ij}\right] = \begin{bmatrix} \dot{\gamma}_{11} & \dot{\gamma}_{12} & \dot{\gamma}_{13} \\ \dot{\gamma}_{21} & \dot{\gamma}_{22} & \dot{\gamma}_{23} \\ \dot{\gamma}_{31} & \dot{\gamma}_{32} & \dot{\gamma}_{33} \end{bmatrix} = \begin{bmatrix} \dot{\gamma}'_{11} & 0 & 0 \\ 0 & \dot{\gamma}'_{22} & 0 \\ 0 & 0 & \dot{\gamma}'_{33} \end{bmatrix} \tag{6.59}$$

The primed values of $\dot{\gamma}'_{mm}$ are the principal strain-rates that act in the principal directions. A particular orientation for the axes exist (principal axes) for which shear rates are zero. The step to find the solution for principal values of a symmetric tensor of strain-rate can be formulated as an eigenvalue (eigenvector) problem. When the strain-rate tensor is symmetric, all eigenvalues and associated eigenvectors have real roots. In this eigenvalue calculation, the convention of Eq. (6.60) is applied in all cases, and

$$\dot{\gamma}'_{11} > \dot{\gamma}'_{22} > \dot{\gamma}'_{33} \tag{6.60}$$

The continuity equation for an incompressible fluid requires that

$$\begin{aligned} &\nabla \cdot \boldsymbol{u} = 0 \quad \text{or} \\ &\frac{\partial \mathrm{u_x}}{\partial \mathrm{x}} + \frac{\partial \mathrm{u_y}}{\partial y} + \frac{\partial \mathrm{u_z}}{\partial z} = 0 \quad \text{or} \\ &\dot{\gamma}'_{11} + \dot{\gamma}'_{22} + \dot{\gamma}'_{33} = 0 \end{aligned} \tag{6.61}$$

Therefore, in order to satisfy the convention of Eq. (6.60) and the continuity equation of Eq. (6.61), the scalars of principal strain-rates tensor are required as,

$$\begin{aligned} &\dot{\gamma}'_{11} > 0 \\ &\dot{\gamma}'_{22} > 0 \quad \text{or} \quad \dot{\gamma}'_{22} < 0 \\ &\dot{\gamma}'_{33} < 0 \end{aligned} \tag{6.62}$$

Consequently, two separate cases are possible. In case A, $\dot{\gamma}'_{11} > |\dot{\gamma}'_{33}|$ results in $\dot{\gamma}'_{22} < 0$ and $\dot{\gamma}'_{11} = |\dot{\gamma}'_{22} + \dot{\gamma}'_{33}|$. In case B, $\dot{\gamma}'_{11} < |\dot{\gamma}'_{33}|$ results in $\dot{\gamma}'_{22} > 0$ and $|\dot{\gamma}'_{33}| = \dot{\gamma}'_{11} + \dot{\gamma}'_{22}$. Therefore, the absolute value of the numerically greatest component (either $\dot{\gamma}'_{11}$ or $|\dot{\gamma}'_{33}|$) will allow for the computation of the equivalent value of the mass entering the collision sphere. This quantity is designated the absolute maximum principal strain-rate (Kramer and Clark 1997).

To obtain the principal strain-rate tensor (the eigenvalues of strain-rate tensor) in two-dimensional flow analysis, the strain-rate tensor ($\dot{\boldsymbol{\gamma}}$) can be written as,

$$\dot{\boldsymbol{\gamma}} = [\dot{\gamma}_{ij}] = \begin{bmatrix} \dot{\gamma}_{11} & \dot{\gamma}_{12} \\ \dot{\gamma}_{21} & \dot{\gamma}_{22} \end{bmatrix} = \begin{bmatrix} \dfrac{\partial \mathrm{u_x}}{\partial \mathrm{x}} & \dfrac{1}{2}\left(\dfrac{\partial \mathrm{u_x}}{\partial \mathrm{y}} + \dfrac{\partial \mathrm{u_y}}{\partial \mathrm{x}}\right) \\ \dfrac{1}{2}\left(\dfrac{\partial \mathrm{u_y}}{\partial \mathrm{x}} + \dfrac{\partial \mathrm{u_x}}{\partial \mathrm{y}}\right) & \dfrac{\partial \mathrm{u_y}}{\partial \mathrm{y}} \end{bmatrix} \tag{6.63}$$

Letting the vector **B** lie along a principal axis of the tensor $\dot{\boldsymbol{\gamma}}$, with eigenvalue λ and its corresponding eigenvectors satisfy the linear algebra equation as,

$$\begin{bmatrix} \dot{\gamma}_{11} & \dot{\gamma}_{12} \\ \dot{\gamma}_{21} & \dot{\gamma}_{22} \end{bmatrix} \begin{bmatrix} \mathrm{b}_1 \\ \mathrm{b}_2 \end{bmatrix} = \lambda \begin{bmatrix} \mathrm{b}_1 \\ \mathrm{b}_2 \end{bmatrix} \tag{6.64}$$

then, its components must satisfy the homogeneous system, which is equivalent to

$$\begin{bmatrix} \dot{\gamma}_{11} - \lambda & \dot{\gamma}_{12} \\ \dot{\gamma}_{21} & \dot{\gamma}_{22} - \lambda \end{bmatrix} \begin{bmatrix} \mathrm{b}_1 \\ \mathrm{b}_2 \end{bmatrix} = \begin{bmatrix} 0 \\ 0 \end{bmatrix} \tag{6.65}$$

Equation (6.65) can be rewritten compactly as,

$$(\dot{\boldsymbol{\gamma}} - \lambda \mathbf{I})\mathbf{B} = 0 \tag{6.66}$$

where **I** is the unit tensor. Equation (6.66) has nontrivial (i.e., nonzero) solutions if the determinant vanishes and thus it can be rewritten as,

$$\det(\mathbf{A} - \lambda \mathbf{I}) = 0 \tag{6.67}$$

or

$$\begin{bmatrix} \dot{\gamma}_{11} - \lambda & \dot{\gamma}_{12} \\ \dot{\gamma}_{21} & \dot{\gamma}_{22} - \lambda \end{bmatrix} = \begin{bmatrix} 0 \\ 0 \end{bmatrix} \tag{6.68}$$

or

$$\lambda^2 - \lambda(\dot{\gamma}_{11} + \dot{\gamma}_{22}) + (\dot{\gamma}_{11}\dot{\gamma}_{22} - \dot{\gamma}_{12}\dot{\gamma}_{21}) = 0 \tag{6.69}$$

Equation (6.69) is well known as the characteristic equation of tensor $\dot{\boldsymbol{\gamma}}$ (i.e., strain-rate tensor). Therefore Eq. (6.65) has its nontrivial solutions (or eigenvalues) if and only if $\lambda = \lambda_1 = \dot{\gamma}'_1$ or $\lambda = \lambda_2 = \dot{\gamma}'_2$, where

$$\lambda_1 = \dot{\gamma}'_1 = \frac{1}{2}\left\{(\dot{\gamma}_{11} + \dot{\gamma}_{22}) + \sqrt{(\dot{\gamma}_{11} - \dot{\gamma}_{22})^2 + 4\dot{\gamma}_{12}\dot{\gamma}_{21}}\right\} \tag{6.70}$$

$$\lambda_2 = \dot{\gamma}'_2 = \frac{1}{2}\left\{(\dot{\gamma}_{11} + \dot{\gamma}_{22}) - \sqrt{(\dot{\gamma}_{11} - \dot{\gamma}_{22})^2 + 4\dot{\gamma}_{12}\dot{\gamma}_{21}}\right\} \tag{6.71}$$

Thus, general strain-rate tensor can be replaced by principal strain-rate tensor using eigenvalues of λ_1 and λ_2 and represented as,

$$\dot{\boldsymbol{\gamma}} = [\dot{\gamma}_{ij}] = \begin{bmatrix} \dot{\gamma}_{11} & \dot{\gamma}_{12} \\ \dot{\gamma}_{21} & \dot{\gamma}_{22} \end{bmatrix} = \begin{bmatrix} \lambda_1 & 0 \\ 0 & \lambda_2 \end{bmatrix} = \begin{bmatrix} \dot{\gamma}'_{11} & 0 \\ 0 & \dot{\gamma}'_{22} \end{bmatrix} \tag{6.72}$$

where eigenvalues can be rewritten using velocity-gradient of each components as,

$$\lambda_1 = \dot{\gamma}'_{11} = \frac{1}{2}\left\{\left(\frac{\partial u_x}{\partial x} + \frac{\partial u_y}{\partial y}\right) + \sqrt{2\left(\frac{\partial u_x}{\partial x} - \frac{\partial u_y}{\partial y}\right)^2 + \left(\frac{\partial u_x}{\partial y} + \frac{\partial u_y}{\partial x}\right)^2}\right\} \tag{6.73}$$

$$\lambda_2 = \dot{\gamma}'_{22} = \frac{1}{2}\left\{\left(\frac{\partial u_x}{\partial x} + \frac{\partial u_y}{\partial y}\right) - \sqrt{2\left(\frac{\partial u_x}{\partial x} - \frac{\partial u_y}{\partial y}\right)^2 + \left(\frac{\partial u_x}{\partial y} + \frac{\partial u_y}{\partial x}\right)^2}\right\} \tag{6.74}$$

Now, the convention of Eq. (6.75) is applied in all two-dimensional flow cases, and

$$\dot{\gamma}'_{11} > \dot{\gamma}'_{22} \tag{6.75}$$

The continuity equation for an incompressible fluid requires that

$$\dot{\gamma}'_{11} + \dot{\gamma}'_{22} = 0 \tag{6.76}$$

In order to satisfy the two limitations, principal strain-rates tensor are required as,

$$\dot{\gamma}'_{11} > 0, \quad \dot{\gamma}'_{22} < 0, \quad \text{and} \quad \dot{\gamma}'_{11} = -(\dot{\gamma}'_{22}) \tag{6.77}$$

Therefore, the absolute value of the numerically greater component ($\dot{\gamma}'_{11}$) will allow for the computation of the equivalent value of the mass entering the collision sphere. This quantity is designated the absolute maximum principal strain-rate $|\dot{\gamma}'_{\max}|$ in a two-dimensional case.

The values of $|\dot{\gamma}'_{\max}|$ and $\alpha_{\mathrm{sh}}(\mathrm{r}_i, \mathrm{r}_j)$ can then be incorporated into the collision frequency function for the normal strain-rate case to yield the total collision frequency for the discrete fluid element.

$$\frac{\mathrm{dn}_k}{\mathrm{dt}} = \frac{1}{2}\sum_{i+j=k} \alpha_{\mathrm{sh}}(\mathrm{r}_i, \mathrm{r}_j)\frac{4\pi}{3}|\dot{\gamma}'_{\max}|(\mathrm{r}_i + \mathrm{r}_j)^3 \mathrm{n}_i \mathrm{n}_j - \sum_{l=1}^{\max} \alpha_{\mathrm{sh}}(\mathrm{r}_l, \mathrm{r}_k)\frac{4\pi}{3}|\dot{\gamma}'_{\max}|(\mathrm{r}_k + \mathrm{r}_l)^3 \mathrm{n}_k \mathrm{n}_l \quad (6.78)$$

A rate equation for the time-dependent population of particles of size class *k* has thus been obtained. Equation (6.78) is valid for any fluid element that is under the influence of continuous velocity-gradient that result in uniform strain-rates within a fluid element. The use of the absolute maximum principal strain-rate accounts for the directional nature of the collision phenomenon and accurately estimates the collision frequency for the modeling assumption for this section.

6.4.2 Computational Fluid Dynamics in Couette Device

A conventional Couette device with concentric rotating inner or outer cylinders have been frequently used in studying mixing, coagulation, and floc break-up in two-dimensional uniform laminar flow (Trevelyan and Mason 1951; Swift and Friedlander 1964; Ives and Dibouni 1979; Zollars and Ali 1986; Torres et al. 1991; Oles 1992; Serra et al. 1997; Mishra et al. 1998; Serra and Casamitjana 1998; Selomulya et al. 2002; Rahmani et al. 2003; Sato et al. 2004). Under the two-dimensional uniform laminar flow conditions generated from Couette device particles in the suspension can undergo pure orthokinetic coagulation through different flow strain-rate which is one of the mass (particle) transport mechanisms.

Although the conventional concentric Couette device having rotating cylinders generates a uniform state of shear flow, this uniform flow is somewhat different than typical mixing flow having spatial variation. To adequately examine the effect of increased strain-rate variance (spatial distribution) within the fluid domain on orthokinetic coagulation, a system with a high strain-rate variance is required.

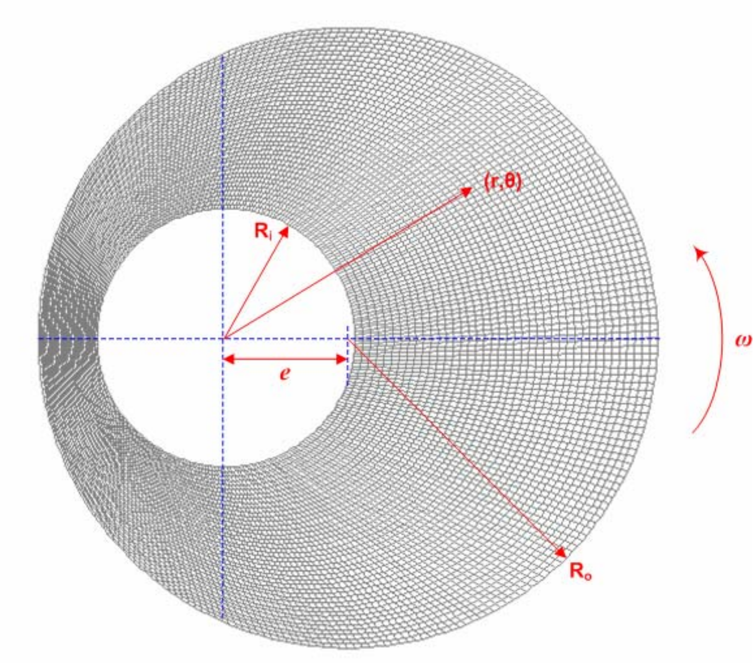

Figure 6.16 Geometry of eccentric Couette apparatus

The conventional concentric Couette apparatus does not generate a high strain-rate variance at a constant angular velocity. An improved system is to reconfigure the

Couette device so that rotational axes of the cylinders are eccentrically located. The geometry of the eccentric Couette device appears in Fig. 6.16.

Fluid flow is induced by the rotation of inner and/or outer cylinder. The fluid dynamic parameters were obtained using FLUENT, a commercial CFD (Computational Fluid Dynamics) code, for the eccentric Couette device with a rotating outer cylinder (see Fig. 6.16). Before the CFD analysis, a grid (mesh) was generated using a commercial code of GAMBIT resulting in 256×40 cells, a total cell number of 10240, a minimum cell area of 2.845×10^{-5} cm^2, and a maximum cell area of 3.465×10^{-5} cm^2. The conditions used for computational fluid dynamic analysis are displayed in Table 6.2.

Table 6.2 CFD Analysis Conditions Using FLUENT

Conditions	Values
Computational grid	Quadratic 40×256 cells
Outer cylinder radius (R_o)	7.620 cm
Inner cylinder radius (R_i)	3.175 cm
Eccentricity (e)*	3.000 cm
Mean Clearance (c)**	4.445 cm
Rotation velocity (ω)	30 rpm (3.14 rad/sec)
Kinematic viscosity (v)	Liquid A = 0.6689 cm^2/sec Liquid B = 0.0100 cm^2/sec

* e = center to center distance between outer and inner cylinders

** $c = R_o - R_i$

The CFD code for the eccentric Couette device with a rotating outer cylinder was verified with two streamlines; generated using GAMBIT and FLUENT CFD code and obtained by experimental data (see the Fig. 6.17). The streamline experiment was conducted under the conditions of; outer cylinder radius (R_o) of 7.62 cm, inner cylinder radius (R_i) of 3.175 cm, eccentricity (e) of 3.00 cm, cylinder depth of 20.32 cm, rotation velocity (ω) of 30 rpm in the counterclockwise direction, and kinematic viscosity (v) of 0.6689 cm^2/sec (Thomas 1999). The smallest width of the gap between cylinders was 1.445 cm and the ratio of depth to gap was about 14. It is reported that in this device geometry, the effect of the bottom of the cylinder on the flow is limited to the range from the bottom to nearly the same height as the gap (Sato et al. 2004). Thomas (1999) obtained flow visualization results through the use of a green dye and aluminum powder as the solid particles. Kinematic viscosity of fluid was controlled using a glycerin and water mixture (see the Fig. 6.17(b)). As shown in Fig. 6.17, the CFD code generated streamlines were in good agreement with the experimental streamlines in Thomas (1999). It is remarkable that the CFD code could achieve and accurately predict the proper development of the streamlines even with an increase in mean clearance (*c*) due to the use of smaller inner cylinder. It was reported that the increased mean clearance caused the analytical solution for the Couette device (Ballal and Rivlin 1976) fail to predict the streamlines accurately even at a small eccentricity ratio. Thus, the CFD code for eccentric rotating cylinder apparatus as a model flocculator was found to be accurate and applicable for the study of particle coagulation. The CFD code applied to this study can determine the flow strain-rate that induces particle collisions through the orthokinetic coagulation mechanism.

The fluid flow properties of laminar shear flow resulting from CFD analysis using a commercial code of GAMBIT and FLUENT were displayed in Figs. 6.18 to 6.20 and summarized in Tables 6.3 to 6.4.

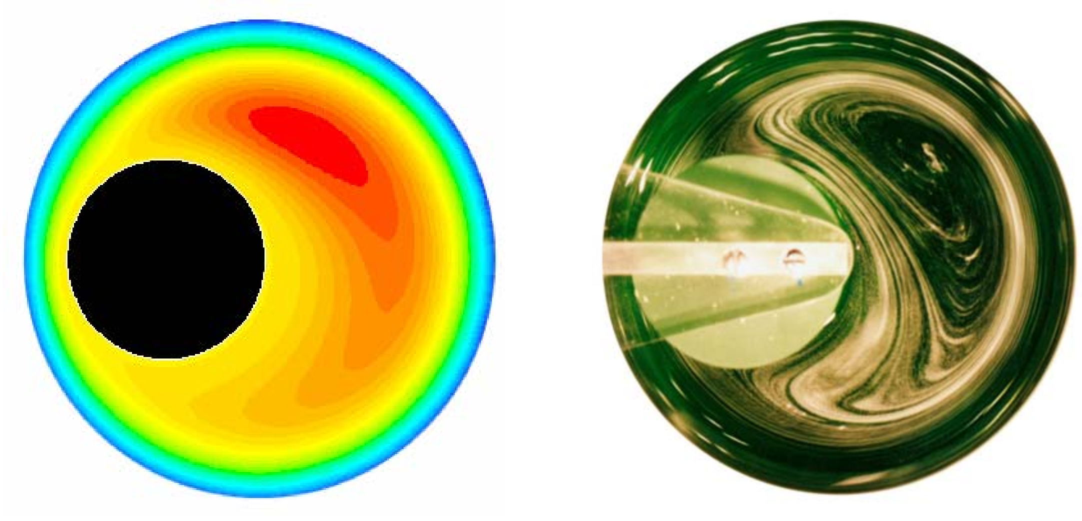

(a) (b)

Figure 6.17 CFD code verification with streamlines generated using counterclockwise rotating outer cylinder with kinematic viscosity (ν) of 0.6689 cm^2/sec and 30 rpm. (a) CFD code and (b) experimental data (Thomas 1999)

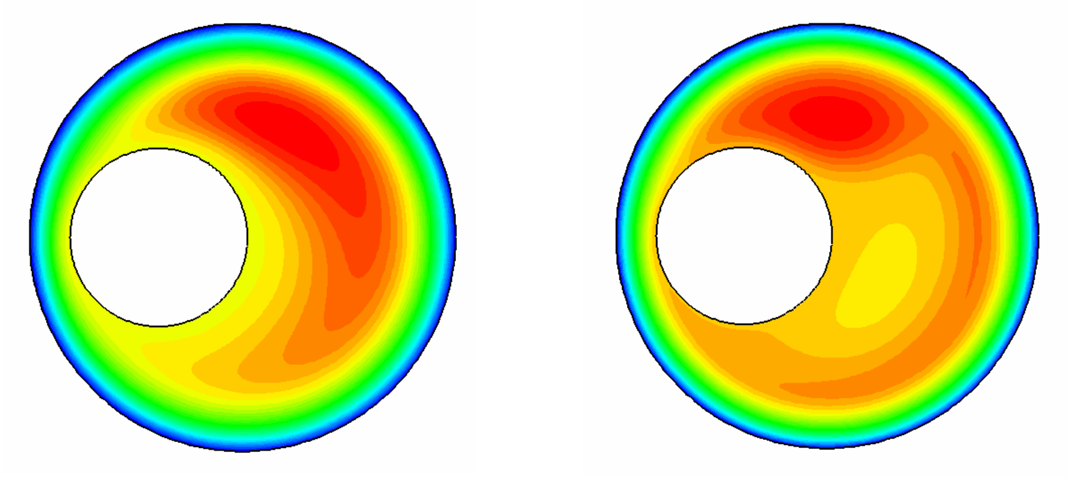

(a) (b)

Figure. 6.18 Streamlines for different fluid viscosity. (a) high viscosity of 0.6689 cm^2/sec and (b) low viscosity of 0.01 cm^2/sec

Two flows having different viscosities of 0.6689 and 0.01 cm^2/sec were used for these CFD analyses. All CFD simulations were conducted under the conditions mentioned in Table 6.2. The results were visualized in terms of streamlines, strain-rates ($\dot{\gamma}$), and maximum principal strain rate ($|\dot{\gamma}'_{max}|$). Furthermore, the variance in flow properties (i.e., strain-rate ($\dot{\gamma}$)) was computed as,

$$\text{Variance} = \frac{1}{\text{Total Cell Area}}\left\{\sum_k \left[(\dot{\gamma})_k - (\dot{\gamma})_{mean}\right]^2 \times (\text{Cell Area})_k\right\} \tag{6.79}$$

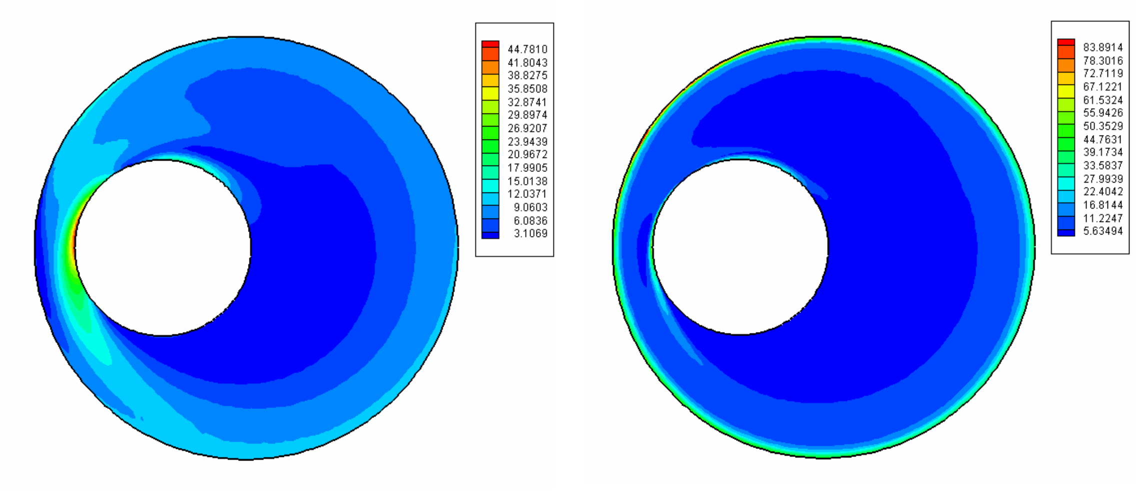

(a) (b)

Figure. 6.19 Flow strain-rate ($\dot{\gamma}$) for different fluid viscosity. (a) high viscosity of 0.6689 cm^2/sec and (b) low viscosity of 0.01 cm^2/sec (unit = 1/s)

Table 6.3 Spatially Varying Flow Strain-Rate ($\dot{\gamma}$)

	Liquid A (High viscosity)	Liquid B (Low viscosity)
Maximum	47.758 (1/s)	89.481 (1/s)
Minimum	0.130 (1/s)	0.045 (1/s)
Average*	6.036 (1/s)	7.666 (1/s)
Variance	16.919 ($1/s^2$)	115.849 ($1/s^2$)

* This average means area weighted value.

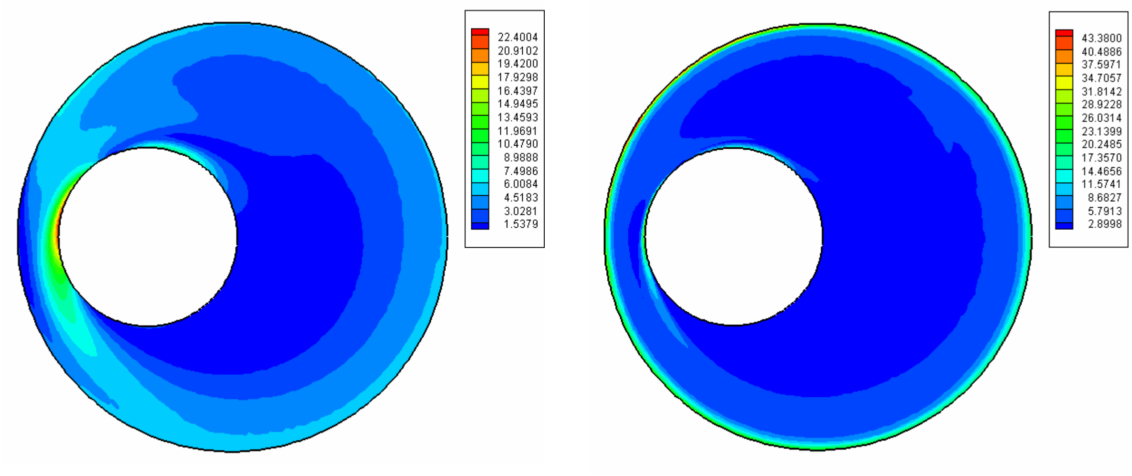

(a)

(b)

Figure. 6.20 Maximum principal strain rate ($|\dot{\gamma}_{max}|$) for different fluid viscosity. (a) high viscosity of 0.6689 cm^2/sec and (b) low viscosity of 0.01 cm^2/sec

Table 6.4 Spatially Varying Maximum Principal Strain-Rate ($|\dot{\gamma}_{max}|$)

	Liquid A (High viscosity)	Liquid B (Low viscosity)
Maximum	23.891 (1/s)	46.271 (1/s)
Minimum	0.048 (1/s)	0.008 (1/s)
Average*	3.046 (1/s)	3.868 (1/s)
Variance	4.319 ($1/s^2$)	31.577 ($1/s^2$)

* This average means area weighted value.

From the results, it was found that fluid viscosity can alter not only stream lines, but also strain-rates. Furthermore, there is a large difference in the strain-rate variance between the two computations. Thus, in the modeling of orthokinetic coagulation, a more complicated approach is required to accurately predict orthokinetic coagulation in complex flows, especially with spatial varying flow having large variance, which is characteristic of most coagulation systems. The summary of energy dissipation rates in incompressible Newtonian fluid was listed on Tables 6.5 to 6.7 and Figures 6.21 to 6.23.

Table 6.5 Shear Flow Comparison with Maximum Value (unit = 1/sec)

	Liquid A (High viscosity)	Liquid B (Low viscosity)
Strain-rate ($\dot{\gamma}$)	47.758	89.481
Maximum principal strain-rate ($\lvert\dot{\gamma}'_{max}\rvert$)	23.891	46.271

Table 6.6 Shear Flow Comparison with Area Weighted Average (unit = 1/sec)

	Liquid A (High viscosity)	Liquid B (Low viscosity)
Strain-rate ($\dot{\gamma}$)	6.034	7.666
Maximum principal strain-rate ($\lvert\dot{\gamma}'_{max}\rvert$)	3.046	3.868

Table 6.7 Shear Flow Comparison with Local Variance (unit = $1/sec^2$)

	Liquid A (High viscosity)	Liquid B (Low viscosity)
Strain-rate ($\dot{\gamma}$)	16.919	115.849
Maximum principal strain-rate ($\lvert\dot{\gamma}'_{max}\rvert$)	4.319	31.577

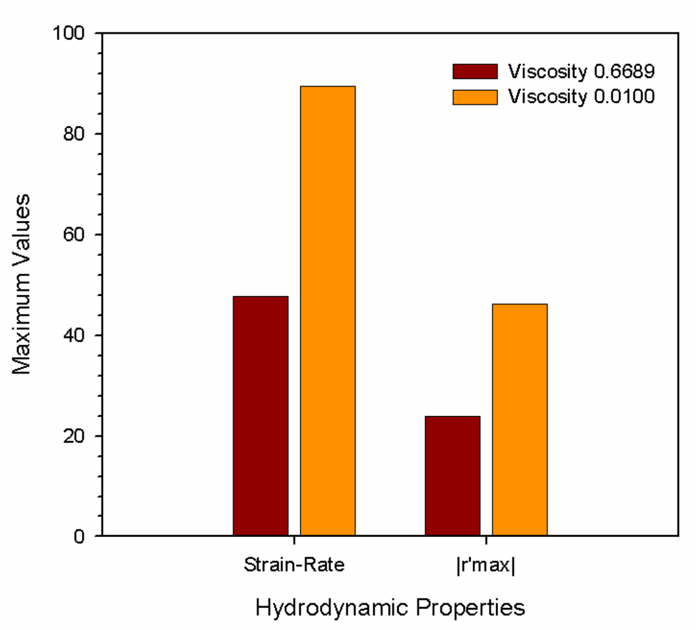

Figure 6.21 The comparison of energy dissipation rates with maximum value

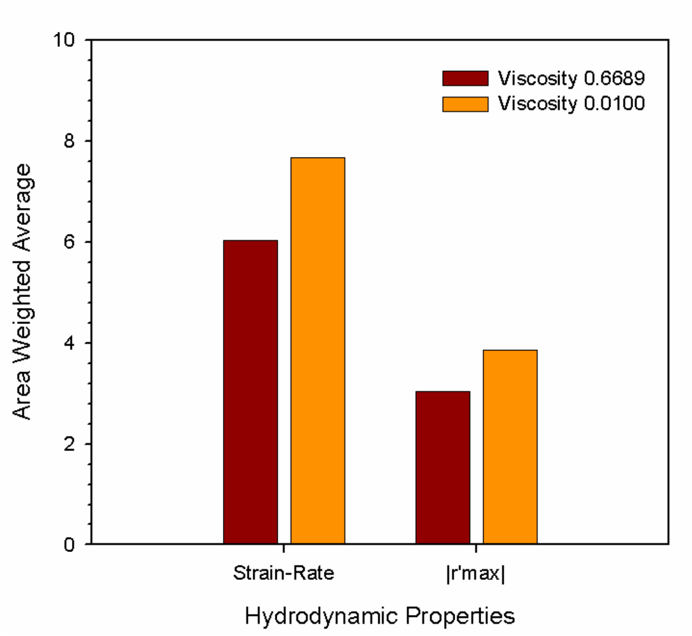

Figure 6.22 The comparison of energy dissipation rates with area weighted average

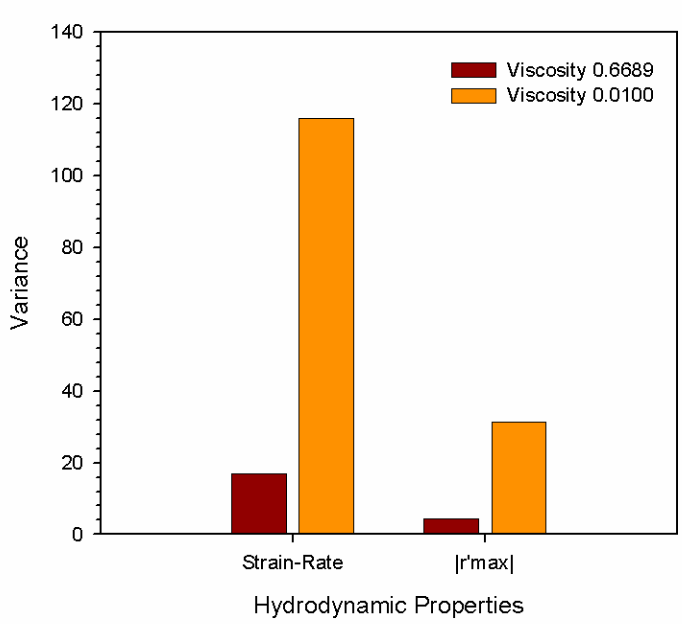

Figure 6.23 The comparison of energy dissipation rates with local variance

In addition, the maximum principal strain-rate concept might be extended from laminar to homogeneous isotropic turbulent flow. The variance of the fluctuating component (velocity fluctuation) of the flow strain-rate can be equated to the fluctuating energy dissipation (*ε*) (Taylor 1935) by

$$\left\{\frac{\partial \overline{\tilde{u}_1}}{\partial x_2}\right\}^2 = \frac{2\varepsilon}{15\mu} \qquad (6.80)$$

The exact value of energy dissipated into the flow system (*ε*) is not easy to determine. Furthermore, the velocity fluctuation *u'* in turbulent flow is difficult to determine. The velocity flocculation can be expressed with specified energy spectrum using random Fourier modes for an isotropic, Gaussian, and pseudo-turbulence flow (Mei and Hu 1999), as

$$\left(\frac{\partial \tilde{\mathrm{u}}_i}{\partial \mathrm{x}_i}\right)_t = \mathrm{u}_i(\boldsymbol{x},t) = \sum_{m=1}^{N_k}\left[A_i^{(m)}\sin(\boldsymbol{k}^{(m)}\cdot\boldsymbol{x}+\omega^{(m)}t)+B_i^{(m)}\cos(\boldsymbol{k}^{(m)}\cdot\boldsymbol{x}+\omega^{(m)}t)\right] \quad (6.81)$$

where, i = 1, 2, and 3 for three-dimension turbulent flow, N_k is the number of the random Fourier modes in one flow realization, $A_i^{(m)}$ and $B_i^{(m)}$ are random coefficient, and $\boldsymbol{k}^{(m)}$ and $\omega^{(m)}$ are the wavenumber and frequency of the m$^{\mathrm{th}}$ model, respectively. Thus, strain-rate for homogeneous isotropic turbulent flow can be calculated as,

$$\left[\dot{\gamma}_{ij}\right]_{Turb} = \sqrt{\frac{2\varepsilon}{15\mu}}\begin{bmatrix}\mathrm{u}_1(x,t) & 0 & 0\\ 0 & \mathrm{u}_2(x,t) & 0\\ 0 & 0 & \mathrm{u}_3(x,t)\end{bmatrix}|\dot{\gamma}'_{\max}| \quad (6.82)$$

6.5 A Unified Coagulation Model with Arsenic Sorption

This chapter provides modeling capability for the complex arsenic removal mechanisms throughout the arsenic sorption and coagulation processes. To develop the unified sorption model, several unit models (kinetic and equilibrium) were derived and described in previous chapters of this study (i.e., the improved coagulation model, arsenic sorption kinetic model, arsenic surface complexation model, and collision efficiency model) and are coupled with each other for each time step. The computational algorithm for the unified kinetic model adopted in this study is represented by the flow chart shown in Fig. 6.24.

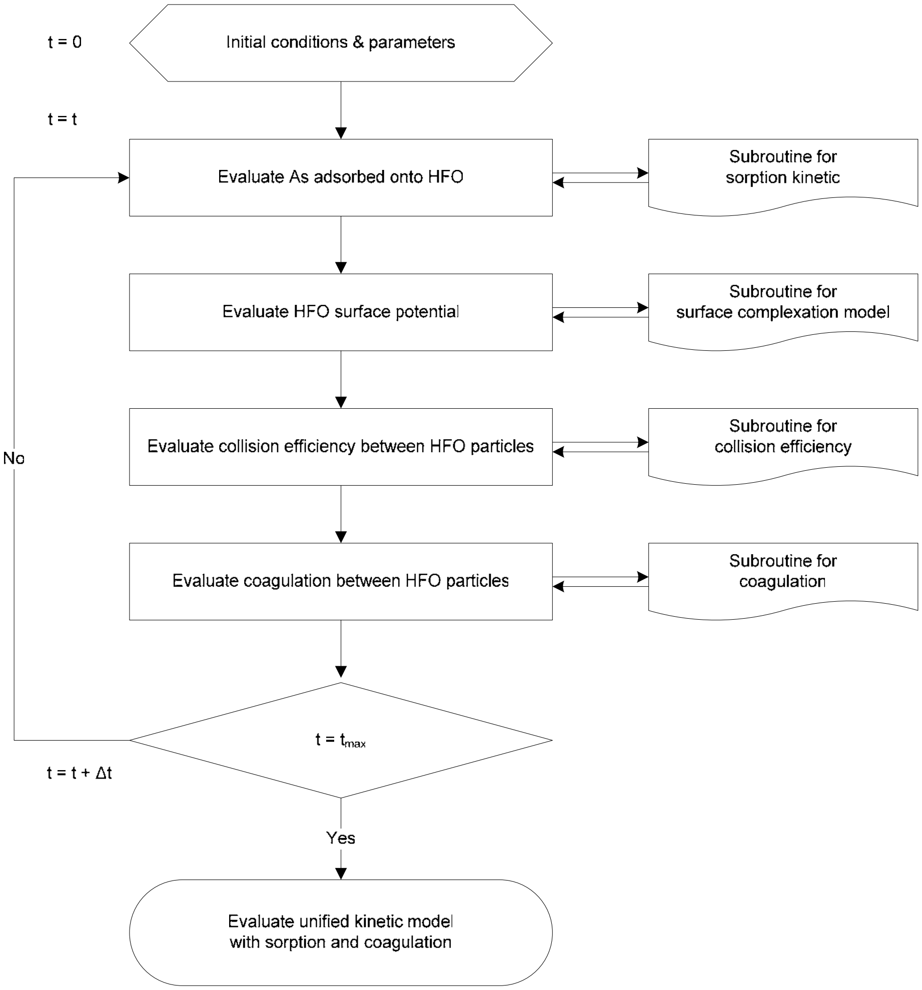

Figure 6.24 The computational algorithm for the unified kinetic model with sorption and coagulation

As shown in Fig. 6.24, model coupling is achieved by combining the sorption model with the improved coagulation model. Using the local equilibrium assumption, arsenic kinetics and equilibrium (surface complexation) are incorporated at each reaction time step. Throughout the arsenic sorption kinetics and equilibrium models extensively discussed in previous chapters, the surface charges/potentials of the HFO particles used for arsenic adsorbent at each time step are calculated. Further, the collision efficiency between colliding HFO particles is calculated by aid of the surface charges/potentials from the HFO particles. Thus, the collision efficiency (α) plays a key role in coupling the sorption model with the improved coagulation model.

6.5.1 A Coupled Perikinetic Coagulation Model with Arsenic Sorption

As shown in Fig. 6.24, a perikinetic coagulation model with arsenic sorption kinetics and equilibrium onto hydrous ferric oxide (HFO) was coupled using the computational algorithm for the unified kinetic model. The detailed coupling procedure was represented as follow steps consisting of Eqs. (6.83) to (6.100). All model equations used for each step were developed or introduced at previous chapters.

Step 1) Diffusion transport (mass transport) arsenic sorption kinetic modeling.

$$\varepsilon_p \frac{\partial[\mathrm{As}]_{\mathrm{Liquid}}}{\partial \mathrm{t}} + \rho_p \frac{\partial[\mathrm{As}]_{\mathrm{Solid}}}{\partial \mathrm{t}} = \frac{1}{\mathrm{r}_p^2}\frac{\partial}{\partial \mathrm{r}_p}\left(D_p \mathrm{r}_p^2 \frac{\partial[\mathrm{As}]_{\mathrm{Liquid}}}{\partial \mathrm{r}_p} \right) \tag{6.83}$$

Step 2) Surface complexation modeling using the sorption local equilibrium assumption.

Acid-Base Reactions

$$HAsO_4^{-2} \Leftrightarrow AsO4^{-3} + H^+ \tag{6.84}$$

$$H_2AsO_4^{-} \Leftrightarrow AsO_4^{-3} + 2H^+ \tag{6.85}$$

$$H_3AsO_4 \Leftrightarrow AsO_4^{-3} + 3H^+ \tag{6.86}$$

Surface protonation constant

$$\equiv XOH + H^+ \Leftrightarrow \equiv XOH_2^+ \tag{6.87}$$

$$\equiv XOH \Leftrightarrow \equiv XO^- + H^+ \tag{6.88}$$

Monodentate As(V) sorption

$$\equiv XOH + AsO_4^{-3} + 3H^+ \Leftrightarrow \equiv XH_2AsO_4 + H_2O \tag{6.89}$$

$$\equiv XOH + AsO_4^{-3} + 2H^+ \Leftrightarrow \equiv XHAsO_4^{-} + H_2O \tag{6.90}$$

$$\equiv XOH + AsO_4^{-3} + H^+ \Leftrightarrow \equiv XAsO_4^{-2} + H_2O \tag{6.91}$$

$$\equiv XOH + AsO_4^{-3} \Leftrightarrow \equiv XAsO_4^{-3} \tag{6.92}$$

Step 3) HFO surface charge evolution modeling.

$$\sigma = \frac{F}{2a}\left\{[\equiv \mathrm{XO^-}]+[\equiv \mathrm{XOH_2^+}]+[\equiv \mathrm{XAsO_4^{-3}}]+[\equiv \mathrm{XAsO_4^{-2}}]+[\equiv \mathrm{XHAsO_3^-}]\right\} \tag{6.93}$$

Step 4) Collision efficiency calculation.

$$\mathrm{V_A} = -\frac{\mathrm{A}\lambda}{3(1+\lambda)^2}\frac{1}{(\mathrm{S}-2)}\left(\frac{2.45}{5p_0}-\frac{2.17}{15p_0^2}+\frac{0.59}{35p_0^3}\right) \qquad p_0 \geq 1.0 \tag{6.94}$$

$$\mathrm{V_A} = -\frac{\mathrm{A}\lambda}{3(1+\lambda)^2}\frac{1}{(\mathrm{S}-2)}\left(\frac{1}{1+1.7692p_0}\right) \qquad p_0 < 1.0 \tag{6.95}$$

$$\mathrm{V_R} = \frac{\varepsilon_r\lambda[\max(\mathrm{r}_i,\mathrm{r}_j)]}{1+\lambda}\psi_{\mathrm{s}}^2 \ln\left\{1+\exp\left[-\kappa\left(\frac{2l}{\mathrm{r}_i+\mathrm{r}_j}-2\right)\right]\right\} \tag{6.96}$$

$$\mathrm{V_T} = \mathrm{V_R} + \mathrm{V_A} \tag{6.97}$$

$$\alpha_{\mathrm{Br}}(\mathrm{r}_i,\mathrm{r}_j) = 2\int_2^{\infty}\left(\frac{1}{G(\mathrm{S},\lambda)}\right)\frac{\exp\left(\mathrm{V_T}/\mathrm{k_B T}\right)}{\mathrm{S}^2}\mathrm{dS} \tag{6.98}$$

Step 5) Unified coagulation modeling.

$$\alpha_{\mathrm{Br}}(\mathrm{r}_i,\mathrm{r}_j) = 2\int_2^{\infty}\left(\frac{1}{G(\mathrm{S},\lambda)}\right)\frac{\exp\left(\mathrm{V_T}/\mathrm{k_B T}\right)}{\mathrm{S}^2}\mathrm{dS} \tag{6.98}$$

$$\beta_{\mathrm{Br}}(\mathrm{r}_i,\mathrm{r}_j) = \frac{2\mathrm{k_B T}}{3\mu}\left(\frac{1}{\mathrm{r}_i}+\frac{1}{\mathrm{r}_j}\right)(\mathrm{r}_i+\mathrm{r}_j) \tag{6.99}$$

$$\frac{\mathrm{dn}_k}{\mathrm{dt}} = \frac{1}{2}\sum_{i+j=k}\alpha_{\mathrm{Br}}(\mathrm{r}_i,\mathrm{r}_j)\beta_{\mathrm{Br}}(\mathrm{r}_i,\mathrm{r}_j)\mathrm{n}_i\mathrm{n}_j - \mathrm{n}_k\sum_{l=1}^{\infty}\alpha_{\mathrm{Br}}(\mathrm{r}_l,\mathrm{r}_k)\beta_{\mathrm{Br}}(\mathrm{r}_l,\mathrm{r}_k)\mathrm{n}_l \tag{6.100}$$

As shown in Eqs. (6.83) to (6.100) of model coupling procedure, perikinetic coagulation model coupling was achieved by combining the arsenic sorption kinetic and equilibrium model with the improved coagulation model that was developed and addressed in previous chapter. First, using the local equilibrium assumption, arsenic sorption kinetics and equilibrium (surface complexation) were incorporated at each reaction time step. Second, the surface charge(potential) of the HFO particles evolution at each time step was simultaneously calculated. Third, the collision efficiency between colliding HFO particles was calculated by aid of the surface charge (potential) from the HFO particles. Finally, introducing the collision efficiency (α) into the improved coagulation model yielded a coupled coagulation model with arsenic sorption kinetics and equilibrium.

The coupled perikinetic coagulation model equations were computed over time using the initial conditions presented in Table 6.8. As shown in Table 6.8, polydisperse initial population was used where each size class has different particle concentrations. The polydisperse initial population is more realistic when applied to an engineered or experimental system than a monodisperse initial population where all of the initial particles have the same particle size. The polydisperse initial population had a particle size distribution similar to a normal distribution. The polydisperse initial population in Table 6.9 corresponds to the experimental study of amorphous iron oxide size distribution of Lo and Waite (2000).

The primary and maximum particle sizes used for the perikientic coagulation were 30 nm and 960 nm in diameter, respectively. In this particle size range, it has been reported that perikinetic coagulation resulting from mass transport due to Brownian random motion is the main particle collision mechanism. Furthermore, most particle aggregates are found to be fractal and not spherical shaped. As shown in previous chapters related to coagulation model development, the improved model proposed in this study was shown to be capable for application in fractal colloidal coagulation simulation. Thus, a fractal geometric dimension value (D_f) of 2.0 was introduced into the unified perikinetic coagulation model and coupled with the arsenic kinetic and equilibrium models. The results from the coupled perikinetic coagulation model are displayed in Figs. 6.25 to 6.45 for various arsenic loading ratios (As/Fe = 0.25 ~ 1.0).

Table 6.8 Parameters for Coupled Perikinetic Coagulation with Arsenic Sorption

Physical Properties	Values
Arsenic concentration (M)	$2.5 \times 10^{-5} \sim 1.0 \times 10^{-4}$
HFO concentration (M)	1.0×10^{-4}
Volume (L)	1.0
Two film mass transfer coefficient (m/sec)	1.82×10^{-5}
Pore diffusion coefficient (m^2/sec)	3.77×10^{-15}
Freundlich isotherm parameters	K = 55.34 (L/μg), n = 3.67
Particle density (g cm^{-3})	3.57
Particle disperstion condition	Polydisperse initial population
Particle concentration (no./cm^3)	$N_{Total} = 1.038 \times 10^9$, $N_{Primary} = 1.003 \times 10^{10}$
Particle diameter (nm)	$d_{Primary} = 30$, $d_{Maximum} = 960$
Fractal dimension (D_f)	2
Break-up coefficieint (K_B)	0
Temperature (°K)	298
Viscosity (g cm^{-1} s^{-1})	7.97
Hamaker constant (J)	4.14×10^{-20}
Boltzmann’s constant (J/K)	1.38×10^{-16}
pH	7.0
Ionic strength (M)	0.01

Perikinetic collision efficiency (α_{Br}) for various surface potential conditions due to arsenic sorption onto hydrous ferric oxide (HFO) was calculated using the unified perikientic coagulation model for fractal colloids coupled with arsenic kinetic and equilibrium models developed in this study and these results are displayed in Fig. 6.25.

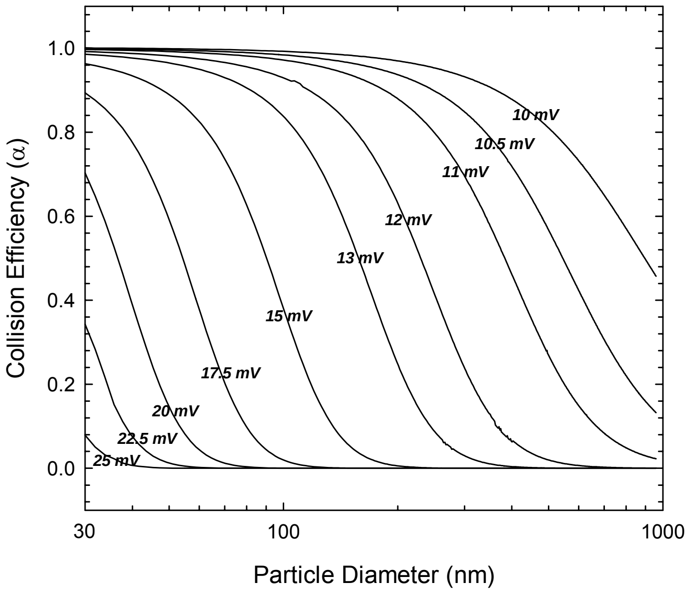

Figure 6.25 Perikinetic collision efficiency (α_{Br}) evolution between two particles during arsenic sorption (d_{min} = 30 nm, d_{max} = 960 nm, D_f = 2.0, and I = 0.01 M)

As shown in Fig. 6.25, the perikinetic collision efficiency (α_{Br}) decreases as the colliding particle size increases under all surface potential regimes and as the surface potential increased from 10 mV to 25 mV. The collision between relatively large particles ($200 \leq d \leq 1000$ nm) can not be expected at a surface potential of larger than 15 mV, which correspond to the previous results of section 6.3.1. However, above the surface potential of 25 mV, particle collisions are not expected to occur even when the size range is less than 30 nm in diameter. It is notable that primary particle size or mean particle size of the colliding particle population is mainly affected by the collision efficiency during perikientic coagulation. Thus, it is expected that surface potential (charge) evolution due to arsenic sorption onto hydrous ferric oxide (HFO) can alter the particle size distribution and thus plays a key role in the perikinetic coagulation process.

The results of the kinetics of As(V) sorption and surface potential evolution for the numerical simulation conditions of As(V) = 2.5×10^{-5} M, Fe = 1.0×10^{-4} M (As/Fe = 0.25), and perikinetic coagulation, are represented in Figs. 6.26 to 6.30 in terms of arsenic sorption kinetics, surface potential evolution with reaction time, particle concentration, coagulation mass conservation factor, particle size distribution, and cumulative particle size distribution.

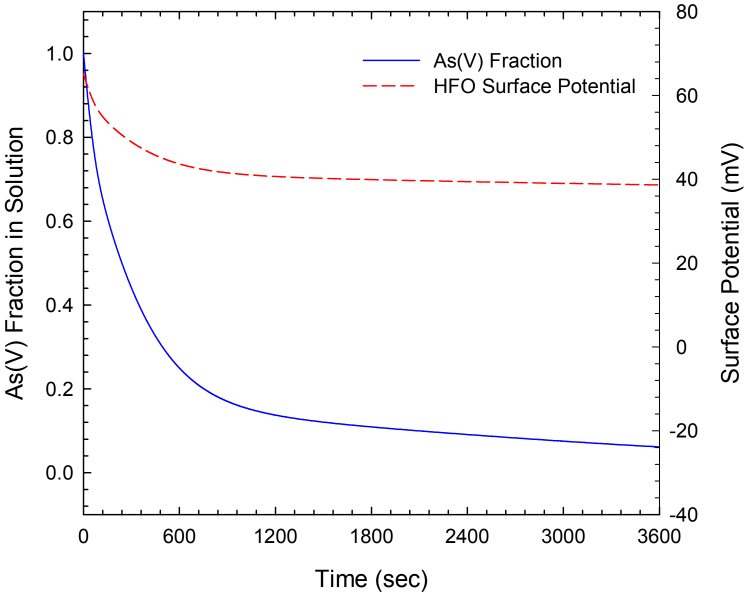

Figure 6.26 Kinetics of As(V) sorption and surface potential ($[As(V)_o] = 2.5\times10^{-5}$ M, Fe = 1.0×10^{-4} M, pH = 7.0, I = 0.01 M, perikinetic coagulation particle range of d_{min} = 30 nm and d_{max} = 960 nm, $D_f = 2.0$)

As can be seen from the results of Figs. 6.25 and 6.26, perikinetic coagulation having the lower arsenic loading ratio (As/Fe = 0.25) could not be expected to occur due to higher surface potential over all arsenic sorption reaction times, where the surface potential are over 38 mV. Thus, these results indicate that poor coagulation having low coagulation intensity or index is expected when perikinetic coagulation occurs with the lower arsenic loading ratio, and these results are displayed in Figs. 6.27 to 6.30.

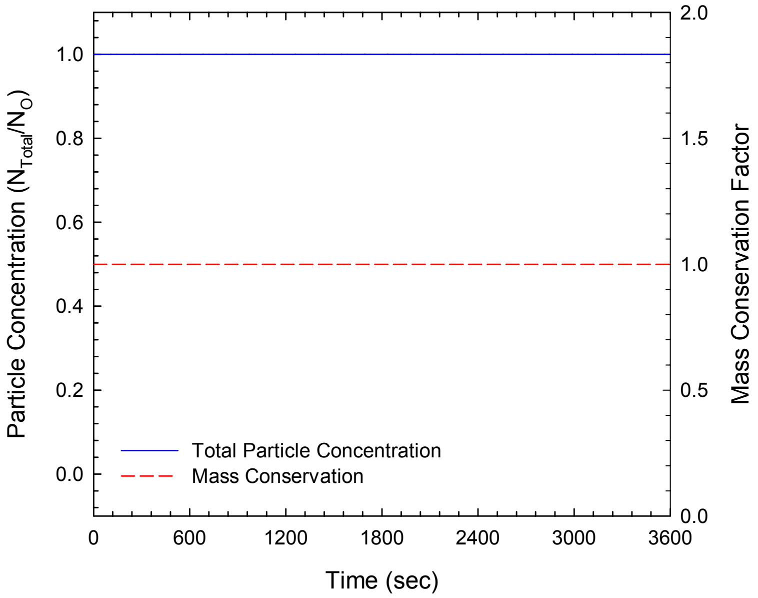

Figure 6.27 Coagulation kinetics ($[As(V)_o] = 2.5\times10^{-5}$ M, Fe = 1.0×10^{-4} M, pH = 7.0, I = 0.01 M, particle range of d_{min} = 30 nm and d_{max} = 960 nm, $D_f = 2.0$)

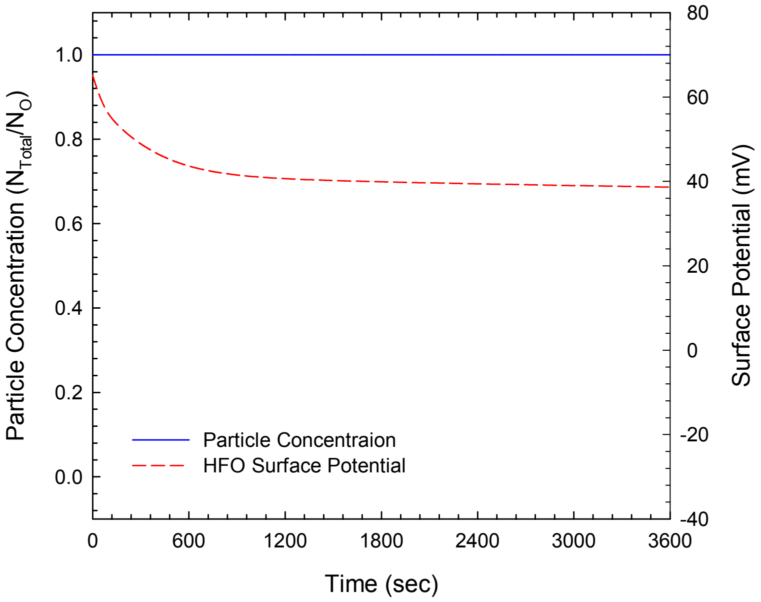

Figure 6.28 Kinetics of coagulation and surface potential ($[As(V)_o] = 2.5\times10^{-5}$ M, Fe = 1.0×10^{-4} M, pH = 7.0, I = 0.01 M, perikinetic coagulation particle range of d_{min} = 30 nm and d_{max} = 960 nm, D_f = 2.0)

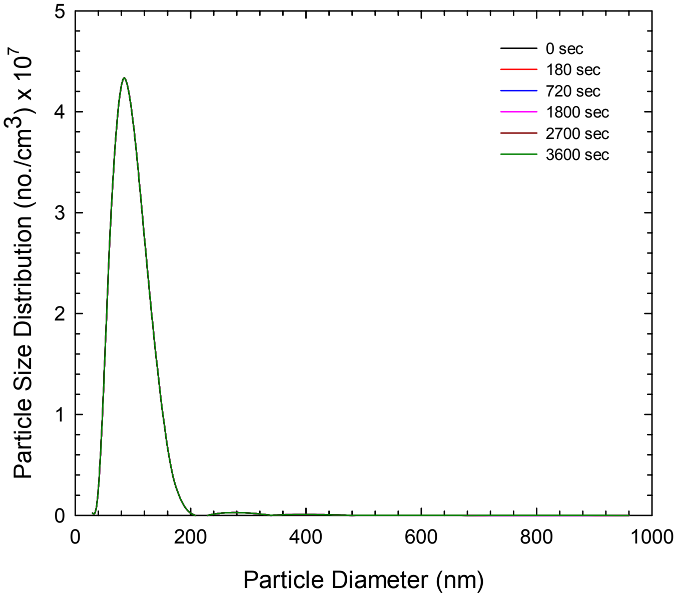

Figure 6.29 Particle size distribution ($[As(V)_o] = 2.5\times10^{-5}$ M, Fe = 1.0×10^{-4} M, pH = 7.0, I = 0.01 M, particle range of d_{min} = 30 nm and d_{max} = 960 nm, D_f = 2.0)

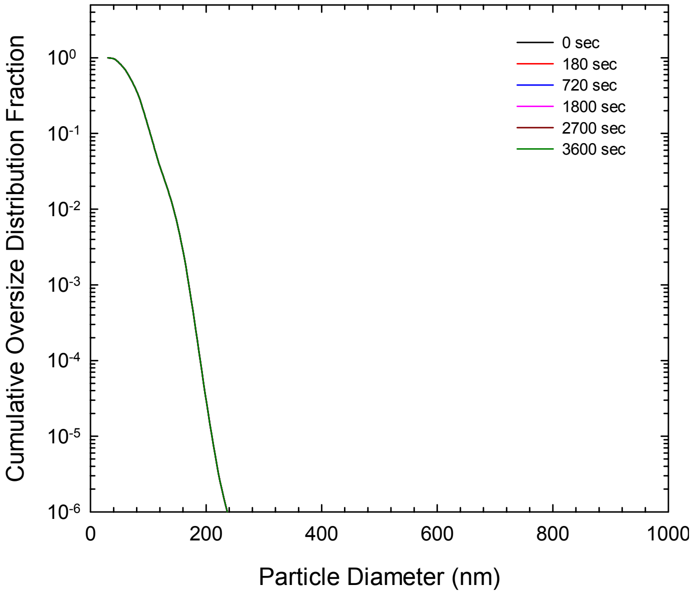

Figure 6.30 Cumulative oversize particle distribution (As(V) = 2.5×10^{-5} M, Fe = 1.0×10^{-4} M, pH = 7.0, I = 0.01 M, particle range of d_{min} = 30 nm and d_{max} = 960 nm, D_f = 2.0)

As initial arsenic sorption loading ratio increased from As/Fe = 0.25 to As/Fe 1.0, numerical simulations using the coupled perikinetic coagulation model produced different results compared to the relatively low As/Fe ratio of 0.25. The initial conditions of various arsenic loading ratios were As/Fe = 0.5 (see Figs. 6.31 to 6.35), As/Fe = 0.75 (see Figs. 6.36 to 6.40), and As/Fe = 1.0 (see Figs. 6.41 to 6.45).

From the results represented by arsenic sorption kinetics and surface potential evolution over time (see Fig. 6.31, 6.36, and 6.41), it was found that as arsenic initial loading ratio (As/Fe) increased from 0.25 to 0.75, minimum surface potentials on hydrous ferric oxide decreased to 0 mV of surface potential. However, in the case of the highest arsenic loading ratio of As/Fe = 1.0, the surface potential exceeded 0 mV and approached -25 mV. From these results, it could be expected that particle collision is dependent on the surface potential magnitude and thus, particle coagulation could not occur when the surface potential magnitude is over 25 mV or under -25 mV. Furthermore, higher coagulation intensity could be found when the surface potential has the lowest value and approaches 0 mV as expected.

As shown in results of coagulation (total particle concentration) kinetics and mass conservation (see Fig. 6.32, 6.37, and 6.42), even though the hydrous ferric oxide (HFO) particle is not a sphere but a fractal aggregate of D_f 2.0, the coagulation mass (represented by the total number of primary particles for each class size) was conserved perfectly for all coupled perikinetic coagulation with the arsenic sorption model simulations. As displayed in the results of total particle concentration (particle coagulation) kinetics, surface potential evolution (see Fig. 6.33, 6.38, and 6.43), particle size distribution evolution over time (see Fig. 6.34, 6.39, and 6.44), and cumulative size distribution evolution (see Fig. 6.35, 6.40, and 6.45), it was found that coagulation did not occur until the surface potential decreased to 20mV. Thus, this very low coagulation intensity resulted in the lag-phase coagulation kinetics during relatively high surface potentials ranging over 20mV. In other words, the coupled perikinetic coagulation with arsenic sorption modeling could be initiated at the point of surface potential of 20 mV or less. Further, from Figs. 6.43, 6.44 and 6.45, as particles adsorbed large amounts of arsenic, the perikinetic collisions between particles stopped, especially when the surface potential decreased under -20 mV. Moreover, from Figs. 6.43, 6.44 and 6.45, the second lag-phase coagulation kinetics and particle size distribution could be found. Thus, the surface potential magnitude of ±20 mV is an important condition and could be used as a primary factor to predict the behavior of perikinetic coagulation kinetics coupled with arsenic sorption.

Table 6.9 Collision Efficiencies and Surface Potentials for Perikinetic Coagulation

As(V) loadings	As/Fe ratio	Average Collision Efficiency	Surface Potential
As = 0.25×10^{-4} M Fe = 1.00×10^{-4} M	0.25	2.1846×10^{-3}	38.65 mV
As = 0.50×10^{-4} M Fe = 1.00×10^{-4} M	0.50	1.6120×10^{-1}	16.25 mV
As = 0.75×10^{-4} M Fe = 1.00×10^{-4} M	0.75	8.2840×10^{-1}	-5.09 mV
As = 1.00×10^{-4} M Fe = 1.00×10^{-4} M	1.00	4.3576×10^{-1}	-23.70 mV

It is possible to compare coagulation intensity, kinetics, and particle size distribution using overall average collision efficiencies between two colliding particles during arsenic sorption kinetics. These overall average collision efficiencies were calculated and are displayed in Table 6.9. These average collision efficiencies can be used for comparing overall collision intensity magnitude (i.e., high, intermediate, and low level coagulation). That is, although this overall average collision efficiency can be introduced into the coagulation model analysis due to its easy handling, it is impossible to predict the coagulation kinetics using average collision efficiency values calculated from Table 6.9. Especially, the average collision efficiency can not predict the lag-phase of the coagulation kinetics and particle size distribution evolution due to a higher surface potential than 20 mV (first lag-phase) or lower surface potential than -20 mV (second lag-phase). Therefore, it is recommended that collision efficiency be calculated for each time step of arsenic sorption and particle coagulation, rather than use an average collision efficiency.

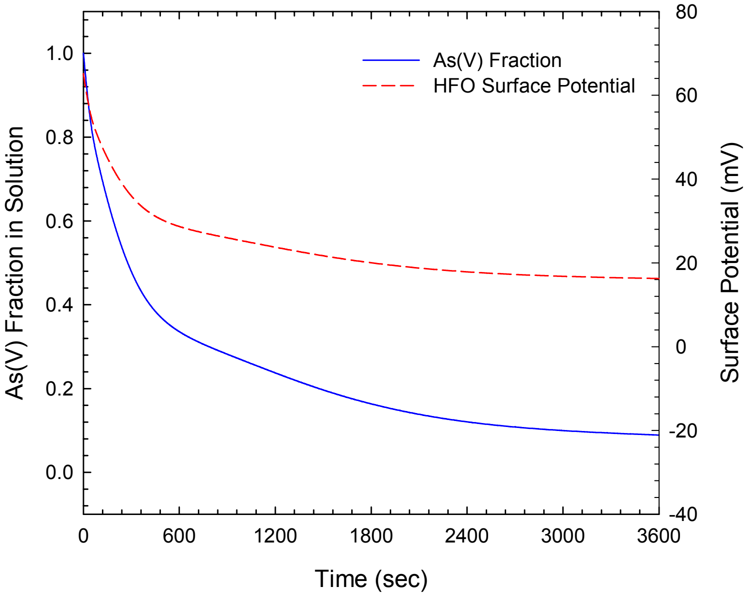

Figure 6.31 Kinetics of As(V) sorption and surface potential ($[As(V)_o] = 5.0\times10^{-5}$ M, Fe $= 1.0\times10^{-4}$ M, pH = 7.0, I = 0.01 M, perikinetic coagulation particle range of $d_{min} = 30$ nm and $d_{max} = 960$ nm, $D_f = 2.0$)

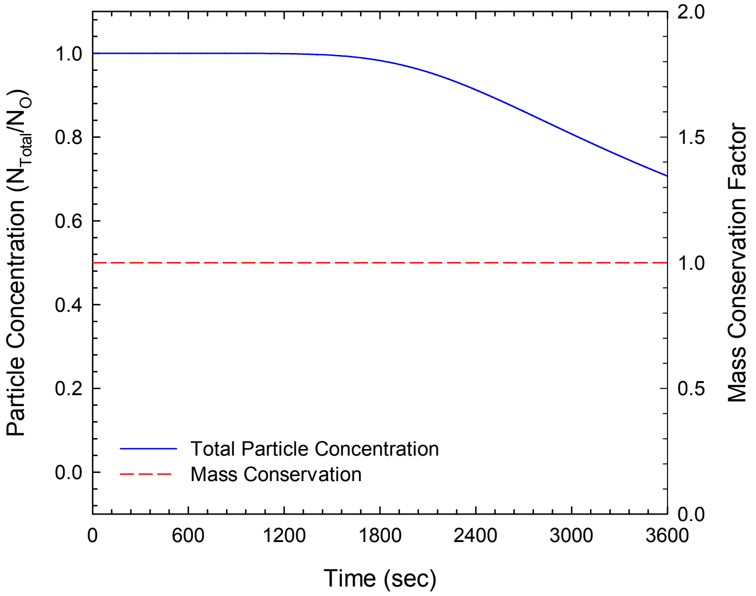

Figure 6.32 Coagulation kinetics ($[As(V)_o] = 5.0\times10^{-5}$ M, Fe = 1.0×10^{-4} M, pH = 7.0, I = 0.01 M, particle range of d_{min} = 30 nm and d_{max} = 960 nm, $D_f = 2.0$)

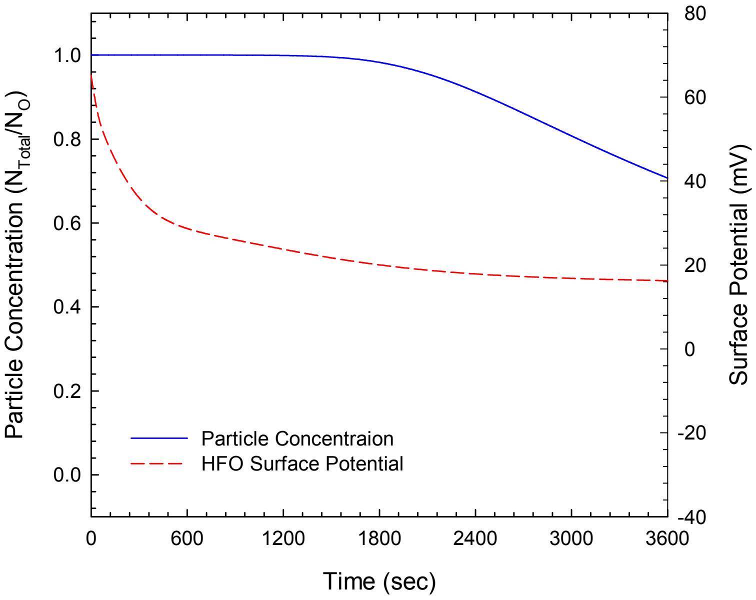

Figure 6.33 Kinetics of coagulation and surface potential (As(V) = 5.0×10^{-5} M, Fe = 1.0×10^{-4} M, pH = 7.0, I = 0.01 M, perikinetic coagulation particle range of d_{min} = 30 nm and d_{max} = 960 nm, $D_f = 2.0$)

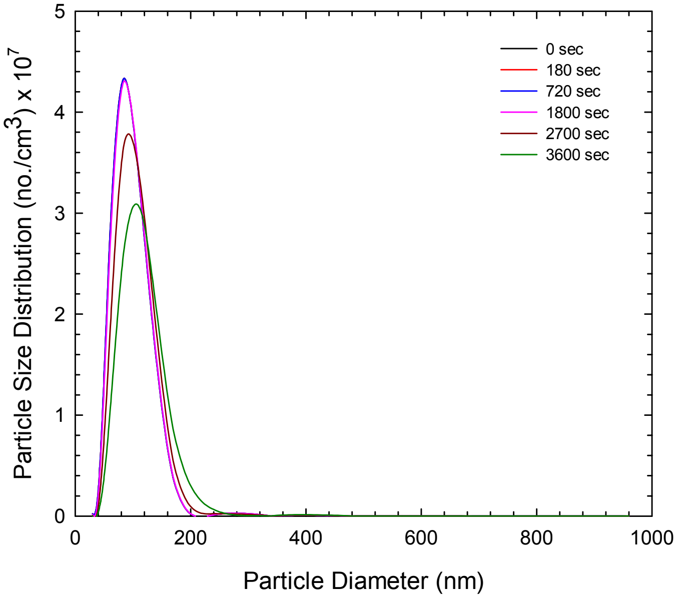

Figure 6.34 Particle size distribution ([As(V)$_o$] = 5.0×10^{-5} M, Fe = 1.0×10^{-4} M, pH = 7.0, I = 0.01 M, particle range of d$_{min}$ = 30 nm and d$_{max}$ = 960 nm, D$_f$ = 2.0)

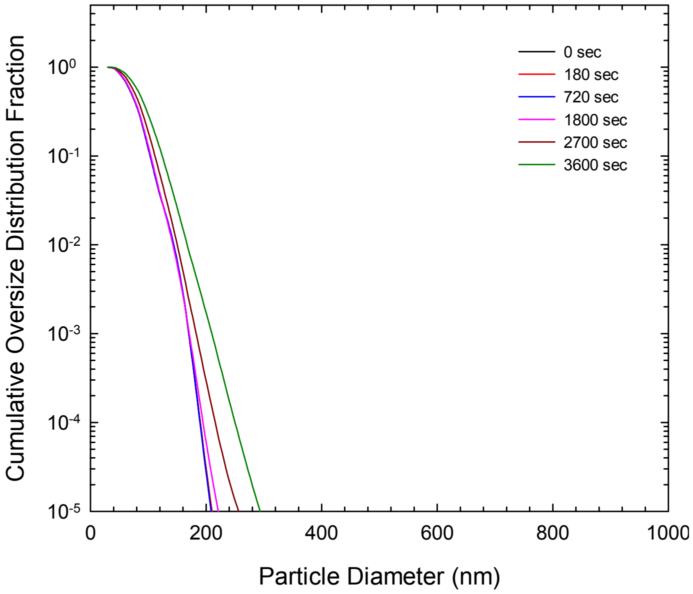

Figure 6.35 Cumulative oversize particle distribution ([As(V)$_o$] = 5.0×10^{-5} M, Fe = 1.0×10^{-4} M, pH 7.0, I = 0.01M, particle range of d$_{min}$=30 nm and d$_{max}$=960 nm, D$_f$ = 2.0)

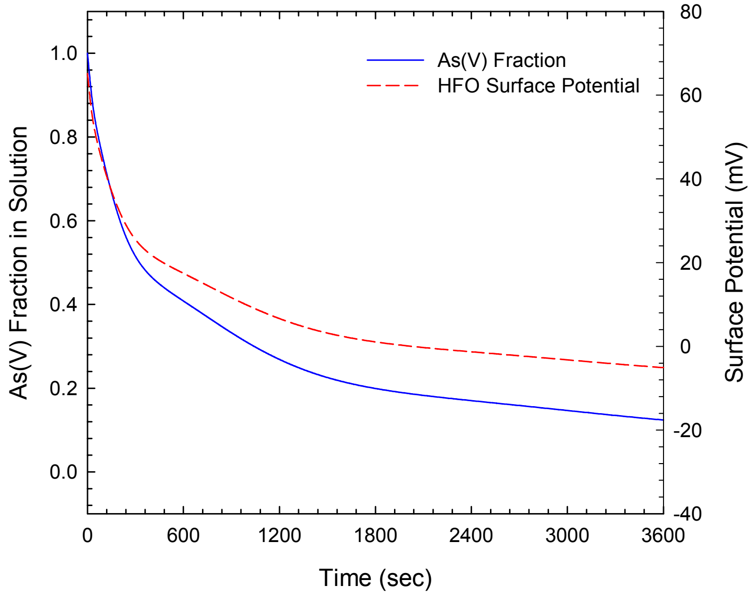

Figure 6.36 Kinetics of As(V) sorption and surface potential ([As(V)$_o$] = 7.5×10^{-5} M, Fe = 1.0×10^{-4} M, pH = 7.0, I = 0.01 M, perikinetic coagulation particle range of d$_{min}$ = 30 nm and d$_{max}$ = 960 nm, D$_f$ = 2.0)

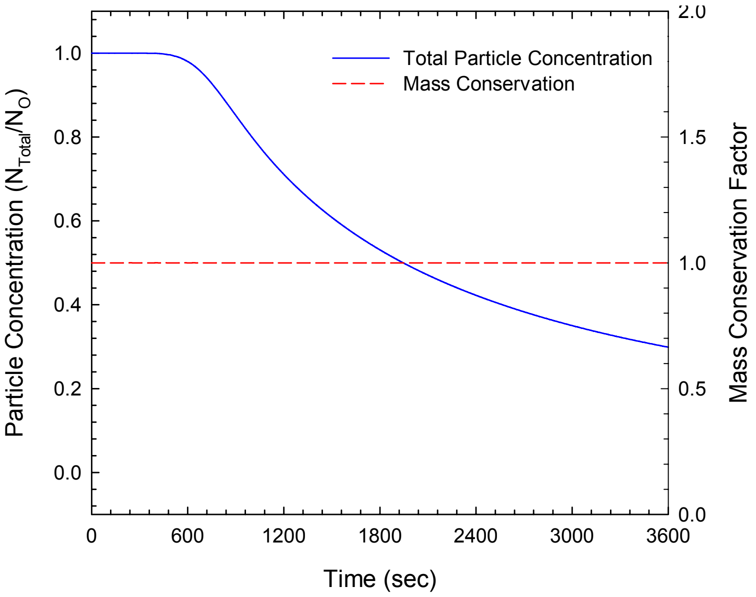

Figure 6.37 Coagulation kinetics ([As(V)$_o$] = 7.5×10^{-5} M, Fe = 1.0×10^{-4} M, pH = 7.0, I = 0.01 M, particle range of d$_{min}$ = 30 nm and d$_{max}$ = 960 nm, D$_f$ = 2.0)

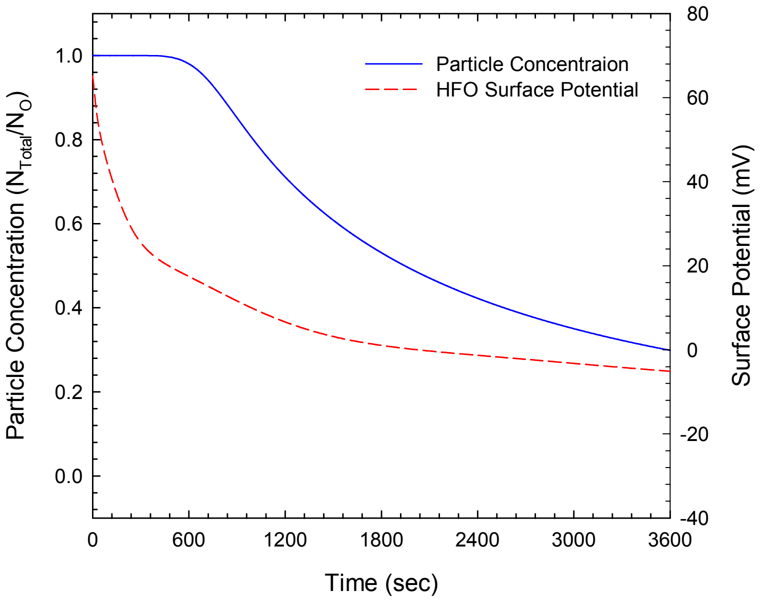

Figure 6.38 Kinetics of coagulation and surface potential ($[As(V)_o] = 7.5\times10^{-5}$ M, Fe = 1.0×10^{-4} M, pH = 7.0, I = 0.01 M, perikinetic coagulation particle range of d_{min} = 30 nm and d_{max} = 960 nm, $D_f = 2.0$)

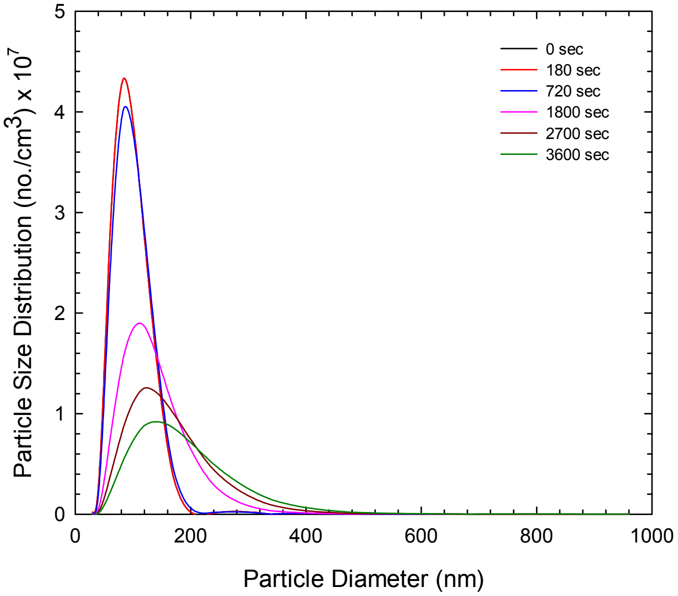

Figure 6.39 Particle size distribution ($[As(V)_o] = 7.5\times10^{-5}$ M, Fe = 1.0×10^{-4} M, pH = 7.0, I = 0.01 M, particle range of d_{min} = 30 nm and d_{max} = 960 nm, $D_f = 2.0$)

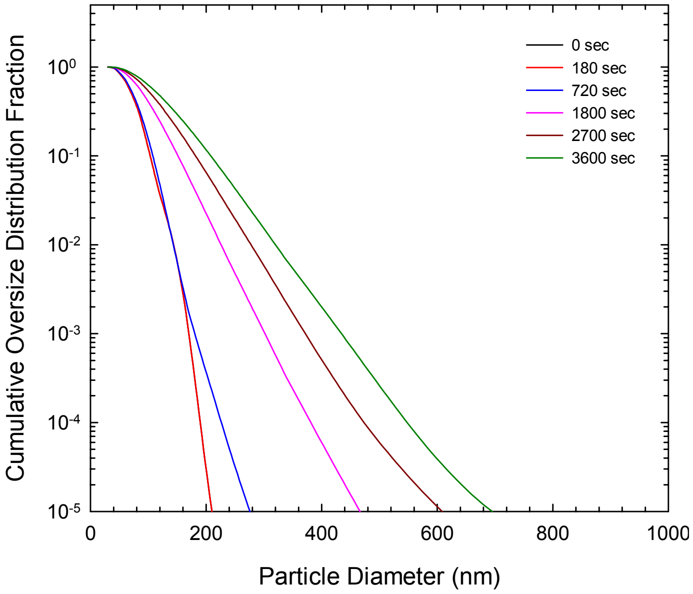

Figure 6.40 Cumulative oversize particle distribution ($[As(V)_o] = 7.5\times10^{-5}$ M, Fe = 1.0×10^{-4} M, pH 7.0, I = 0.01M, particle range of d_{min}=30 nm and d_{max}=960 nm, $D_f = 2.0$)

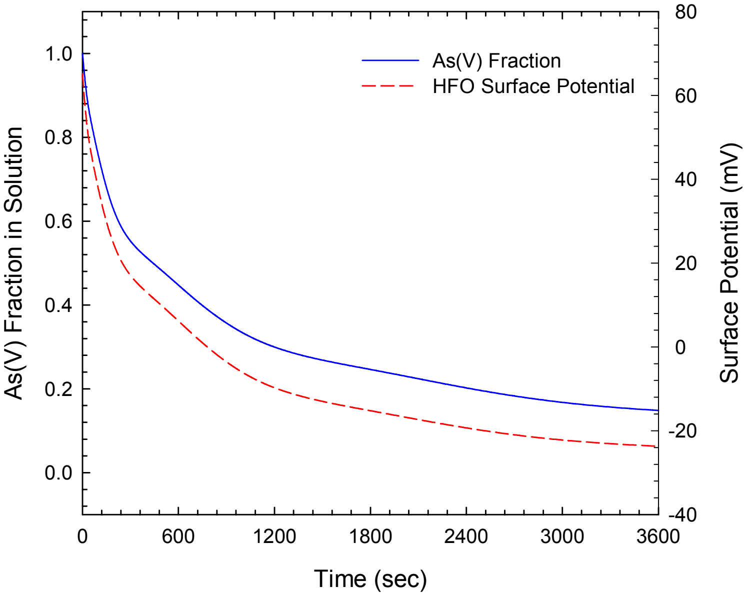

Figure 6.41 Kinetics of As(V) sorption and surface potential (As(V) = 1.0×10^{-4} M, Fe = 1.0×10^{-4} M, pH 7.0, I = 0.01 M, perikinetic coagulation particle range of d_{min} = 30 nm and d_{max} = 960 nm, $D_f = 2.0$)

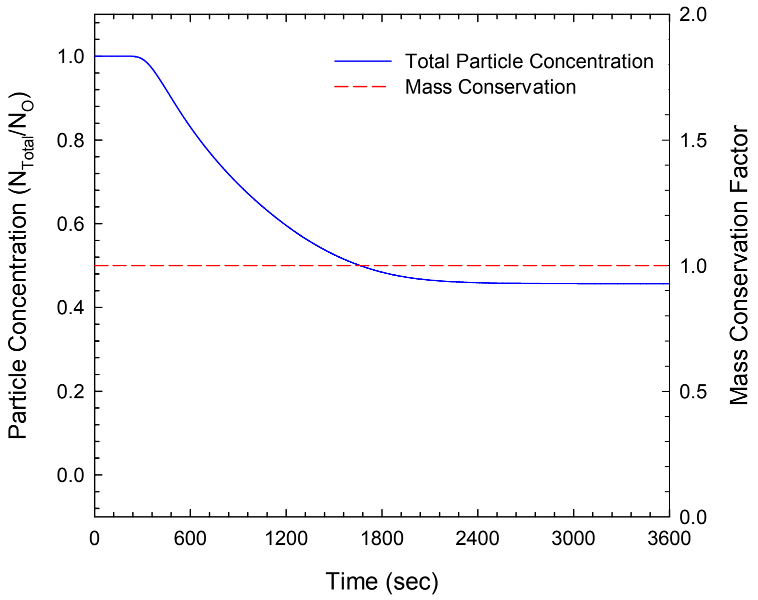

Figure 6.42 Coagulation kinetics ($[As(V)_o] = 1.0\times10^{-4}$ M, Fe = 1.0×10^{-4} M, pH = 7.0, I = 0.01 M, particle range of d_{min} = 30 nm and d_{max} = 960 nm, D_f = 2.0)

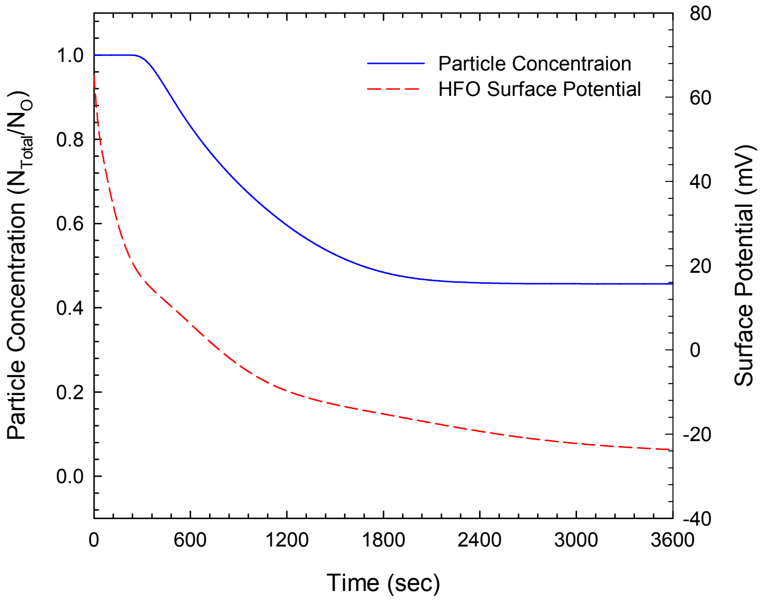

Figure 6.43 Kinetics of coagulation and surface potential ($[As(V)_o] = 1.0\times10^{-4}$ M, Fe = 1.0×10^{-4} M, pH = 7.0, I = 0.01 M, perikinetic coagulation particle range of d_{min} = 30 nm and d_{max} = 960 nm, D_f = 2.0)

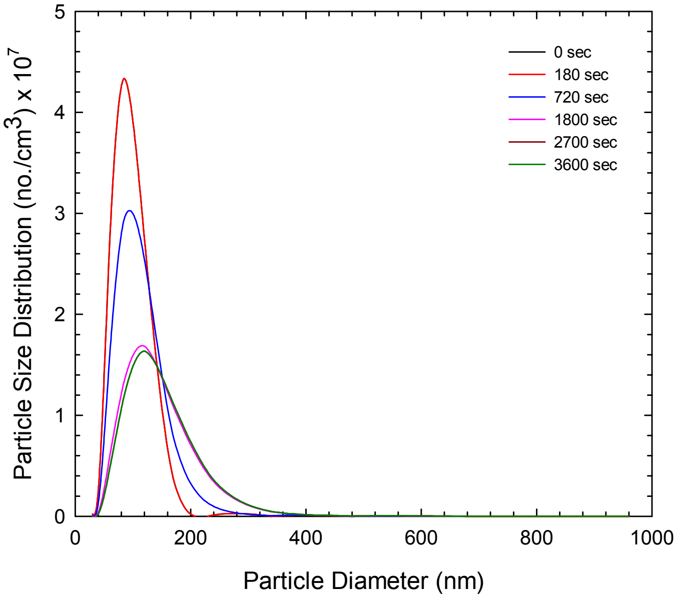

Figure 6.44 Particle size distribution ($[As(V)_o] = 1.0\times10^{-4}$ M, Fe = 1.0×10^{-4} M, pH = 7.0, I = 0.01 M, particle range of d_{min} = 30 nm and d_{max} = 960 nm, $D_f = 2.0$)

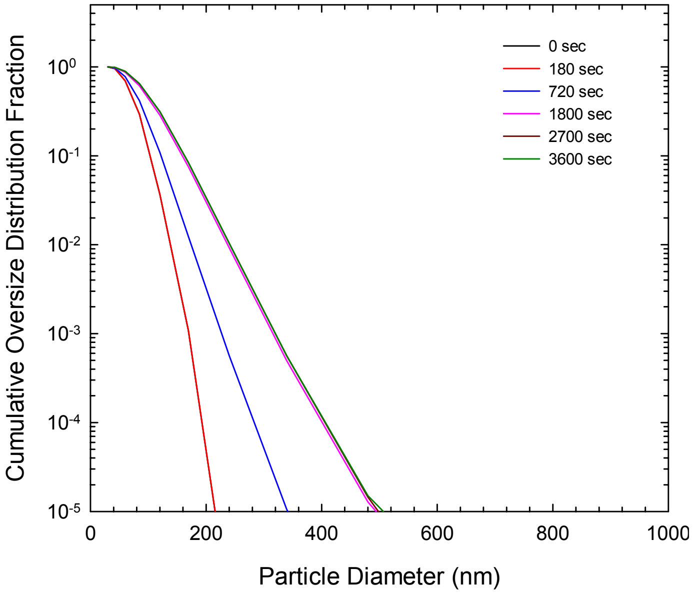

Figure 6.45 Cumulative oversize particle distribution ($[As(V)_o] = 1.0\times10^{-4}$ M, Fe = 1.0×10^{-4} M, pH 7.0, I = 0.01M, particle range of d_{min}=30 nm and d_{max}=960 nm, $D_f = 2.0$)

6.5.2 A Coupled Orthokinetic Coagulation Model with Arsenic Sorption

Using the computational algorithm proposed in the section 6.5.1 (see Fig. 6.24), arsenic sorption kinetics and equilibrium onto hydrous ferric oxide (HFO) were unified with the improved orthokinetic coagulation model developed in previous chapter. The detailed coupling procedure was identical to that sued in the unified perikinetic coagulation model study of Eqs. (6.83) to (6.100), except for the collision efficiency model $\alpha_{\mathrm{sh}}(\mathrm{r}_i,\mathrm{r}_j)$ and the collision frequency kernel $\beta_{\mathrm{sh}}(\mathrm{r}_i,\mathrm{r}_j)$, rather than $\alpha_{\mathrm{Br}}(\mathrm{r}_i,\mathrm{r}_j)$ and $\beta_{\mathrm{Br}}(\mathrm{r}_i,\mathrm{r}_j)$.

Step 1) Diffusion transport (mass transport) arsenic sorption kinetic modeling.

$$\varepsilon_p \frac{\partial[\mathrm{As}]_{\mathrm{Liquid}}}{\partial \mathrm{t}} + \rho_p \frac{\partial[\mathrm{As}]_{\mathrm{Solid}}}{\partial \mathrm{t}} = \frac{1}{\mathrm{r}_p^2}\frac{\partial}{\partial \mathrm{r}_p}\left(D_p \mathrm{r}_p^2 \frac{\partial[\mathrm{As}]_{\mathrm{Liquid}}}{\partial \mathrm{r}_p} \right) \tag{6.83}$$

Step 2) Surface complexation modeling using the sorption local equilibrium assumption.

Acid-Base Reactions

$HAsO_4^{-2} \Leftrightarrow AsO4^{-3} + H^+$ (6.84)

$H_2AsO_4^- \Leftrightarrow AsO_4^{-3} + 2H^+$ (6.85)

$H_3AsO_4 \Leftrightarrow AsO_4^{-3} + 3H^+$ (6.86)

Surface protonation constant

$\equiv XOH + H^+ \Leftrightarrow \equiv XOH_2^+$ (6.87)

$\equiv XOH \Leftrightarrow \equiv XO^- + H^+$ (6.88)

Monodentate As(V) sorption

$\equiv XOH + AsO_4^{-3} + 3H^+ \Leftrightarrow \equiv XH_2AsO_4 + H_2O$ (6.89)

$\equiv XOH + AsO_4^{-3} + 2H^+ \Leftrightarrow \equiv XHAsO_4^- + H_2O$ (6.90)

$\equiv XOH + AsO_4^{-3} + H^+ \Leftrightarrow \equiv XAsO_4^{-2} + H_2O$ (6.91)

$\equiv XOH + AsO_4^{-3} \Leftrightarrow \equiv XAsO_4^{-3}$ (6.92)

Step 3) HFO surface charge evolution modeling.

$$\sigma = \frac{F}{2a}\left\{[\equiv \mathrm{XO^-}]+[\equiv \mathrm{XOH_2^+}]+[\equiv \mathrm{XAsO_4^{-3}}]+[\equiv \mathrm{XAsO_4^{-2}}]+[\equiv \mathrm{XHAsO_3^-}]\right\} \quad (6.93)$$

Step 4) Collision efficiency calculation.

$$\mathrm{F_A} = -\frac{\mathrm{A_{1,2}r_2}}{(1+\lambda)h^2}\left[\frac{2.45}{15p}-\frac{2.17}{30p^2}+\frac{1.18}{105p^3}\right] \qquad p \geq 1.0 \quad (6.101)$$

$$\mathrm{F_A} = -\frac{\mathrm{A_{1,2}r_2}}{(1+\lambda)h^2}\left[\frac{1+3.54p}{6(1+1.77p)^2}\right] \qquad p < 1.0 \quad (6.102)$$

$$\mathrm{F_R} = \frac{\pi\varepsilon_0\varepsilon_r\kappa \mathrm{r_2}}{1+\lambda}\left[\frac{2\psi_1\psi_2-(\psi_1^2+\psi_2^2)\exp(-\kappa h)}{\sinh(\kappa h)}\right] \quad (6.103)$$

$$\mathrm{F_T} = \mathrm{F_R} + \mathrm{F_A} \quad (6.104)$$

$$\frac{\mathrm{dr^*}}{\mathrm{dt}} = |\dot{\gamma}'_{\max}|\mathrm{r^*}(1-\mathcal{A})\sin^2\theta\sin\phi\cos\phi + \frac{\mathcal{C}}{6\pi\mu \mathrm{r_1^2}}(\mathrm{F_T}) \quad (6.105)$$

$$\frac{\mathrm{d}\theta}{\mathrm{dt}} = |\dot{\gamma}'_{\max}|(1-\mathcal{B})\sin\theta\cos\theta\sin\phi\cos\phi \quad (6.106)$$

$$\frac{\mathrm{d}\phi}{\mathrm{dt}} = |\dot{\gamma}'_{\max}|\left(\cos^2\phi-\frac{\mathcal{B}}{2}\cos 2\phi\right) \quad (6.107)$$

$$\alpha_{\mathrm{sh}}(\mathrm{r}_i,\mathrm{r}_j) = \frac{3/2}{(\mathrm{r}_i+\mathrm{r}_j)^3}\int_0^{z_{\max}}[x(z)]^2\,dz \quad (6.108)$$

Step 5) Unified coagulation modeling.

$$\alpha_{\mathrm{sh}}(\mathrm{r}_i,\mathrm{r}_j) = \frac{3/2}{(\mathrm{r}_i+\mathrm{r}_j)^3}\int_0^{z_{\max}}[x(z)]^2\,dz \quad (6.108)$$

$$\beta_{\mathrm{sh}}(\mathrm{r}_i,\mathrm{r}_j) = \frac{4\pi}{3}|\dot{\gamma}'_{\max}|(\mathrm{r}_i+\mathrm{r}_j)^3 \quad (6.109)$$

$$\frac{dn_k}{dt} = \frac{1}{2}\sum_{i+j=k}\alpha_{sh}(r_i, r_j)\beta_{sh}(r_i, r_j)n_i n_j - n_k\sum_{l=1}^{\infty}\alpha_{sh}(r_l, r_k)\beta_{sh}(r_l, r_k)n_l + \sum_{j=1}^{\infty}b_{k,j}s_j(n_l)^{\eta} - s_k(n_k)^{\eta} \tag{6.110}$$

All modeling equations used for each step were developed or introduced in previous chapters and sections. A unified orthokinetic coagulation model coupled with arsenic sorption kinetics and equilibrium was simulated using the modeling procedure described in the previous unified perikinetic coagulation model study. Unlike the perikinetic coagulation model coupled with arsenic sorption, the particle trajectory analysis of Eqs. (6.105) to (6.108) was used to calculate orthokinetic collision efficiency $\alpha_{sh}(r_i, r_j)$ and an aggregate break-up kernel was introduced to apply flow induced stresses that produces floc disintegration into the overall orthokinetic coagulation model of Eq. (6.110). Introducing the orthokinetic collision efficiency $\alpha_{sh}(r_i, r_j)$, which is related to arsenic sorption and surface potential into the improved coagulation model previously developed yields a unified orthokinetic coagulation model coupled with arsenic sorption.

The unified orthokinetic coagulation model was computed using the initial conditions presented in Table 6.10. As shown in the unified perikinetic coagulation model simulation, a polydisperse initial population where each size class has different particle concentrations was examined due to the more realistic conditions for engineered or experimental systems than a monodisperse initial population where all of the initial particles have the same particle size. The polydisperse initial population had a particle size distribution similar to a normal distribution curve. The primary and maximum particle sizes used for the orthokinetic coagulation were 1 μm and 32 μm in diameter, respectively. In this particle size range, it has been reported that orthokinetic coagulation resulting from mass transport phenomenon due to fluid flow strain-rate is the main particle collision mechanism, rather than Brownian random motion or differential sedimentation or buoyancy. Furthermore, a fractal geometric dimension value (D_f) of 2.0 was introduced into the orthokinetic coagulation model.

Table 6.10 Parameters for Coupled Orthokinetic Coagulation with Arsenic Sorption

Physical Properties	Values
Arsenic concentration (M)	$0.25 \times 10^{-4} \sim 2.00 \times 10^{-4}$
HFO concentration (M)	1.00×10^{-3}
Volume (L)	1.0
Two film mass transfer coefficient (m/sec)	1.82×10^{-5}
Pore diffusion coefficient (m^2/sec)	3.77×10^{-15}
Freundlich isotherm parameters	$K = 55.34$ (L/μg), $n = 3.67$
Particle density (g cm^{-3})	3.57
Particle disperstion condition	Polydisperse initial population
Particle concentration (no./cm^3)	$N_{Total} = 1.071\times10^8$, $N_{Primary} = 1.035\times10^9$
Particle diameter (μm)	$d_{Primary} = 1.0$, $d_{Maximum} = 32.0$
Fractal dimension (D_f)	2
Break-up coefficieint (K_B)	0.1
Fluid strain-rate (1/sec)	15
Temperature (°K)	298
Viscosity (g cm^{-1} s^{-1})	7.97
Hamaker constant (J)	4.14×10^{-20}
Boltzmann's constant (J/K)	1.38×10^{-16}
pH	7.0
Ionic strength (M)	0.01

The results from the coupled orthokinetic coagulation model for fractal colloids with arsenic sorption kinetics and equilibrium model are displayed in Figs. 6.47 to 6.66

for various arsenic loading ratios (As/Fe = 0.025~0.2). It should be noted that the values of arsenic loading ratios (As/Fe = 0.025~0.2) used in the orthokinetic coagulation simulation are lower than the values of perikinetic coagulation study (As/Fe = 0.25~1.0). The inconsistency of arsenic loading ratio between two coagulation numerical simulations results from the relationship between arsenic sorption capacity (or specific surface area) and adsorbent particle size. For both perikinetic and orthokinetic coagulation simulations, the initial particle size rage were 0.03~0.96 μm and 1~32 μm, respectively. In general, the arsenic sorption capacity is inversely proportional to the adsorbent particle size. Therefore, the arsenic loading ratios were controlled to obtain moderate sorption data for both perikinetic and orthokinetic coagulation modeling. Orthokinetic collision efficiency (α_{sh}) for various surface potential conditions due to arsenic sorption onto hydrous ferric oxide (HFO) was calculated and displayed in Fig. 6.46. As expected from the perikinetic collision efficiency study, the orthokinetic collision efficiency (α_{sh}) decreases as the colliding particle size increases under all surface potential regimes and as the surface potential increased from 5 mV to 50 mV (see Fig. 6.46). Orthokinetic collisions between relatively large particles (d > 20 μm) can hardly be expected at the relatively high surface potentials. As shown in the previous unified perikinetic coagulation model results, primary particle size or mean particle size of the colliding particle population and its surface potential mainly affect the collision efficiency during orthokinetic coagulation. Thus, it is expected that surface potential (charge) evolution due to arsenic sorption onto hydrous ferric oxide (HFO) can alter the particle size distribution and thus plays a key role in the orthokinetic coagulation process.

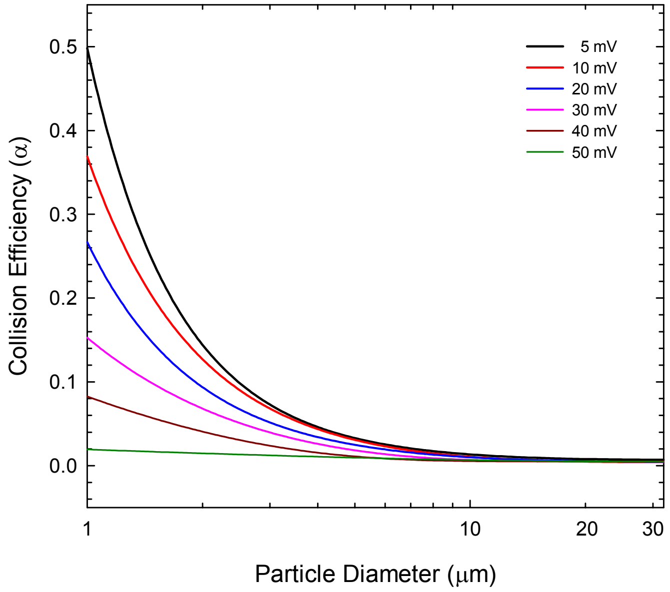

Figure 6.46 Orthokinetic collision efficiency (α_{sh}) evolution between two particles during arsenic sorption (d_{min} = 1.0 μm, d_{max} = 32.0 μm, D_f = 2.0, and I = 0.01 M)

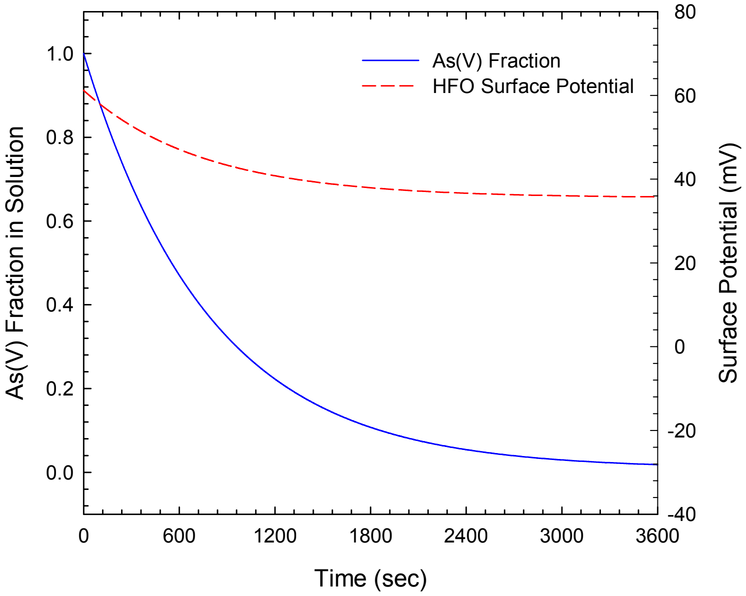

Figure 6.47 Kinetics of As(V) sorption and surface potential ($[As(V)_o] = 0.25\times10^{-4}$ M, Fe = 1.0×10^{-3} M, pH = 7.0, I = 0.01 M, orthokinetic coagulation particle range of d_{min} = 1.0 μm and d_{max} = 32.0 μm, D_f = 2.0)

The results of the kinetics of As(V) sorption and surface potential evolution for the numerical simulation conditions of As(V) = 0.25×10^{-4} M, Fe = 1.0×10^{-3} M (As/Fe = 0.025), and orthokinetic coagulation, are shown in Figs. 6.47 to 6.51 in terms of arsenic sorption kinetics, surface potential evolution, particle concentration, coagulation mass conservation factor, particle size distribution, and cumulative particle size distribution.

Even though orthokinetic coagulation having the lower arsenic loading ratio could not be expected due to the relatively higher surface potential during all arsenic sorption reaction times, it could be possible that orthokinetic coagulation can occur at the relatively higher surface potential conditions of 35 mV (see Figs. 6.46 and 6.47). However, these results indicate that coagulation having low coagulation intensity or index is expected when orthokinetic coagulation occurs with the lower arsenic loading ratio resulting in higher surface potential, and the results are displayed in Figs. 6.48 to 6.51.

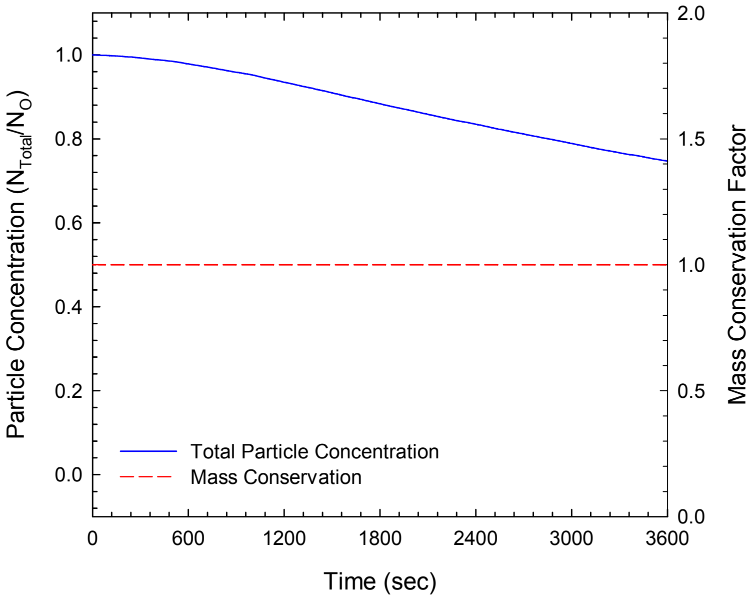

Figure 6.48 Coagulation kinetics ([As(V)$_o$] = 0.25×10^{-4} M, Fe = 1.0×10^{-3} M, pH = 7.0, I = 0.01 M, particle range of d$_{min}$ = 1 μm and d$_{max}$ = 32 μm, D$_f$ = 2.0)

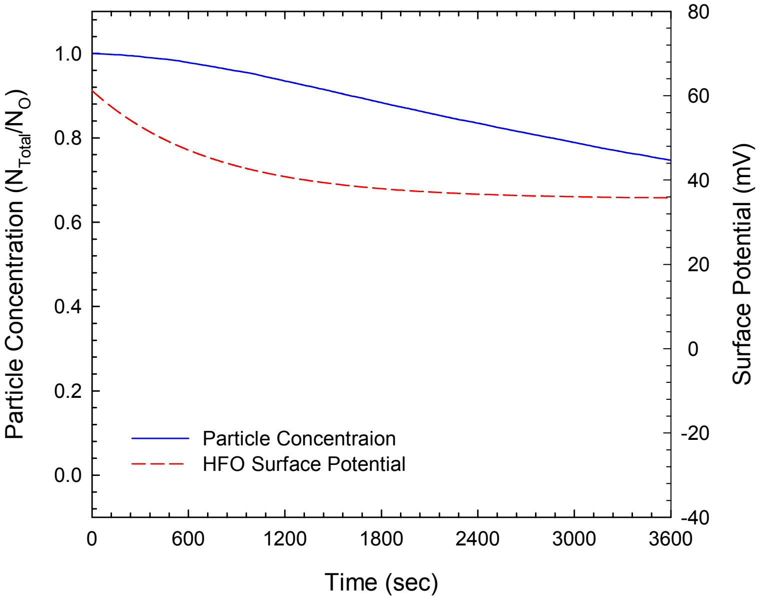

Figure 6.49 Kinetics of coagulation and surface potential ([As(V)$_o$] = 0.25×10^{-4} M, Fe = 1.0×10^{-3} M, pH = 7.0, I = 0.01 M, orthokinetic coagulation particle range of d$_{min}$ = 1 μm and d$_{max}$ = 32 μm, D$_f$ = 2.0)

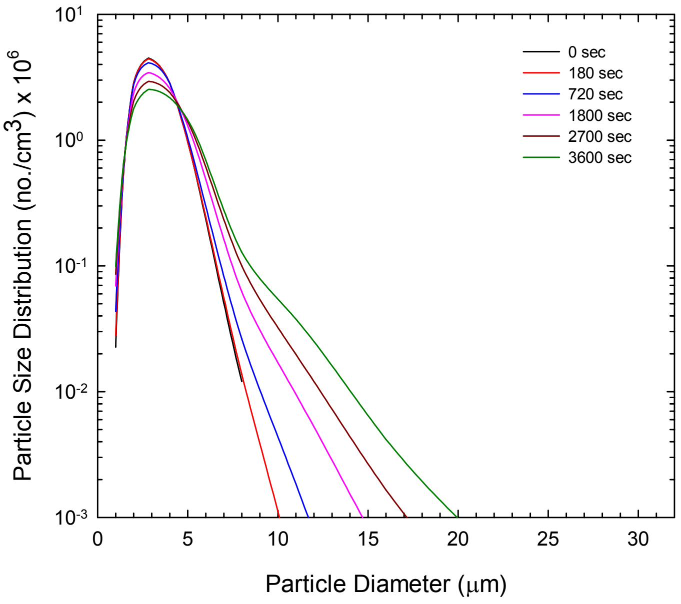

Figure 6.50 Particle size distribution ([As(V)$_o$] = 0.25×10^{-4} M, Fe = 1.0×10^{-3} M, pH = 7.0, I = 0.01 M, particle range of d$_{min}$ = 1 μm and d$_{max}$ = 32 μm, D$_f$ = 2.0)

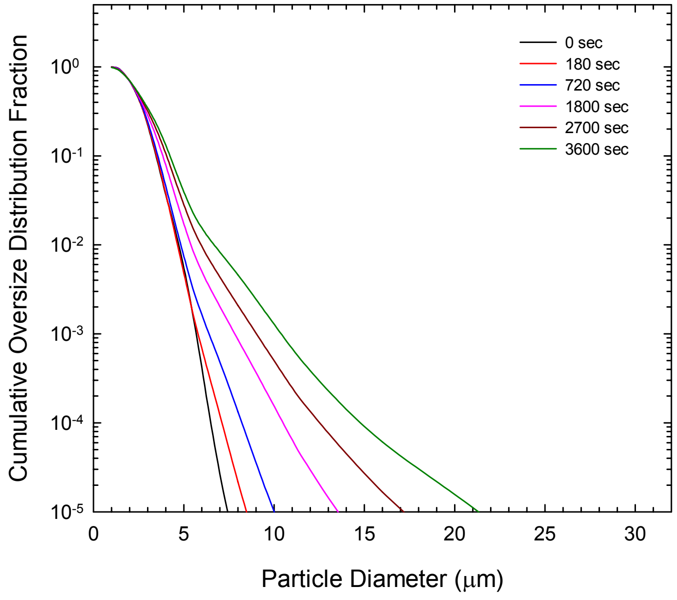

Figure 6.51 Cumulative oversize particle distribution ([As(V)$_o$] = 0.25×10^{-4} M, Fe = 1.0×10^{-3} M, pH 7.0, I = 0.01M, particle range of d$_{min}$=1 μm and d$_{max}$ = 32 μm, D$_f$ = 2.0)

As initial arsenic sorption loading ratio increased from As/Fe = 0.025 to As/Fe 0.2, numerical simulations using the coupled orthokinetic coagulation model demonstrated different results when compared to the relatively low As/Fe ratio of 0.025. The initial conditions of various arsenic loading ratios were As/Fe = 0.05 (see Figs. 6.52 to 6.56), As/Fe = 0.1 (see Figs. 6.57 to 6.61), and As/Fe = 0.2 (see Figs. 6.62 to 6.66).

From the results represented by the arsenic sorption kinetics and surface potential time evolution (see Fig. 6.52, 6.57, and 6.62), it was found that as arsenic initial loading ratio (As/Fe) increased from 0.025 to 0.2, minimum surface potentials on hydrous ferric oxide were decreased and changed from 35 mV to -40 mV, respectively. From these results, it could be expected that particle collision is dependent on surface potential magnitude. Furthermore, the higher coagulation intensity could be found when the surface potential has least value and approaches 0 mV.

As shown in results of coagulation (total particle concentration) kinetics and mass conservation factor (see Fig. 6.53, 6.58, and 6.63), even though the hydrous ferric oxide (HFO) particle is not a sphere but a fractal aggregate of D_f 2.0, the coagulation mass (represented by the total number of primary particles for each class size) was perfectly conserved for all coupled orthokinetic coagulation with arsenic sorption simulations. As displayed in the results from total particle concentration kinetics and surface potential evolution with reaction time (see Figs. 6.54, 6.59, and 6.64), particle size distribution time evolution (see Fig. 6.55, 6.60, and 6.65), and cumulative size distribution time evolution (see Fig. 6.56, 6.61, and 6.66), it was found that coagulation did not occur until the surface potential decreased to 30mV thus very low coagulation intensity resulted in lag-phase coagulation kinetics during the relatively high surface potentials ranging over 30mV. In other words, the coupled orthokinetic coagulation with arsenic sorption could only be initiated at the point of surface potential of 30 mV or less. Compared to the perikinetic study, it is worth while to note that surface potential has less influence on the orthokinetic collisions than perikinetic coagulation. This influence is especially true when particles have higher surface potentials, orthokinetic coagulation can be expected and the orthokinetic coagulation lag-phases that were easily found in the perikinetic coagulation study were found to be very short in the initial steps and were not found during arsenic sorption reaction period. That is, it can be expected that orthokinetic coagulation occurs even when surface potential is greater than 30 mV or under -30 mV.

Table 6.11 Collision Efficiencies and Surface Potentials for Orthokinetic Coagulation

As(V) loadings	As/Fe ratio	Average Collision Efficiency	Surface Potential
As = 0.25×10^{-4} M Fe = 1.00×10^{-3} M	0.025	4.8166×10^{-3}	35.76 mV
As = 0.50×10^{-4} M Fe = 1.00×10^{-3} M	0.050	1.4229×10^{-2}	13.77 mV
As = 1.00×10^{-4} M Fe = 1.00×10^{-3} M	0.100	1.6206×10^{-2}	-20.93 mV
As = 2.00×10^{-4} M Fe = 1.00×10^{-3} M	0.200	6.5944×10^{-3}	-40.35 mV

It is possible to compare coagulation intensity, kinetics, and particle size distribution using overall average collision efficiencies between two colliding particles during arsenic sorption. These overall average collision efficiencies were calculated and displayed in Table 6.11. As mentioned in the perikinetic study, although this overall average collision efficiency can be introduced into coagulation model analysis easily, it is impossible to predict the coagulation kinetics using average collision efficiency values calculated from Table 6.11. Thus, it is recommended that collision efficiency calculated from each time step of arsenic sorption and particle coagulation, rather than an overall average collision efficiency be used.

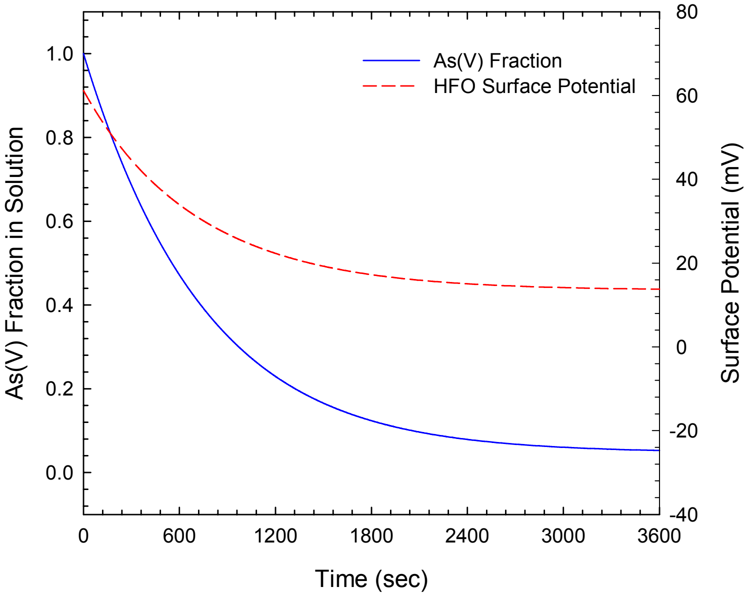

Figure 6.52 Kinetics of As(V) sorption and surface potential ($[As(V)_o] = 0.5\times10^{-4}$ M, Fe $= 1.0\times10^{-3}$ M, pH = 7.0, I = 0.01 M, orthokinetic coagulation particle range of $d_{min} = 1.0$ μm and $d_{max} = 32.0$ μm, $D_f = 2.0$)

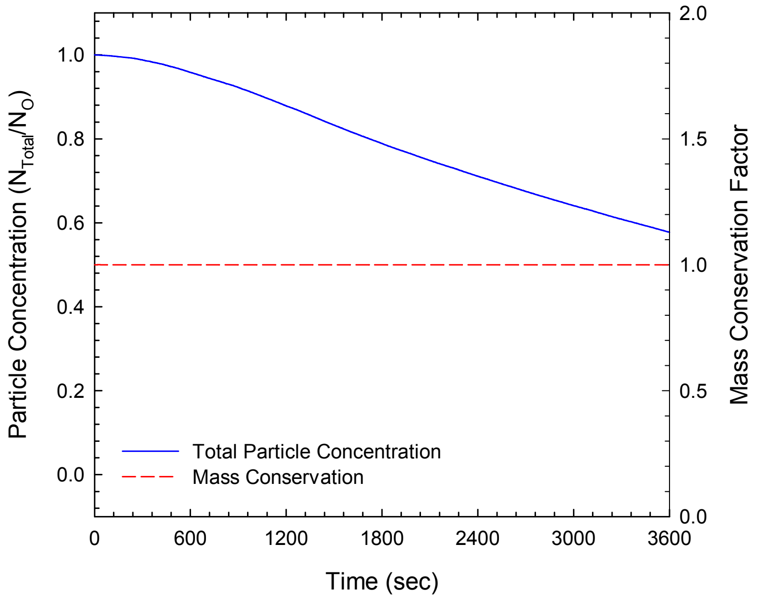

Figure 6.53 Coagulation kinetics ($[As(V)_o] = 0.5\times10^{-4}$ M, Fe = 1.0×10^{-3} M, pH = 7.0, I = 0.01 M, particle range of $d_{min} = 1$ μm and $d_{max} = 32$ μm, $D_f = 2.0$)

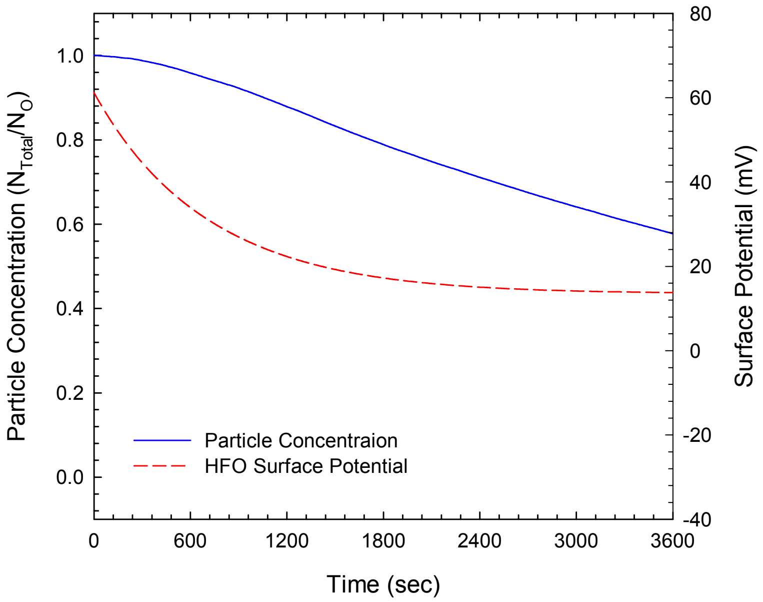

Figure 6.54 Kinetics of coagulation and surface potential ($[As(V)_o] = 0.5\times10^{-4}$ M, Fe = 1.0×10^{-3} M, pH = 7.0, I = 0.01 M, orthokinetic coagulation particle range of $d_{min} = 1$ μm and $d_{max} = 32$ μm, $D_f = 2.0$)

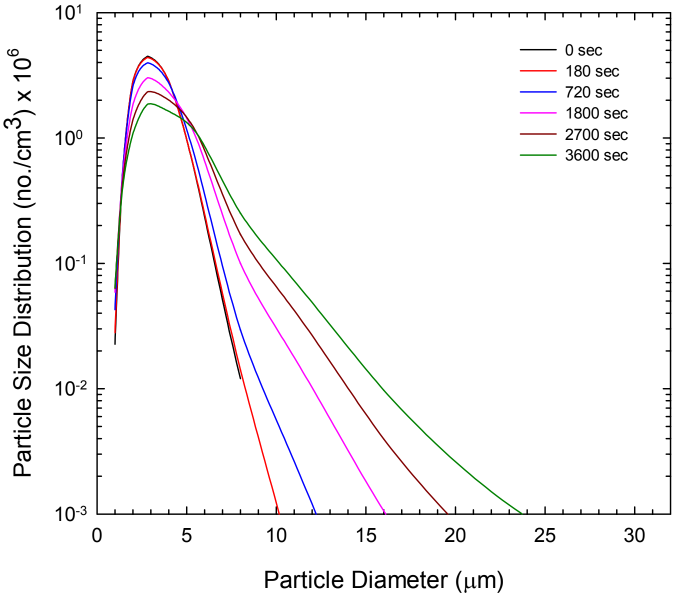

Figure 6.55 Particle size distribution ($[As(V)_o] = 0.5\times10^{-4}$ M, Fe = 1.0×10^{-3} M, pH = 7.0, I = 0.01 M, particle range of d_{min} = 1 μm and d_{max} = 32 μm, $D_f = 2.0$)

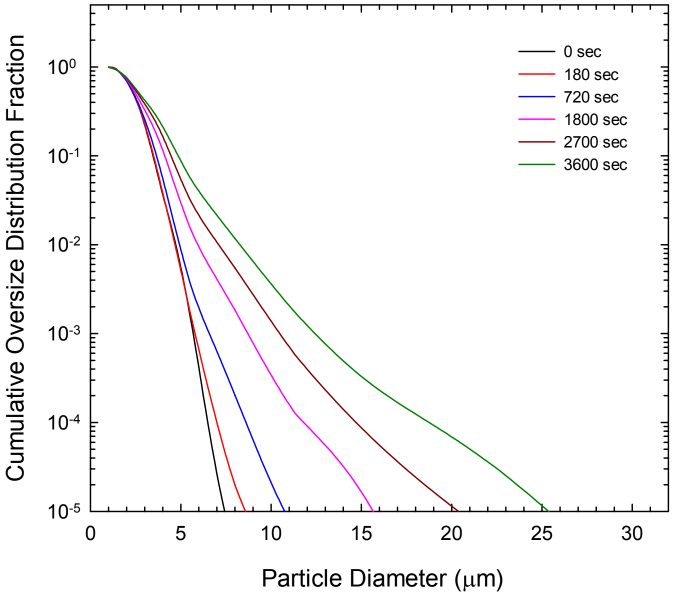

Figure 6.56 Cumulative oversize particle distribution ($[As(V)o] = 0.5\times10^{-4}$ M, Fe = 1.0×10^{-3} M, pH 7.0, I = 0.01 M, particle range of d_{min}= 1 μm and d_{max}= 32 μm, $D_f = 2.0$)

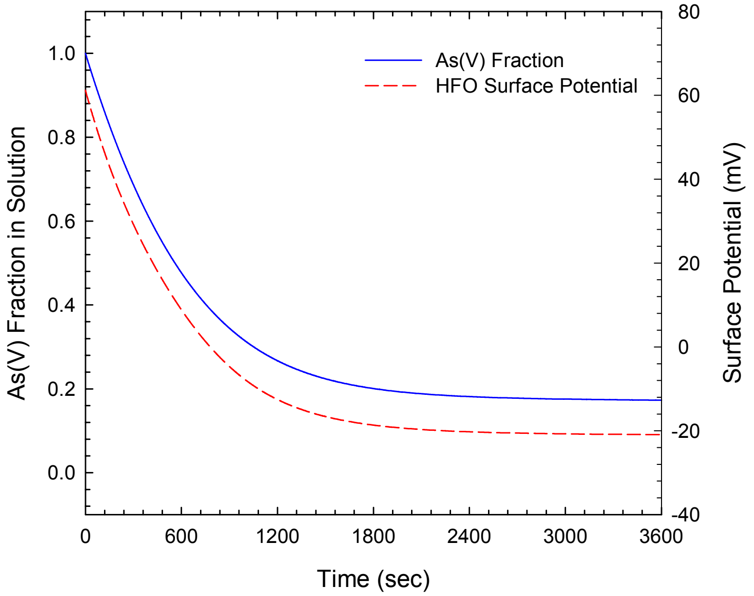

Figure 6.57 Kinetics of As(V) sorption and surface potential ([As(V)$_o$] = 1.0×10^{-4} M, Fe = 1.0×10^{-3} M, pH = 7.0, I = 0.01 M, orthokinetic coagulation particle range of d$_{min}$ = 1.0 μm and d$_{max}$ = 32.0 μm, D$_f$ = 2.0)

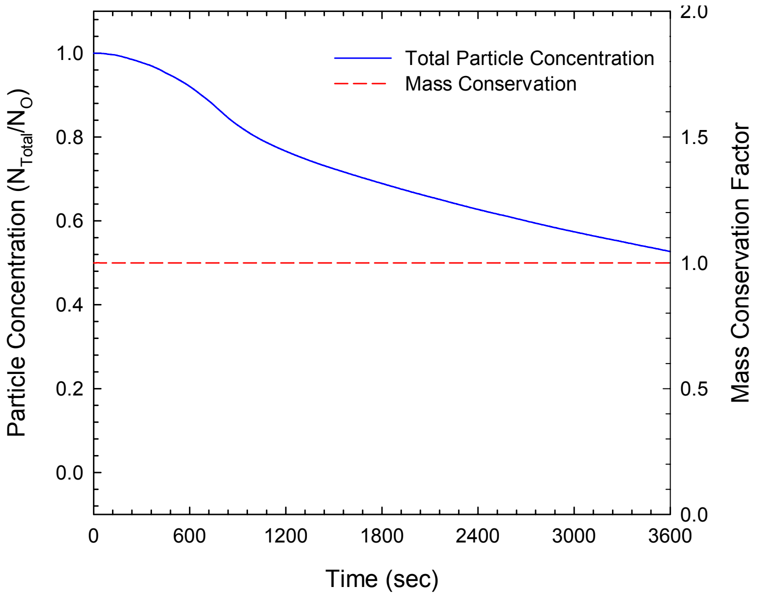

Figure 6.58 Coagulation kinetics ([As(V)$_o$] = 1.0×10^{-4} M, Fe = 1.0×10^{-3} M, pH = 7.0, I = 0.01 M, particle range of d$_{min}$ = 1 μm and d$_{max}$ = 32 μm, D$_f$ = 2.0)

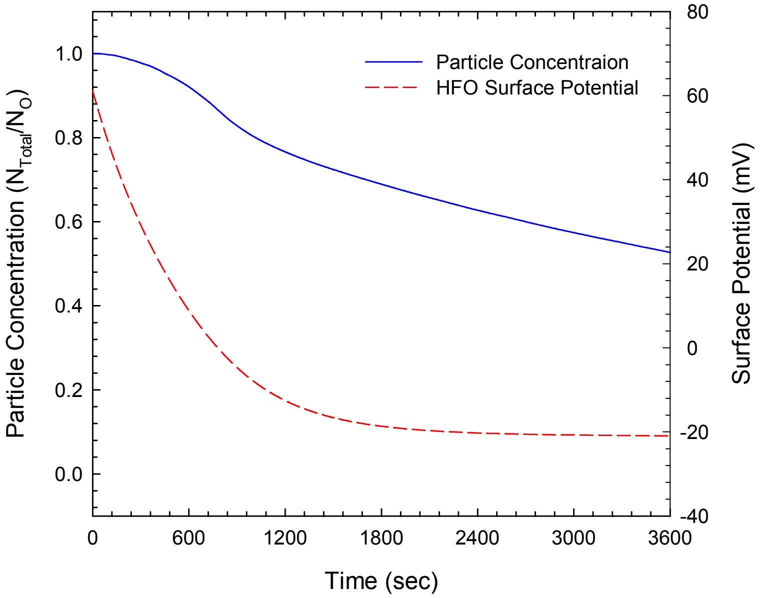

Figure 6.59 Kinetics of coagulation and surface potential ($[As(V)_o] = 1.0\times10^{-4}$ M, Fe = 1.0×10^{-3} M, pH = 7.0, I = 0.01 M, orthokinetic coagulation particle range of $d_{min} = 1$ µm and $d_{max} = 32$ µm, $D_f = 2.0$)

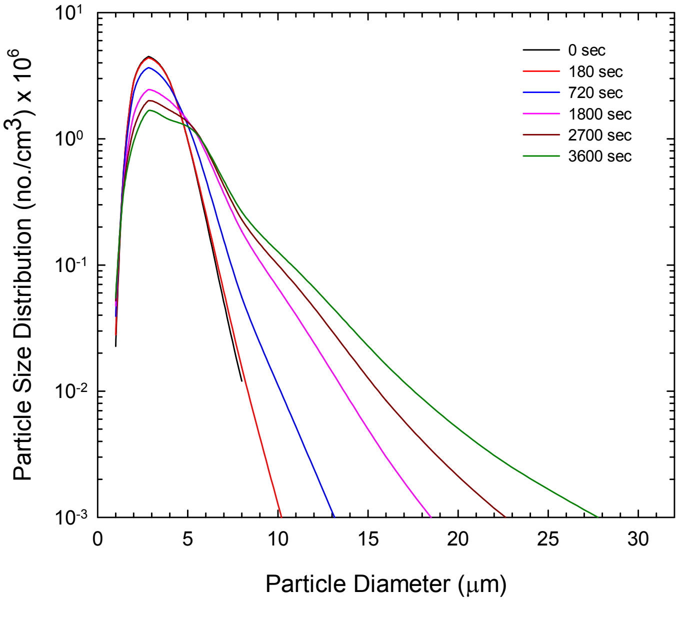

Figure 6.60 Particle size distribution ($[As(V)_o] = 1.0\times10^{-4}$ M, Fe = 1.0×10^{-3} M, pH = 7.0, I = 0.01 M, particle range of $d_{min} = 1$ µm and $d_{max} = 32$ µm, $D_f = 2.0$)

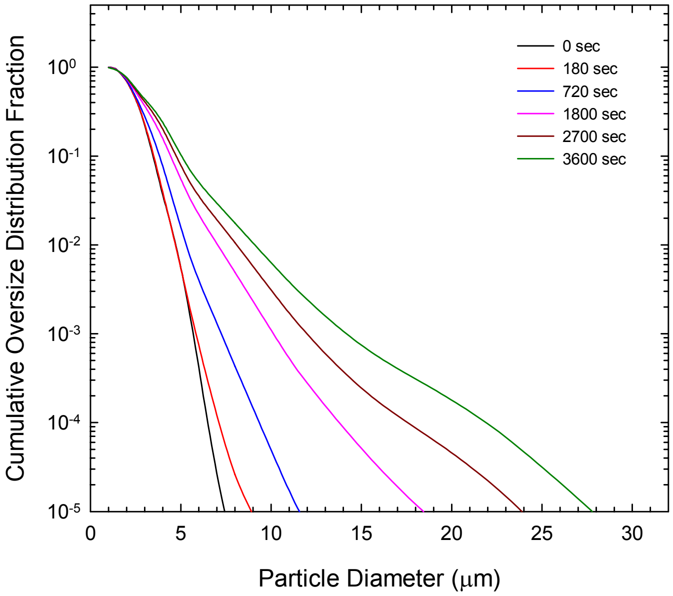

Figure 6.61 Cumulative oversize particle distribution ([As(V)$_o$] = 1.0×10^{-4} M, Fe = 1.0×10^{-3} M, pH 7.0, I = 0.01 M, particle range of d_{min}= 1 μm and d_{max}= 32 μm, D_f = 2.0)

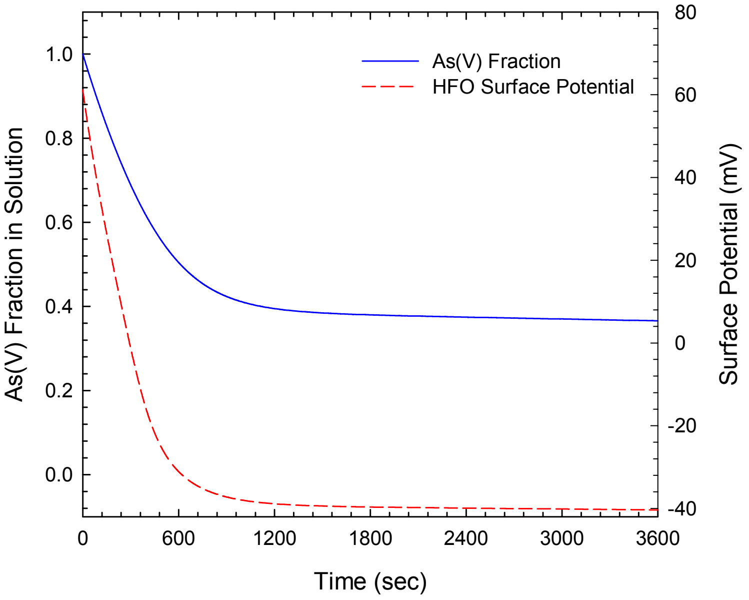

Figure 6.62 Kinetics of As(V) sorption and surface potential ([As(V)$_o$] = 2.0×10^{-4} M, Fe = 1.0×10^{-3} M, pH = 7.0, I = 0.01 M, orthokinetic coagulation particle range of d_{min} = 1.0 μm and d_{max} = 32.0 μm, D_f = 2.0)

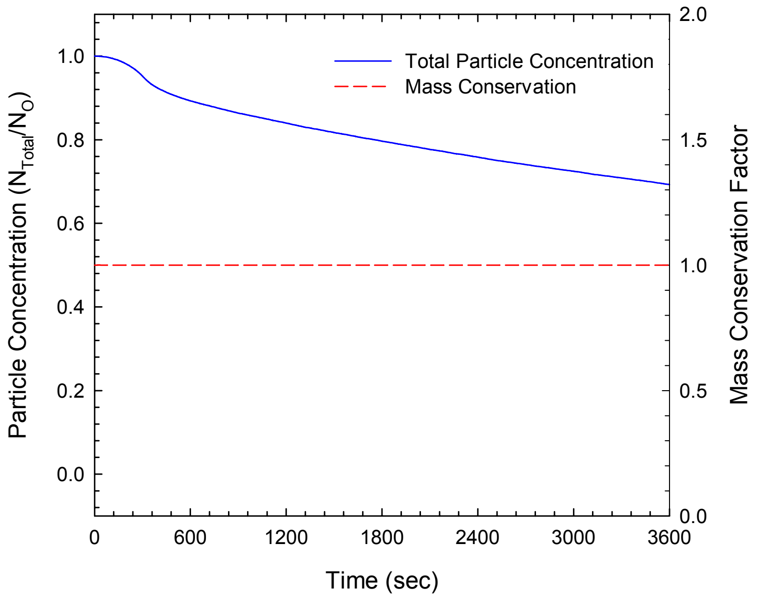

Figure 6.63 Coagulation kinetics ([As(V)$_o$] = 2.0×10^{-4} M, Fe = 1.0×10^{-3} M, pH = 7.0, I = 0.01 M, particle range of d_{min} = 1 μm and d_{max} = 32 μm, D_f = 2.0)

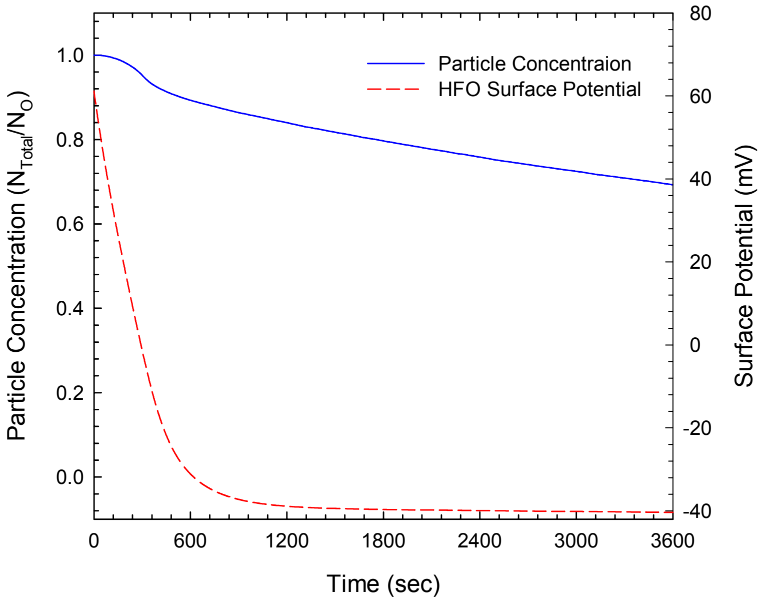

Figure 6.64 Kinetics of coagulation and surface potential ([As(V)$_o$] = 2.0×10^{-4} M, Fe = 1.0×10^{-3} M, pH = 7.0, I = 0.01 M, orthokinetic coagulation particle range of d_{min} = 1 μm and d_{max} = 32 μm, D_f = 2.0)

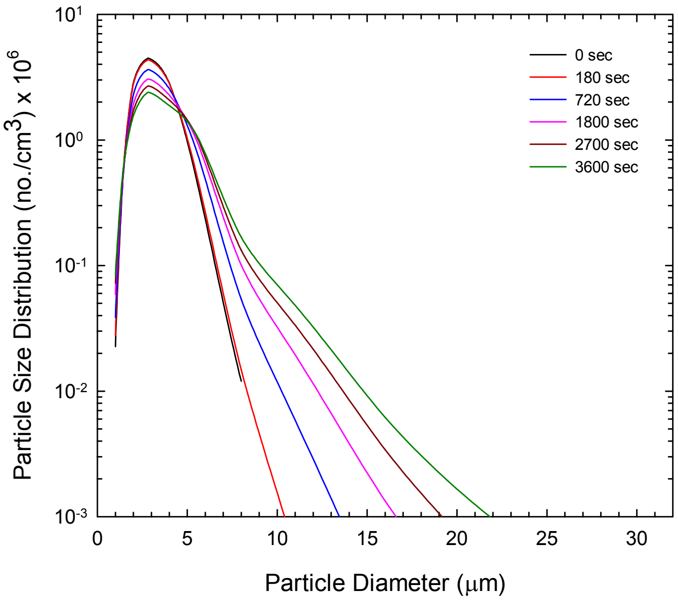

Figure 6.65 Particle size distribution ($[As(V)_o] = 2.0\times10^{-4}$ M, Fe = 1.0×10^{-3} M, pH = 7.0, I = 0.01 M, particle range of d_{min} = 1 μm and d_{max} = 32 μm,, $D_f = 2.0$)

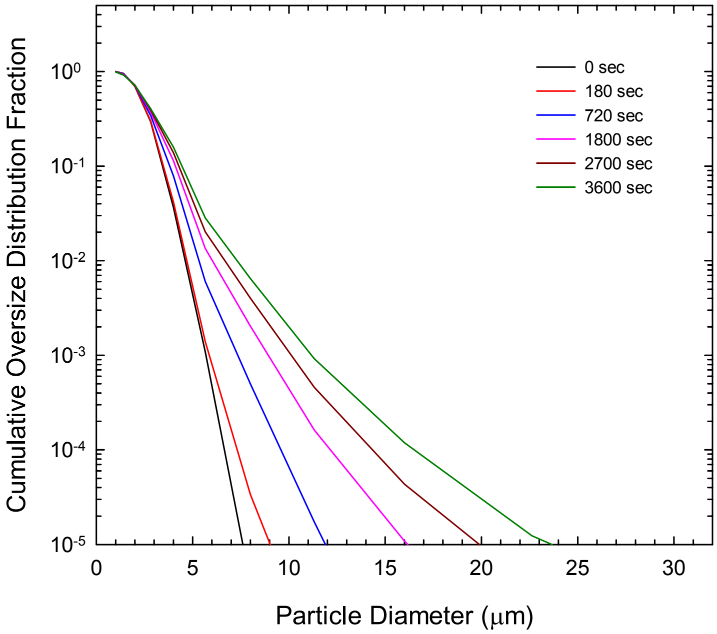

Figure 6.66 Cumulative oversize particle distribution ($[As(V)_o] = 2.0\times10^{-4}$ M, Fe = 1.0×10^{-3} M, pH 7.0, I = 0.01 M, particle range of d_{min}= 1 μm and d_{max}= 32 μm, $D_f = 2.0$)

6.6 Conclusions

In this study, this improved coagulation model developed was coupled with arsenic sorption equilibrium and kinetics on fractal colloids of hydrous ferric oxide (HFO). The model coupling was achieved by using the particle collision efficiency $\alpha(\mathrm{r}_i, \mathrm{r}_j)$ that is a main function for coupling a coagulation model with chemical reactions such as arsenic sorption. The study reviewed the collision efficiency studies for perikientic and orthokientic mechanisms and provided the numerical algorithms to calculate collision efficiency for two different transport mechanisms, depending on two colliding particle geometric sizes and surface potentials (charges). Finally, unified model that is coupled coagulation modeling with arsenic sorption kinetics consisting of a sorption diffusion transport model and surface complexation model was developed. Using the coupled model developed in this study, it was possible to predict arsenic sorption (equilibrium and kinetics) and colloid particle collision (surface potential time evolution, coagulation kinetics and particle size distributions) during the arsenic sorption and coagulation, simultaneously.

Using the computational algorithm proposed arsenic sorption kinetics and equilibrium onto hydrous ferric oxide (HFO) were unified with the perikinetic and orthokinetic coagulation models. It is expected that surface potential (charge) evolution due to arsenic sorption onto hydrous ferric oxide (HFO) can alter the particle size distribution and thus plays a key role in the orthokinetic coagulation process. Numerical simulation using the unified coagulation model provided the information of arsenic sorption kinetics, surface potential evolution, particle concentration, coagulation mass conservation, particle size distribution, and cumulative particle size distribution. Even though orthokinetic coagulation having the lower arsenic loading ratio could not be expected due to the relatively higher surface potential during all arsenic sorption reaction times, it could be possible that orthokinetic coagulation can occur at the relatively higher surface potential conditions of 35 mV. Although overall average collision efficiency can be introduced into the coagulation model analysis due to its easy handling, it is impossible to predict the coagulation kinetics. Especially, the average collision efficiency can not predict the lag-phase of the coagulation kinetics and particle size distribution evolution due to a higher surface potential than 20 mV (first lag-phase) or lower surface potential than -20 mV (second lag-phase). Therefore, it is recommended that collision efficiency be calculated for each time step of arsenic sorption and particle coagulation, rather than use an average collision efficiency.

Finally, it is anticipated that the unified coagulation model coupled with arsenic sorption kinetics and equilibrium modes will provide a more complete understanding of arsenic removal mechanism and its application to water and wastewater treatment. For this purpose, arsenic sorption modeling and improved coagulation modeling was used to develop this coupled model.

CHAPTER VII

SUMMARY AND CONCLUSIONS

The current lowering of the maximum contaminant level (MCL) established by the USEPA for arsenic in drinking water is 10 ppb. Thus, the need for adequate methods for removal of arsenic has become urgent. The sorption of the toxic metals on a hydrous metal oxide (HMO) is the most practical method for removing the toxic compounds from contaminated water. However, the hydrous metal oxide particle behavior, such as aggregation and break-up in the applied fluid flow, are not easily predicted especially when arsenic coexists within the fluid system applied. This surface behavior is due to particle surface charge evolution with time resulting from arsenic sorption onto the particle surface. To achieve predictive capability for the complex environmental system with coagulation and metal sorption, a unified coagulation model coupled with arsenic sorption should be developed. A unified coagulation model coupled with arsenic sorption was achieved by the following steps.

First, an improved discretized population balance equation (PBE) was developed to obtain the exact solution of a conventional coagulation model coupled with chemical reactions (i.e., arsenic sorption kinetics and equilibrium). Furthermore, relatively little attention has been paid to fractal aggregate modeling including agglomeration and fragmentation. Spherical particle coalescence applies only to ideal bubbles and droplets and most particle aggregates has been found to be fractal, especially in solid colloidal particle coagulation. Thus, fractal aggregate coagulation via the higher numerical stability and accuracy was needed for realistic simulation.

Second, a surface complexation equilibrium model using a thermodynamic equilibrium database and a sorption kinetic model using diffusion mass transport was introduced. This was to predict arsenic sorption behavior onto the hydrous metal oxide surface and particle collision rate resulting in charged colloid particle coagulation phenomenon.

Third, an improved coagulation model coupled with arsenic sorption kinetics and equilibrium was developed. The collision efficiency $\alpha(\mathrm{r}_i, \mathrm{r}_j)$ between colliding hydrous metal oxide particles was calculated by aid of the surface charge/potentials on the hydrous metal oxide particles.

Finally, introducing the collision efficiency $\alpha(\mathrm{r}_i, \mathrm{r}_j)$ into the improved coagulation model for fractal aggregate yielded a unified improved coagulation model coupled with arsenic sorption kinetics and equilibrium. Thus, an improved unified coagulation model, consisting of a simplified non-uniform discretized population balance equations for fractal aggregate and arsenic sorption reactions, could provide high statistical accuracy, numerical stability, and computational efficiency to enhance predictive capability for behavior of arsenic sorption and fractal colloid particle aggregation and break-up, simultaneously.

In the course of the investigation several discoveries were made. These discoveries are outlined below.

(1) A variety of modeling techniques for the population balances resulting from particle coagulation were examined. The simplified models using the non-uniform discretization scheme were compared to uniform discrete models. Further, new algorithms that incorporate a non-uniform discretization were developed. In the course of the investigation the new algorithms were found to be substantial improvements in terms of computational time over the other models and compared favorably to the discrete/continuous model with respect to accuracy. New probability distribution functions for aggregates produced in non-uniform discrete coagulation modeling were derived and incorporated into the population balance equations. These new algorithms made it possible to simulate fractal aggregate coagulation with high accuracy, perfect mass conservation and exceptional computational efficiency. Parameter sensitivity analysis showed that a break-up kernel does not influence total particle concentration within the limited range of having the break-up coefficient less than collision efficiency, but does influence the particle size distribution and coagulation patterns. An aggregate break-up study with various kernel parameters indicated that break-up rate was more influenced by particle volume and not size class or diameter as previously suspected. The new probability distribution functions were found to be useful in fractal aggregation modeling via the higher numerical stability and accuracy. The new particle population model was shown in the investigation to be superior to all of the other models, having mass conservation factor of over 0.99 and computation time of 3.125×10^{-2} sec, thus the new coagulation model can be used to develop predictive simulations for coagulation in computational fluid dynamics and reaction modeling.

(2) An improved particle coagulation model previously developed was extended to an adjustable geometric size interval (*q*), where *q* is a volume ratio of class *k*+1 particles to class *k* particles ($\upsilon_{k+1}/\upsilon_k = q$). This model was compared with exact numerical solutions of continuous (uniform discretized) population balance equations and applied to simulate the particle aggregation and breakup with fractal dimensions lower than 3. Further, comparisons were made using the fractal aggregate collision mechanisms of orthokinetic coagulation with the inclusion of flow induced breakup. In the course of the investigation the new algorithm was found to be a substantial improvement in terms of numerical accuracy, stability, and computational efficiency over the continuous model. This model was verified with the time derivative of the zero and first moments to show mass conservation and compared with previous analytical and numerical solutions. Also, the self-preserving distribution test was conducted by using size-independent and size-dependent kernels. After direct numerical simulations (DNS), the proposed model was found to have excellent agreement with the analytical and continuous numerical solutions. In addition, this proposed model was converted to a dimensionless form to enhance computational efficiency in order to be coupled with computational fluid dynamic solutions in the future. Furthermore, a parameter estimation scheme was created to computationally determine the two key parameters, the collision efficiency $\alpha(\mathrm{r}_i, \mathrm{r}_j)$ and the break-up coefficient (K_B), from orthokinetic experimental data. This parameter estimation scheme was able to compute the coefficients in the coagulation model rapidly, especially in particle systems having a fractal aggregate structure. In addition, an attempt to find an optimum graphical method for representing the two

different results (non-uniform discretized and continuous populations) on an identical 2D plane was conducted and the results indicate that the particle cumulative population distribution curve is convenient to compare these results due to different aggregate class size scales. Using the reproduction of a continuous distribution from discrete data, it was concluded that this method has close agreement between non-uniform discretized and continuous data. This new algorithm made it possible to solve fractal particle aggregation and break-up problems with high accuracy, perfect mass conservation and exceptional computational efficiency.

(3) To enhance the predictive capability for arsenic sorption onto metal oxy-hydroxide surfaces, a surface complexation equilibrium model using a thermodynamic equilibrium database and a sorption kinetic model using diffusion mass transport were introduced in this study. A surface complexation model was incorporated to predict arsenic sorption equilibrium behavior (i.e., pH envelop and isotherm). A set of equations representing the surface complexation model, which are related to arsenic acid-base reactions, hydrous ferric oxide surface protonation/deprotonation, and inner-sphere monodentate surface complexations for arsenic sorption on HFO surfaces, was solved with a public domain computer program PHREEQC. Further, the introduced surface complexation model was coupled with an arsenic sorption kinetic model using the sorption local equilibrium assumption to provide easy to use software that establishes predictive capability for the water treatment community. To verify two arsenic sorption equilibrium and kinetic models, the model results were compared to literature experimental data such as arsenic pH envelop data for equilibrium model verification

and arsenic sorption rate data for kinetic model. Thus, the improved arsenic sorption modeling technique coupled with arsenic sorption kinetics and equilibrium could provide enhanced predictive capability for the exact arsenic sorption behavior especially related to arsenic sorption kinetics, equilibrium, and hydrous ferric oxide surface charge/potential evolution with reaction time, as well as required sorption process design parameters, sorption media capacity, sorption media doses, sorption media operation life-times, residuals production, and sorption process operating costs. Furthermore, the surface charge/potential evolution with reaction time can be used to couple the two models of arsenic sorption and coagulation. That is, a unified coagulation model is coupled with arsenic sorption using surface charge (potential) which is one of the major variables in collision efficiency calculation.

(4) An improved discretized population balance equation (PBE) proposed in this study, which has new probability distribution functions for fractal aggregates produced in non-uniform discrete coagulation modeling, was coupled with arsenic sorption equilibrium and kinetics on fractal colloids of hydrous ferric oxide. The model coupling was achieved by using the colloid particle collision efficiency $\alpha(\mathrm{r}_i, \mathrm{r}_j)$ as one component of the aggregation rate constant ($k_{agg} = \alpha\beta$) and a main function for coupling coagulation model with chemical reactions such as arsenic sorption. The study reviewed the collision efficiency studies for perikientic and orthokientic mechanisms and provided the numerical algorithms to calculate collision efficiency for two different transport mechanisms, depending on two colliding particle geometric sizes and surface potentials or surface charges. Finally, a unified model that couples coagulation modeling with

arsenic sorption kinetics consisting of sorption diffusion transport and surface complexation was developed. Using the coupled model developed in this study, it was possible to predict arsenic sorption (equilibrium and kinetics) and particle collision rate (surface potential time evolution, coagulation kinetics and particle size distributions) during the arsenic sorption and coagulation, simultaneously.

From the investigation, it is anticipated that the unified coagulation model coupled with arsenic sorption kinetics and equilibrium will provide a more complete understanding of arsenic removal mechanism and its application to water/wastewater treatment. Further, this coupled model can be applied to other water and wastewater treatment systems combined with sorption and filtration processes. These combined processes can be optimized by the coupled model that was developed in this study. By simulating the arsenic sorption and particle size distribution as a pretreatment before filtration (sand filtration or membrane filtration), the overall arsenic removal efficiency and operation cost can be estimated.

REFERENCES

Adachi, Y., Cohen, C., and Fokkink, R. (1994). "Kinetics of Turbulent Coagulatioin Studied by Means of End-Over-End Rotation." *J. Colloid Interface Sci.*, 165, 310-317.

Adler, P. M. (1981a). "Heterocoagulation in Shear Flow." *J. Colloid Interface Sci.*, 83, 106-115.

Adler, P. M. (1981b). "Interactions of Unequal Spheres - 1. Hydrodynamic Interaction: Colloidal Forces." *J. Colloid Interface Sci.*, 84(2), 461-474.

Amal, R., Coury, J. R., Raper, J. A., Walsh, W. P., and Waite, T. D. (1990a). "Structure and Kinetics of Aggregating Colloidal Haematite." *Colloids and Surfaces A*, 46, 1-19.

Amal, R., Gazeau, D., and Waite, T. D. (1994). "Small Angle X-Ray Scattering of Hematite Aggregates." *Part. Part. Syst. Charact.*, 11, 315-319.

Amal, R., Raper, J., and Waite, T. D. (1990b). "Fractal Structure of Hematite Aggregates." *J. Colloid and Interface Sci.*, 140(1), 158-168.

Anderson, M. A., Ferguson, J. F., and Gavis, J. (1976). "Arsenate Adsorption on Amorphous Aluminum Hydroxide." *J. Colloid Interface Sci.*, 54(3), 391-399.

Anderson, M. A., and Malotky, D. T. (1979). "The Adsorption of Protolyzable Anions on Hydrous Oxides at the Isoelectric pH." *J. Colloid Interface Sci.*, 72, 413-427.

Arai, Y., Elzinga, E. J., and Sparks, D. L. (2001). "X-Ray Absorption Spectroscopic Investigation of Arsenite and Arsenate Adsorption at the Aluminum Oxide-Water Interface." *J. Colloid Interface Sci.*, 235, 80-88.

Argaman, Y., and Kaufman, W. J. (1970). "Turbulent and Flocculation." *J. Sanit. Eng. Div. ASCE*, 96, 223-241.

Asnaghi, D., Carpineti, M., Giglio, M., and Sozzi, M. (1992). "Coagulation Kinetics and Aggregate Morphology in the Intermediate Regimes between Diffusion-Limited and Reaction-Limited Cluster Aggregation." *Phys. Rev. A*, 45(2), 1018-1023.

Aubert, C., and Cannell, D. S. (1986). "Restructuring of Colloidal Silica Aggregates." *Phys. Rev. Lett.*, 56(7), 738-741.

Axe, L., and Anderson, P. R. (1995). "Sr Diffusion and Reaction within Fe Oxides: Evaluation of the Rate-Limitting Mechanism for Sorption." *J. Colloid and Interface Sci.*, 175, 157-165.

Axford, S. D. T. (1996). "Non-Preserving Cluster Size Distributions in the Initial Stages of Orthokinetic Aggregation." *J. Chem. Soc. Faraday Trans.*, 92, 1007-1016.

Axford, S. D. T. (1997). "Aggregation of Colloidal Silica: Reaction-Limited Kernel, Stability Ratio and Distribution Moments." *J. Chem. Soc. Faraday Trans.*, 93(2), 303-311.

Axford, S. D. T., and Herrington, T. M. (1994). "Determination of Aggregate Structures by Combined Light-Scattering and Rheological Studies." *J. Chem. Soc. Faraday Trans.*, 90(14), 2085-2093.

Ballal, B. Y., and Rivlin, R. S. (1976). "Flow of a Newtonian Fluid Between Eccentric Rotating Cylinders." *Arch. Rational Mech. Anal.*, 62, 237-294.

Batchelor, G. K. (1976). "Brownian Diffusion of Particles with Hydrodynamic Interaction." *J. Fluid Mech.*, 74, 1-29.

Batchelor, G. K., and Green, J. T. (1972). "The Hydrodynamic Interaction of Two Small Freely-Moving Spheres in a Linear Flow Field." *J. Fluid Mech.*, 56, 375-400.

Batterham, R. J., Hall, J. S., and Barton, G. (1981). "Pelletizing Kinetics and Simulation of Full Scale Balling Circuits." *International Symposium on Agglomeration (3rd)*, Nürnberg, A136-A150.

Biggs, C. A., and Lant, P. A. (2002). "Modeling Activated Sludge Flocculation Using Population Balances." *Powder Technol.*, 124, 201-211.

Boer, G. B. J., Hoedemakers, G. F. M., and Thoenes, D. (1989). "Coagulation in Turbulent Flow." *Chem. Eng. Res. Des.*, 67, 301-307.

Bolle, G., Cametti, C., Codastefano, P., and Tartaglia, P. (1987). "Kinetics of Salt-Induced Aggregation in Polystyrene Lattices Studied by Quasielastic Light Scattering." *Phys. Rev. A*, 35(2), 837-841.

Borisenko, A. I., and Tarapov, I. E. (1980). *Vector and Tensor Analysis with Applications*. Dover Publications, Inc., New York.

Bostick, B. C., and Fendorf, S. (2003). "Arsenite Sorption on Troilite (FeS) and Pyrite (FeS_2)." *Geochim. Cosmochim. Acta*, 67(5), 909-921.

Bowell, R. J. (1994). "Sorption of Arsenic by Iron Oxides and Oxyhydroxides in Soils."

Applied Geochemistry, 9, 279-286.

Bowen, W. R., and Jenner, F. (1995). "The Calculation of Dispersion Forces for Engineering Applications." *Adv. Colloid Interface Sci.*, 56, 201-243.

Brady, N. C., and Weil, R. R. (2002). *The Nature and Properties of Soil,* 13th edition, Prentice Hall, Upper Saddle River, NJ.

Brenner, H., and O'Neill, M. E. (1972). "On the Stokes Resistance of Multiparticle Systems in a Linear Shear Field." *Chem. Eng. Sci.*, 27, 1421-1439.

Brewster, M. D. (1992). "Removing Arsenic from Contaminated Wastewater." *Wat. Environ. Technol.*, 4(11), 54-57.

Burns, J. L., Yan, Y., Jameson, G. J., and Biggs, S. (1997). "A Light Scattering Study of the Fractal Aggregation Behavior of a Model Colloidal System." *Langmuir*, 13, 6413-6420.

Camp, T. R., and Stein, P. C. (1943). "Velocity Gradients and Internal Work in Fluid Motion." *J. Boston Sociey of Civil Engineers*, 30, 219-237.

Chakraborti, R. K., Atkinson, J. F., and Benschoten, J. E. (2000). "Characterization of Alum Floc by Image Analysis." *Environ. Sci. Technol.*, 34, 3969-3676.

Chakraborti, R. K., Gardner, K. H., Atkinson, J. F., and Benschoten, J. E. (2003). "Changes in Fractal Dimension during Aggregation." *Water Research*, 37, 873-883.

Chen, W., Fisher, R. R., and Berg, J. C. (1990). "Simulation of Particle Size Distribution in an Aggregation-Breakup Process." *Chem. Eng. Sci.*, 45(9), 3003-3006.

Cheng, R. C., Liang, S., Wang, H., and Beuhler, M. D. (1994). "Enhanced Coagulation for Arsenic Removal." *J. AWWA*, 86(9), 79-90.

Chin, C. J., Yiacoumi, S., and Tsouris, C. (1998). "Shear-Induced Flocculation of Colloidal Particles in Stirred Tanks." *J. Colloid Interface Sci.*, 206, 532-545.

Clark, M. M. (1985). "Critique of Camp and Stein's RMS Velocity Gradient." *J. Environ. Eng., ASCE*, 111, 741-754.

Clark, M. M., and Flora, J. R. V. (1991). "Floc Restructuring in Varied Turbulent Mixing." *J. Colloid Interface Sci.*, 147, 407-421.

Constantinides, A., and Mostoufi, N. (1999). *Numerical Methods for Chemical*

Engineers with MATLAB Applications. Prentice Hall, Upper Saddle River, NJ.

Cornell, R. M., Giovanoli, R., and Schneider, W. (1989). "Review of the Hydrolysis of Iron(III) and the Crystallization of Amorphous Iron(III) Hydroxide Hydrate." *J. Chem. Tech. Biotechnol.*, 46, 115-134.

Coulaloglou, C. A., and Tavlarides, L. L. (1977). "Description of Interaction Processes in Agitated Liquid-Liquid Dispersions." *Chem. Eng. Sci.*, 32, 1289-1297.

Crittenden, J. C., Hand, D. W., Arora, H., and Lykins, B. W. (1987). "Design Considerations for GAC Treatment of Organic Chemicals." *J. AWWA*, 79(1), 74-82.

Curtis, A. S. G., and Hocking, L. M. (1969). "Collision Efficiency of Equal Spherical Particles in a Shear Flow." *Trans. Faraday Soc.*, 66, 1381-1390.

Daus, B., Wennrich, R., and Weiss, H. (2004). "Sorption Materials for Arsenic Removal from Water: A Comparative Study." *Water Research*, 38, 2948-2954.

Davis, J. A., and Leckie, J. O. (1978). "Surface Ionization and Complexation at the Oxide/Water Interface 2. Surface Properties of Amorphous Iron Oxyhydroxide and Adsorption of Metal Ions." *J. Colloid Interface Sci.*, 67(1), 90-107.

Delichatsios, M. A., and Probstein, R. F. (1975). "Coagulation in Turbulent Flow: Theory and Experiment." *J. Colloid Interface Sci.*, 51, 394-405.

Diemer, R. B., and Olson, J. H. (2002a). "A Moment Methodology for Coagulation and Breakage Problems: Part 1 - Analytical Solution of the Steady-State Population Balance." *Chem. Eng. Sci.*, 57, 2193-2209.

Diemer, R. B., and Olson, J. H. (2002b). "A Moment Methodology for Coagulation and Breakage Problems: Part 3 - Generalized Daughter Distribution Functions." *Chem. Eng. Sci.*, 57, 4187-4198.

Dixit, S., and Hering, J. G. (2003). "Comparison of Arsenic(V) and Arsenic(III) Sorption onto Iron Oxide Minerals: Implications for Arsenic Mobility." *Environ. Sci. Technol.*, 37,4182-4189

Drake, R. L. (1972). "A General Mathematical Survey of the Coagulation Equation." *Topics in Current Aerosel Research*, G. M. Hidy and J. R. Brock, eds., Pergamon, New York, 201-376.

Driehaus, W., Jekel, M., and Hildebrandt, U. (1998). "Granular Ferric Hydroxide - A New Adsorbent for the Removal of Arsenic from Natural Water." *J. Water Supp. Res.*

Technol. - Aqua, 47, 30-35.

Driehaus, W., Seith, R., and Jekel, M. (1995). "Oxidation of Arsenate(III) with Manganese Oxides in Water Treatment." *Water Research*, 29(1), 297-305.

Dzombak, D. A., and Morel, F. M. M. (1990). *Surface Complexation Modeling*. Wiley Interscience Publication, New York.

Edwards, M. (1994). "Chemistry of Arsenic Removal During Cogulatioin and Fe-Mn Oxidation." *J. AWWA*, 86(9), 64-78.

Elimelch, M., Gregory, J., Jia, X., and Williams, R. A. (1995). *Particle Deposition and Aggregation*. Butterworth Heinemann, Oxford [England]; Boston.

Ernest, A. N., Bonner, J. S., and Autenrieth, R. L. (1991). "Model Parameter Estimation for Particle Transport." *J. Environ. Eng., ASCE*, 117(5), 573-594.

Farley, K. J., Dzombak, D. A., and Morel, F. M. M. (1985). "A Surface Precipitation Model for the Sorption of Cations on Metal Oxides." *J. Colloid and Interface Sci.*, 106, 226-242.

Fendorf, S. E., Eick, M. J., Grossl, P., and Sparks, D. L. (1997). "Arsenate and Chromate Retention Mechanisms on Goethite. 1.Surface Structure." *Environ. Sci. Technol.*, 31(2), 315-320.

Ferguson, J. F., and Anderson, M. A. (1974). "Chemical Forms of Arsenic in Water Supplies and Their Removal." *Chemistry of Water Supply, Treatment, and Distribution*, A. J. Rubin, ed., Ann Arbor Science, 137-158.

Fields, K. A., Chen, A., and Wang, L. (2000). "Arsenic Removal from Drinking Water by Coagulation/Filtration and Lime Softening Plants." *EPA/600/R-00/063*, EPA.

Filella, M., and Buffle, J. (1993). "Factors Controlling the Stability of Submicron Colloids in Natural Waters." *Colloids and Surfaces A*, 73, 255-273.

Flesch, J. C., Spicer, P. T., and Pratsinis, S. E. (1999). "Laminar and Turbulent Shear-Induced Flocculation of Fractal Aggregates." *AIChE J.*, 45(5), 1114-1124.

Fox, K. R. (1989). "Field Experience with Point-of-Use Treatment Systems for Arsenic Removal." *J. AWWA*, 81(2), 94-101.

Frank, P., and Clifford, D. (1986). "Arsenic(III) Oxidation and Removal from Drinking Water." EPA.

Friedlander, S. K. (2000). *Smoke, Dust, and Haze: Fundamentals of Aerosol Dynamics*. Oxford University Press, New York.

Frost, R. R., and Griffin, R. A. (1977). "Effect of pH on Adsorption of Arsenic and Selenium from Landfill Leachate by Clay Minerals." *Soil Sci. Sco. Am. J.*, 41, 53-57.

Fuchs, N. (1934). "Uber die Stabilitat und Aufladung der Aerosole." *Z. Physk.*, 89, 736-743.

Fuller, C. C., Davis, J. A., and Waychunas, G. A. (1993). "Surface Chemistry of Ferrihydrite: Part 2. Kinetics of Arsenic Adsorption and Coprecipitation." *Geochimica et Cosmochimica Acta*, 57, 2271-2282.

Gao, Y., and Mucci, A. (2001). "Acid Base Reactions, Phosphate and Arsenate Complexation, and Their Competitive Adsorption at the Surface of Geothite in 0.7 M NaCl Solution." *Geochim. Cosmochim. Acta*, 65(14), 2361-2378.

Gardner, K. H., Theis, T. L., and Young, T. C. (1998). "Colloid Aggregation: Numerical Solution and Measurements." *Colloids and Surfaces A*, 141, 237-252.

Gelbard, F., and Seinfeld, J. H. (1978). "Numerical Solution of the Dynamic Equation for Particulate Systems." *J. Computational Physics*, 28, 357-375.

Gelbard, F., Tambour, Y., and Seinfeld, J. H. (1980). "Sectional Representation of Simulating Aerosol Dynamics." *J. Colloid Interface Sci.*, 76, 541-556.

Ghosh, M. M., and Yuan, J. R. (1987). "Adsorption of Inorganic Arsenic and Organoarsenicals on Hydrous Oxides." *Environmental Progress*, 6(3), 150-157.

Glasgow, L. A. (1989). "Effects of the Physicochemical Environments on Floc Properties." *Chem. Eng. Prog.*, 85, 51-55.

Goldberg, S. (1986). "Chemical Modeling of Arsenate Adsorption on Aluminum and Iron Oxide Minerals." *Soil Sci. Sco. Am. J.*, 50, 1154-1157.

Goldberg, S., and Johnston, C. T. (2001). "Mechanisms of Arsenic Adsorption on Amorphous Oxides Evaluated Using Macroscopic Measurements, Vibrational Spectroscopy, and Surface Complexation Modeling." *J. Colloid Interface Sci.*, 234, 204-216.

Goldberg, S., Lebron, I., Suarez, D. L., and Hinedi, Z. R. (2001). "Surface Characterization of Amorphous Aluminum Oxides." *Soil Sci. Soc. Am. J.*, 65, 78-86.

Gorczyca, B., and Ganczarczyk, J. (1996). "Image Analysis of Alum Coagulated Mineral Suspensions." *Environmental Technology*, 17, 1361-1369.

Graber, S. D. (1994). "A Critical Review of the Use of G-Values (RMS Velocity Gradient) in Environmental Engineering." *Developments in Theoretical and Applied Mechanics*, XVII, 533-556.

Grafe, M., Eick, M. J., and Grossl, P. R. (2001). "Adsorption of Arsenate (V) and Arsenite (III) on Goethite in the Presence and Absence of Dissolved Organic Carbon." *Soil Sci. Sco. Am. J.*, 65(6), 1680-1687.

Gregor, J. (2001). "Arsenic Removal during Conventional Aluminum-Based Drinking-Water Treatment." *Water Research*, 35(7), 1659-1664.

Grossl, P. R., Eick, M. J., Sparks, D. L., and Ainsworth, C. C. (1997). "Arsenate and Chromate Retention Mechanisms on Goethite. 2.Kinetic Evaluation Using a pressure-Jump Relaxation Technique." *Environ. Sci. Technol.*, 31(2), 321-326.

Gulledge, J. H., and O'Connor, J. T. (1973). "Removal of Arsenic (V) from Water by Adsorption on Aluminum and Ferric Hydroxides." *J. AWWA*, 65(8), 548-552.

Gupta, S. K., and Chen, K. Y. (1978). "Arsenic Removal by Adsorption." *J. WPCF*, 50(3), 493-506.

Hackley, V. A., and Anderson, M. A. (1989). "Effects of Short-Range Forces on the Long-Range Structure of Hydrous Iron Oxide Aggregates." *Langmuir*, 5, 191-198.

Han, M. Y., and Lawler, D. F. (1992). "The (Relative) Insignificance of G in Flocculation." *J. AWWA*, 84, 79-91.

Han, M. Y., and Lee, H. G. (2002). "Collision Efficiency Factor in Brownian Coagulation (a_{Br}): Calculation and Experimental Verification." *Colloids and Surfaces A*, 202, 23-31.

Harper, T. R., and Kingham, N. W. (1992). "Removal of Arsenic from Wastewater Using Chemical Precipitation Methods." *Wat. Environ. Research*, 64(3), 200-203.

Harrison, J. B., and Berkheiser, V. E. (1982). "Anion Interactions with Freshly Prepared Hydrous Iron Oxides." *Calys and Clay Minerals*, 30(2), 97-102.

Hering, J. G., Chen, P., Wilkie, J. A., and Elimelch, M. (1997). "Arsenic Removal from Drinking Water during Coagulation." *J. Environ. Eng., ASCE*, 123, 800-807.

Hering, J. G., Chen, P., Wilkie, J. A., Elimelch, M., and Liang, S. (1996). "Arsenic Removal by Ferric Chloride." *J. AWWA*, 88(4), 155-167.

Herrington, T. M., and Midmore, B. R. (1993). "Investigation of Scaling Effects in the Aggregation of Dilute Kaolinite Suspensions by Quasi-Elastic Light Scattering." *Colloids and Surfaces A*, 70, 199-202.

Hiemenz, P. C., and Rajagopalan, R. (1997). *Principles of Colloid and Surface Chemistry*, 3rd edition, Marcel Dekker, Inc, New York.

Hiemstra, T., and van Riemsdijk, W. H. (1999). "Surface Structure Ion Adsorption Modeling of Competitive Binding of Oxyanions by Metal (Hydr)oxides." *J. Colloid Interface Sci.*, 210, 182-193.

Higashitani, K., Ogawa, R., and Hosokawa, G. (1982). "Kinetic Theory of Shear Coagulation for Particles in a Viscous Fluid." *J. Chem. Engr. Japan*, 15(4), 299-304.

Higashitani, K., Yamauchi, K., Matsuno, Y., and Hosokawa, G. (1983). "Turbulent Coagulation of Particles Dispersed in a Viscous Fluid." *J. Chem. Engr. Japan*, 16(4), 299-304.

Hill, P. J., and Ng, K. M. (1995). "New Discretization Procedure for the Breakage Equation." *AIChE J.*, 41(5), 1204-1216.

Hill, P. J., and Ng, K. M. (1996). "New Discretization Procedure for the Agglomeration Equation." *AIChE J.*, 42(3), 727-741.

Ho, N. F. H., and Higuchi, W. I. (1968). "Preferential Aggregation and Coalescence in Heterodispersed System." *J. Pharmaceutical Sci.*, 57(3), 436-442.

Hoekstra, L. L., Vreeker, R., and Agterof, W. G. (1992). "Aggregation of Colloidal Nickel Hydroxycarbonate Studied by Light Scattering." *J. Colloid Interface Sci.*, 151, 17-25.

Hofmann, A., Pelletier, M., Michot, L., Stradner, A., Schurtenberger, P., and Kretzschmar, R. (2004). "Characterization of the Pores in Hydrous Ferric Oxide Aggregates Formed by Freezing and Thawing." *J. Colloid and Interface Sci.*, 271, 163-173.

Hogg, R., Healy, T., and Furstenau, D. W. (1966). "Mutual Coagulation of Colloidal Dispersions." *Trans. Faraday Soc.*, 62, 1638-1651.

Honig, E. P. (1971). "Effect of Hydrodynamic Interaction of the Coagulation Rate of Hydrophobic Colloids." *J. Colloid Interface Sci.*, 36(1), 97-109.

Hounslow, M. J., Ryall, R. L., and Marshall, V. R. (1988). "A Discretized Population Balance for Nucleation, Growth, and Aggregation." *AIChE J.*, 34(11), 1821-1832.

Hsia, T. H., Lo, S. L., and Lin, C. F. (1992). "As(V) Adsorption on Amorphous Iron Oxide: Triple Layer Modeling." *Chemosphere*, 25(12), 1825-1837.

Hsia, T. H., Loa, S. L., Lid, C. F., and Leeb, D. Y. (1994). "Characterization of Arsenate Adsorption on Hydrous Iron Oxide using Chemical and Physical Methods." *Colloids and Surfaces A*, 85, l-7.

Huang, C. P., and Fu, P. L. K. (1984). "Treatment of Arsenic(V)-Containing Water by the Activated Carbon Process." *J. WPCF*, 56(3), 233-242.

Huang, C. P., and Stumm, W. (1973). "Specific Adsorption of Cations on Hydrous g-Al_2O_3." *J. Colloid Interface Sci.*, 43, 409-420.

IMSL Fortran Library User's Guide, Math/Library (2003), Visual Numerics Inc., Houston, TX.

Ives, K. J., and Dibouni, M. A. (1979). "Orthokinetic Flocculation of Latex Microspheres." *Chem. Eng. Sci.*, 34, 989-991.

Jain, A., Raven, K. P., and Loeppert, R. H. (1999). "Arsenite and Arsenate Adsorption on Ferrihydrite: Surface Charge Reduction and Net OH^- Release Stoichiometry." *Environ. Sci. Technol.*, 33, 1179-1184.

Jeffrey, D. J., and Onishi, Y. (1984). "Calculation of the Resistance and Mobility Functions for Two Unequal Rigid Spheres in Low-Reynolds- Number Flow." *J. Fluid Mech.*, 139, 261-290.

Jiang, J. Q. (2001). "Removing Arsenic from Groundwater for the Developing World - A Review." *Wat. Sci. Tech.*, 44(6), 89-98.

Jiang, Q., and Logan, B. E. (1996). "Fractal Dimensions of Aggregates from Shear Devices." *J. AWWA*, 88, 100-113.

Johnson, C. P., Li, X., and Logan, B. E. (1996). "Settling Velocities of Fractal Aggregates." *Environ. Sci. Technol.*, 30(6), 1911-1918.

Jung, S. J., Amal, R., and Raper, J. A. (1996). "Monitoring Effects of Shearing on Floc

Structure Using Small-Angle Light Scattering." *Powder Technol.*, 88, 51-54.

Kao, S. V., and Mason, S. G. (1975). "Dispersion of Particles by Shear." *Nature*, 253, 619-621.

Kartinen, E. O., and Martin, C. J. (1995). "An Overview of Arsenic Removal Processes." *Desalination*, 103, 79-88.

Kihira, H., Ryde, N., and Matijevic, E. (1992). "Kinetics of Heterocoagulation 1. A Comparison of Theory and Experiment." *Colloids and Surfaces A*, 64, 317-324.

Kilps, J. R., Logan, B. E., and Alldredge, A. L. (1994). "Fractal Dimensions of Marine Snow Determined from Image Analysis of in situ Photographs." *Deep-Sea Research I.*, 41, 1159-1169.

Kim, J. W., and Kramer, T. A. (2005). "Improved Models for Fractal Colloidal Agglomeration: Computationally Efficient Algorithms." *Colloids and Surfaces A*, 253, 33-49

Kostoglou, M., and Konstandopoulos, A. G. (2001). "Evolution of Aggregate Size and Fractal Dimension during Brownian Coagulation." *J. Aerosol Sci.*, 32, 1399-1420.

Kramer, T. A. (2000). "Analytical Solutions for Bikinetic Coagulation: Incorporation of a Maximum Size Class." *J. Colloid Interface Sci.*, 227, 16-23.

Kramer, T. A., and Clark, M. M. (1997). "Influence of Strain-Rate on Coagulation Kinetics." *J. Environ. Eng., ASCE*, 123(5), 444-452.

Kramer, T. A., and Clark, M. M. (1999). "Incorporation of Aggregate Breakup in the Simulation of Orthokinetic Coagulation." *J. Colloid Interface Sci.*, 216, 116-126.

Kramer, T. A., and Clark, M. M. (2000). "Modeling Orthokinetic Coagulation in Spatially Varying Laminar Flow." *J. Colloid Interface Sci.*, 227, 251-261.

Kuhlmeier, P. D., and Sherwood, S. P. (1996). "Treatability of Inorganic Arsenic and Organoarsenicals in Groundwater." *Wat. Environ. Research*, 68(5), 946-951.

Kumar, S., and Ramkrishna, D. (1996a). "On the Solution of Population Balance Equations by Discretization - I. A fixed Pivot Technique." *Chem. Eng. Sci.*, 51(8), 1311-1332.

Kumar, S., and Ramkrishna, D. (1996b). "On the Solution of Population Balance Equations by Discretization - II. A Moving Pivot Technique." *Chem. Eng. Sci.*, 51(8), 1333-1342.

Kusters, K. A. (1991). *The Influence of Turbulence on Aggregate of Small Particles in Agitated Vessels*, Ph.D. dissertation, Eindhoven University of Technology, Netherlands.

Kusters, K. A., Wijers, J. G., and Thoenes, D. (1997). "Aggregation Kinetics of Small Particles in Agitated Vessels." *Chem. Eng. Sci.*, 52, 107-121.

Lagavankar, A. L., and Gemmell, R. S. (1968). "A Size-Density Relationship for Flocs." *J. AWWA*, 60, 1040-1046.

Lattuada, M., Wu, H., and Morbidelli, M. (2003). "A Simple Model for the Structure of Fractal Aggregates." *J. Colloid and Interface Sci.*, 268, 106-120.

Leckie, J. O., Benjamin, M., Hayes, K. F., Kaufman, G., and Altmann, S. (1980). "Adsoprtion/Coprecipitation of Trace Elements from Water with Iron Oxyhydroxide." *EPRI RP-910-1*, Electric Power Research Institute, Palo Alto, CA.

Letterman, R. D., Amirtharajah, A., and O'Melia, C. R. (1999). "Coagulation and Flocculation." *Water Quality and Treatment: A Handbook of Community Water Supplies*, R. D. Letterman, ed., McGraw-Hill, New York, 6.1-6.66

Levich, V. G. (1962). *Physicochemical Hydrodynamics*. Prentice-Hall, Englewood Cliffs, NJ.

Li, D. H., and Ganczarczyk, J. (1989). "Fractal Geometry of Particle Aggregates Generated in Water and Wastewater Treatment Processes." *Environ. Sci. Technol.*, 23, 1385-1389.

Li, X., and Zhang, J. (2003). "Numerical Simulation and Experimental Verification of Particle Coagulation Dynamics for a Pulsed Input." *J. Colloid Interface Sci.*, 262, 149-161.

Lin, M. Y., Klein, R., Lindsay, H. M., Weitz, D. A., Ball, R. C., and Meakin, P. (1990a). "The Structure of Fractal Colloidal Aggregates of Finite Extent." *J. Colloid and Interface Sci.*, 137(1), 263-280.

Lin, M. Y., Lindsay, H. M., Weitz, D. A., Ball, R. C., Klein, R., and Meakin, P. (1989a). "Universality in Colloid Aggregation." *Nature*, 339, 360-362.

Lin, M. Y., Lindsay, H. M., Weitz, D. A., Ball, R. C., Klein, R., and Meakin, P. (1989b). "Universality of Fractal Aggregates as Probed by Light Scattering." *Proc. R. Soc. Lond. A*, 423, 71-87.

Lin, M. Y., Lindsay, H. M., Weitz, D. A., Ball, R. C., Klein, R., and Meakin, P. (1990b). "Universal Reaction-Limited Colloid Aggregation." *Phys. Rev. A*, 41(4), 2005-2020.

Lin, M. Y., Lindsay, H. M., Weitz, D. A., Klein, R., Ball, R. C., and Meakin, P. (1990c). "Universal Diffusion-Limited Colloid Aggregation." *J. Phys.:Condens. Matter 2*, 2, 3093-3113.

Lin, T. F., and Wu, J. K. (2001). "Adsorption of Arsenite and Arsenate within Activated Alumina Granis: Equilibrium and Kinetics." *Water Research*, 35(8), 2049-2057.

Litster, J. D., Smit, D. J., and Hounslow, M. J. (1995). "Adjustable Discretized Population Balance for Growth and Aggregation." *AIChE J.*, 41(3), 591-603.

Lo, B., and Waite, T. D. (2000). "Structure of Hydrous Ferric Oxide Aggregates." *J. Colloid and Interface Sci.*, 222, 83-89.

Logan, B. E., and Kilps, J. R. (1995). "Fractal Dimensions of Aggregates Formed in Different Fluid Mechanical Environments." *Water Research*, 29(2), 443-453.

Lu, C. F., and Spielman, L. A. (1985). "Kinetics of Floc Breakage and Agglomeration in Agitated Liquid Suspensions." *J. Colloid Interface Sci.*, 103(1), 95-105.

Lumsdon, D. G., Fraser, A. R., Russel, J. D., and Livesey, N. T. (1984). "New Infrared Band Assignments for the Arsenate Ion Adsorbed on Synthetic Goethite (a-FeOOH)." *J. Soil Science*, 35, 381-386.

Magazu, S., Majolino, D., and Mallamace, F. (1989). "Fractal-Like Structures in Polystyrene Solutions Studied by Light Scattering Intensity." *Solid State Communications*, 70(3), 233-236.

Mahanty, J., and Ninham, B. W. (1976). *Dispersion Forces*. Academic Press, London ; New York.

Manceau, A. A. (1995). "The Mechanism of Anion Adsorption on Iron Oxides: Evidence for the Bonding of Arsenate Tetrahedra on Free $Fe(O,OH)_6$ Edges." *Geochim. Cosmochim. Acta*, 59(17), 3647-3653.

Manna, B. R., Dey, S., Debnath, S., and Ghosh, U. C. (2003). "Removal of Arsenic from Groundwater Using Crystalline Hydrous Ferric Oxide (CHFO)." *Water Qual. Res. J. Canada*, 38(1), 193-210.

Manning, B. A., and Goldberg, S. (1977). "Adsorption and Stability of Arsenic(III) at the Clay Mineral-Water Interface." *Environ. Sci. Technol.*, 31, 2005-2011.

Manning, B. A., and Goldberg, S. (1996). "Modeling Competitive Adsorption of Arsenate with Phosphate and Molybdate on Oxide Minerals." *Soil Sci. Sco. Am. J.*, 60, 121-131.

Manning, B. A., and Goldberg, S. (1997). "Adsorption and Stability of Arsenic(III) at the Clay Mineral-Water Interface." *Environ. Sci. Technol.*, 31, 2005-2011.

Manning, B. A., Fendorf, S. E., and Goldberg, S. (1998). "Surface Structures and Stability of Arsenic(III) on Goethite: Spectroscopic Evidence for Inner-Sphere Complexes." *Environ. Sci. Technol.*, 32, 2383-2388.

Marchal, P., David, R., Klein, J. P., and Villermaux, J. (1988). "Crystallization and Precipitation Engineering: I. An Efficient Method for Solving Population Balance in Crystallization with Agglomeration." *Chem. Eng. Sci.*, 43, 59-67.

Masscheleyn, P. H., Pardue, J. H., DeLaune, R. D., and Patrick, J., W. H. (1992). "Chromium Redox Chemistry in a Lower Mississippi Valley Bottomland Hardwood Wetland." *Environ. Sci. Technol.*, 26(6), 1217-1226.

Matis, K. A., Zouboulis, A. I., Malamas, F. B., Afonso, M. D. R., and Hudson, M. J. (1997). "Flotation Removal of As(V) onto Goethite." *Environmental Pollution*, 97, 239-245.

Matis, K. A., Zouboulis, A. I., and Valtadorou, A. V. (1999). "Sorption of As(V) by Goethite Particles and Study of Their Flocculation." *Water, Air, and Soil Pollution*, 111, 297-316.

McNeill, L. S., and Edwards, M. (1995). "Soluble Arsenic Removal at Water Treatment Plants." *J. AWWA*, 87(4), 105-113.

McNeill, L. S., and Edwards, M. (1997). "Predicting As Removal during Metal Hydroxide Precipitation." *J. AWWA*, 89(1), 75-86.

Meakin, P. (1988). "Fractal Aggregates." *Adv. Colloid Interface Sci.*, 28, 249-331.

Meakin, P., and Jullien, R. (1988). "The Effects of Restructuring on the Geometry of Clusters Formed by Diffusion-Limited, Ballistic, and Reaction-Limited Cluster-Cluster Aggregation." *J. Chem. Phys.*, 89, 246-250.

Mei, R., and Hu, K. C. (1999). "On the Collision Rate of Small Particles in Turbulent Flows." *J. Fluid Mech.*, 391, 67-89.

Melis, S., Verduyn, M., Storti, G., Morbidelli, M., and Baldyga, J. (1999). "Effect of Fluid Motion on the Aggregatin of Small Particles Subject to Interaction Forces." *AIChE J.*, 45(7), 1383-1393.

Meng, X., Bang, S., and Korfiatis, G. P. (2000). "Effects of Silicate, Sulfate, and Carbonate on Arsenic Removal by Ferric Chrolide." *Water Research*, 34(4), 1255-1261.

Mishra, V., Kresta, S. M., and Masliyah, J. H. (1998). "Self-Preserving of the Drop Size Distribution Function and Variation in the Stability Ratio for Rapid Coalescence of a Polydisperse Emulsion in a Simple Field." *J. Colloid Interface Sci.*, 197, 57-67.

Odriozola, G., Schmitt, A., Callejas-Fernandez, J., Martinez-Garcia, R., and Hidalgo-Alvarez, R. (1999). "Dynamic Scaling Concepts Applied to Numerical Solutions of Smoluchowski's Rate Equation." *J. Chem. Phys.*, 111(16), 7657-7667.

Odriozola, G., Tirado-Miranda, M., Schmitt, A., Lopez, F. M., Callejas-Fernandez, J., Martinez-Garcia, R., and Hidalgo-Alvarez, R. (2001). "A Light Scattering Study of the Transition Region between Diffusion- and Reaction-Limited Cluster Aggregation." *J. Colloid and Interface Sci.*, 240, 90-96.

Oles, V. (1992). "Shear-Induced Aggregation and Breakup of Polystyrene Latex Particles." *J. Colloid Interface Sci.*, 154(2), 351-358.

O'Melia, C. R., and Tiller, C. L. (1993). "Physicochemical Aggregation and Deposition in Aquatic Environments." *Environmental Particles*, J. Buffle and H. P. Leeuwen, eds., Lewis Publishers, Boca Raton, FL, 353-386.

Oscarson, D. W., Huang, P. M., Liaw, W. K., and Hammer, U. T. (1983). "Kinetics of Oxidation of Arsenite by Various Manganese Dioxides." *Soil Sci. Sco. Am. J.*, 47, 644-648.

Overbeek, J. T. G. (1952). "Kinetics of Flocculation." *Colloid Science*, H. R. Kruyt, ed., Elsevier, Amsterdam ; Houston, 278-301.

Pailthorpe, B. A., and Russel, W. B. (1982). "The Retarded van der Waals Interaction between Spheres." *J. Colloid Interface Sci.*, 89, 563-566.

Pandya, J. D., and Spielman, L. A. (1982). "Floc Breakage in Agitated Suspensions: Effect of Agitation Rate." *Chem. Eng. Sci.*, 38(12), 1983-1992.

Papadiamas, S. P., Chowdhury, Z. K., and Fery, M. (1997). "Development of Treatment and Residual Cost Curves for Arsenic Removal." *Proceedings of the AWWA Annual*

Conference, Atlanta, GA, 629-673.

Parker, D. S., Kaufman, W. J., and Jenkins, D. (1972). "Floc Breakup in Turbulent Flocculation Process." *J. Sanit. Eng. Div. ASCE*, 98(SA1), 79-99.

Patil, D. P., Andrews, J. R. G., and Uhlherr, P. H. T. (2001). "Shear Flocculation - Kinetics of Floc Coalescence and Breakage." *Int. J. Miner Process.*, 61, 171-188.

Peterson, T. W. (1986). "Similarity Solutions for the Population Balance Equation Describing Particle Fragmentation." *Aerosol Sci. Technol.*, 5, 93-101.

Pierce, M. L., and Moore, C. B. (1980). "Adsorption of Arsenite on Amorphous Iron Hydroxide from Dilute Aqeous Solution." *Environ. Sci. Technol.*, 14(2), 214-216.

Pierce, M. L., and Moore, C. B. (1982). "Adsorption of Arsenite and Arsenate on Amorphous Iron Hydroxide." *Water Research*, 16, 1247-1253.

Pontius, F. W., Brown, K. G., and Chen, C. J. (1994). "Health Implications of Arsenic in Drinking Water." *J. AWWA*, 86(9), 52-61.

Prasher, C. L. (1987). *Crushing and Grinding Process Handbook*, Wiley, New York.

Rahmani, N. H. G., Masliyah, J. H., and Dabros, T. (2003). "Characterization of Asphaltenes Aggregation and Fragmentation in a Shear Field." *AIChE J.*, 49(7), 1645-1655.

Ramkrishna, D. (1985). "The Status of Population Balance." *Reviews in Chemical Engineering*, 3(1), 49-95.

Randolph, A. D., and Larson, M. A. (1988). *Theory of Particulate Processes*, Academic Press, New York.

Raven, K. P., Jain, A., and Loeppert, R. H. (1998). "Arsenite and Arsenate Adsorption on Ferrihydrite: Kinetics, Equilibrium, and Adsorption Envelopes." *Environ. Sci. Technol.*, 32, 344-349.

Ray, D. T., and Hogg, R. (1986). "Agglomerate Breakage in Polymer-Flocculated Suspensions." *J. Colloid Interface Sci.*, 116(1), 256-268.

Robins, R. G. (2001). "Removal of Arsenic from Drinking Water by Precipitation, Adsorption or Cementation." *BUET-UNU International Workshop on Technologies for Arsenic Removal from Drinking Water*, Dhaka, Bangladesh, 31-42.

Robinson, R. B., Demirel, T., and Baumann, E. R. (1981). "Identity and Character of Iron Precipitates." *J. Environ. Eng., ASCE*, 107(EE6), 1211-1227.

Rosenblum, E., and Clifford, D. (1982). "The Equilibrium Arsenic Capacity of Activated Alumina." *UHCE 83-06*, US EPA.

Russel, W. B., Saville, D. A., and Schowalter, W. R. (1989). *Colloidal Dispersions*. Cambridge University Press, Cambridge.

Saffman, P. G., and Turner, J. S. (1956). "On the Collision of Drops in Turbulent Clouds." *J. Fluid Mech.*, 1, 16-30.

Sandkuhler, P., Sefcik, J., Lattuada, M., Wu, H., and Morbidelli, M. (2003). "Modeling Structure Effects on Aggregation Kinetics in Colloidal Dispersions." *AIChE J.*, 49(6), 1542-1555.

Sato, D., Kobayashi, M., and Adachi, Y. (2004). "Effect of Floc Structure on the Rate of Shear Coagulation." *J. Colloid and Interface Sci.*, 272, 345-351.

Schaefer, D. W. (1989). "Polymers, Fractals, and Ceramic Materials." *Science*, 243(4894), 1023-1027.

Schaefer, D. W., Martin, E., Wiltzius, P., and Cannell, D. S. (1984). "Fractal Geometry of Colloidal Aggregates." *Phys. Rev. Lett.*, 52(26), 2371-2374.

Schenkel, J. H., and Kitchener, J. A. (1960). "A Test of the Derjaguin-Verwey-Overbeek Theory with a Colloidal Suspension." *Trans. Faraday Soc.*, 56, 161-173.

Schindler, P. W., and Stumm, W. (1987). "The Surface Chemistry of Oxides, Hydroxides, and Oxide Minerals." *Aquatic Surface Chemistry*, W. Stumm, ed., Wiley-Interscience, New York, 83-110.

Schmitt, A., Odriozola, G., Moncho-Jorda, A., Callejas-Fernandez, J., Martinez-Garcia, R., and Hidalgo-Alvarez, R. (2000). "Multiple Contact Kernel for Diffusionlike Aggregation." *Phys. Rev. E*, 62(6), 8335-8343.

Schwertmann, U., and Cornell, R. M. (2000). *Iron Oxides in the Laboratory: Preparation and Characterization*. Wiley-VCH, Weinheim ; New York.

Schwertmann, U., Friedl, J., and Stanjek, H. (1999). "From Fe(III) Ions to Ferrihydrite and then to Hematite." *J. Colloid Interface Sci.*, 209, 215-223.

Scott, K. N., Green, J. F., Do, H. D., and McLean, S. J. (1995). "Arsenic Removal by

Coagulation." *J. AWWA*, 87(4), 114-126.

Scott, W. T. (1968). "Analytical Studies of Cloud Droplet Coalescence I." *J. Atmos. Sci.*, 25, 54-65.

Selomulya, C., Amal, R., Bushell, G., and Waite, T. D. (2001). "Evidence of Shear Rate Dependence on Restructuring and Breakup of Latex Aggregates." *J. Colloid Interface Sci.*, 236, 66-77.

Selomulya, C., Bushell, G., Amal, R., and Waite, T. D. (2002). "Aggregation Mechanisms of Latex of Different Particle Sizes in a Controlled Shear Environment." *Langmuir*, 18(6), 1974-1984.

Serra, T., and Casamitjana, X. (1998a). "Effect of the Shear and Volume Fraction on the Aggregation and Breakup of Particles." *AIChE J.*, 44(8), 1724-1730.

Serra, T., and Casamitjana, X. (1998b). "Structure of the Aggregates during the Process of Aggregation and Breakup under a Shear Flow." *J. Colloid Interface Sci.*, 206, 505-511.

Serra, T., and Casamitjana, X. (1999). "Effect of the Shear and Volume Fraction on the Aggregation and Breakup of Particles." *AIChE J.*, 44(8), 1724-1730.

Serra, T., Colomer, J., and Casamitjana, X. (1997). "Aggregation and Breakup of Particles in a Shear Flow." *J. Colloid Interface Sci.*, 187, 466-173.

Shen, Y. S. (1973). "Study of Arsenic Removal from Drinking Water." *J. AWWA*, 65(9), 543-548.

Singh, U., and Uehara, G. (1998). "Electrochemistry of the Double-Layer: Principles and Applications to Soils." *Soil Physical Chemistry*, D. L. Sparks, ed., CRC Press, Boca Raton, FL, 1-46

Smoluchowski, M. V. (1917). "Versuch einer mathematischen Theorie der Koagulationskinetik kolloider Losungen." *Z. Physk. Chem.*, 92, 129-168.

Sonntag, R. C., and Russel, W. B. (1986). "Structure and Breakup of Floc Subjected to Fluid Stresses: I. Shear Experiments." *J. Colloid Interface Sci.*, 113, 399-413.

Sonntag, R. C., and Russel, W. B. (1987). "Structure and Breakup of Floc Subjected to Fluid Stresses: II. Theory." *J. Colloid Interface Sci.*, 115, 378-389.

Sorg, T. J., and Logsdon, G. S. (1978). "Treatment Technology to Meet the Interim

Primary Drinking Water Regulations for Inorganics: Part 2." *J. AWWA*, 70(7), 379-393.

Sparks, D. L. (1999). "Kinetics and Mechanisms of Chemical Reactions at the Soil Mineral/Water Interface." *Soil Physical Chemistry*, D. L. Sparks, ed., CRC Press, Boca Raton, FL, 135-191.

Spicer, P. T., Keller, W., and Pratsinis, S. E. (1996). "The Effects of Impeller Type on Floc Size and Structure during Shear-Induced Flocculation." *J. Colloid Interface Sci.*, 184, 112-122.

Spicer, P. T., and Pratsinis, S. E. (1996a). "Coagulation and Fragmentation: Universal Steady-State Particle-Size Distribution." *AIChE J.*, 42(6), 1612-1620.

Spicer, P. T., and Pratsinis, S. E. (1996b). "Shear-Induced Flocculatoin: The Evolution of Floc Structure and the Shape of the Size Distribution at Steady State." *Water Research*, 30(5), 1049-1056.

Spicer, P. T., Pratsinis, S. E., Raper, J., Amal, R., Bushell, G., and Meesters, G. (1998). "Effect of Shear Schedule on Particle Size, Density, and Structure During Flocculation in Stirred Tanks." *Powder Technol.*, 97(1), 26-34.

Spielman, L. A. (1970). "Viscous Interactions in Brownian Coagulation." *J. Colloid Interface Sci.*, 33, 562-571.

Squires, T. M., and Brenner, M. P. (2000). "Like-Charge Attraction and Hydrodynamic Interaction." *Phys. Rev. Lett.*, 85, 4976-4979.

Stumm, W., and Morgan, J. J. (1995). *Aquatic Chemistry: Chemical Equilibria and Rates in Natural Waters*. Wiley Interscience, New York.

Suarez, D. L., Goldberg, S., and Su, C. (1998). "Evaluation of Oxyanion Adsorption Mechanisms on Oxides Using FTIR Spectroscopy and Electrophoretic Mobility." *Mineral-Water Interfacial Reactions - Kinetics and Mechanisms*, D. L. Sparks and T. J. Grundl, eds., ACS, Washington, D.C., 136-178.

Subramaniam, K., Yiacoumi, S., and Tsouris, C. (1998). "A Unified Model for Ion Sorption Kinetics and Colloidal Particle Flocculation Rates." *Fundamentals of Adsorption,* 6, 951-956.

Sun, X., and Doner, H. E. (1996). "An Investigation of Arsenate and Arsenite Bonding Structures on Goethite by FTIR." *Soil Science*, 161(12), 865-872.

Suzuki, T. M., Bomani, J. O., Matsunaga, H., and Yokoyama, T. (2000). "Preparation of

Porous Resin Loaded with Crystalline Hydrous Zirconium Oxide and Its Application to the Removal of Arsenic." *Reactive & Functional Polymers*, 43, 165-172.

Swedlund, P. J., and Webster, J. G. (1999). "Adsorption and Polymerisation of Silicic Acid on Ferrihydrite, and Its Effect on Arsenic Adsorption." *Water Research*, 33(16), 3413-3422.

Swift, D. L., and Friedlander, S. K. (1964). "The Coagulation of Hydrosols by Brownian Motion and Laminar Shear Flow." *J. Colloid Science*, 19, 621-647.

Tambo, N., and Watanabe, Y. (1979a). "Physical Aspect of Flocculation Process-I. Fundemental Treatise." *Water Research*, 13, 429-439.

Tambo, N., and Watanabe, Y. (1979b). "Physical Characteristics of Flocs-I. The Floc Density Fuction and Aluminium Floc." *Water Research*, 13, 409-419.

Tang, S. (1999). "Prediction of Fractal Properties of Polystyrene Aggregates." *Colloids and Surfaces A*, 157, 185-192.

Tang, S., Ma, Y., and Shiu, C. (2001). "Modeling the Mechanical Strength of Fractal Aggregates." *Colloids and Surfaces A*, 180, 7-16.

Tang, S., Preece, J. M., McFarlance, M., and Zhang, Z. (2000). "Fractal Morphology and Breakage of DLCA and RLCA Aggregates." *J. Colloid and Interface Sci.*, 221, 114-123.

Taylor, G. I. (1935). "Statistical Theory of Turbulence." *Proceedings of the Royal Society, Series A. Mathematical and Physical Science*, 151, 421-478.

Tchoubar, D., Bottero, J. Y., Quienne, P., and Arnaud, M. (1991). "Partial Hydrolysis of Ferric Chloride Salt. Structural Investigation by Photon-Correlation Sepctroscopy and Small-Angle X-ray Scattering." *Langmuir*, 7, 398-402.

Thanabalasingam, P., and Pickering, W. F. (1986). "Effect of pH on Interaction between As(III) or As(V) and Manganese(IV) Oxide." *Water, Air, and Soil Pollution*, 29, 205-216.

Thirunavukkarasu, O. (2002). "Removal of Arsenic From Drinking Water," Ph.D. Thesis, University of Regina (Canada).

Thirunavukkarasu, O., Viraraghavan, T., and Subramaniam, K. (2003). "Arsenic Removal from Drinking Water Using Granular Ferric Hydroxide." *Water SA*, 29(2), 161-170.

Thomas, C. J. (1999). "Design and Analysis of An Improved Apparatus for the Study of Mixing and Coagulation," M.S. thesis, Auburn University, Auburn, AL.

Thomas, D. G. (1964). "Turbulent Disruption of Flocs in Small Particle Suspensions." *AIChE J.*, 10, 517-523.

Tien, C. (1994). *Adsorption Calculations and Modeling*. Butterworth-Heinemann, Boston.

Torres, F. E., Russel, W. B., and Schowalter, W. R. (1991). "Floc Structure and Growth Kinetics for Rapid Shear Coagulation of Polystyrene Colloids." *J. Colloid and Interface Sci.*, 142(2), 554-574.

Torres, F. E., Russel, W. B., and Schowalter, W. R. (1991). "Simulation of Coagulation in Viscous Flows." *J. Colloid Interface Sci.*, 145(1), 51-73.

Trevelyan, B. J., and Mason, S. G. (1951). "Particle Motions in Sheared Suspension: I. Rotations." *J. Colloid and Interface Sci.*, 6, 354-367.

USEPA. (2000). "Arsenic Occurrence in Public Drinking Water Supplies." *EPA-815-R-00-023*, US EPA, Washington, D.C.

USEPA. (2001a). "Drinking Water Standard for Arsenic." U.S. EPA, Washington, D.C.

USEPA. (2001b). "Arsenic in Drinking Water - Treatment Technologies: Removal." U.S. EPA, Washington, D.C.

Vaishya, R. C., and Gupta, S. K. (2003). "Arsenic Removal from Groundwater by Iron Impregnated Sand." *J. Environ. Eng., ASCE*, 129(1), 89-92.

Valioulis, I. A., and List, E. J. (1984). "Collision Efficiencies of Diffusing Spherical Particles: Hydrodynamic, van der Waals and Electrostatic Forces." *Adv. Colloid Interface Sci.*, 20, 1-20.

van de Ven, T. G. M., and Mason, S. G. (1976). "The Microrheology of Colloidal Dispersions - IV. Paris of Interacting Spheres in Shear Flow." *J. Colloid Interface Sci.*, 57(3), 505-516.

van de Ven, T. G. M., and Mason, S. G. (1977). "The Microrheology of Colloidal Dispersions VII. Orthokinetic Doublet Formation of Spheres." *Colloid & Polymer Sci.*, 255, 468-479.

Vanni, M. (1999). "Discretization Procedure for the Breakage Equation." *AIChE J.*, 45(4), 916-919.

Vanni, M. (2000). "Approximate Population Balance Equations for Aggregation-Breakage Processes." *J. Colloid Interface Sci.*, 221, 143-160.

Vanni, M., and Baldi, G. (2002). "Coagulation Efficiency of Colloidal Particles in Shear Flow." *Adv. Colloid Interface Sci.*, 97, 151-177.

Venema, P., Hiemstra, T., and Riemsdijk, W. H. (1996). "Comparison of Different Site Binding Models for Cation Sorption: Description of pH Dependency, Salt Dependency, and Cation-Proton Exchange." *J. Colloid and Interface Sci.*, 181, 45-59.

Waite, T. D., Cleaver, J. K., and Beattie, J. K. (2001). "Aggregation Kinetics and Fractal Structure of g-Alumina Assemblages." *J. Colloid Interface Sci.*, 241, 333-339.

Wang, G. M., and Sorensen, C. M. (1999). "Diffusive Mobility of Fractal Aggregates over Entire Knudsen Number Range." *Phys. Rev. E*, 60(3), 3036-3044.

Wang, Q. (1992). "A Study on Shear Coagulation and Heterocoagulation." *J. Colloid Interface Sci.*, 150(2), 418-427.

Waychunas, G. A., Davis, J. A., and Fuller, C. C. (1995). "Geometry of Sorbed Arsenate on Ferrihydrite and Crystalline FeOOH: Re-Evaluation of EXAFS Results and Topological Factors in Predicting Sorbate Geomtry, and Evidence for Monodentate Complexes." *Geochimica et Cosmochimica Acta*, 59(17), 3655-3661.

Waychunas, G. A., Fuller, C. C., Rea, B. A., and Davis, J. A. (1996). "Wide Angle X-ray Scattering, WAXS Study of Two-Line Ferrihydrite Structure: Effect of Arsenate Sorption and Counterion Variation and Comparison with EXAFS Results." *Geochim. Cosmochim. Acta*, 60, 1765-1781.

Waychunas, G. A., Rea, B. A., Fuller, C. C., and Davis, J. A. (1993). "Surface Chemistry of Ferrihydrite: Part 1. EXAFS Studies of the Geometry of Coprecipitated and Adsorbed Arsenate." *Geochimica et Cosmochimica Acta*, 57, 2251-2269.

Weerasooriya, R., Tobschall, H. J., Wijesekara, H. K. D. K., Arachchige, E. K. I. A. U. K., and Pathirathne, K. A. S. (2003). "On the Mechanistic Modeling of As(III) Adsorption on Gibbsite." *Chemosphere*, 51, 1001-1013.

Weidler, P. G., and Stanjek, H. (1998). "The Effect of Dry Heating of Synthetic 2-Line and 6-Line Ferrihydrite: II. Surface Area, Porosity and Fractal Dimension." *Clay Minerals*, 33, 277-284.

Weitz, D. A., Huang, J. S., Lin, M. Y., and Sung, J. (1984). "Dynamics of Diffusion-Limited Kinetic Aggregation." *Phys. Rev. Lett.*, 53(17), 1657-1660.

Weitz, D. A., and Oliveria, M. (1984). "Fractal Structures Formed by Kinetic Aggregation of Aqueous Gold Colloids." *J. Phys. Rev. Lett.*, 52, 1433-1436.

Weitz, D. A., Huang, J. S., Lin, M. Y., and Sung, J. (1985). "Limits of the Fractal Dimension for Irreversible Kinetic Aggregation of Gold Colloids." J. Phys. Rev. Lett., 54, 1416-1419.

Westall, J. C., and Hohl, H. (1980). "A Comparison of Electrostatic Models for the Oxide/Solution Interface." *Adv. Colloid Interface Sci.*, 12, 265-294.

White, F. M. (1991). *Viscous Fluid Flow*, 2 ed. McGraw-Hill Inc., New York, NY.

Wiesner, M. R., and Mazounie, K. (1987). "Raw Water Characteristics and Selection of Water Treatment Configurations for Particle Removal." *J. AWWA*, 81(5), 80-89.

Wilkie, J. A., and Hering, J. G. (1996). "Adsorption of Arsenic onto Hydrous Ferric Oxide: Effects of Adsorbate/Adsorbent Ratio and Co-occuring Solutes." *Colloids and Surfaces A*, 109, 97-110.

Witten, T. A., and Cates, M. E. (1986). "Tenuous Structures from Disorderly Growth Processes." *Science*, 232(4758), 1607-1612.

Xu, H., Allard, B., and Grimvall, A. (1988). "Influence on pH and Organic Substance on the Adsorption of As(V) on Geologic Materials." *Water, Air, and Soil Pollution*, 40, 293-305.

Xu, H., Allard, B., and Grimvall, A. (1991). "Effects of Acidification and Natural Organic Materials on the Mobility of Arsenic in the Environment." *Water, Air, and Soil Pollution*, 57-58, 269-278.

Yeung, A. K. C., and Pelton, R. (1996). "Micromechanics: A New Approach to Studying the Strength and Breakup of Flocs." *J. Colloid Interface Sci.*, 184, 579-585.

Yoshida, I., Kobayashi, H., and Ueno, K. (1976). "Selective Adsorption of Arsenic Ions on Silica Gel Impregnated with Ferric Hydroxide." *Analytical Letters*, 9(12), 1125-1133.

Zeichner, G. R., and Schowalter, W. R. (1977). "Use of Trajectory Analysis to Study Stability of Colloidal Dispersions in Flow Fields." *AIChE J.*, 23(3), 243-254.

Zeichner, G. R., and Schowalter, W. R. (1979). "Effects of Hydrodynamic and Colloidal

Forces on the Coagulation of Dispersions." *J. Colloid Interface Sci.*, 71(2), 237-253.

Zhang, J., and Buffle, J. (1996). "Multi-method Determination of the Fractal Dimension of Hematite Aggregates." *Colloids and Surfaces A*, 107, 175-187.

Zhang, J., and Li, X. (2003). "Modeling Particle-Size Distribution Dynamics in a Flocculation Systems." *AIChE J.*, 49(7), 1870-1882.

Zhang, Y. U., Yang, M., and Huang, X. (2003). "Arsenic(V) Removal with a Ce(IV)-Doped Iron Oxide Adsorbent." *Chemosphere*, 51, 945-952.

Ziff, R. M. (1991). "New Solutions to the Fragmentation Equation." *J. Phys. A: Math. Gen.*, 24, 2821-2828.

Ziff, R. M., and McGrady, E. D. (1985). "The Kinetics of Cluster Fragmentation and Depolymerisation." *J. Phys. A: Math. Gen.*, 18, 3027-3037.

Zollars, R. L., and Ali, S. I. (1986). "Shear Coagulation in the Presence of Repulsive Interparticle Forces." *J. Colloid Interface Sci.*, 114(1), 149-166.

Zouboulis, A. I., Kydros, K. A., and Matis, K. A. (1993). "Arsenic(III) and Arsenic(V) Removal from Solution by Pyrite Fines." *Separation Science and Technology*, 28, 2449-2463.

VITA

Jin-Wook Kim (email: waterkim@hotmail.com)

Academic History

- Ph.D. Civil Engineering, Texas A&M University, Texas (August 2005)
- M.S. Civil Engineering, Yonsei University, South Korea (February 1994)
- B.S. Civil Engineering, Yonsei University, South Korea (February 1992)

Experience

- *Research Assistant, Texas A&M University, Texas (2001 to 2005)*

- Removal of Toxic Compounds from Contaminated Water by Sorption and Coagulation.
- Advanced Simultaneous Oxidation and Reduction of Toxic Compounds.
- North Texas Municipal Water District Taste and Odor Study (PAC Testing)
- Desalination Using Capacitive De-ionization: An Evaluation of the CDT Aquacell.

- *Researcher, Yonsei University Engineering Research Institute, Korea (1998 to 2000)*

- Development of Decontamination System for Dredged Materials from River and Lake.
- Waste Sludge Volume Reduction & Contaminated Soil Washing Using Ultrasound.

- *Assistant manager, Daewoo E&C Co., Korea (1995 to 1998)*

- Design/Construct Project to Provide Wastewater Reuse and Tertiary Treatment System
- Preparation of a Management Plan for Large Scale Sewage Treatment Plants, Korea.

Intellectual Contributions

“Adjustable Discretized Population Balance Equations: Numerical Simulation and Parameter Estimation for Fractal Aggregation and Break-up”, J. W. Kim and T. A. Kramer (2005), *Colloids and Surfaces A* (Submitted for Review).

“Improved Orthokinetic Coagulation Models for Fractal Colloids: Aggregation and Break-Up”, J. W. Kim and T. A. Kramer (2005), *Chemical Engineering Science* (In Press).

“Improved Models for Fractal Colloidal Agglomeration: Computationally Efficient Algorithms”, J. W. Kim and T. A. Kramer (2005), *Colloids and Surfaces A,* 253(1-3), 33-49.

“Particle Aggregation and Break-up Modeling”, T. A. Kramer and J. W. Kim, *Recent Development in Colloids & Interface Research* (S. G. Pandalai, Managing Ed.), 1, 313-346, Transworld Research Network (2003).